Records of paleomagnetic field intensity in sediments : Crossover approach between relative paleointensity and cosmogenic ^{10}Be

Tatiana Savranskaia

Thèse préparée

A L'UNIVERSITÉ DE PARIS

École doctorale STEP'UP - ED №560

IPGP-Équipe de paléomagnétisme

Records of paleomagnetic field intensity in sediments: Crossover approach between relative paleointensity and cosmogenic ^{10}Be

Par

Tatiana Savranskaia

présentée et soutenue publiquement

le 20 juillet 2020

Thèse de doctorat de Science de la Terre et de l'Environnement

dirigée par **Dr. Jean-Pierre Valet**

& **Dr. Ramon Egli**

devant un jury composé de :

Pr. Valeriy Shcherbakov, (Institute of Physics of the Earth RAS, Russia)	Rapporteur
Dr. Hella Wittmann-Oelze, (GFZ, Germany)	Rapporteur
Dr. Julien Bouchez , (Institut de Physique du Globe de Paris, France)	Examinateur
Pr. Raimund Muscheler, (Lund University, Sweden)	Examinateur
Dr. Mioara Mandea, (CNES, France)	Présidente du jury
Dr. Jean-Pierre Valet, (Institut de Physique du Globe de Paris, France)	Directeur de thèse
Dr. Ramon Egli, (Central Institution for Meteorology and Geodynamics, Austria)	Co-Directeur de thèse

Acknowledgements

This thesis is the result of multiple interactions, each of which have contributed to the final result. First of all, I would like to thank my Ph.D. adviser Jean-Pierre Valet, who had faith in me and involved me in EDIFICE project, giving a chance to work on such a spectacular subject. I infinitely grateful to my co - adviser Ramon Egli for his enthusiasm and inquiring mind set, from whom I have learnt a lot. I definitely indebted to my advisers for the support, encouragements, and being a great model of great researchers. I also thank Laure Meynadier for her guidance, advising, and original ideas, that definitely helped for achieving the final result. My deepest thanks to all jury members for their careful examination of the thesis as well as for their valuable comments and remarks, that helped to improve the final version of this manuscript.

I want to thank the people, with whom we spend many hours of sampling : Anojh Thevarasan, Anouk Villedieu, Naoufel Haddam, Laetitia Gacem, Sandrine Choy. Thanks to Anojh Thevarasan for helping with magnetic measurements, Anouk and Naoufel - with microtektite counting and carbonate measurement, Franck Bassinot and Isabelle Billy - with XRF measurements, the whole CEREGE team (Simon Quentin, Didier Bourlès, Nicolas Thouveny, ASTER team) - with measurements of beryllium isotopes. Many thanks to the whole paleomagnetism group at IPGP, especially Sylvie Larousse for managing the administrative routines and France Lagroix for her encouragments. I'm grateful to be surrounded by great people during this project at IPGP, with whom we have made friendship, spent very good moments, and shared delicious dark chocolate - Delphine Tardif, Marie Troyano, Martin Fillon, Venkatesh Gopinath, Stasya Akimova, Guillaume Ropp, Sophie Vicente De Gouveia, Marina Rosas Carbajal, Jian Gong, Sergei Abramenkov, and special thanks to Sabrina Sanchez for guiding my first steps in Matlab!

Enormous support of my parents and sister have made this work possible. Finally, I dedicate this thesis to my soulmate Mehdi Ouadjou, who have made with me this thorny way to the PhD.

Summary

The direction and strength of geomagnetic field had been evolving continuously in the past. One of the few means of obtaining continuous reconstructions of this evolution relies on sedimentary records. The latter are therefore important for understanding the geodynamo and the underlying evolution of the Earth's interior, as well as providing an important dating tool through magnetostratigraphy. Sedimentary records of geomagnetic field variations rely on two main recording mechanisms: the alignment of magnetic particles, which underlies continuous records of relative paleointensity (RPI), and the archivation of cosmogenic isotopes, in particular ^{10}Be, whose production by cosmic ray spallation is modulated by the screening action of the dipole component of the Earth's field.

Previous studies reported similarities as well as significant differences between RPI and cosmogenic ^{10}Be (expressed as ^{10}Be/^{9}Be) records. While a perfect match of the two records is not expected due to environmental contaminations present in both records, the similar changes during the periods characterised by significant decrease of the dipole moment are suggested owning to global field strength control of ^{10}Be production and attenuation of non-dipolar features in RPI records measured within the sediments with the low sedimentation rates (<10 cm/ka). The exact field recording mechanism and its environmental modulation is poorly understood. The aim of the present work was to improve our present knowledge on the field recording mechanisms of marine sediments, in particular:

1. The environmental factors responsible for ^{10}Be transport and removal from the water column, and the effect of source distributions on ^{9}Be supply.

2. The effect of post-depositional processes, in particular sediment mixing, on ^{10}Be and RPI records.

3. The mechanism by which a post-depositional magnetization is acquired near the bottom of the surface mixed layer.

4. The causes of a systematic lag between ^{10}Be and RPI records, and the environmental factors affecting RPI.

In order to disentangle the environmental and magnetic contribution in sedimentary ^{10}Be/^{9}Be records, we analysed five records, covering the last geomagnetic reversal. The different recording characteristics at the five sites have been described in terms of additive and multiplicative climatic modulations, which depend essentially on water depth, location along large oceanic current systems, and distance to the coast. Simple criteria have been derived for the identification of most suited sites yielding minimal environmental contaminations. Even so, climatic overprints remain significant, especially outside of large geomagnetic events.

RPI records are strongly affected by post-depositionary processes, in particular sediment mixing, which is entirely responsible for the natural remanent magnetization (NRM) acquired by bioturbated sediments, and its lag with respect to ^{10}Be records. A new bioturbation model has been developed to explain sedimentary NRM in bioturbated sediment. This model includes a newly discovered phenomenon of size segregation in the surface mixed layer (SML), analogous to the well-known Brazil nut effect. Size segregation is responsible for the longer permanence of larger particles in the SML, up to the limit case of ferromanganese nodules. Size segregation has important implications for sediment dating with benthic foraminifera, since large tests tend to be shifted upwards with respect of regular-sized sediment particles of same age. Calibration of the bioturbation model with microtektite profiles from two Indian Ocean cores enabled to reproduce the correct degree of delay between ^{10}Be and RPI records, as well the environmental dependence of RPI in two cores from the North Atlantic and the Equatorial Pacific Oceans.

The results obtained in this work can help in developing integrated approaches for the correction of climatic contaminations in ^{10}Be and RPI records. Examples include the integration of ^{10}Be and ^{9}Be transport in global oceanic circulation models and the separated normalization of individual magnetic mineral contributions to the RPI signal. Furthermore, the predictive power of the bioturbation-based model for NRM acquisition can be used to design new laboratory experiments for the simulation of specific magnetic recording mechanisms.

For the first time, commonly used for stratigraphic records reconstruction, microtektite profile was shown to be an inappropriate function. We have demonstrated the Brazilian-nut effect on the microtektite particles, that consists in size-dependent fragments segregation. Size segregation model allows to estimate the actual depth of sediment mixing due to the bioturbation, once the additional velocity component related to the migration of larger particles upwards in the sedimentary column has been accounted for. The results of this research have significant importance not only for the sediment mixing response characterisation and reconstruction of affected by bioturbation processes records (e.g. ^{10}Be/^{9}Be), but also for assessment the age models validity, that are constrained by conservative tracer ages.

In-detail comparison of ^{10}Be/^{9}Be and RPI allowed to determine the lock-in depth in the sediments from West-Pacific and North Atlantic Oceans. Among various sediment properties, the magnetic minerals concentration was shown to correlate with lock-in depths estimates in West-Pacific sediments. The decrease in magnetic minerals sizes seems to be related to global temperature / sea level variations. Linear decrease of magnetic particle sizes with decreasing water depth during glacial isotopic stages, was figured out in terms of enhanced primary productivity for equatorial West-Pacific site.

Résumé

La direction et l'intensité du champ géomagnétique ont continuellement évolué dans le passé. L'un des rares moyens d'obtenir des reconstitutions continues de cette évolution repose sur les enregistrements sédimentaires. Ces dernières sont donc importants pour comprendre la géodynamo et l'évolution sous-jacente de l'intérieur de la Terre, ainsi que pour fournir un outil de datation important grâce à la magnétostratigraphie. Les enregistrements sédimentaires des variations du champ géomagnétique reposent sur deux mécanismes d'enregistrement principaux : l'alignement des particules magnétiques, qui sous-tend les enregistrements continus de la paléointensité relative (RPI), et l'archivage des isotopes cosmogéniques, en particulier le ^{10}Be, dont la production s'effectue par la spallation des rayons cosmiques est modulée par l'action de filtrage de la composante dipolaire du champ terrestre.

Des études antérieures ont fait état de similitudes ainsi que de différences significatives entre les enregistrements RPI et ^{10}Be cosmogéniques (exprimés en ^{10}Be/^{9}Be). Bien que l'on ne s'attende pas à une concordance parfaite des deux enregistrements en raison des contaminations environnementales présentes dans les deux enregistrements, les changements similaires au cours des périodes caractérisées par une diminution significative du moment dipolaire sont suggérés grâce au contrôle global du champ de production de ^{10}Be et à l'atténuation des caractéristiques non dipolaires dans les enregistrements RPI mesurés dans les sédiments avec les faibles taux de sédimentation (<10 cm/ka). Le mécanisme exact d'enregistrement du champ et sa modulation environnementale sont mal compris. L'objectif du présent travail était d'améliorer nos connaissances actuelles sur les mécanismes d'enregistrement dans le cas des sédiments marins, en particulier :

1. Les facteurs environnementaux responsables du transport et du retrait du ^{10}Be de la colonne d'eau, et l'effet de la distribution des sources sur l'approvisionnement en ^{9}Be.

2. L'effet des processus post-dépôt, en particulier celui du mélange des sédiments, sur le ^{10}Be et les enregistrements RPI.

3. Le mécanisme par lequel une magnétisation post-déposition est acquise près du fond de la couche mélangée en surface.

4. Les causes d'un décalage systématique entre les enregistrements ^{10}Be et RPI, et les facteurs environnementaux affectant le RPI.

Afin de démêler l'apport environnemental et magnétique dans les couches sédimentaires de ^{10}Be/^{9}Be, nous avons analysé cinq enregistrements, couvrant la dernière inversion géomagnétique. Les différentes caractéristiques d'enregistrement sur les cinq sites ont été décrites en termes de modulations climatiques additives et multiplicatives, qui dépendent essentiellement

de la profondeur de l'eau, de la localisation le long des grands systèmes de courants océaniques, et de la distance à la côte. Des critères simples ont été établis pour l'identification des sites les plus adaptés et présentant une contamination minimale de l'environnement. Malgré cela, les surcharges climatiques restent importantes, surtout en dehors des grands événements géomagnétiques.

Les enregistrements RPI sont fortement affectés par les processus post-dépôt, en particulier le mélange des sédiments, qui est entièrement responsable de l'aimantation rémanente naturelle (NRM) acquise par les sédiments bioturbés, et son retard par rapport aux enregistrements ^{10}Be. Un nouveau modèle de bioturbation a été développé pour expliquer la NRM sédimentaire dans les sédiments bioturbés. Ce modèle inclut un phénomène récemment découvert de ségrégation de taille dans la couche mélangée de surface (SML), analogue à l'effet bien connu de la noix du Brésil (Brazilian-nut). La ségrégation de taille est responsable de la plus longue permanence des grandes particules dans la SML, jusqu'au cas limite des nodules de ferromanganèse. La ségrégation granulométrique a des implications importantes pour la datation des sédiments avec les foraminifères benthiques, puisque les grands tests ont tendance à être décalés vers le haut par rapport aux particules sédimentaires de taille régulière du même âge. La calibration du modèle de bioturbation avec les profils de microtektite de deux carottes de l'océan Indien a permis de reproduire le bon degré de décalage entre les enregistrements ^{10}Be et RPI, ainsi que la dépendance environnementale de RPI dans deux carottes provenant des Océans Atlantique Nord et Pacifique équatorial.

Les résultats obtenus dans ce travail peuvent aider à développer des approches intégrées pour la correction des contaminations climatiques dans les enregistrements ^{10}Be et RPI. Les exemples comprennent l'intégration du transport ^{10}Be et ^{9}Be dans les modèles de circulation océanique globale et la normalisation séparée des contributions minérales magnétiques individuelles au signal RPI. En outre, la puissance prédictive du modèle basé sur la bioturbation pour l'acquisition de NRM peut être utilisée pour concevoir de nouvelles expériences de laboratoire pour la simulation de mécanismes d'enregistrement magnétique spécifiques.Pour la première fois, couramment utilisé pour la reconstitution de données stratigraphiques, le profil de microtektite s'est révélé être une fonction inappropriée. Nous avons démontré l'effet de noix du Brésil sur les particules de microtektite, qui consiste en une ségrégation des fragments en fonction de leur taille. Le modèle de ségrégation par taille permet d'estimer la profondeur réelle du mélange sédimentaire dû à la bioturbation, une fois prise en compte la composante supplémentaire de vitesse liée à la migration des plus grosses particules vers le haut de la colonne sédimentaire.

Les résultats de cette recherche ont une importance significative non seulement pour la caractérisation de la réponse au mélange des sédiments et la reconstruction des enregistrements affectés des processus de bioturbation (par exemple ^{10}Be/^{9}Be), mais aussi pour l'évaluation de la validité des modèles d'âge qui sont limités par les âges des traceurs conservateurs. La comparaison détaillée du ^{10}Be/^{9}Be et du RPI a permis de déterminer la profondeur d'enfouissement

dans les sédiments des océans Pacifique Ouest et Atlantique Nord. Parmi les diverses propriétés des sédiments, il a été démontré que la concentration en minéraux magnétiques était en corrélation avec les estimations de la profondeur de blocage dans les sédiments du Pacifique occidental. La diminution de la taille des minéraux magnétiques semble être liée aux variations globales de la température et du niveau de la mer. La diminution linéaire de la taille des particules magnétiques avec la diminution de la profondeur de l'eau pendant les stades isotopiques glaciaires a été calculée en termes de productivité primaire accrue pour le site situé dans l'océan équatorial Ouest-Pacifique.

Contents

List of Figures

Chapter 1

Introduction

1.1 The science of geomagnetism: retrospective

The origins of Earth's magnetic field studies are coming from pre-scientific era. Greek and Roman philosophers noticed the magnetic properties of rocks, but in order to explain this phenomena they divided principally into two camps. The first (mainly Aristotle, Platon, Thales) perceives the magnetism as a divin act and associates it with the manifestation of life : in 600 B.C. the Greek philosopher Thales of Miletus suggested that it is a soul of loadstone that moves the iron. The second group - the atomists (Democritus, Epicurus et Lucretius) tries to explain the magnetic attraction between the magnetite and an iron taking the atoms and voids in their principles. The most precise expression of atomists thoughts was expressed by Lucretius in the I century B.C. in his epic poem *"De Rerum Natura"* (The Nature of things). He suggests that magnetite emits the particles (atoms) that fill the space between the loadstone and the iron. According to Lucretius, this dissipation create a vacuum and the particles are darting into the iron, creating the *'ring'* that has the force to move the whole mass. Apart from the observations and attempts to explain the physical force of magnetism, there is no documented proofs of magnetite's practical use except the medical treatment (the first references of its medical use made by Hippocrates - in the V-IV century B.C).

It is generally accepted that the discovery of tendency of magnet to point to the north or south was made by Chinese scholars between the VI and I century B.C.. They demonstrated that magnetic directivity could be induced in small iron needles by stroking them on loadstones: this observation led to the development of the first compass. English physicist and author of the first treaty on the magnetism- Sir William Gilbert mentions in *De Magnete (1600)* that Chinese invention was used for navigation by Catalan and Basques sailors even before the middle of the XIII century. At the same time, there are evidences of use of piece of iron rubbed by a magnet for marine navigation according to the Persian collection of histories Jāmi-al-Hekayat (around 1232) written by Muhammad al-Awhi. Whoever was the the first, these evidences indicate the

rational use of magnetite in order to solve the issue of the utmost importance - navigation in the sea.

The experimental works of Italian scientist Petrus Peregrinus were the demonstration of significant progress in the understanding of physics of the geomagnetism: the notion of general existence of magnetic meridians, different determination of poles positions, dipolar nature of the magnets - are discussed in his work (*Epistola de Magnete (1269)*. Sir William Gilbert develops the model of Terella (latin of 'little earth'), which is a small magnetised ball representing the Earth (Fig.1.1). He hypothesises that iron or other magnetic body should lay within the sphere (Earth) to create the force, acting in all the directions around the body.

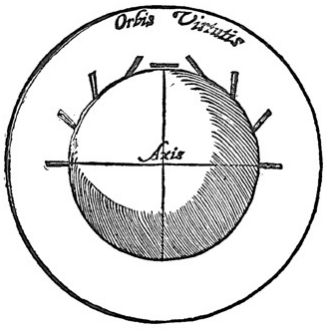

Figure 1.1: A sketch of the Terrella from *De Magnete* of Wiliam Gilbert

1.2 Time scale of geomagnetic field variations

Awareness of magnetic field variability appears with the discovery of magnetic declination change over time, made by Henry Gellibrand in 1634. These rapid changes of magnetic field are called *secular variations* and are characterised by the unsteady rate of their changes over the Earth's surface, moving faster in the western direction (Edmund Halley,1692). Nowadays this westward drift is generally associated with non-dipolar components of the magnetic field, that are attributed to different angular velocities of Earth's lithosphere and outer core. The first surveys of another fundamental characteristic of magnetic field - its intensity, were conducted by Admiral De Rossel during the Entrecasteux expedition (1791-1794) and even before by Robert de Lamanon (Pérouse expedition, 1788), but no records of the latter survived the wreck. The Rossel's expedition reported six magnetic intensity measurements made between 3° S and 49° N (Fig.1.2) as well as the period of magnetic needle's oscillations, that showed the higher oscillation near the equator, leading de Rossel to the conclusion that the magnetic force near the poles is greater than at the equator.

Station	Date	Latitude	Longitude (E)	Magnetic Dip	Time of Vibration
Brest	Sept. 20, 1791	48°24′N	355°34′	71°30′N	2.02″
Teneriffe	Oct. 21, 1791	28°28′N	343°42′	62°25′N	2.081
Van Diemen's Land	May 11, 1792	43°32′S	146°57′	70°50′S	1.869
Amboyna	Oct. 9, 1792	3°42′S	128°08′	20°37′S	2.403
Van Diemen's Land	Feb. 7, 1793	43°34′S	146°57′	72°22′S	1.850
Surabaya	May 9, 1794	7°14′S	112°42′	25°20′S	2.429

Figure 1.2: Summary of de Rossel's intensity measurements. The *"time of vibration"* (period of oscillation) of the deep needle in seconds. Credti: Lilley and Anan A.Day (1993)

German explorer Alexander von Humboldt (1798-1803) made several scientific journeys to South and central America, Siberia and Central Asia in order to investigate the change of magnetic intensities in varying distances from the magnetic equator and came up with the conclusion that magnetic field intensity also fluctuates (as previously observed for inclination and declination) and increases from the equator to the poles.

The variations in time of geomagnetic field have a wide spectrum, ranging from seconds to million years. The lower frequency variations (longer periods) arise from internal sources, whereas higher terms - from crustal field and external sources, such as ionosphere and above into magnetosphere (Fig.1.3). In 1835 Gauss made the field approximation using the harmonics of degree up to 4, whereas nowadays the field is approximated from harmonics up to degree 14, which coming from electric currents in the Earth's core, while the field of higher degrees comes from the magnetisation of crustal rocks.

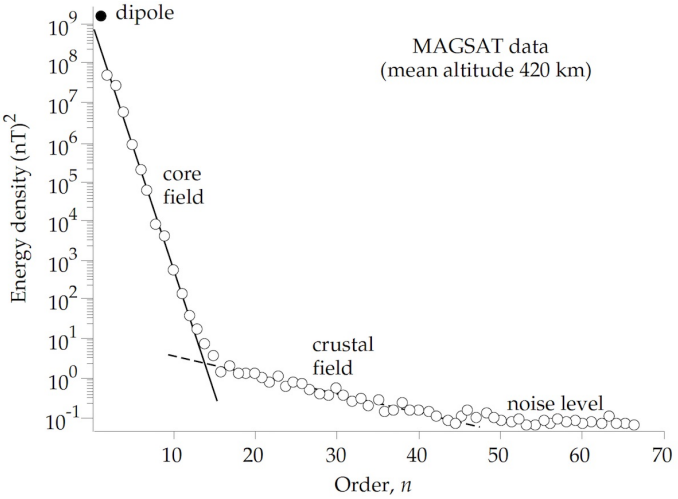

Figure 1.3: Geomagnetic field spectrum of the Earth's main field obtained by MAGSAT Earth-orbiting satellite (mean altitude 420 km). The lithospheric field is shown to be measurable for degrees of about 14 and above. There is a sharp break in the spectrum at about degree 14, what could be interpreted in terms of the dipolar field dominance and the largest scale components of the lithospheric field are unknown.

The modern spherical harmonic analysis led to the conclusion that the magnetic field is indeed has almost entire internal origin and $\sim$90% of observed field on the Earth's surface is explained in terms of the inclined to the Earth's axes of rotation by $\sim$11.5°. The remaining part of the field component is generally referred to the non-dipolar component. Extrapolated up to the Earth's surface, these axes off this dipole intersect it in 79°.7′N, 288°.2′E and 79°.7′S; 108°.2′E. These two points are called geomagnetic poles: north and south respectively and do not coincide neither with geographic nor with magnetic poles (Fig.1.4).

On the time scales of 10^5 - 10^9 years, the geomagnetic field is dominantly dipolar. Regional and global geomagnetic field variations of its intensity and direction throughout the time, hint on the evolution of geodynamo, that is primarily controlled by the thermochemical processes happening in the mantle and core. The paleomagnetic data indicate the geomagnetic field fluctuations with timescales of 10^4 years and shorter are often related to geomagnetic field reversals and excursions.

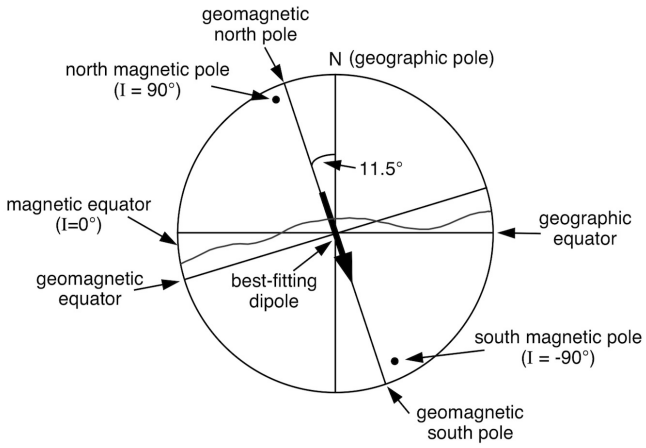

Figure 1.4: Relation between geographic, geomagnetic and magnetic coordinates. Redrawn after McElhinny (1973).

1.3 Transitional behaviour of geomagentic field

The records of paleomagnetic field have shown that reversal process of geomagnetic field polarity is unsteady and occur as Poisson process, implying no memory of the previous reversal history. Reversals are non-periodic and can certainly be seen as the most dramatic and impressive feature of the Earth's magnetic field, occurring with frequencies from 2-3 to 10-15 reversals/million years (*Gallet et al., 2019*). The detailed reversal time scale is very well known for the past 160Ma and with rather good confidence for the past $\sim$ 300Ma. The intervals of stable polarity are stuttered by polarity excursions, that are the magnetic field features representing departures from the normal secular variation, but failing to accomplish

the complete polarity reversal. There are several significant differences between these two phenomena, regarding the dynamo behaviour and time scales.

First, both excursions and reversals are involving significant decay of dipole intensity, however the reversals are characterised by the chaotic behaviour of geodynamo, contrary to the excursions. Second, the geomagnetic excursions appear less frequently and are considered to be the intrinsic part of secular variations. *Gubbins (1999)* linked the faster changes in the outer liquide core compare to the solid inner core to the excursion occurence, while the magnetic inertia imposed by the inner core delays full reversal for several thousands years, resulting in longer characteristic times. The reversal duration is relatively short compare to the periods of stable mode field and is estimated from few thousands (*Valet et al.,2012*) to tens of thousands years (*Clement, 2004*), but it has longer characteristic time compare to the excursion that is estimated within 1-10 thousand years range (*Lund et al., 1998; Roberts, 2008*).

The situation is somehow different when we refer to field intensity. Indeed, the magnetisation intensity of rocks and artefacts is mostly related to the geomagnetic field intensity, but it depends also on factors that are not field dependant. Their contribution must be completely removed by appropriate techniques that are not always fully efficient and therefore can generate discrepancies between parallel records. The records derived from marine sediments provide detailed and continuous curves of relative field intensity, but at the present time they only cover the past 2Myr with the exception of one record that goes back to the past 4Myr. The absolute paleointensity data from volcanic lava flows and dykes explore much older periods, but as the volcanic events are very punctuated, they allow to retrieve only the long-term trends of the field changes with time. A dominant and common feature of relative and absolute paleointensity records is the reflection of a large drop of the field intensity during all reversals to about 5-10% of its value during stable polarity.

Acquiring high quality paleointensity data and constraining the origin of discrepancies between the individual records remains a crucial challenge. In the second half of the 20th century cosmogenic nuclides concentration changes within the Earth's archives were proposed as an alternative and complementary approach to measurements of paleointensity for geomagnetic field intensity changes documentation (e.g. *Arnold, 1956*). Beryllium-10 is the most appropriate candidate due to its long half-life ($\approx$1.38 $\pm$ 0.016 Myr). The ^{10}Be measurements of sediment deposited during the period of the last reversal indicated a large peak production of ^{10}Be (*Carcaillet et al., 2003; Valet et al., 2014; Simon et al., 2016*), what is in direct link with the large intensity drop present in all paleomagnetic reversal records. Similar characteristics were also reported for the excursions (*Ménabréaz et al., 2011*). Below we give a rapid summary of the methods and techniques that are currently used to extract pertinent paleointensity determinations with a special attention for sedimentary records. In a second step, we describe the basic principles of cosmogenic ^{10}Be production and its subsequent deposition in the sedimentary archives.

1.4 Extracting the geomagnetic field intensity from the magnetization

The observations of the geomagneic field's changes over the time are of the importance for understanding the evolution of processes in the Earth's deep interior and understanding the geodynamo mechanism. "How fast doest it change?" and "when the geodynamo appeared?" are the fundamental questions of paleomagnetism. There are several ways to trace the magnetic field's variations in the past. Among the sources of paleomagnetic data are observatory measurements, archeological materials, volcanic rocks, lake and marine sediments, soils and biogenic material and each method possesses characteristic temporal coverage of magnetic field changes.

A common approach to study the paleomagnetic field variations relies on the measurements of induced and remanent magnetisation of ferrimagnetic mineral grains in rocks. When a rock forms it usually acquires a magnetisation parallel to the ambient magnetic field, which is a primary magnetisation that provides information about the field intensity and its direction at the time of magnetisation's acquisition. However, due to the physical and metamorphic processes occurring afterwards, rocks (volcanic or sedimentary) are often a subject of secondary magnetisation of various types that must be removed by appropriate and selective demagnetisation technique.

The records of paleomagnetic field strength rely on the two kinds of magnetisation characterised by the very different acquisition process and timing. The first requires a thermal origin for the magnetic remanence and is so-called the absoute paleointesnity because the magnetisation acquisition in a rock can be almost reproduced in the laboratory conditions. The second approach is relative and the magnetisation is acquired within sediments. In a natural conditions, thermoremanent magnetisation is acquired over a few days for archeological objects and few years for volcanic rocks, therefore the remanence retains both dipolar and non-dipolar contributions of the magnetic field at the site. In contrast, pelagic marine sediments are deposited at a rate of several centimetres per thousand year, what leads to averaging out the rapid non-dipolar field variations.

1.4.1 Absolute paleointensity

The paleointensity of the geomagnetic field from magnetic remanence of the rock might be extracted by duplicating the acquisition of magnetisation by laboratory experiments in the presence of a known field's intensity. The rock can be magnetised by the thermal activation, which leads to magnetic moments rotation in the direction of set-up field. This process is related to the thermoremanent magnetisation acquisition (TRM), that is carried by the igneous rocks, such as basalt lava or diabase dykes as well as baked archeomagnetic materials.

After the eruption, igneous rocks are cooling down from a molten state from above the the Curie temperature (T_c) in the presence of geomagnetic field. The assemblage of identical magnetic grains has a characteristic relaxation time, which is the measure of the time taken to reach a new thermodynamic equilibrium following a change in the external magnetic field. As the temperature decreases below the critical value, corresponding to the blocking temperature (T_b), single particles are undergo a significant increase in relaxation time, what leads to locked magnetisation in a sample. Lava flows "capture" magnetic field that dominates during the short period of volcanic eruption, hereby providing the discontinuous paleomagnetic record. The archeomagnetic material (oven, furnaces, kilns, etc..) acquires magnetisation through the same process and reflect the field configuration in a very narrow, "instantaneous" period of time.

For paleointensity estimation, the TRM is imparted in a laboratory conditions in a known field and directly compared to the natural remanent magnetisation (NRM). As an igneous rock contains different assemblages of ferromagnetic minerals, the full TRM of a sample can be seen as a summation of the remanences acquired within successive temperature intervals up to T_c. In presence of single domain grains, the pioneered Thellier technique (Thellier and Thellier, 1959) and all variants that were subsequently developed assume the same linear proportionality between the NRM demagnetised in zero field and the TRM acquired by heating in presence of a known laboratory field for each successive temperature interval. Mineralogical alterations can cause different response of sample to the laboratory induced field and the proportionality condition will not be met. The paleointensity estimate is based on the value of the slope, that characterise the change of NRM as a function of imparted TRM after each heating step.

The magnetic field intensity varies by a factor of two from equator to pole, therefore to compare the results, the latitudinal differences must be accounted. It is convenient to refer to an equivalent dipole moment that is that is calculated by assuming that the geomagnetic field vector would be generated by a geocentric dipole (GAD). The GAD assumes that averaged over several thousand years, the Earth's magnetic field is reduced to that of an axial dipole with the mean positions of geomagnetic poles coinciding with North and South poles of the rotation axis. The moment of the hypothetic geocentric axial dipole that would produce the measured field intensity at the site latitude is referred as the virtual axial dipole moment (VADM). If directions are present, it is assumed that the inclination deviation at the site latitude reflects the tilt of the dipole. The calculation of the corresponding virtual dipole moment incorporates the equatorial dipole and thus provides an estimate of the total dipole moment (eq.1.1). Both VADM and virtual dipole moment (VDM) calculations do not account for the non-dipole field components.

$$p = \frac{4\pi a^3}{\mu_0} \frac{B}{\sqrt{1 + 3cos^2\theta}}, \tag{1.1}$$

where p is VDM, a is an average radius of the earth, μ_0 is a permeability of a free space and θ is the geomagnetic colatitude at which B (magnetic field) is measured. The difference

in case of the VADM is that θ is a geographic latitude. To derive the value of magnetic θ colatitude, the magnetic inclination should be known:

$$tanI = 2cot\theta_m \tag{1.2}$$

However, the inclination data is often unavailable along with intensity results, and only VADM could be determined.

1.4.2 Relative paleointensity

Sedimentary archives - lacustrine and marine sediments - can provide continuous and long records of paleomagnetic field due to their continuous deposition: they can cover several million years of the Earth's magnetic field history. Records of magnetic field could be measured in sediments sampled at sparsely located sites, providing an opportunity of generating a global composite curves of the field changes with time.

Sediments become magnetised in a quite different manner than igneous bodies. In the marine pelagic environment, magnetised grains of detrital origin settle through the water column before being incorporated within the sediment and these processes are referred to detrital remanent magnetisation(DRM). The magnetic grains continue to rotate in water-filled voids within the upper unconsolidated sediment layer at the ocean bottom, until reaching a critical depth where the water content within the sediment pore spaces is low enough to allow the magnetic grains realigning along the magnetic field lines. Therefore, because the magnetization of most marine sediments is progressively locked-in with depth, it is referred as post-depositional magnetisation (pDRM), and depends on dewatering, compaction and bioturbation processes.

Post-depositional magnetisation is acquired on a scale ranging from minutes to several years after the deposition, as shown by laboratory experiments (*e.g. Tucker, 1980*). Consequently, the fast variations of magnetic field are often smoothed out. Another difficulty when dealing with marine sedimentary records is linked to the processes of remanent magnetisation acquisition that is influenced by lithological factors, such as mineralogy, concentration of magnetic grains and grain sizes of magnetic phases. Since that remanent magnetization is carried by detrital grains, the influence of the factors listed above requires to compensate for the effects that are irrelevant to the field behaviour.

Relative paleointensity (RPI) is based on the measurements of sediments natural remanent magnetisation (NRM), that results from orientation of magnetic moments contained within the detrital particles along the magnetic field lines. The NRM is a function of alignment of magnetic field moments as well as the concentration of magnetic particles, their size and mineralogy. In presence of magnetically homogeneous sediment, thus with similar size and mineralogy within the sedimentary column, the field intensity changes can be estimated after taking into account the variations in magnetic concentration. The magnetic grain sizes usually

divided into the four categories: superparamagnetic or SP (respond reversibly to magnetic field and have zero remanence); single - domain or SD (the magnetisation is uniform in zero field); pseudo-single domain (PSD) and multi-domain (MD), which have a non-uniform remanent state. In order to analyse the intrinsic paleomagnetic record, the NRM record must be accounted by the concentration of stable single - domain magnetic grains. There are three commonly used techniques, that could potentially be used for that purpose.

The anhysteretic remanent magnetisation (ARM) is generated by superimposing a small direct field on a slowly decreasing alternative field from a peak value to zero. It has been shown that ARM has a strong acquisition efficiency in presence of fine-grained magnetite is non-interactive SD particles (*Moscowitz, 2007*). The second normalisation parameter is low-magnetic field susceptibility (χ), that as ARM depends on the magnetic grain size. Lastly, the isothermal remanent magnetisation (IRM) is imparted in presence of very strong magnetic field (up to 3T), and at a constant temperature. The principle of this method is based on the assumption, that the field at which saturation is reached, depends on the composition and microstructure of a sample, including the grain size.

Because optimal conditions for stable magnetic remanence is the existence of single-domain magnetite, it is recommended to use a magnetic normalisation parameter that responds to the same grain fraction. The suitability of ARM for relative paleointensity experiments can be tested by comparing the NRM and ARM demagnetization curves. If the same magnetic grains are involved in both parameters, they should be characterised by a similar coercivity distribution and therefore by similar demagnetisation curves. In this case, relative paleointensity estimates can be obtained by averaging the successive NRM/ARM estimates at different demagnetisation levels or from the slope of regression line fit for the association between NRM and ARM. The magnetic homogeneity of the sediment can be tested by scrutinising the coherence of the evolution of the three parameters (ARM, K and IRM) within the sedimentary column. If three normalisers yields identical results, any of them could be used with the confidence for fair paleointensity determination (*Valet, 2003*). However, it might also occur that the three methods produce different paleointensity estimates, what signifies that magnetic grain-size variations were not successfully accounted by the normalisation or that mineralogical changes affected the magnetisation. In all cases the correlation check between the RPI and rock magnetic parameter should evidently show no coherence with the normaliser. Finally, one cannot exclude that the response of the sediment magnetisation varies for other reasons that would be linked to the sediment structure and thus the magnetisation process itself. This is one of the limits inherent to this technique that requires other approaches performed in parallel with the paleointensity experiments.

1.5 Tracing the geomagnetic field variation with cosmogenic nuclides

Galactic cosmic rays (CR) are charged particles, supposedly produced by nucleosynthesis processes in the stellar interior, where they are ejected at a rate of speed sufficient to charge other atoms and diffused throughout the whole Galaxy. The interaction of CR with the Earth's atmosphere produce a cascade of secondary cosmic ray neutrons and a variety of cosmogenic nuclides (e.g. ^{26}Al, ^{7}Be, ^{10}Be, ^{14}C, ^{36}Cl). These reactions take place in the lower stratosphere($\approx$35%) and upper troposphere ($\approx$ 65%) at the 10-20 km altitude. Each nuclide is characterised by a specific number of protons and neutrons in the nucleus and different half-live - time during which 50 % of the radiogenic isotope (parent) decays to produce a daughter isotope. For long time-scale geophysical and geochemical problems, the cosmogenic isotopes with long-lives have a greater importance.

There are three main sources controlling the production rate of cosmogenic nuclides: i) primary cosmic ray flux; ii) geomagnetic field modulation; iii) solar modulation.

Primary cosmic rays

The production rate of cosmogenic nuclides primarily depends on the intensity of incoming galactic cosmic rays at the top of the atmosphere. It was argued that the primary cosmic flux may have been changed over the time due to the supernova explosion (*Stozhkov et al., 2000*) or changes in the magnetic state of the heliosphere (*Ahluwalia,2000*). A measurement of cosmogenic isotope ^{10}Be is an integral measurement of primary cosmic ray flux and can be presented as :

$$P(\lambda, \phi, t) = \sum_i \int_{E_c(i,\lambda,\phi)}^{\infty} S_i(E) \cdot j_i(E,t) dE, \tag{1.3}$$

where P(λ, ϕ, t) is the production rate of ^{10}Be atoms at time t, at point P at geographical latitude λ, and longitude ϕ. The summation is over the i components of the cosmic radiation, and $S_i(E)$ is the specific yield function (*Fonger, 1953*) of component i.

Geomagnetic field control

The relation between the cosmogenic radionuclide production and geomagnetic field was first proposed by Walter Elsasser in 1956. He suggested that the rate of production of cosmogenic nuclides is proportional to the particle flux of cosmic rays over the Earth's surface. Based on the measurements of cosmic rays flux at different latitudes, Walter derived first-order inverse relationship between the strength of magnetic dipole moment and cosmogenic nuclide production rate:

$$P(t) = \frac{C}{M(t)^{0.52}}, \tag{1.4}$$

where $P(t)$ - cosmonuclide production rate of as a function of time, C - is a constant (depending on the isotope), and $M(t)$ - magnetic moment of the Earth, that varies in time.

The geomagnetic field deflects incoming cosmic ray particles depending on their magnetic rigidity and the angle of incidence. The rigidity of a particle is defined as the momentum per unit charge $R = pc/Ze$, where p is the momentum and Ze the charge of the particle and c is the velocity of light. The Earth's magnetic field approximation as a dipole field, made a basis for the model, allowing to examine the motion of charged cosmic ray particles in the geomagnetic field. In 1955 Carl Störmer (1955) found that in a dipole field, there is an axial symmetric cone about a direction to the east in which charged particle access below a specific momentum is forbidden (Fig.1.5).

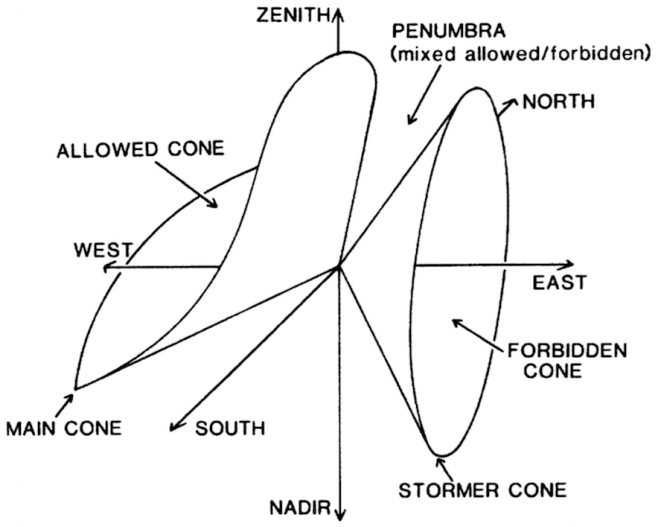

Figure 1.5: Geometric visualisation of cutoffs as defined by exact solution of Störmer (1955) integral. The axis of Störmer cone is perpendicular to the dipole axis and to the radius vector from the dipole center to the point concerned. Forbidden cone is referred to the solid angle within which all access is forbidden for charged particles of a specified rigidity and sign. Within the *allowed main cone* all possible directions of arrival are accessible to charged particles entering the field from infinity (*Cooke et al.,1991*). *Penumbra* is a region of alternating allowed and forbidden bands of directions of arrival.

Thus, obtained Störmer integral of the equations of motion, provides substantial information about the allowed motion of the particles. Most importantly, it was found that the cutoff rigidity P_c, a coordinate that describes charged particle access at any position in the magnetosphere in a dipole field, is given by:

$$P_c = pc = \frac{M}{R^2} \frac{cos^4\lambda}{[(1 + cos\theta \cdot cos^3\lambda)^{1/2} + 1]^2}, \tag{1.5}$$

where λ - certain geomagnetic latitude, θ - angle between the trajectory of arriving particle and the vector to the (magnetic) West in the horizontal plane, M and R are magnetic dipole moment and radius of the Earth, respectively.

Production of cosmogenic isotopes depends on the atmospheric depth and the geomagnetic latitude, where the production takes place. Figure 1.6 (left panel) demonstrates, that cosmic rays arriving near the equator (θ = 0°), confront the maximum cut-off rigidity of $\approx$ 15 GV, whereas the right panel shows that the production rate of cosmogenic isotope ^{10}Be for a fixed value of magnetic dipole moment, is highest at high geomagnetic latitudes, as a result of decreasing cut-off rigidity, i.e. shielding of the primary cosmic rays by geomagnetic field.

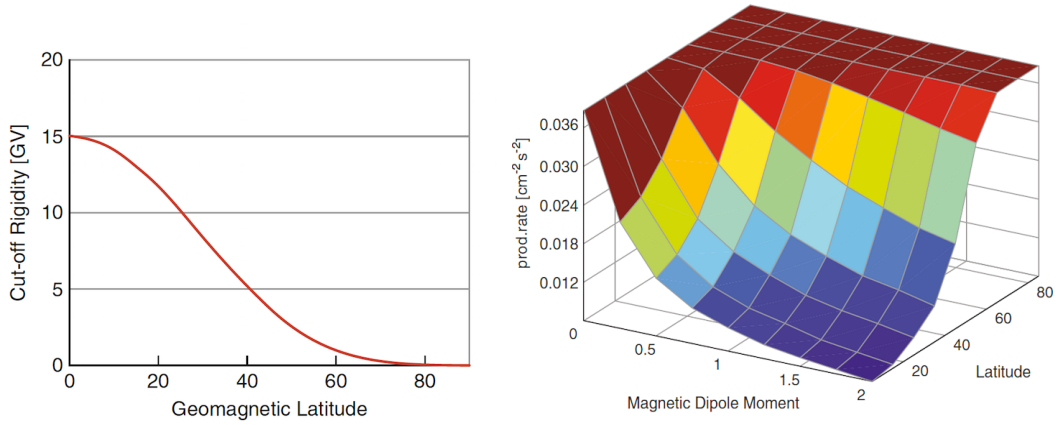

Figure 1.6: ^{10}Be production rate as a function of latitude in the Earth's atmosphere and magnetic dipole moment for Φ = 550 MeV. The production rate is integrated over all atmospheric depth and shown to increase for higher latitudes. Credit : Jürg Ken McCracken, and Rudolf Steiger (2012)

Production rate of a j cosmogenic nuclide at an atmospheric depth D is :

$$P_j(D) = \sum_i N_i \sum_k \int_0^\infty \sigma_{ijk}(E_k) J_k(E_k, D) dE_k, \tag{1.6}$$

where N_i is the number of atoms of a target element i per kg material in the sample, σ_{ijk} the cross- section for the production of cosmogenic nuclide j from the target element i by particles of type k with energy E_k, and $J_k(E_k$, D) is the flux of particles of type k with energy E_k at depth D inside the Earth's atmosphere.

Solar modulation The third control of the cosmogenic nuclides production in the atmosphere is solar activity. The solar modulation in Heliosphere (that could be roughly described as a spherical vast bubble-like region which surrounds and is created by the Sun) is defined by *Gleeson and Axford (1968)* as:

$$J_e(E, \Phi) = J_{IS}(E + \Phi)(E^2 + 2m_p c^2 E)/[(E + \Phi)^2 + 2m_p c^2 (E + \Phi)], \tag{1.7}$$

where J_e is the spectrum measured on the Earth,J_{IS} is the interstellar spectrum at energy E+Φ, Φ is the modulation potential (MV), m_pc^2 is the proton rest mass energy.

Magnetic field of the solar wind deflects the primary flux of charged cosmic particles, which leads to the reduction of cosmonuclides production in the Earth's atmosphere. This effect was recognised though the Maunder minimum (the most famous cold period of the Little Ice age, resulting from the very low solar activity), that is characterised by a 20-30% higher rate of atmospheric ^{14}C, comparing to the modern time (*Bard et al, 1997*). As shown on the Fig.1.7, the mean global ^{10}Be production rate strongly depends on the magnetic dipole moment strength and solar modulation (Φ). For the case of zero magnetic dipole moment, global mean ^{10}Be rate is minimal when the sun is the most active and is twice as high when the sun is quiet (Φ = 0 MeV).

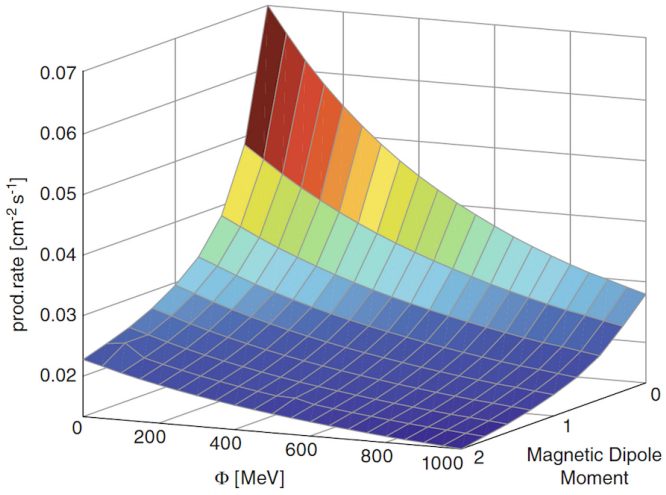

Figure 1.7: Dependence of the mean global production rate of ^{10}Be upon the strength of the magnetic dipole, and solar modulation. Credit : Jürg Ken McCracken, and Rudolf Steiger (2012)

Recent models (*Masarik and Beer, 2009; Heikkilä et al.,2009*) show that due to the geomagnetic field variations , the global production change of ^{10}Be would increase by a factor superior to 2 in case of complete disappearance of dipolar magnetic field, that might be expected during the magnetic reversal. Although it is often impossible to separate the solar and galactic cosmic rays modulation of cosmogenic isotopes production, the observed 11-years changes in ^{10}Be concentration in ice core DYE 3 in Greenland (*Beer et al., 1994*), that is likely induced by the Solar activity, lead to an estimation that the solar modulation of ^{10}Be production during the period of stable polarity might be responsible for the factor $\sim$ 1.5 - 2.0.

1.6 ^{10}Be cycle

Owing to its long half-life, ^{10}Be ($T_{1/2}$ = 1.386 My $\pm$ 0.016) is a worthy candidate for paleomagentic studies. One of the main advantages of this method for paleomagnetic field reconstruction is that the measurements of cosmogenic ^{10}Be concentration could be done within the marine sediments, that are also commonly used for magnetic measurements. Thus, paleomagnetic field reconstructions based on ^{10}Be signal is an independent and alternative technique, allowing to avoid the stratigraphy bias.

To produce a cosmogenic nuclide in the atmosphere it is necessary to change the number of nucleus in an atmospheric atom: for example, ^{10}Be is almost completely produced by the interaction of secondary particles of cosmic ray - induced atmospheric cascade with ^{14}N and ^{16}O atoms (stage 1, Fig. 1.8, according to *Lal and Peters, 1967*), which are the most abundant isotopes in the atmosphere. The latter leads to its high production rate: 10^{-2} - 10^{-3} atoms/cm^2 versus 10^{-5} - 10^{-6} for ^{26}Al and ^{36}Cl. Around 65 %, 17 %, 13 % and 5% of ^{10}Be fraction is produced in the stratosphere, tropical troposphere, subtropical troposphere, and polar troposphere respectively (*Heikkilä, 2011*).

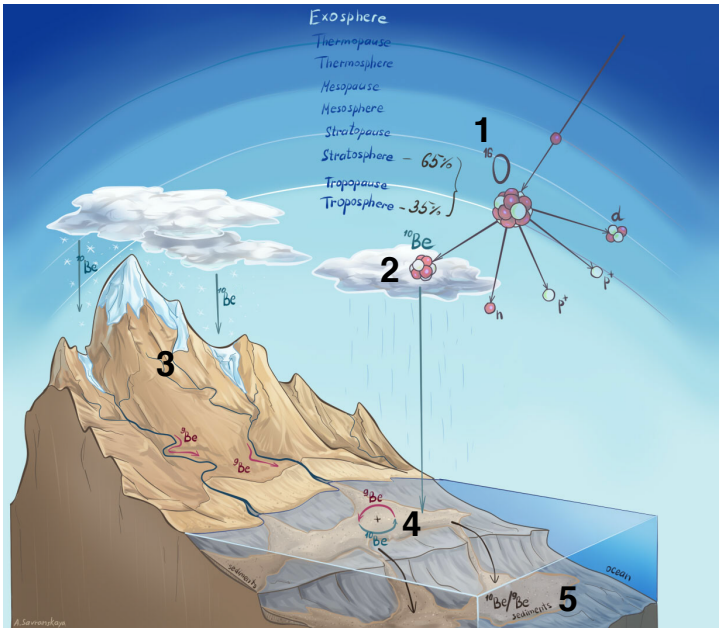

Figure 1.8: The scheme of cosmogenic Be cycle. Stage (**1**) - collision of Galactic Cosmic Rays with atmospheric isotopes and ^{10}Be production; (**2**) - scavenging ^{10}Be from the atmosphere by aerosols; (**3**) - ^{10}Be deposition at the Earth's surface; (**4**) - ^{10}Be scavenging in the ocean and homogenisation with ^{9}Be isotope and (**5**) - its deposition within the sediments.

The approximate residency time of 1-2 years in the stratosphere and 3 weeks in the troposphere leads to global homogenisation of ^{10}Be, which production is initially latitude - dependent. The circulation of cosmogenic nuclides depends on their chemical nature, what

allows us to categorise them in three main groups: 1) the noble gases which do not form compounds; 2) the cosmogenic nuclides which form compounds with constituent molecules in the atmosphere and the hydrosphere, and 3) those which form compounds but being particle active, also attach to aerosols/particles. ^{10}Be belongs to the third group and gets attached at first as oxide to aerosols in the atmosphere. The removal of ^{10}Be from the atmosphere occurs through the scavenging by aerosols (stage (**2**), Fig.1.8) and its further deposition is strongly controlled by the precipitation rate at the site (*Heikkilä et al., 2008*). Atmospherically produced ^{10}Be is stored in the Earth's archives, such as ice sheets, soils and terrestrial sediments, continental shelf sediments, river and lakes, and in the Ocean (stage (**3**), Fig.1.8). Some fraction of ^{10}Be is produced in-situ in continental soils, ice- sheets and oceans, constituting less than a few percent, whereas nearly 70 % enters the ocean and 30% are deposited in the continents (stages (**3**)-(**4**), Fig.1.8).

The atmospheric ^{10}Be is delivered to the ocean by wet and dry precipitation as well as by the rivers discharge and is rapidly scavenged by the solid particles in the water column. Its enhanced deposition takes place at the ocean margin due to the high concentration of particulates, whereas in the open ocean particulate ^{10}Be concentration decreases due to the fewer sediment remobilisation (*McHargue, 1991*). Scavenging of beryllium isotope within marine sediments is strongly compositionally dependent, and is shown to be more effective in fine allumino - silicate particles (*Sharma et al., 1987*). Thus, the absolute ^{10}Be concentration in marine sediments is prone to environmental factors and can not be directly used for paleomagnetic field studies.

The non-radiogenic ^{9}Be is a product of weathering of continental crust, which enters the oceans mainly at its boundaries (*Blanckenburg and Igel, 1999*). Both beryllium isotopes have similar chemical properties and are likely scavenged by the same carrier. This assumption makes ^{9}Be isotope to be a suitable candidate for compositional effect compensation when analysing the concentration of cosmogenic ^{10}Be within the sediments for paleomagnetic studies.

A sedimentary particle entered the ocean, would carry an intrinsic beryllium of terrestrial origin, that is adsorbed to the particle-substrate (inner layer), and beryllium isotopes (^{9}Be and ^{10}Be) that are scavenged in the water column and forming an outer layer (Fig.1.9). The authigenic (outer rim) marine sedimentary phase of ^{10}Be/^{9}Be ratio includes amorphous Fe-Al oxydroxides, carbonates and opal fractions, whereas an inner detrital layer consists of mineral matrix containing the insoluble ^{9}Be.

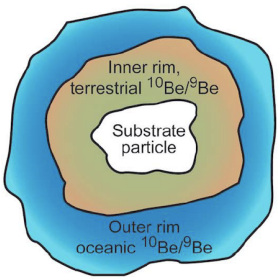

Figure 1.9: Inner and outer layers of sedimentary particle, carrying the authigenic and terrestrial phases of Be isotopes. Credit: *Wittmann et al., 2017*

The long residency residency time within the ocean, estimated between 600 and 1200 years (*Ku et al 1990; Kusakabe et al., 1990*), is assumed to be sufficient for homogenisation of ^{10}Be and ^{9}Be in the ocean, therefore, the isotopic ratio ^{10}Be/^{9}Be that is extracted from authigenic marine sedimentary phase is supposed to reflect the oceanic water composition. Laboratory experiments and studies on estuarine scavenging of ^{9}Be have shown that beryllium mobility is strongly pH-dependent (*Measures and Edmond (1983); E.T. Brown et al., 1992*). When the level of pH>5, beryllium isotopes are adsorbed on solid surfaces and are not put into the solution until the pH is lower than 5, what explains the most efficient beryllium adsorption in the river estuaries, comparing to the open ocean, with the average pH level of $\sim$ 8. The latter condition favours the hypothesis that beryllium isotopes in the ocean follow the non - reversible scavenging (*Wittmann et al.,2017*).

Vertical distribution of dissolved ^{10}Be and ^{9}Be in the ocean generally demonstrates nutrient-like profiles, characterised by the sharp depletion within several top meters and subsequent increase with depth, what could be explained by biological recycling (*Kusakabe et al.,1987; Ku et al., 1990*). However, the ^{10}Be/^{9}Be ratio exhibit quasi - constant value over the whole water column (Fig. 1.10), suggesting effective isotopes homogenisation in the ocean.

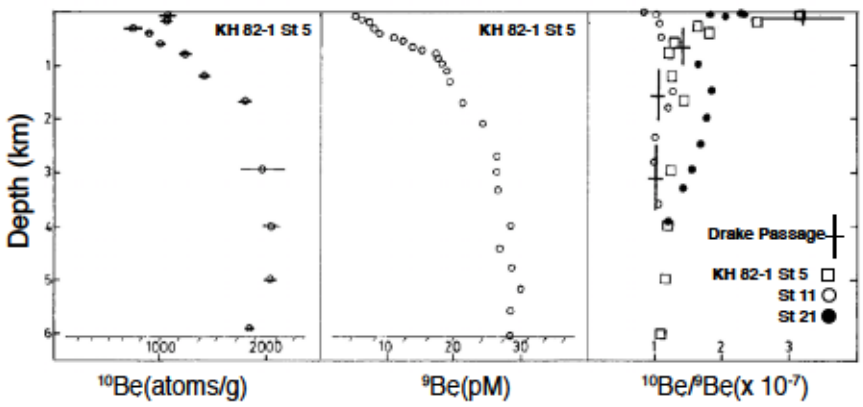

Figure 1.10: Beryllium vertical profiles in the water column of Pacific Ocean and Drake Passage : left- ^{10}Be profile; middle- ^{9}Be profile, and right- ^{10}Be/^{9}Be profile in the water column. Credit: *Kusakabe et al., 1987*

Notwithstanding, the ^{10}Be/^{9}Be ratios, measured in seawater as well as in ferromanganese nodules were shown to significantly differ between the oceans (*Blanckenburg et al.,1996*). Inter-ocean differences, reflected by authigenic ^{10}Be/^{9}Be records (Fig.1.11), lead to the question in which degree the ^{10}Be/^{9}Be ratio is controlled by the dipole variations and environmental factors. This is the question of primarily importance for dipole intensity reconstruction based on beryllium records.

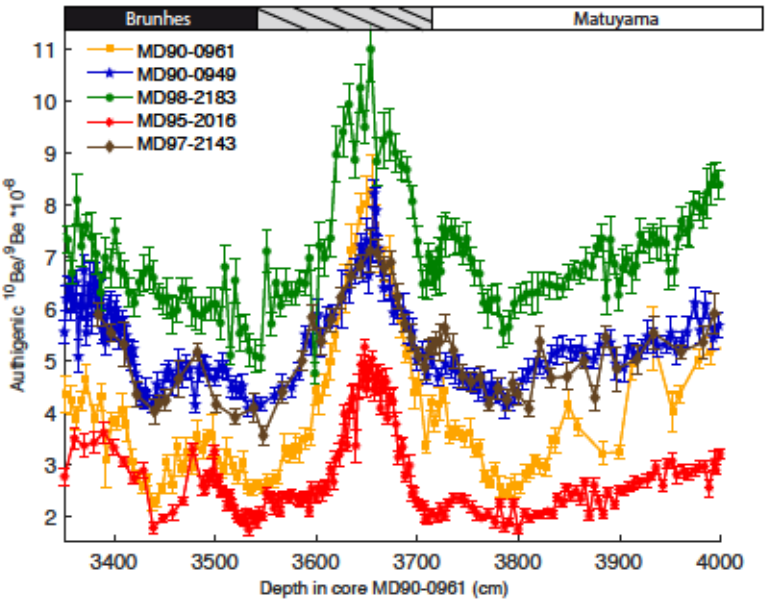

Figure 1.11: ^{10}Be/^{9}Be records, correlated to the signal from MD90-0961 to analyse whether they similarly reflect the magnetic field variations during the last geomagnetic reversal Matuyama - Brunhes

1.7 Recording the magnetic field changes by RPI and ^{10}Be/^{9}Be: similarities and differences

Marine sedimentary records provide an opportunity of comparison the paleomagentic field intensity registered by RPI and ^{10}Be/^{9}Be ratio at the same stratigraphic level. The two proxies are at the first order controlled by the dipole intensity and generally show synchronous variations during the most significant changes of geomagnetic field, such excursions and reversals. However, a comparison during the stable polarity should be done with the great care, because both proxies subjected to climatic and environmental processes. The non-magnetic controls of ^{10}Be/^{9}Be are thoroughly studied in the chapter 3. The individual RPI records obtained from different sites often demonstrate similar long-term but distinct short-term variations (e.g. RPIs compilation at Fig.26 in: *Tauxe and Yamazaki, 2007*), what allows us to separate geomagnetic and environmental contributions (*Stoner et al., 2002*). This could be achieved through producing a composite paleointensity curve, that basically retains only the changes of fundamental frequency or global magnetic field changes (e.g. *Guyodo and Valet, 1999*) or/and via comparison with independent proxy such ^{10}Be/^{9}Be. However, the second alternative is also subjected to the local conditions, yet implies different mechanisms of modulations.

Comparison of RPI with ^{10}Be/^{9}Be signal measured within the same sediments, pointing out to the concordance between two proxies during the periods of transient field regime (Fig.1.12, Fig.1.13).

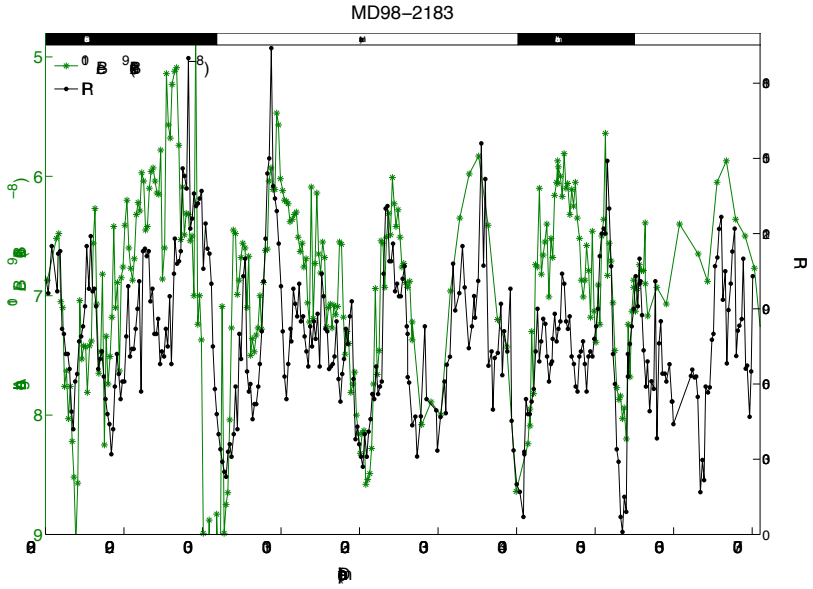

Figure 1.12: RPI and Be-ratio records in West-Pacific core MD98-2183. Results of this study.

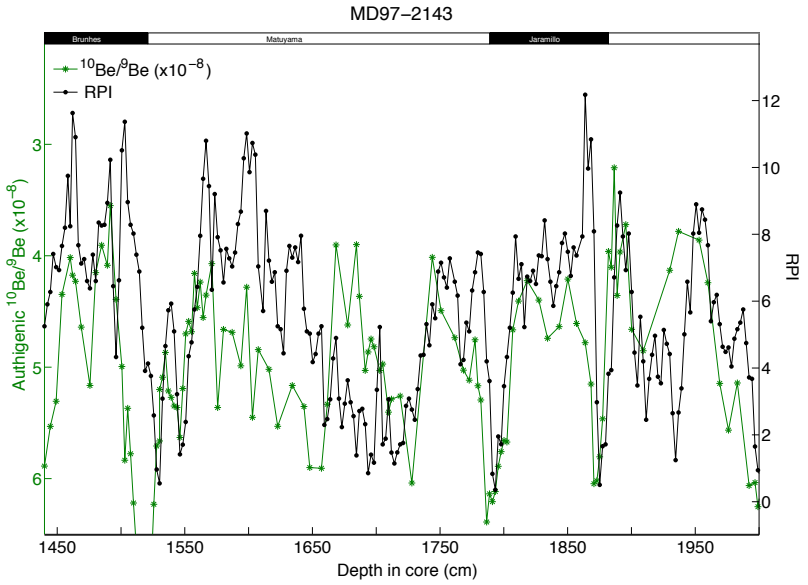

Figure 1.13: RPI and Be-ratio records in West-Pacific core MD97-2143. Results of this study.

Strikingly, ^{10}Be/^{9}Be and RPI in these two West - Pacific cores have compatible amplitudes of variations, except for the Matuyama - Brunhes interval. However, several discrepancies between the records are existing, during the transitional as well as stable polarity periods. The dipole's low during the Matuyama - Brunhes reversal is accompanied by the time-lag between the RPI's minima and the peak of ^{10}Be/^{9}Be in both cores. During the stable Matuyama chron, the ^{10}Be/^{9}Be record does not mimic the RPI response at $\sim$ 3130 cm in MD98-2183 and in MD97-2143 ^{10}Be/^{9}Be ratio is characterised by a slight decrease at $\sim$ 1700 cm, whereas the RPI displays the opposite trend.

The coupled RPI and ^{10}Be/^{9}Be records obtained from other locations also highlighted existing disagreements. The ^{10}Be/^{9}Be and RPI from the West-Pacific core MD05-2920 (*Ménabréaz et al., 2012*, Fig.1.14) display several significant offsets. The ones observed at $\sim$ 2560 cm and $\sim$ 2820 cm might be related to the delayed record of magnetic field due to the post-depositional processes (chapter 1.4.2). Remarkably, the decrease of magnetic dipole at $\sim$ 1890, captured by RPI was not reflected by the ^{10}Be/^{9}Be increase (note that the Y axis at Fig.1.14 is reversed), yet this interval is characterised by significant change of RPI's amplitude. The minor dipole changes, reflected by RPI's low at $\sim$ 690 cm, $\sim$ 950 cm, and $\sim$ 1200 neither mirrored by the ^{10}Be/^{9}Be ratio. That might be an evidence of different environmental modulation mechanisms of two proxies or a failure to capture non-dipolar field variations by ^{10}Be/^{9}Be due to the atmospheric averaging and the ocean's residency time prior to the deposition.

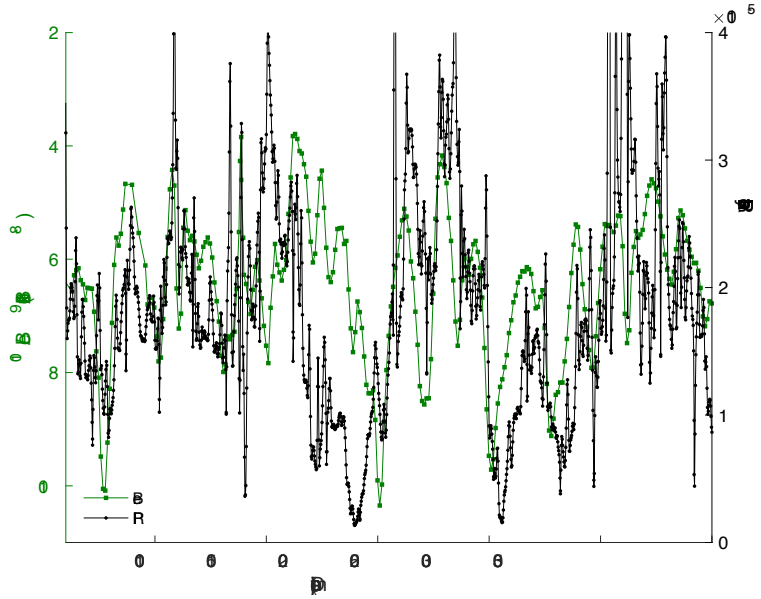

Figure 1.14: RPI and Be-ratio records in core MD05-2920 sampled at -2°85' N; 144°53' W

The quality of $^{10}Be/^{9}Be$ records is strongly controlled by the lithological composition of the sediments. Beryllium isotopes are shown to be ineffectively scavenged when carbonate fraction dominates in sedimentary sequence. This is reflected by an irregular $^{10}Be/^{9}Be$ profile in ODP 851, where the $CaCO_3$ content is >75% (Fig.1.15), whereas a smooth $^{10}Be/^{9}Be$ increase is expected during the reversal.

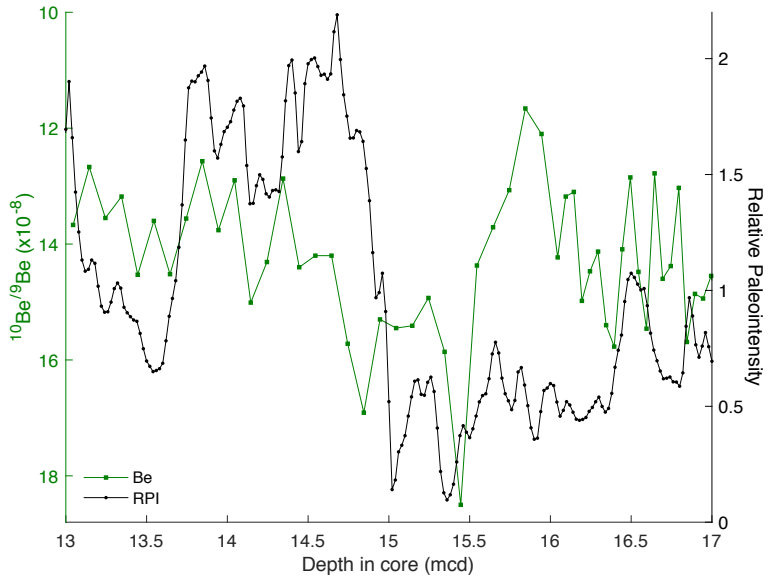

Figure 1.15: RPI and Be-ratio records during the Matyuama- Brunhes geomagentic reversal in core ODP851

1.8 Objectives and outline of the phD thesis

Comprehension of underlying causes of concordances and disagreements between the $^{10}Be/^{9}Be$ and Relative Paleointensities series requires in-deep understanding of acquisition mechanisms of magnetic field intensity by each of the proxy. The primary aim of this phD thesis is to improve the understanding of mechanisms of magnetic field acquisition by $^{10}Be/^{9}Be$ and RPI in order to estimate their reliability for paleomagnetic field reconstructions.

This manuscript is organised as follows. Chapter 2 includes two studies, focused on the 1) reconstruction of unperturbed by sedimentary processes, cosmogenic Beryllium-10 records, and 2) sediment impulse response function modelling. Obtained results describe the diffusion process in homogeneous mixing layer as depicted by microtektite fragments distribution and allow to estimate the sediment mixing depth resulting from bioturbation disturbances. Chapter 3 presents detailed comparison of $^{10}Be/^{9}Be$ records from sedimentary cores, sampled in North Atlantic, Indian and West Pacific oceans during Matuyama-Brunhes geomagnetic reversal. For the first time, the results explain the $^{10}Be/^{9}Be$ inter-sites differences in terms of common climatic modulation model. Chapter 4 thoroughly describes the magnetic field acquisition mechanisms by RPI and $^{10}Be/^{9}Be$ through the depth-dependent sediment mixing model. This chapter consists in comparison of RPI and $^{10}Be/^{9}Be$ records during 17 selected geomagnetic events, covering the last 1100 ka in North Atlantic and West Pacific sediments. Finally, Chapter 5 and 6 summarise the main conclusions of this thesis and further research perspectives.

Chapter 2

Sedimentary processes impact on cosmogenic ^{10}Be signal : smoothing and offset

2.1 Sedimentary ^{10}Be signal

Variations of cosmogenic isotope Beryllium -10 in the Earth's archives is an alternative method to trace the variations of magnetic field intensity in the past. It is produced by the spallation reactions of charged cosmic ray particles with atmospheric isotopes, mainly ^{14}N and ^{16}O. Beryllium -10 production is inversely proportional to the magnetic field intensity due to the magnetosphere shielding effect (*Masarik and Beer,1999*) but is also controlled by the intensity of incoming flux of galactic cosmic rays, solar activity (*Konstantinov and Kocharov, 1984*), and atmospheric depth and geomagnetic latitude, where the production takes place. But in the first approximation it can be assumed that ^{10}Be is well mixed between all latitudes and thus close to the global average due to the atmospheric mixing processes and long residence time in the stratosphere (1-2 years) (*Beer et al.,2012*). After being produced, ^{10}Be is attached to aerosols and subsequently removed from from the atmosphere in the lower part of the troposphere where clouds are formed (*Beer et al.,2012*) and is finally deposited at the Earth's surface.

However, the ^{10}Be flux is strongly modulated by transport paths on land and in the oceans, and by scavenging through suspended particles in the water column (*Measures and Edmond, 1983; von Blanckenburg et al., 2012*), making it dependent on site and sediment composition. Therefore, it cannot be used as a direct proxy of the geomagnetic dipole moment until the environmental contributions are withdrawn. Two techniques are commonly used to filter out non-magnetic field contributions : normalisation by concentration of stable isotopes such as ^{9}Be (*Bourlès et al., 1989*) or ^{230}Th (*Frank et al., 1997*). Enhancement of normalised ^{10}Be production was shown to be associated with weakening of geomagnetic field strength by

measuring its concentration in the ice (*Raisbeck et al.,1985*), marine sediments (*Frank et al., 1997; Valet et al.,2014; Simon et al.,2016*), loess depositions (*Zhou et al.,2014*) and also by the numerical modelling (*Poluianov et al., 2016*).

Beryllium-10 normalisation, however, does not provide a globally homogeneous proxy for ^{10}Be production, due to the modulation of isotopic record by environmental variations (*von Blanckenburg et al., 2012*) and processes of bioturbation within the sediments (*Bard et al., 1987, Wheatcroft, 1990*). Therefore, changes in ^{10}Be/^{9}Be (referred to Be-ratio below) with time could be seen as a convolution of the magnetic field signal with the impulse response function of the sediment due to the mixing induced by benthic animals. Solving an inverse problem should lead to the unperturbed magnetic field record, but the non-uniqueness of the solutions and numerical instabilities make this task difficult. The main challenge is to correctly describe the function's impulse response (sediment mixing), that could not be directly observed and is therefore prone to uncertainties.

2.2 Impulse response function description

Benthic sediment mixing is described in terms of the mixing organisms activities. Several approaches have been applied to describe the mixing pattern that relies on isotope tracers (*Peng and Broecker, 1984; Steiner et al.,2016*) and foraminifera distributions (*Hutson, 1980; Anderson, 2001*), or on evaluation of conservative tracers profiles like glass beads (*Wheatcroft, 1992*), ash (*Ruddiman and Glover, 1972*) or microtektite fragments (*Guinasso and Schink, 1975*).

In the present study, the mixing response of sediments was identified with the profiles of microtektite fragments found in two cores from Indian Ocean (*Valet et al., 2014*), assuming that without the bioturbation the microtektite profiles would be represented by a thin layer with the sharp upper and lower boundaries (*Berner, 1980*). The microtektite layer is associated with the Australasian strewn field which has an approximate age of 788 ka (*Jourdan et al., 2019*). The source crater remains unknown, but the microtektite were produced about 12-15 kyr prior to the last reversal (*Glass, 1979; Schneider and Kent, 1990; Suganuma et al., 2011*). Atoms of beryllium isotopes are deposited within the same stratigraphic unit and therefore are expected to undergo identical sediment mixing processes as in case of microtektite fragments.

As it is seen on the Fig.2.1, two microtektite profiles from cores MD90-0949 and MD90-0961 share common triangular shapes but with a larger width in the case of MD90-0949. The number of counts is constrained by the sedimentation rates, which are 1.83 and 3.6 cm/kyr for MD90-0949 and MD90-0961 respectively. Due to the sampling, preparation and measurements routines, the impulse response function deduced from microtektite distribution in the sediments contains a large amount of "noise" that could mask useful information in the signal, making the inverse problem meaningless (*Matuson, 1986*). To avoid this problem, the noise and complexity of the beryllium and tektite signals can be reduced by fitting the curves in the

time domain. First, the sediment mixing profiles were approximated by *Guinasso* function (*Guinasso and Shink, 1975*) in the time domain, which is controlled by scaling factor s, that is proportional to the thickness of mixing layer and by inverse Péclet number G, which is the ratio between diffusive and advective transport in the mixing layer :

$$G = D/(L * v_{sed}), \tag{2.1}$$

where D is the diffusion coefficient (cm^2/ka) , L - thickens of mixed sediments (cm), and v_{sed} is the sedimentation rate (cm/ka). Parameter G controls the shapes of the microtektite profiles and L/v_{sed} their width and further expressed as parameter s.

The tektite profiles were modelled with:

$$N(t) = \frac{N_0}{s}\int_{-\infty}^{+\infty} \mathcal{N}(g, \mu_g, \sigma_g)\mathcal{G}\Big(\frac{t_k - t}{s}, e^g\Big)dg, \tag{2.2}$$

where t is the age, $\mathcal{G}(x, G)$ the Guinasso function with bioturbation intensity G, N_0 is the total number of counts, t_k is the age of the impulsive tektite input, s is the inverse of the sedimentation rate. It is assumed that beryllium isotopes are attached to sedimentary particles of different sizes, that diffuse with various D and therefore have distinct G. This is taken into consideration by $\mathcal{N}(g, \mu_g, \sigma_g)$, a lognormal distribution of inverse Péclet number G, where g is $ln(G)$, μ_g and σ_g are the mean and standard deviation respectively. This implies that the distribution of G reflects a distribution of tektite sizes. The fitting parameters are $C = N_0/s, t_k$, and σ_k.

Eq. 2.2 can be approximated by $\mathcal{G}(x, \bar{G})$ with $\bar{G} = exp(\mu_g)$ for sufficiently small values of σ_g, however a better fit of the data is obtained with the above definition, which should be used to solve the inverse problem.

$$\mathcal{L}(t) = \frac{1}{s}\int_{-\infty}^{+\infty} \mathcal{N}(g, \mu_g, \sigma_g)\mathcal{G}(-t/v, e^g)dg, \tag{2.3}$$

where the negative argument of $\mathcal{G}$ comes from the opposite time direction of age and the factor s^{-1} ensures that the integral of $\mathcal{L}$ over time is equal to 1, as required by the definition of impulse response. The Fourrier transform of eq. (2.3) is

$$\mathcal{L}^*(\nu) = \int_{-\infty}^{+\infty} \mathcal{N}(g, \mu_g, \sigma_g)\mathcal{G}^*(-s\nu, e^g)dg \tag{2.4}$$

The analytical expression of *Guinasso* function in the time domain is:

$$\mathcal{G}(t) \approx \mathcal{H}(t)exp\Big[\gamma_1 + \gamma_2 - \alpha_1 t - \alpha_2 (t)^{-1} e^{-1/\beta}\Big] \tag{2.5}$$

for $G \geq 10^{-4}$, where $\mathcal{H}$ is the Heavyside unit step function and

$$\gamma_1 = \frac{0.337}{G} + \frac{0.1594}{G} - \left[\frac{1}{2} - \frac{1}{2}tanh\Big(0.2228ln\frac{G}{1.8452}\Big)\right]^8$$

$$\gamma_2 = \left(\frac{0.002209}{G}\right)^2 - (0.8843e^{\frac{-G}{0.001174}}) + 5.77563e^{\frac{-G}{0.00007863}}$$

$$\alpha_1 = 1 + \frac{0.1691}{G} + \frac{0.0816}{G}\left[\frac{1}{2} - \frac{1}{2}tanh(0.3391 * ln(\frac{G}{0.4893})\right]^{3.287} \tag{2.6}$$

$$\alpha_2 = \frac{0.2334}{G} + \frac{0.0167}{G}\left[\frac{1}{2} - \frac{1}{2}tanh(0.3979 * ln(\frac{G}{0.5723})\right]^{4.13}$$

$$\beta = \frac{0.1664}{G^{0.688}}\left[sech^{0.576} * (0.5376ln\frac{G}{0.2158})\right]^{0.576}$$

Fitting the data with eq. (2.2) provides the optimal parameters listed above, that can be used to define the impulse response in the frequency domain $F(s, G; v)$:

$$\mathcal{G}^*(\nu) \approx (1 - i\theta_1\nu)^{-\lambda_1}(1 - i\theta_2\nu)^{-\lambda_2} \tag{2.7}$$

with

$$\begin{aligned} \theta_1 &= \tfrac{6.3i}{(1+(0.29/G)^{1.12})^{(1/1.12)}} & \theta_2 &= 0.316sech^2(0.572 + 0.51ln(G)) \\ \lambda_1 &= 1 + \tfrac{0.147}{(G+2.2*G^2)} & \lambda_2 &= 2.73 + \tfrac{0.849}{G} \end{aligned} \tag{2.8}$$

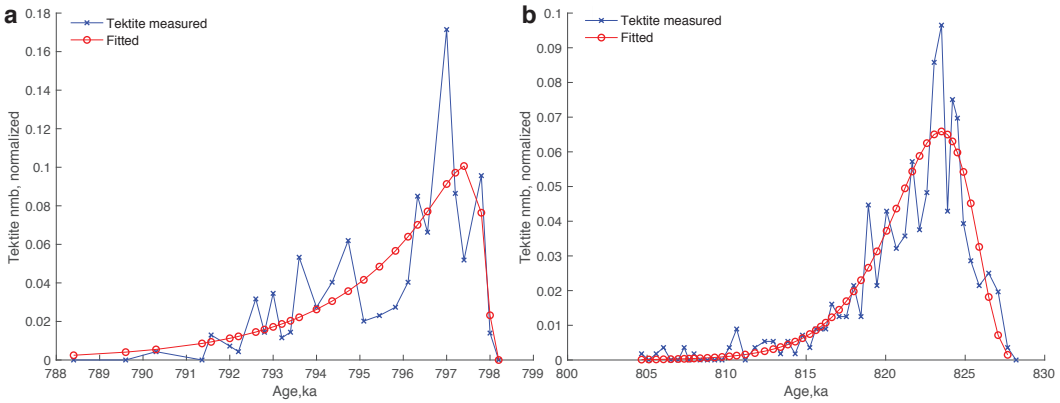

Figure 2.1: Fit to measured microtektite profiles with Guinasso function (eq. 2.2) in the time domain. G and s parameters are 1.023 and 2.76 respectively for a) MD90-0961 profile, and 0.084 and 8.3 for b) MD90-0949.

2.3 Approximation of beryllium records

Beryllium records were obtained for cores MD90-0949 and MD90-0961 from the Indian Ocean (*Valet et al., 2014; Simon et al., 2018*) that contain microtektite levels and from two cores from the Western Pacific Ocean (MD98-2183 and MD97-2143). Cosmogenic beryllium is assumed to be mainly controlled by the geomagnetic dipole changes (see Chapter 1). Therefore, identical Be-ratio profiles might be expected to be found elsewhere within the pelagic sediments, if the environmental contribution was properly normalised. Calculating a mean Be-ratio record (or its stack) should contribute to reduce signal complexities related to sampling site-related inhomogeneities and measurements/sampling inaccuracies. We assume that stack of Be-ratio curves is supposed to contain only features that are common to all cores, that is, the field signal and a global climatic modulation.

Prior to stacking, the Be-ratios from cores MD90-0949, MD98-2183, and MD97-2143 were transformed with the linear coefficients, which minimise the mean quadratic differences with respect to MD90-0961:

$$\frac{^{10}Be}{^{9}Be}_{trasformed(i)} = \left[(\frac{^{10}Be}{^{9}Be})_i - \beta(i) \right] * \frac{1}{\alpha(i)}, \tag{2.9}$$

where α and β are additive and multiplicative coefficients respectively.

The linear transformation is justified by the presence of additive and multiplicative terms in *Blackenburg and Bouchez, (2014)* expression for the average dissolved Be-ratio in the ocean:

$$\left(\frac{^{10}Be}{^{9}Be}\right)_{oc} = \frac{(\frac{A_{oc}}{A_{riv}})F_{oc}^{^{10}Be} + \phi_{del}F_{riv}^{^{10}Be}}{\phi_{del}D_{riv}[^{9}Be]_{parent}(f_{reac}^{^{9}Be} + f_{diss}^{^{9}Be})}, \tag{2.10}$$

where A_{oc} - surface area of the ocean (m^2), A_{riv} - total surface are of rivers discharging basins into the ocean (m^2), ${F_{oc}}^{^{10}Be}$ - flux of meteoric ^{10}Be deposited into the ocean surface (at.m$^{-2}yr^{-1}$), ${F_{riv}}^{^{10}Be}$ - atmospheric flux of ^{10}Be onto the river basin (at.m^{-2}yr^{-1}), ϕ_{del} - beryllium fractional factor, quantifying overall efficiency of Be delivery to the Ocean, $f_{reac}^{^9Be}$ and $f_{diss}^{^9Be}$ are the reactive and dissolved fractions respectively of ^9Be, released during the weathering from the parent rock, and D_{riv} is the average denudation rate.

Core MD90-0961 has been chosen as the reference because of its largest sedimentation rate (3.8 cm/ka) compared to the other sites (see Table 2.1) and thus its better signal resolution and regularity. As it is seen on the Fig.2.2a, the measured Be-ratios are characterised by the similar bell-like shapes during the Matuyama-Brunhes reversal, but also by different ranges of variations, which are explained in terms of water depth differences (*Savranskaia et al., submitted*).

The strong positive correlation with water depth indicates that the Be-ratio signal is affected by environmental effects, despite the ^{9}Be normalisation, that is supposed to eliminate the heterogeneities related to the ocean mixing, core location and sediment type (*Blanckenburg and Igen, 1999; Carcaillet et al., 2003*). Consequently, we might expect a stronger influence of the climatic components during periods of stable field polarity with respect to periods of instabilities like reversals and excursions. Besides, the mean value of Be-ratio estimated outside of the M-B reversal period is not affected by the sediment smoothing since it has been averaged over a long interval.

Interestingly, there is a systematic difference between MD90 - 0961 and the other cores, as seen from the linear transformation coefficients (Table 2.1). The additive coefficient ($-\alpha$) varies between 3.32 and 4.37 and is strongly correlated with water depth at the site. The multiplicative coefficient (β) of all other cores is comprised between 0.445 and 0.596 and positively correlates with the standard deviations of the unscaled Be-ratios. This correlation is another evidence for an environmental contribution to the Be-ratio record and reflects the degree of signals irregularity.

Following the linear transformation of Be-ratio curves, we estimated the mean value of transformed records for the periods, excluding the reversal (Fig.2.2b). This mean or *baseline* was consequently rescaled with α and β coefficients (Table 2.1) and subtracted from each record to produce the stacked curve :

$$\Delta(\frac{^{10}Be}{^{9}Be})_i = \left(\frac{^{10}Be}{^{9}Be}\right)_i - \left[\left(\frac{^{10}Be}{^{9}Be}\right)_{baseline} * \alpha(i) + \beta(i)\right] \tag{2.11}$$

The differences between the amplitudes of rescaled Be-ratios on the Fig.2.2c are expressed by the Be-increment factor for each site (K, Table 2.1),which is positively correlated with sedimentation rate (Table 2.1). That is the indicative that Be-ratio change at each site results from

	MD90-0949	MD90-0961	MD97-2143	MD98-2183
-α	3.32	0	3.05	4.37
β	0.445	1	0.469	0.596
v_{sed}	1.83	3.79	1.28	2
H_w	3600	2450	2989	4388
K	3.54	5.22	4.82	2.63
σ	7.2	0	10.89	16.54

Table 2.1: Additive (α) and multiplicative (β) coefficients used for linear transformations to collapse the Be-ratio profiles on the basis of MD90-0961. H_w and v_{sed} are water depth and sedimentation rate at each site respectively, K is the Be-ratio enhancement factor, estimated as the ratio between the maximum value of rescaled Be-ratio and baseline value, σ is the standard deviation of measured Be-ratios.

the dipole collapse and additional spurious variations due to (1) the worldwide distribution of ^{9}Be and of ^{10}Be (*Blackenburg and Bouchez, 2014)*, (2) global and local environmental variations, and (3) residual sediment-specific effects that were not eliminated by ^{9}Be normalisation. The overall shape of the curves appears to be the only feature that is controlled by the dipole while at this stage we infer that all the other variations may or may not carry a geomagnetic signal.

The model function is bell-shaped in order to account for the dipole collapse and recovery during a reversal and skewed - to account for a slight asymmetry between the timing of dipole collapse and recovery. The data were fitted using the generalised inverse Gaussian (GIG) function because of its meaning as the probability density function of first cross-over times of a random walk (that is, the time required by a sediment particle to reach the historical layer and contribute to the final signal):

$$C(t) = C_0 GIG\Big[ç(t_0 - t), a, b, p\Big] \tag{2.12}$$

with fit parameters C_0, $a > 0$, $b > 0$, p, ç = sgn(p) and

$$GIG(x) = \mathcal{H}\frac{(\frac{a}{b})^{p/2}}{2K_p(\sqrt{ab})}x^{p-1}e^{-(ax+\frac{b}{x})/2}, \quad x > 0, \tag{2.13}$$

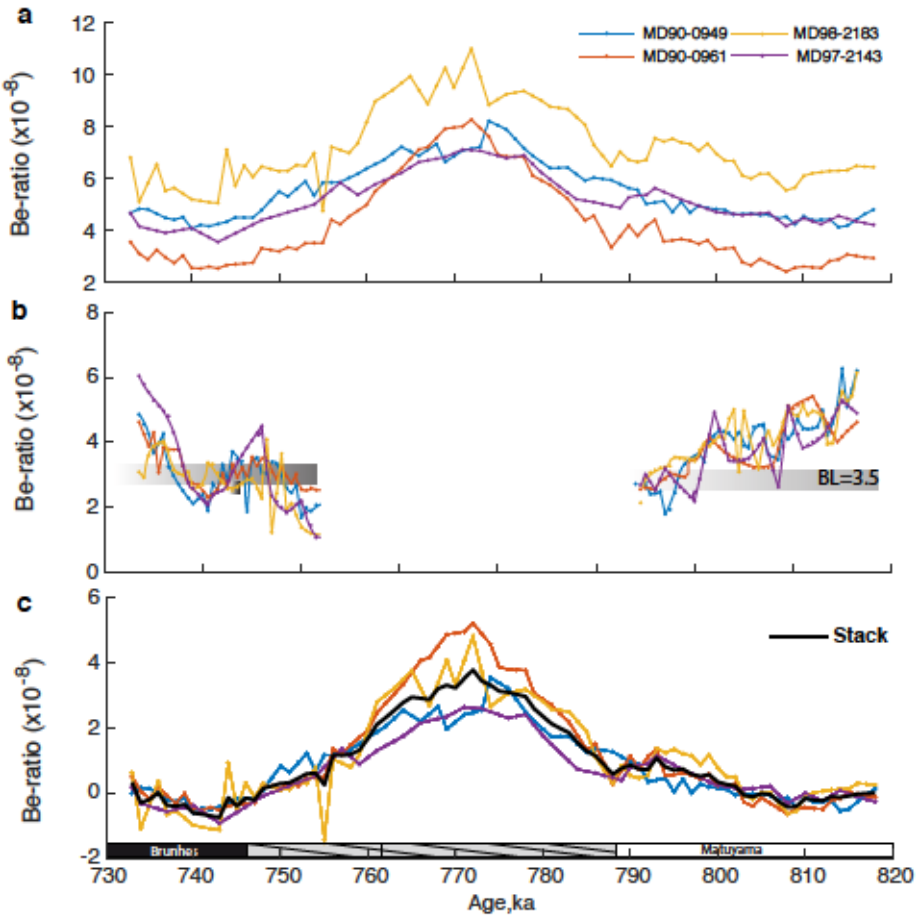

Figure 2.2: a) Measured ^{10}Be/^{9}Be profiles in four sedimentary cores. b) Linearly transformed profiles on the basis of MD90-0961 with additive and multiplicative coefficients as indicated in table 2.1. The baseline estimate (gray stripe) corresponds to an averaged Be-ratio during the period, surrounding the M/B reversal; c) ^{10}Be/^{9}Be profiles after subtraction of rescaled baseline. Thick black line is the ^{10}Be/^{9}Be averaged profile (Stack).

The choice of a physically meaningful function helps to better separate the geomagnetic component of ^{10}Be/^{9}Be from spurious signals and is therefore an important element of the inverse model. Moreover, the existence of characteristic function of GIG enables an easy transition from time (eq. 2.13) to frequency domain:

$$GIG(\nu) = \left(\frac{a}{a-2i\nu}\right)^{\frac{p}{2}} \frac{K_p(\sqrt{b(a-2i\nu)})}{K_p(\sqrt{ab})} \tag{2.14}$$

with $a > 0$, $b > 0$, p - a real constant, and K_p - is modified Bessel function:

$$K_p(x) = \frac{\pi}{2}\frac{I_{-p}(x) - I_p(x)}{sin\pi p}$$
$$I_p(x) = \sum_{k=0} \frac{(x/2)^{2k+p}}{k!\Gamma(p+k+1)} \tag{2.15}$$

$K_p(x)$ and $L_p(x)$ are the solutions of the first and second kind of linear second order ordinary differential equation of type:

$$x^2\frac{d^2y}{dx^2} + x\frac{dy}{dx} - (x^2 + p^2)y = 0 \tag{2.16}$$

To fit data with GIG function, one should have an initial guess for the following parameters a, b, and p. The stacked Be-ratios curve (Fig.2.2c) was first fitted *GIG* function and allowed to deduce a = 1.5, b = 58.9, and p = 34.99. The optimal parameters for MD90-0961 and MD90-0949 are indicated on the Fig.2.3. Because of the asymmetry of the Be-ratio profiles, one must determine the direction of fitting to obtain the best match. In order to achieve the most optimum fit, each Be-ratio profile was fitted twice: with right and left handed *GIG* function.

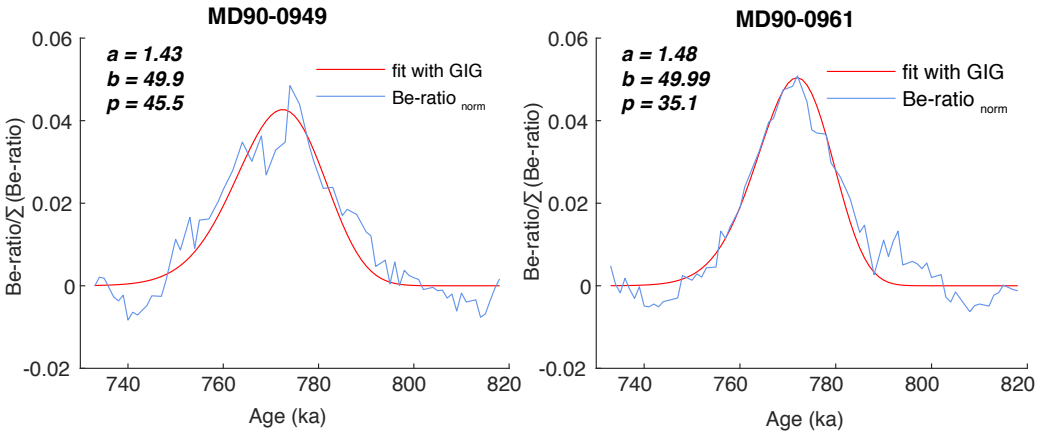

Figure 2.3: Fitted normalised Be-ratio profiles with Generalised Inverse Gaussian function. Indicated parameters a, b, and p are the coefficients that enable the best fit of GIG function with the data.

For each pair of obtained fit parameters (right and left handed *GIG*) we estimated the value of residuals in order to choose the best case. The averaged Be-ratio was in turn fitted with right and left handed GIG function and based on the smallest residuals, the fitting parameters were used to fit Be-ratio in the frequency domain. The best case (minimal residuals) is right -hand *GIG* fit for all the cores.

2.4 Modelling the noise of Be-ratios

The noise, present in measured Be-ratios, could hide the useful information in the signal and thus corrupt the solution for the inversion. The approximation of the Be-ratio curves (section 2.3) implies that only the fundamental part of the signal is preserved so that it is no longer possible to estimate the records uncertainties. Therefore, the noise of the Be-ratio records must be incorporated as an unknown into the model.

A standard approach to tackle this problem is a Monte Carlo simulation in which a noise amplitude that corresponds to the standard deviations of residuals is added to the data. A general model for the data noise is the white noise, because all frequencies contribute equally to the noise signal and all samples are regarded as a sequence of uncorrelated random variables. However, the case of sedimentary beryllium records is different, because the records are controlled by the geomagnetic dipole as well as by environmental changes, that are considered as a noise. The environmental modulation has a certain periodicity (see Chapter 4), and thus cannot be described by the white noise model. The best way to simulate the noise is thus to consider the character of the noise by analysing its frequency spectrum, i.e. the spectrum of Be-ratio fit's residuals. The advantage of this method is that the simulated noise will have the same statistical properties as for the fit residuals (e.g. mean and standard deviation).

Monte Carlo noise simulation comprises the following steps. First, because a part of residuals (Be-ratio$_{fit}$-Be-ratio) is systematic in all the cores and likely results from climatic contamination, their mean was discarded prior to their spectrum estimation (Fig.2.4). Second, we estimated and fitted the power spectrum of Be-ratio's residuals with the following model :

$$H(f) = \frac{a}{1 + (\frac{\nu}{\nu_0})^{\alpha}} + w^2, \tag{2.17}$$

where α is scaling exponent, that was fixed as 2, ν_0 is cutting frequency, ν -is frequency, a - white noise additive factor, and w is a minimum spectral power.

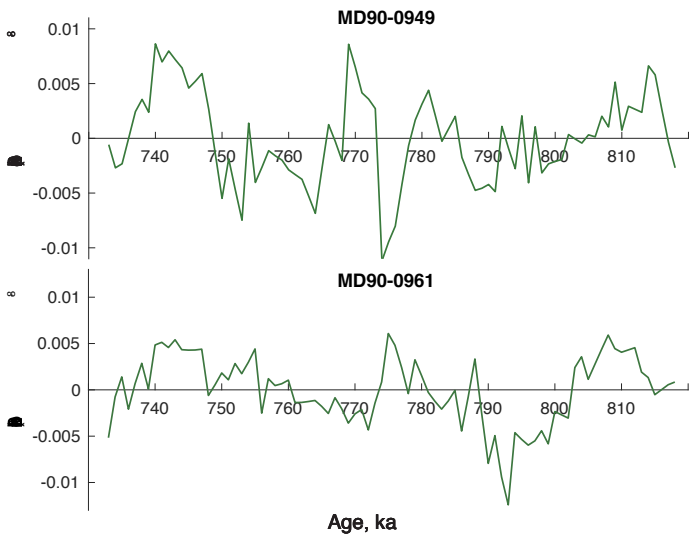

Figure 2.4: Residuals from fitting normalised linearly transformed records (Fig.2.2c) with the GIG function (eq. 2.11) with subtracted mean value.

The standard method of generating noise series is based on the phase randomness, thus 100 random phases have been created $\left[\phi \in (0, 2\pi)\right]$ and were used to create 100 spectrums of residuals ($r(\nu) = \sqrt{H(f)}e^{i*\phi}$). Finally, simulated noise spectrums were transformed to the time domain and added to Be-ratios. The results are shown on the Fig.2.5.

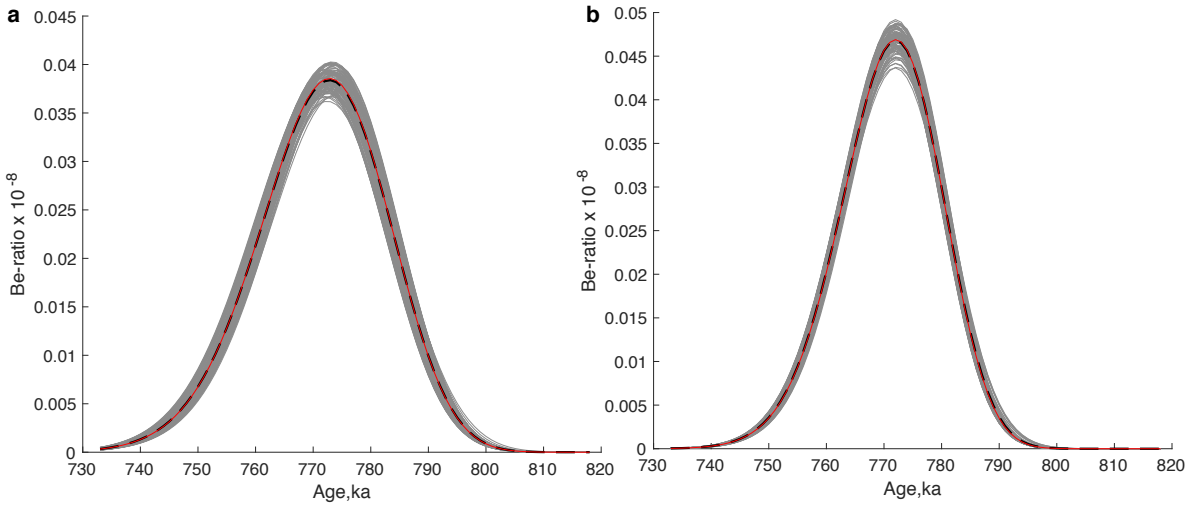

Figure 2.5: 100 Be-ratio Monte Carlo simulated curves (gray colour): a) MD90-0949; b) MD90-0961. Red and black curves represents fit with GIG function and mean simulated curve respectively. Please notice that Be-ratio records have been normalised by their integrals.

2.5 Modelling the noise of microtektite records

Like for the beryllium records, the uncertainties inherent to the microtektite counting have to be estimated. To simulate the noise characteristic for the microtektite measurements, we generated 100 profiles with a Poisson distribution in which the distribution parameter lambda was set as an initial microtektite vector. Generated Monte Carlo curves with Poisson distribution showed several families among the 100 profiles and therefore they must belong to the distribution characterised by σ and μ. The following function was used to estimate the integral of product of $Guinasso$ and normal probability density functions.

$$\int_{\mu-3*\sigma}^{\mu+3*\sigma} (g', \mu', \sigma) * \mathcal{G}(\frac{t_0 - t}{s}, e^{g'})\mathrm{d}g \tag{2.18}$$

Analysis of residuals distribution (Fig. 2.6 a,c) allowed to establish the selecting criteria. Curves, with residuals < (-2.28) for MD90-0949 and < (-1.6) for MD90-0961 were discarded. Selected microtektite profiles were fitted with the *Guinasso* model (eq.2.2) and the best fit parameters (G, s) of the averaged records were kept to generate the microtektite profiles in frequency space for the inversion.

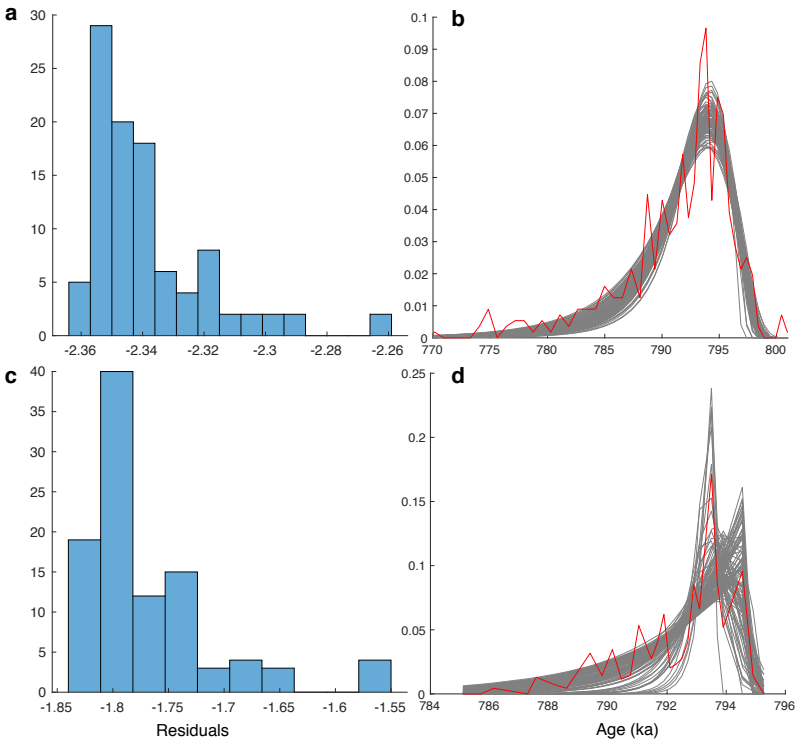

Figure 2.6: a;c); Histograms of tektite fit residual estimates for MD90-0949 and MD90-0961 respectively. b);d) Monte Carlo simulated profiles (gray curves) and measured microtektite profiles (red curves) of MD90 - 0949 and MD90-0961 cores respectively.

2.6 Inversion

The geomagnetic field signals during the Matuyama - Brunhes reversal obtained by solving the inverse problem with microtektite profiles. The Be-ratio record was expressed as the convolution of magnetic field with sedimentary response function and therefore the field can be recovered in the frequency domain by :

$$B^*(\nu) = \frac{C^*(\nu)}{\mathcal{L}^*(\nu)}, \tag{2.19}$$

where $B^*(\nu)$ is magnetic field, $C^*(\nu)$ fit of Be-ratio records in the frequency domain, and $\mathcal{L}^*(\nu)$ is fit of microtektite.

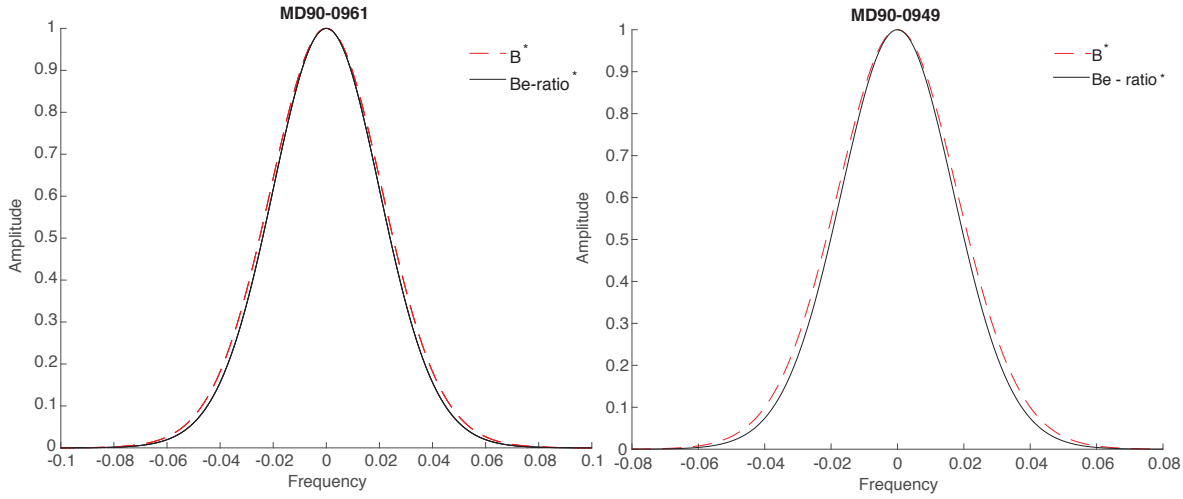

Figure 2.7: Comparison of fitted and reconstructed Be-ratios spectrums. Continuous black line is Be-ratio spectrum, dashed red - reconstructed field.

Transformation back to the time domain by the inverse Fourrier transform could be achieved by:

$$B(t) = \int_{-\infty}^{+\infty} B^*(\nu) e^{2\pi i \nu t} d(\nu) \tag{2.20}$$

Because of the large mean age $\bar{t} \approx 770$ kyr of $C(t)$, the argument of the integral is highly oscillatory. Numerical integration problems are avoided by removing the mean age using the shift theorem of Fourrier transform, whence

$$B(t - t_0) = \int_{-\infty}^{+\infty} \frac{C^*(\nu)}{\mathcal{L}^*(\nu)} e^{2\pi i \nu t} d\nu \tag{2.21}$$

Substituting the fit results finally gives:

$$B(t-t_0) = \int_{-\infty}^{+\infty} \frac{C_0 GIG^*(-\varsigma\nu, a, b, p)}{\int_{-\infty}^{+\infty} \mathcal{N}(g, \mu_g, \sigma_g)\mathcal{G}^*(-s\nu, e^g)dg} e^{2\pi i\nu(t-\bar{t}-t_0)} d\nu, \tag{2.22}$$

with relative ages $t - t_0$ limited to an interval of few tens of kyr around 0. The correct age is then recovered by adding $\bar{t}$ to the relative ages.

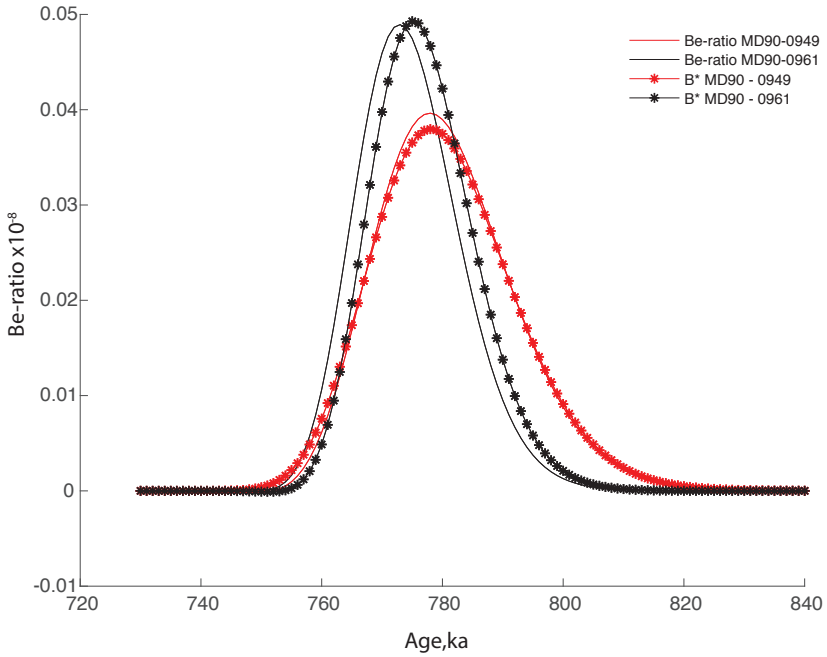

Figure 2.8: Comparison of fitted and reconstructed Be-ratios, that are assumed to be proportional to geomagnetic dipole moment. Continuous lines are fitted Be-ratios (red- MD90-0949, black- MD90-0961), lines with stars - reconstructed Be-ratios (field). Notice, that the records are normalised by their integrals.

It is expected that sediment mixing smears and broadens the isotope signal. The Be-ratio peak width (Fig.2.8) exceeds 60 ka at both sites which seems to be a long duration of reversal phase based on recent estimates (e.g. *Valet et al., 2012*). The inverted Be-ratio profiles are expected to be narrower than the initial fit but the fitted and inverted Be-ratios are almost identical (Fig.2.7-2.8). We might also expect that the microtektite profiles at each site account for local sediment distribution processes. In this manner, the inversion should allow to get back to the 'true' magnetic dipole field changes that are identical at all locations. On the contrary, the field signals that were obtained after inversion with the microtektite profiles have different widths and are thus inconsistent (Fig. 2.9). Note that the discrepancy is related to the width of the reconstructed field signals and therefore independent from any normalisation procedure.

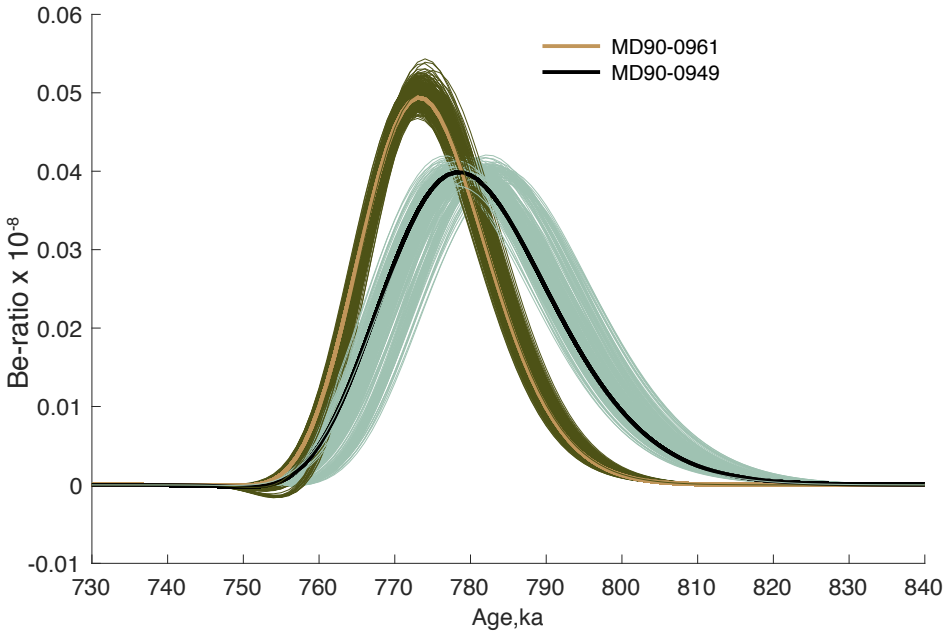

Figure 2.9: Unsmoothed Be-ratio profiled with impulse response function (microtektite fit). The confidence limits are shown by simulated Monte Carlo records.

There are two possible explanations of these results : (1) differences in the event duration recorded by Be-ratio, and/or (2) different mixing impulse responses for Be and the microtektites. Given the global nature of the dipole, (1) can only be explained by reservoir effects, that is, the storage and delayed release of ^{10}Be in the different pools (continents, atmosphere, oceans). The maximum width difference of the reconstructed signal is about 3 kyr, which is longer than the residence time estimates of 1-2 years in the atmosphere (*Masarik and Beer, 1999*) and 500-1000 years in the ocean (e.g. *Kusakabe et al., 1987*). Hypothesis (2) is thus favoured because it is supported by the size dependency of mixing which is linked to the selective ingestion of smaller particles (*Wheatcroft, 1992*) and to the Brazilian nut effect (Chapter 2.8). In other words, beryllium and microtektites would not be affected by mixing processes in the same manner. A direct consequence is that the sedimentary mixing impulse response derived from the microtektite distribution cannot be used for inversion of the beryllium signal. This assumption (2) is studied further in Chapter 2.8.

2.7 Analysis of residuals

So far, we analysed the principal component of the Be-ratio signal during a reversal obtaining a minimalistic model, based just on the few parameters. One can ask now whether the remaining features of the Be-ratio signal contain further details related to the dipole strength and its evolution during the reversal. In this respect we scrutinise the Be signal residuals, defined as differences between measured and fitted Be-ratio signals. Fig. 2.10a

shows that the residuals share a common harmonic signal with a period of about 40 kyr, as well as random short-term variations that seem to be a white noise.

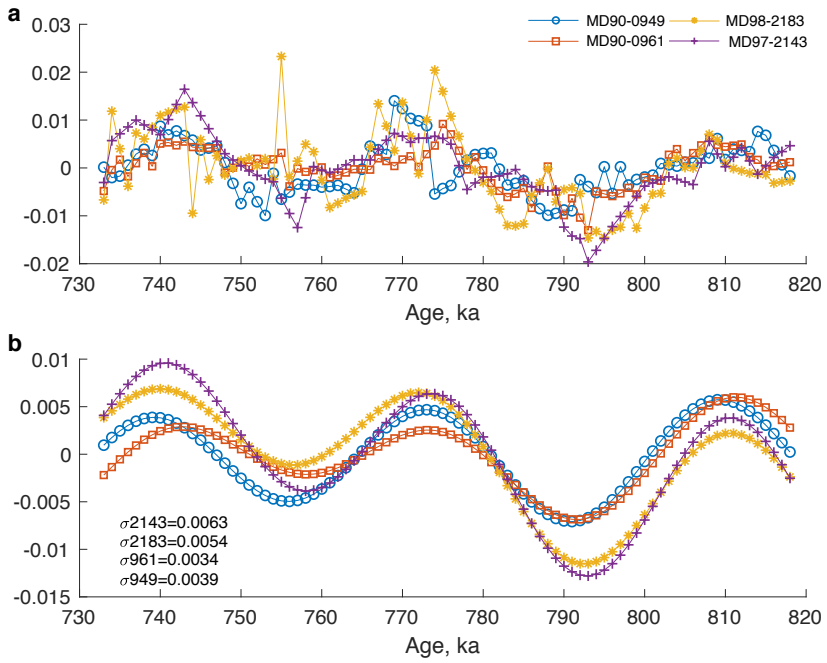

Figure 2.10: a) Residuals of Be-ratio fit and measured normalised Be-ratios; b)Fits of residuals with sin function with 3 frequencies (ν_1 = 1/35 ka is the dominant).

The 40 kyr apparent period is strikingly close to that of the obliquity of the Earth's orbit. If we assume that this harmonic signal has a magnetic origin that is properly recorded by the Be-ratio, then the deconvolution with the mixing impulse responses should yield a reconstructed "residual" field variation that is identical in all cores. To check this hypothesis and exclude the noise component, beryllium residuals are fitted with a linear combination of three sinusoidal signals, of which one has the 35 kyr period (Fig. 2.10a). Because these signals are harmonic, the deconvolution was simply obtained by dividing the amplitude of each sin term (r^*) with the impulse response spectrum value ($\mathcal{L}^*(\nu)$) for the same frequency:

$$B^* = r^*(\nu)/\mathcal{L}^*(\nu), \tag{2.23}$$

A better agreement should be obtained between the deconvolved harmonic signals. In all cases the minimum and maximum amplitudes differ by a factor of two, but it noticeable that the cores with lower sedimentation rates are characterised by larger amplitudes, which is opposite to the situation that would be induced by smoothing. Therefore, we can confidently say that the harmonic residuals in the Be signal, and especially the one with a period of 40 kyr, does not originate from field variations.

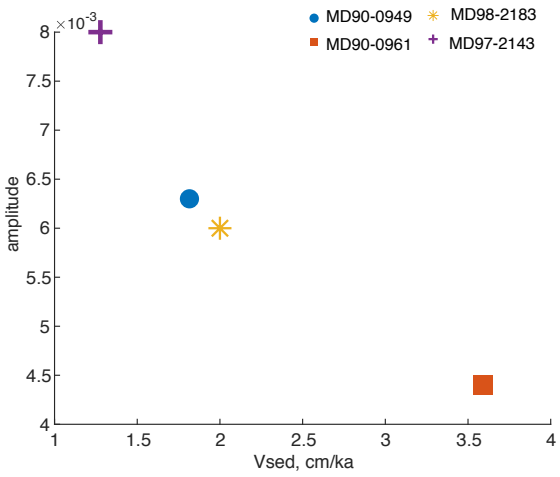

Figure 2.11: Amplitude of the inverted Be-ratio residuals with microtektite fit as a function of sedimentation rate ($\nu = 0.0285$).

The amplitude of the harmonic residuals is about 0.005 and represents 10% of the Be-ratio increase during the reversal. Therefore, >10% of the total Be variations would be related to the influence of the earth's orbital changes that are responsible for global climatic changes with significant consequences for beryllium distribution in sediments. Even if the harmonic signals are unrelated to field variations, they are still subjected to sediment mixing, so that the true amplitudes are those resulting from deconvolution with the proper mixing impulse response, that are shown in Fig. 2.11.

2.8 Tektite profiles modelling

2.8.1 General settings

As sediment is buried through the surface mixed layer, bioturbation affect the spatial positions of individual particles in a random manner, so that particles originally deposited in an infinitely thin layer are found, after a certain time t, across a range of depths z. This is, for instance, the typical case of tektites deposited after a large impact. The burial depth is thus described by a statistical variable $Z(t)$ evolving from a Dirac impulse $\delta(t)$ at $t = 0$ to a probability density function $_z(z|t)$ at $t > 0$. Below the maximum mixing depth L, all particles share the same depth-dependent burial velocity $v_b(z)$, so that the relation between depth and age of any sediment particle is given by $t_s = t_L + t_b$, where t_L the time required for burial below $z = L$ and

$$t_b(z) = \int_L^z \frac{du}{v_b(u)}, \tag{2.24}$$

with t_b the time required for further burial to final depth z. If the depth $Z(t)$ of a particle in the

surface mixed layer is modelled as a biased 1D random walk (*Reible and Mohanty, 2002*) with reflecting boundary at $z = 0$, t_L is a random variate corresponding to the first passage time of Z (*Wencour, 1988; Schwarz, 1992*). The probability density function, $_t$,(*t*, **b**) of t_L is the impulse response of the surface mixed layer at $z = L$, and is controlled by a set of parameters **b** describing the bioturbation process. Depth profiles of the volumetric concentration of a conservative tracer are obtained from the impulse response using the transformation rule of stochastic variables, which gives

$$_z(z|t) = \ (t_s, \mathbf{b})\left|\frac{dt_s}{dz}\right| = \frac{1}{v_b(z)} \ _t(t_s, \mathbf{b}) \tag{2.25}$$

for $z \geq L$. The factor v_b^{-1} on the right-hand side of eq. (2.25) accounts for the volume concentration increase due to compaction. In absence of diagenetic processes affecting the mass of sediment particles, the product $J_s = v_b\varphi_s$ between burial velocity and the volume fraction φ_s of solids is constant and represents the bulk volumetric flux of sediments (*Muslow et al., 1998; Meysman et al., 2005*). Similarly, the impulse response function can be recovered from concentration profiles recorded at a time t_0 after an impulsive event, using

$$_t = \ _z(L + \zeta(t)|t_0)\left|\frac{dt_b(\zeta)}{d\zeta}\right|^{-1} = v_b(\zeta(t)) \ _z(L + \zeta(t)|t_0), \tag{2.26}$$

where ζ is the inverse function of t_b. The age of a particle found at depth $z \geq L$ coincides with the random variate t_L +$t_b(z)$ with probability density function $_t(t - t_b)$.

Grain size segregation occurs when one or more elements of the parameter vector **b** describing the bioturbation process depends on particle size. In this case, different concentration profiles and different age distributions are found for different size classes. Segregation effects typically involve both the systematic and the random component of particle displacement, which, in the context of bioturbation, corresponds to diffusion and burial within the mixed layer. Until present, bioturbation-related segregation mechanisms were considered to include the percolation of small particles through sediment pores, and the selective ingestion of smaller particles by deposit feeders (*Wheatcroft, 1992*). Particle size-dependent segregation in natural environments could be also illustrated by the rise of manganese nodules (*Piper and Fowler, 1980*) and by migration of very coarse debris (ice rafting) to the surface of deep-sea sediments (*McCave, 1988*). Abiogenic particle size segregation has been intensively investigated in the framework of granular flows and powder processing (*Bridgwater, 1994; Kudrolli, 2004*).

2.8.2 Diffusive model of bioturbation

At a microscopic level, bioturbation is described by a stochastic process, which characterise the displacement of individual particles by a succession of discrete displacements (*Meysman*

et al., 2008). Small displacements, e.g. by sediment reworking, lead to a macroscopic description of bioturbation as a local (diffusive) transport mechanism, while large displacements (e.g. by ingestion and egestion), produce a non-local (advective) transport (*Boudreau, 1986a, b; Robbins, 1986; Boudreau and Imboden, 1987*). Long-term bioturbation effects converge to a diffusive model, except for systems heavily dominated by head-down feeders (*Boudreau and Imboden, 1987; Meysman et al., 2010; Reible and Mohanty, 2002*). Furthermore, the importance of nonlocal mixing decreases with increasing water depth (*Soetaert et al., 1996*), and increasing time integration (*Gerino et al., 1994; Aquino et al., 2017*). Diffusive models require fewer species-independent parameters and are therefore widely used to model radioactive (*Peng et al., 1979*) and stable (*Officer and Lynch, 1983*) tracer profiles.

2.8.3 General diffusion-advection equation

We begin with a general formulation of the diffusion-advection equation for tracer and sediment particles in a stationary sediment column characterised by a constant depth-dependent volume fraction φ_s, defined as the fraction of total volume occupied by solids. Similarly, φ_t is the volume fraction of a tracer, whereby it is assumed that $\varphi_t \ll \varphi_s$, so that the bulk sediment properties are independent of the tracer content, which is usually expressed as volume concentration $C = \varphi_t/\varphi_s$ or mass concentration $C_m = \varphi_t/\varphi_s\varrho_s$, with ϱ_s being the density of solid particles. The sediment column is assumed to be laterally homogeneous, so that the diffusive and advective fluxes depend only on vertical gradients and vertical velocities, respectively. In a coordinate system where z is the depth below the sediment-water interface, the downward diffusive fluxes of sediment and tracer are given by $-D_s\partial\varphi_s/\partial z$ and $-D_t\partial\varphi_t/\partial z$, respectively, where D_s is the self-diffusion coefficient of sediment particles, and D_t the diffusion coefficient of tracer particles. If the tracer diffusion is passively driven by sediment diffusion, $D_t = \alpha D_s$, where α is a proportionality constant that depends on the characteristics of the tracer particles, in particular their size.

Sediment particles also experience an advective transport due to burial and bioturbation. Accordingly, the total advective flux of bulk sediment is given by $(v_b + v_a)\varphi_s$, where v_b is the burial velocity resulting from continuous sedimentation and compaction, and v_a an additional velocity term generated by diffusion in a compacting sediment, as explained later. Tracer particles might move relatively to the sediment because of biological selectivity (e.g. preferential ingestion), or mechanical effects associated with size segregation phenomena. As a result, tracer particles possess an additional velocity term $-v_t$, where the negative sign accounts for the upward migration of large tracer particles in case of size segregation. Mass conservation in a stationary column, where $\partial\varphi_s/\partial t = 0$, yields the following diffusion-advection equations:

$$\begin{aligned} \frac{\partial\varphi_t}{\partial t} &= \frac{\partial}{\partial z}\Big[D_t\frac{\partial\varphi_t}{\partial z} - (v_b + v_a - v_t)\varphi_t\Big] \\ 0 &= \frac{\partial}{\partial z}\Big[D_s\frac{\partial\varphi_s}{\partial z} - (v_b + v_a)\varphi_s\Big] \end{aligned} \tag{2.27}$$

for the volume fractions of tracer and sediment. The right-hand side of the second line in eq. (2.27) is equivalent to the gradient of the depth-independent flux

$$J_s = (v_b + v_a)\varphi_s - D_s \frac{\partial \varphi_s}{\partial z} \tag{2.28}$$

of sediment particles, with boundary condition $J_s(z = 0) = \varrho_s^{-1} F_s$ at the sediment-water interface, where F_s is the incoming flux of settling particles, as mass per unit of surface and time. Below the maximum bioturbation depth L, where $D_s = D_t = 0$, $J_s = v_b \varphi_s$ coincides with the burial flux, and $v_b = J_s/\varphi_s$ is entirely determined by φ_s, and thus by the porosity profile. If the same definition of v_b is used within the mixed layer, eq. (2.28) yields the flux

$$\varphi_s v_a = D_s \frac{\partial \varphi_s}{\partial z} \tag{2.29}$$

associated with the bulk diffusion of porosity, also known as 'interphase mixing', as opposed to the 'intraphase mixing' affecting the tracer concentration (*Muslow et al., 1988; Meysman et al., 2005*). In practice, interphase mixing transfers particles from less porous to more porous regions, regardless of their composition, while intraphase mixing equalises compositional differences. Substitution of eq. (2.29) into the first row of eq. (2.27) with $\varphi_t = \varphi_s C$ yields the diffusion-advection equation

$$\varphi_s \frac{\partial C}{\partial t} = \frac{\partial}{\partial z}\Big[D_t \frac{\partial \varphi_s C}{\partial z} - \Big(D_s \frac{\partial \varphi_s}{\partial z} + J_s - \varphi_s v_t\Big) C\Big] \tag{2.30}$$

for the tracer concentration. The tracer flux at the sediment-water interface $z = 0$ must equal the incoming tracer flux F_t, expressed as tracer mass per unit of surface and time. This defines the boundary condition

$$\Big[(D_s - D_t)\frac{\partial \varphi_s}{\partial z} + J_s - \varphi_s v_t\Big] C - \varphi_s D_t \frac{\partial C}{\partial z}\Big|_{z=0} = \varrho_t^{-1} F_t(t) \tag{2.31}$$

for tracer particles with density ϱ_t. In case of size segregation, eq. (2.31) must hold for every size class, requiring a redefinition of C as the concentration of tracer particles per size class width. In this case, eq. (2.31) needs to be rewritten as

$$\Big[(D_s - D_t)\frac{\partial \varphi_s}{\partial z} + J_s - \varphi_s v_t\Big] C - \varphi_s D_t \frac{\partial C}{\partial z}\Big|_{z=0} = \varrho_t^{-1} g_t(s,t) F_t(t) \tag{2.32}$$

where F_t is the total flux of tracer particles, and g_t a (time - dependent) tracer size distribution. If g_t is defined on a logarithmic scale, C maintains its original unitless definition as ratio between the tracer and sediment volumes.

2.8.4 Size segregation

Various studies report the tendency of larger particles initially deposited on the surface of bioturbated sediment to penetrate less rapidly into the sediment (*DeMaster and Cochran, 1982*; *Wheatcroft et al., 1994*; *Thomson et al., 1995*). This effect has been attributed to the preferential ingestion of finer particles by deposit feeders (*Whitlatch, 1989*; *Shull and Yasuda, 2001*), which, in a diffusive bioturbation model, leads to a grain size-dependent diffusion coefficient. Experiments with sorted glass beads suggest a power law dependency of the form $D_t \propto s^{-q}$, where s is the bead size and $q \approx 0.52$ (*Wheatcroft et al., 1992*). Much stronger ingestion selectivity of deposit feeders ($q \approx 2.8$ according to data from *Shull and Yasuda, 2001*) suggests that less selective mixing mechanisms, must contribute, possibly in a predominant manner, to the observed tracer diffusion. The diffusion of particles percolating through random media, of which sediments are an example, is controlled by micro-structures, which are often fractal over a finite range of length scales. This gives rise to anomalous diffusion (*Saxton, 1994*), which depends on the ratio between particle size and the length scale of pores (*Fatin-Rouge et al., 2004*). For instance, the diffusion coefficient in fractal soil structures has been modelled with $D = D_0(r/r_0)^{-q}$, where r is a length scale, D_0 the effective Fickian diffusion coefficient at scales smaller than the smallest size r_0 of fractal structures, and q an exponent comprised between ∼0.28 and ∼0.66 (*Anderson et al., 2000*). The results of glass bead experiments of *Wheatcroft et al. (1994)* lie in this range. For comparison, the diffusion coefficient of Brownian diffusion is characterised by $q = 1$ (*Kubo, 1966*), while $q = 0$ is expected for infinite fractals (*Bunde and Havlin, 2012*). The tracer diffusion coefficient is therefore modelled assuming

$$D_t = \alpha D_s \tag{2.33}$$

with $\alpha = \psi^{-q}$ and $0 < q < 1$, where D_s is the solid self-diffusion coefficient of the bulk sediment, and $\psi = s/s_0$ the ratio between the size s of tracer particles, and the characteristic (mean or median) size s_0 of sediment particles.

The advective component of size segregation is proportional to the segregation velocity v_t (positive upwards) of large tracer particles with respect to the bulk sediment. Advective segregation, or granular convection, can be explained by the selective downward percolation of smaller grains through pores when particle assemblages are agitated or mixed. The resulting tendency of large particles to rise to the top is also known as kinetic sieving (*Lajoie, 1970*) or Brazil nut phenomenon. The most prominent examples in sedimentary environments are the persistence of ferromanganese nodules at the sediment surface (*Heath, 1979; Piper and Flower, 1980*) and occurence of glacial gravels (*McCave, 1988*). Granular convection is also affected by density, with the counterintuitive tendency of large, less dense particles to raise

less rapidly (*Liffman et al., 2001*). In analogy with laboratory experiments (*Kudrolli, 2004*), we assume the grain size dependence of v_t to be given by the ramp function

$$v_t = \propto \begin{cases} 0, & \psi \leq \psi_c \\ \psi - \psi_c, & \psi > \psi_c \end{cases} \tag{2.34}$$

where ψ_c is threshold value of the size ratio above which size separation occurs. Very different experimental settings yield similar values of ψ_c around 3 (*Duran et al., 1994; Vanel et al., 1997*). In dry bed vibrating experiments, the relative upward velocity of a large sphere is proportional to the vibration frequency in the low-frequency limit [1]. A similar behaviour is obtained also for cohesive materials simulated by wet powders, whereby increasing cohesion forces are found to decrease the segregation effect (*Zhao et al., 2019*). If episodic sediment disturbances produce, on average, a certain size segregation effect, it can be assumed that these effects add in time, in analogy with the microscopic particle displacements underlying diffusive models of bioturbation-driven sediment mixing. In this case, v_t is proportional to the frequency of bioturbation events and thus to D_s, regardless of micromechanical details, and eq. (2.34) can be rewritten as

$$v_t = \beta(\psi) D_s \tag{2.35}$$

with

$$\beta(\psi) = \beta_0 \begin{cases} 0, & \psi \leq \psi_c, \\ \psi - \psi_c, & \psi > \psi_c \end{cases} \tag{2.36}$$

where β_0 is a constant coefficient with the unit of an inverse length.

2.8.5 Diffusion in a homogeneous mixed layer

Analytical solutions for the general form of the diffusion-advection equations formulated in Section 2.8.3 do not exist. Furthermore, the depth dependence of the diffusion coefficient is controlled by the distribution of benthic organisms, which is not known a priori and is difficult to determine. In practice, different models of depth-dependent diffusion yield similar fits to experimental data after proper parameter choice (*Kadko and Heath, 1984; Swift et al., 1996; Deleersnijder et al., 2006; Meysman et al., 2007*). This means that simple universal models can effectively reproduce tracer profiles and their grain size dependence. The simplest diffusive bioturbation model assumes a homogeneous mixing layer of thickness L,

[1] Vanel et al. (1997) found that the rise time T of a large sphere in a granular bed is proportional to $[e^{(v/v_c)^2} - 1](\Gamma - \Gamma_c)^{-\beta} v^{-1}$, where v is the vibrating frequency, v_c a critical value of v, Γ the unitless acceleration of vibrations, Γ_c a critical value of Γ, and $\beta \approx 2$. The limit of this expression for $v \to 0$ is $T \propto v^{-1}$, so that the rising velocity is proportional to v.

where porosity and diffusion coefficient do not depend on depth (*Guinasso and Schink, 1975*). In this case, the diffusion-advection equation for the volumetric tracer concentration C becomes

$$\frac{\partial C}{\partial t} = D_t \frac{\partial^2 C}{\partial z^2} - (v_b - vt)\frac{\partial C}{\partial z} \tag{2.37}$$

with boundary condition

$$(v_b - v_t)C - D_t \frac{\partial C}{\partial z}\bigg|_{z=0} = \frac{1}{\phi_s \varrho_t} F_t(t) \tag{2.38}$$

corresponding to the incoming tracer flux F_t at the water-sediment interface, expressed as tracer mass per unit of surface and time. As discussed in Section 2.8.3, v_b is the burial velocity of sediment particles, and v_t the upward velocity of tracer particles with respect to the sediment, associated with size segregation effects. All coefficients in eq. (2.37-2.38) are constant and do not depend on depth. Solutions can be limit to the $[0, L]$ interval by adding a second boundary condition at $z = L$ that follows from the continuity of C. Being $v_b C$ the tracer flux below the mixed layer,

$$v_t C + D_t \frac{\partial C}{\partial z}\bigg|_{z=L} = 0 \tag{2.39}$$

In the case of no size segregation ($v_t = 0$), the variable transformations $x = z/L$ and $t^* = v_b t/L$ reduce eq. (2.37-2.39) to the nondimensionalized diffusion-advection equation of the form

$$\frac{\partial C}{\partial t^*} = G_s \frac{\partial^2 C}{\partial x^2} - \frac{\partial C}{\partial x} \tag{2.40}$$

which depends on a single parameter $G_s = Pe^{-1} = D_s/Lv_b$ with the meaning of an inverse Péclet number (*Guinasso and Schink, 1975*). The Péclet number Pe is defined as the ratio between advective and diffusive transport over the typical length scale L of the mixed layer. A similar nondimensionalization is obtained for $v_t > 0$ upon replacing v_b in the definition of G_s by the total tracer particle velocity $|v_b - v_t|$. In this case, the variable substitutions $x = z/L$ and $t^* = |v_b - v_t|t/L$ for $v_t \neq v_b$ give

$$\frac{\partial C}{\partial t^*} = G \frac{\partial^2 C}{\partial x^2} \pm \frac{\partial C}{\partial x}, \tag{2.41}$$

with $G = G_s \alpha |1 - v_t/v_b|^{-1}$. The negative (positive) sign of $\partial C/\partial x$ in eq. (2.41) applies to the case of net downward (upward) advection, that is, $v_t < v_b \quad (v_b < v_t)$. The boundary conditions at the sediment-water interface and at the bottom of the mixed layer are given by

$$\pm C - G \frac{\partial C}{\partial x}\bigg|_{x=0} = \frac{1}{\phi_s \varrho_t |v_b - v_t|} F_t(t) \tag{2.42}$$

and

$$wC - G\frac{\partial C}{\partial x}\bigg|_{x=L} = 0, \tag{2.43}$$

respectively, with $w = |v_b/v_t - 1|^{-1}$ being the normalised amplitude of the burial velocity discontinuity across $x = 1$ caused by v_t. The case of no tracer advection ($v_t = v_b$) must be treated separately, since the $t^* = 0$ is not a valid variable substitution. The variable transformations $x = z/L$ and $t^* = v_b t/L$ yield the pure diffusion equation

$$\frac{\partial C}{\partial t^*} = G_s \frac{\partial^2 C}{\partial x^2} \tag{2.44}$$

and the boundary conditions

$$-G_s\frac{\partial C}{\partial x}\bigg|_{x=0} = \frac{1}{\phi_s \varrho_t v_b} F_t(t) \qquad G_s\frac{\partial C}{\partial x}\bigg|_{x=1} = 0 \tag{2.45}$$

These equations are governed by two parameters: the Péclet number $Pe_t = |v_b - v_t|L/D_t$ of tracer particles, and the so-called segregation Péclet number $Pe_\Delta = v_t L/D_t$, defined as the ratio between the advective segregation transport v_t and the diffusive transport D_t/L. With these definitions, $G = Pe_t^{-1}$ and $w = Pe_\Delta/Pe_t$. Percolation-driven segregation is characterised by $Pe_\Delta \approx 6 \sim 12$ and no systematic grain size dependence for $s/s_0 \geq 1.5$ (*Thornton et al., 2012; Khola and Wassgreen, 2016*).

2.8.5.1 The impulse response

The impulse response of the surface mixed layer is defined as the tracer concentration produced by a tracer flux pulse $F_t(t) = \Phi_t \delta(t)$ at $t = 0$, where δ is the Dirac impulse and Φ_t the tracer fluence, defined as the total tracer mass deposited on a unit area of the sediment-water interface. It is given by the solution of eq. (2.37-2.38) with the initial concentration $C(z, t = 0) = 0$. At a microscopic level, the impulse response describes the probability distribution of the position of a tracer particle performing a random walk after being released from its initial position $z(t = 0) = 0$. In particular, the impulse response, $C(z = L, t)$ at the bottom of the mixed layer is formally equivalent to the so-called first-passage or escape time of a particle performing this type of motion (*Palyulin et al., 2019*). The most general formulation of a random walk is the so-called Lévy flight, where jump sizes and times obey a general class of stable probability distributions called Lévy functions (*Reible and Mohanty, 2002*). The Brownian motion is a special case of Lévy flight with gaussian step sizes. Up to few pathological exceptions, bioturbation is correctly described by a Brownian motion and its continuous limit, the Wiener process (*Meysman et al., 2008*). Solutions have been obtained for

the first-passage time distribution of several problems, including Wiener processes with drift and two elastic barriers (*Dominé, 1996*). The solution of *Guinasso and Schink (1975)* for a homogeneous mixed layer correspond to the first passage time at level L of a Wiener process with drift and a single reflecting barrier at $z = 0$, which keeps the moving particle inside the sedimentary column. Unfortunately, this solution is limited to the case of $v_t = 0$. However, the original solution approach based on the eigenfunction expansion of the diffusion-advection equation can be applied to the $v_t \neq 0$ case, following *Schwarz (1992)*.

The calculation of the impulse response associated with eq. (2.41-2.43) begins by replacing tracer flux pulse with the initial condition $C(x, 0) = L^{-1}\delta(x)$, where the factor L^{-1} arises from the variable substitution for depth [2]. This initial condition represents the tracer concentration immediately after the tracer pulse has formed an infinitely thin layer at the top of the sedimentary column. From this time on, $F_t(t) = 0$ in eq. (2.42). Let $\mathcal{G}$(x,t*) be the solution of the unitless diffusion-advection equation with $\mathcal{G}(x, 0) = \delta(x)$, as in *Guinasso and Schink (1975)*. If $v_t < v_b$, the substitution

$$\mathcal{G}(x, t^*) = exp\Big(\frac{2x - t^*}{4G}\Big)c(x, t^*) \tag{2.46}$$

transforms eq. (2.41) into the diffusion equation

$$\frac{\partial c}{\partial t^*} = G\frac{\partial^2 C}{\partial x^2} \tag{2.47}$$

with initial and boundary conditions

$$\begin{aligned} c &= \delta, \quad t^* = 0 \\ \frac{\partial c}{\partial x} &= \frac{1}{2G}c, \quad x = 0 \\ \frac{\partial c}{\partial x} &= -\frac{1 + 2w}{2G}c, \quad x = 1 \end{aligned} \tag{2.48}$$

[2]The initial condition is expressed as $C(z, 0) = \delta(z)$ in original coordinates, with the functional definition of the Dirac impulse as the limit $z_0 \to 0$ of $z_0^{-1} f(z/z_0)$, where f is a regular function with unit integral. The variable substitution $x = z/L$ transform the initial condition into $\mathcal{G}(x, 0) = z_0^{-1} f(Lx/z_0)$ with the limit $\mathcal{G}(x, 0) = L^{-1}\delta(x)$ for $z_0 \to 0$.

Eq. (2.47) is solved with the method of separation of variables assuming $c = X(x)T(t^*)$, obtaining

$$\frac{T'}{GT} = \frac{X''}{X} \tag{2.49}$$

Eq. (2.49) holds for all values of x and t if the left- and right-hand sides are equal to a constant. Calling this constant $-\lambda^2$, one obtains the ordinary differential equations

$$\begin{aligned} T' + \lambda^2 GT = 0 \\ X'' + \lambda^2 X = 0 \end{aligned} \tag{2.50}$$

with general solutions

$$\begin{aligned} T(t^*) = Se^{-G\lambda^2 t^*}, \\ X(x) = Acos\lambda x + Bsin\lambda x \end{aligned} \tag{2.51}$$

for $t^* \geq 0$ and 0 $\leq$ x $\leq$ 1, where S, A, and B are arbitrary constants. The spatial boundary conditions in eq. (2.48) impose $B\lambda = A/2G$ and

$$cot\lambda = \frac{1}{1+w}\left[G\lambda - \frac{1+2w}{4G\lambda}\right] \tag{2.52}$$

Eq. (2.52) has one real solution λ_k every continuous interval $](k-1)\pi, k\pi[$ of $\cot\lambda$ with $k = 1, 2, ...,$, which must be found numerically. These are the eigenvalues to the eigenfunctions $X_k T_k$ with $X_k = cos\lambda_k x + sin\lambda_k x/2G\lambda_k$ and $T_k = e^{-G\lambda_k^2 t^*}$. The general solution of the diffusion equation is a linear combination of these eigenfunctions, that is

$$c(x, t^*) = \sum_{k=1}^{\infty} a_k X_k(x) e^{-G\lambda_k^2 t^*}, \tag{2.53}$$

whereby the coefficients a_k must satisfy the initial condition

$$c(x, 0) = \sum_{k=1}^{\infty} a_k X_k(x) = \delta(x) \tag{2.54}$$

at $t^* = 0$ for $0 \leq x \leq 1$. The eigenfunctions fulfil the orthogonality relations

$$\int_0^1 X_k(x) X_l(x) dx = \delta_{kl\gamma_k} \tag{2.55}$$

with $\delta_{kl} = 1$ for $k = l$ and 0 else, and

$$\gamma_k = \frac{1}{2} + \frac{1}{8G^2\lambda_k^2} + \frac{1+w}{2G\lambda_k^2} + \frac{w}{4G^2\lambda_k^3}\frac{cot\lambda_k - 2G\lambda_k}{1+cot^2\lambda_k} \tag{2.56}$$

Multiplication of eq. (2.54) with X_l, integration over $0 \leq x \leq 1$, and use of the selection property of the Dirac impulse yields $a_l = \gamma_l^{-1}$. The solution of the diffusion-advection equation for $v_t < v_b$ is thus finally given by

$$\mathcal{G}(x,t^*) = \sum_{k=1}^{\infty} \gamma_k^{-1}\Big[cos\lambda_k x + \frac{1}{2G\lambda_k x} sin\lambda_k x\Big] e^{x/2G-(1/4G+G\lambda_k^2)t^*} \tag{2.57}$$

In the limit case of $G \to \infty$,$\lambda_k = k\pi$, $\gamma_1 = 1/2$, and $\gamma_{k>1} = 0$, so that $\mathcal{G}(x,t^*) = 2^{-1}e^{(2x-t^*/4G)}$ is a pure exponential function. The $v_t > v_b$ case can be solved in a similar manner, using the substitution

$$\mathcal{G}(x,t^*) = exp\Big(\frac{-2x-t^*}{4G}\Big) c(x,t^*) \tag{2.58}$$

with temporal and spatial boundary conditions

$$\begin{aligned} &c = \delta, \quad t^* = 0 \\ &\frac{\partial c}{\partial x} = -\frac{1}{2G}c, \quad x = 0 \\ &\frac{\partial c}{\partial x} = \frac{1-2w}{2G}c, \quad x = 1 \end{aligned} \tag{2.59}$$

Application of the spatial boundary conditions on $c = X(x)T(t^*)$ with X and T defined by eq. (2.51) yields $B\lambda = -A/2G$ and

$$cot\lambda = \frac{1}{w-1}\Big[G\lambda + \frac{2w-1}{4G\lambda}\Big] \tag{2.60}$$

Eq. (2.60) defines one eigenvalue λ_k for every continuous interval $](k-1)\pi, k\pi[$ of cot λ with $k = 1, 2, ...,$, which must be found numerically. The eigenvalues are always real for $k > 1$. The first eigenvalue is real if $G \geq 1/2$ and $w \geq$ (4G-1)/(4G-2), and imaginary otherwise. The imaginary eigenvalue $\lambda = i\lambda_1$ defines the eigenfunction X_1T_1 with

$$\begin{aligned} &T_1 = Se^{+G\lambda_1^2 t^*}, \\ &X_1 = Acosh\lambda_1 x + iBsinh\lambda_1 x \end{aligned} \tag{2.61}$$

which satisfies the spatial boundary conditions in eq. (2.59) if $iB\lambda_1 = -A/2G$ and

$$cot\lambda_1 = \frac{1}{w-1}\Big[\frac{2w-1}{4G\lambda_1} - G\lambda_1\Big] \tag{2.62}$$

Using the same approach for the calculation of the integrals of X_k^2 as for $v_t < v_b$, the solution of the diffusion-advection equation for $v_t > v_b$ becomes

$$\mathcal{G}(x,t^*) = \sum_{k=1}^{\infty} \gamma_k^{-1}\Big[cos\lambda_k x + \frac{1}{2G\lambda_k x} sin\lambda_k x\Big] e^{-x/2G-(1/4G+G\lambda_k^2)t^*} \tag{2.63}$$

with

$$\gamma_k = \frac{1}{2} + \frac{1}{8G^2\lambda_k^2} + \frac{w-1}{2G\lambda_k^2} - \frac{w}{4G^2\lambda_k^3}\frac{cot\lambda_k + 2G\lambda_k}{1+cot^2\lambda_k} \tag{2.64}$$

if $G \geq 1/2$ and $w \geq (4G-1)/(4G-2)$, or

$$\begin{aligned}\mathcal{G}(x,t^*) = \gamma_1^{-1}\Big[cosh\lambda_1 x - \frac{1}{2G\lambda_1 x} sinh\lambda_1 x\Big] e^{-x/2G-(1/4G)-G\lambda_1^2)t^*} + \\ \sum_{k=2}^{\infty} \gamma_k^{-1}\Big[cos\lambda_k x - \frac{1}{2G\lambda_k x} sin\lambda_k x\Big] e^{-x/2G-(1/4G+G\lambda_k^2)t^*}\end{aligned} \tag{2.65}$$

with

$$\gamma_1 = \frac{1}{2} - \frac{1}{8G^2\lambda_1^2} - \frac{w-1}{2G\lambda_1^2} + \frac{w}{4G^2\lambda_1^3}\frac{coth\lambda_1 - 2G\lambda_1}{coth^2\lambda_1 - 1} \tag{2.66}$$

in the other cases.

The last case to discuss is that of $v_t = v_b$, which describes a purely diffusive process. The definition of a unitless depth $x = z/L$ and time $t^* = v_b t/L$ yield

$$\frac{\partial \mathcal{G}}{\partial t^*} = G\frac{\partial^2 \mathcal{G}}{\partial x^2} \tag{2.67}$$

with $G = G_0$, subjected to the initial and boundary conditions

$$\begin{aligned}&\mathcal{G} = \delta, \quad t^* = 0 \\ &\frac{\partial \mathcal{G}}{\partial x} = 0, \quad x = 0 \\ &\frac{\partial \mathcal{G}}{\partial x} = -\frac{1}{G}\mathcal{G}, \quad x = 1\end{aligned} \tag{2.68}$$

Application of the spatial boundary conditions on $\mathcal{G} = X(x)T(t^*)$with X and T defined by eq. (2.51) yields $B = 0$ and real eigenvalues λ_k satisfying $cot\lambda_k = G\lambda_k$. The corresponding solution is

$$\mathcal{G}(x, t^*) = \sum_{k=1}^{\infty} \gamma_k^{-1} e^{-G\lambda_k^2 t^*} cos\lambda_k x \tag{2.69}$$

with

$$\gamma_k = \frac{1}{2} + \frac{G}{2(1 + G^2\lambda_k^2)} \tag{2.70}$$

As mentioned above, the motion of individual particles is described by a Wiener process with constant drift starting at $(t, z) = (0, 0)$ and ending at $(t, z) = (t_e, L)$, where t_e is the escape time. The boundary conditions impose a reflecting barrier at $z = 0$ and a partially absorbing, or elastic, barrier at $z = L$ (*Dominé, 1996*). The age T of tracer particles found at a depth z below the mixed layer is related to t_e by $T = t_e + (z - L)/v_b$. The probability density function (PDF) of the unitless escape time $t_e^* = |v_b - v_t|t/L$ is determined by the survival probability

$$\mathcal{S}(t^*) = \frac{1}{L}\int_0^L \mathcal{G}(z/L, t^*)dz = \int_0^1 \mathcal{G}(x, t^*)dx, \tag{2.71}$$

defined as the probability that a tracer particle initially localised at $x = 0$ by $G(x, 0) = \delta(x)$ remains in the mixed layer for a time t^*. The probability that this particle escapes the mixed layer between t^* and $t^* + dt^*$ is then given by $\mathcal{E}(t^*)dt^*$ = $\mathcal{S}(t^*)$ - $\mathcal{S}(t^* + dt^*)$, where $\mathcal{E}$ is the PDF of t_e^*. Using eq. (2.71),

$$\mathcal{E}(t^*) = -\frac{\partial}{\partial t^*}\int_0^1 \mathcal{G}(x, t^*)dx \tag{2.72}$$

Furthermore, it can be verified that

$$\mathcal{G}(1, t^*) = \frac{|v_b - v_t|}{v_b}\mathcal{E}(t^*), \tag{2.73}$$

as expected from the equivalency between the diffusion-advection equation and its microscopic description in terms of a biased random walk [3]. Application of eq. (2.72) to the solutions for $\mathcal{G}$ obtained above yields

[3]Let $C(z, t)$ be the tracer concentration generated by an impulsive flux $\Phi_t\delta(t)$ with fluence Φ_t. Because of mass conservation, the depth integration of C must be equal to Φ_t. Below the mixed layer, depth and time are related by the burial velocity v_b, so that

$$\mathcal{E}(t^*) = e^{1/2G} \sum_{k=1}^{\infty} \frac{1 + 4G^2\lambda_k^2}{4\gamma_k G\lambda_k} e^{(-1/4G + G\lambda_k^2)t^*} sin\lambda_k \tag{2.74}$$

for $v_t < v_b$,

$$\mathcal{E}(t^*) = e^{-1/2G} \sum_{k=1}^{\infty} \frac{1 + 4G^2\lambda_k^2}{4\gamma_k G\lambda_k} e^{(-1/4G + G\lambda_k^2)t^*} sin\lambda_k \tag{2.75}$$

for $v_t > v_b$ (with $i\lambda_1$ instead of λ_1 if the first eigenvalue is imaginary), and

$$\mathcal{E}(t^*) = \sum_{k=1}^{\infty} \frac{G\lambda_k}{\gamma_k} e^{(-G\lambda_k^2)t^*} sin\lambda_k \tag{2.76}$$

for $v_t = v_b$, respectively. The simpler form taken by the eigenfunction expansion of $\mathcal{E}$ yields a more convenient formulation of $\mathcal{G}$, and therefore of the impulse response

$$(t) = \frac{\eta}{L}\mathcal{E}\Big(\frac{v_b\eta}{L}t\Big), \tag{2.77}$$

with $\eta = 1$ for $v_t = v_b$, or $\eta = |1 - v_t/v_b|$ for $v_t \neq v_b$ (Fig. 2.12). The escape time distribution $\mathcal{E}$ approaches an exponential function with decay time determined by the first eigenvalue λ_1 if $G \to \infty$(pure diffusion), and a Gaussian function with expectation $t^* = 1$ and vanishing standard deviation if $G \to 0$ (pure advection). A certain similarity exists between $\mathcal{E}$ and the inverse Gaussian distribution

$$(t) = \frac{L}{\sqrt{2\pi Dt^3}} exp\Big(- \frac{(L - vt)^2}{2Dt}\Big), \tag{2.78}$$

which describes the first passage time through $z = L$ of a drifting Wiener process $Z_t = vt + \sigma W_t$ with no barriers, where v is the drift velocity, W_t the standard Brownian motion with variance $\sigma^2 t = Dt$, and D the equivalent diffusion coefficient (*Folks and Chhikara, 1978*). This similarity, however, is only apparent, since is defined only for $v \geq 0$ and its expectation

$$\int_0^{\infty} C(L,t)dt = \frac{L}{|v_b - v_t|} \int_0^{\infty} C(L,t^*)dt^* = \frac{\Phi_t}{v_b}$$

Using $C(z,t) = L^{-1}\mathcal{G}(z/L, t^*)$, which follows from the definition of $\mathcal{G}$, the above equation become

$$\int_0^{\infty} \mathcal{G}(L,t^*)dt^* = \frac{|v_b - v_t|}{v_b}\Phi_t$$

If the equivalency between the diffusion-advection equation and the random walk model holds, the special case $\Phi_t = 1$ coincides with the total probability of the escape time, and thus with the integral of $\mathcal{E}(t^*)$, yielding the stated equivalence between $\mathcal{G}$ and $\mathcal{E}$.

diverges at $v = 0$, due to the lack of a reflecting barrier that keeps the diffusing particle at a finite distance from the passage threshold.

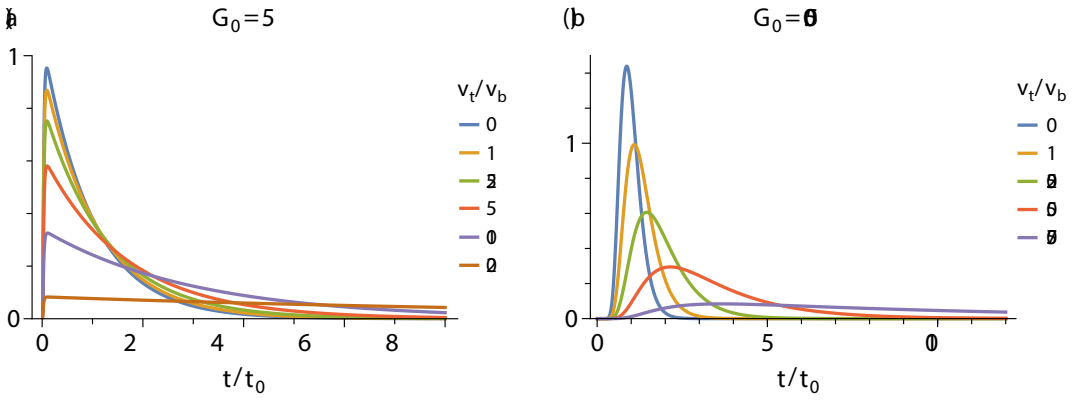

Figure 2.12: Impulse responses defined by eq. (2.77), with $t_0 = L/v_b$ being the transit time of regular sediment particles, for two values of the inverse Péclet number G_0, and selected ratios between the tracer segregation velocity v_t and the burial velocity v_b

The eigenfunction expansion of $\mathcal{E}$ is an infinite series of terms with exponential time decay, which does not converge for $t^* = 0$ or $G = 0$. Rapid convergence, however, occurs for sufficiently large values of t^* and G. Moreover, $\mathcal{E}$ can be adequately approximated by truncating the series expansion to the first n terms at any $t^* > 0$ and $G > 0$ for a sufficiently large n. In this case, there is a threshold time $t_0^*(G, n) = \mathcal{E}(n)G^{-1}$, with $\mathcal{E} \sim n^{-1}$, below which $\mathcal{E}(t^*)$ becomes negative (Fig. 2.13a). This threshold represents a practical lower limit for the numerical support of $\mathcal{E}$ (Fig. 2.13b). For small values of G, numerical instabilities occur even for $t^* > t_0^*$, due to the small net result of adding terms with alternating sign and very large amplitude (Fig.2.13c,d). In these cases, arbitrary numerical precision (e.g. using *Mathematica*) is required for a correct evaluation of $\mathcal{E}$.

The normalised escape time expectation is defined by

$$\left\langle t_e^* \right\rangle = \lim_{\varepsilon \to 0} \int_{\varepsilon}^{\infty} \mathcal{E}(t) t dt \tag{2.79}$$

where the limit avoids the numerical convergence problems at $t^* \to 0$. Integration of the exponential terms in eq. (2.74-2.76) gives

$$\left\langle t_e \right\rangle = \frac{L}{v_b - v_t} \lim_{\mathcal{E} \to 0} e^{1/2G} \sum_{k=1}^{\infty} \frac{sin\lambda_k}{\gamma_k \lambda k} \frac{4G + (1 + 4G^2\lambda_k^2)\mathcal{E}}{1 + 4G^2\lambda_k^2} e^{-(1/4G + G\lambda_k^2)\mathcal{E}} \tag{2.80}$$

for $v_t < v_b$,

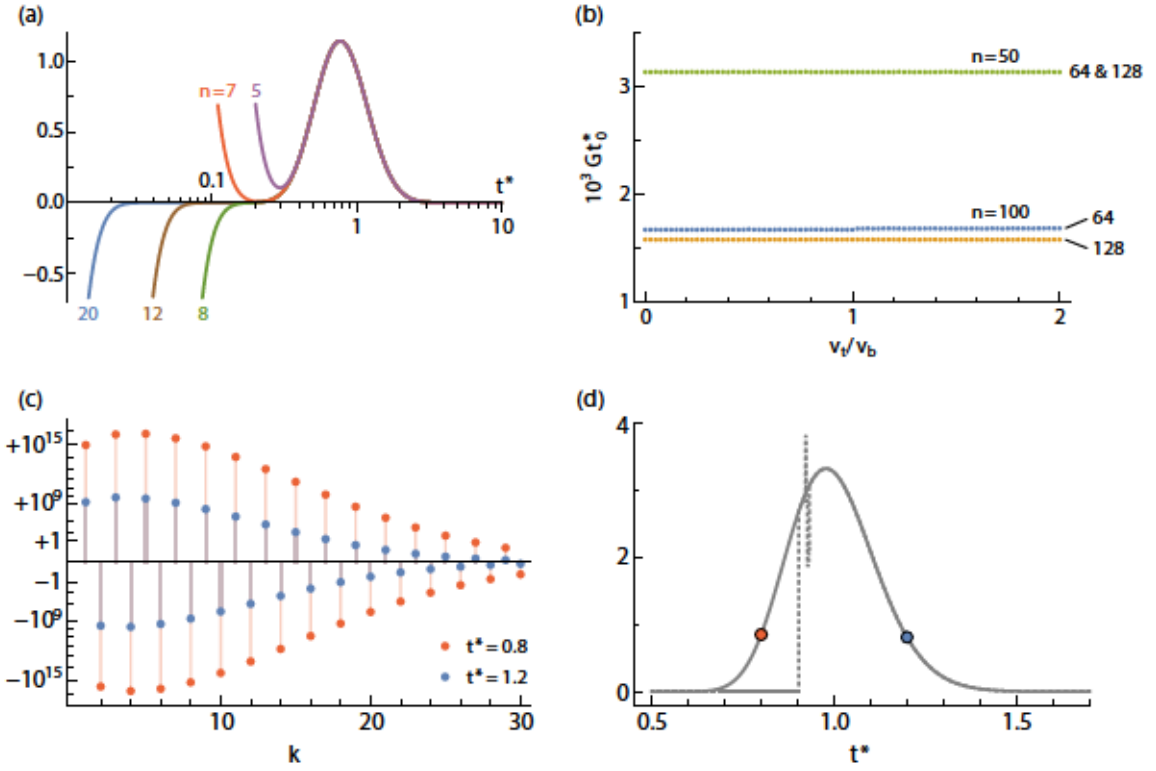

Figure 2.13: (a) Numerical evaluations of $\mathcal{E}(t^*)$ for $G = 0.1$ and $v_t = 0$, using the first n terms of the eigenfunction expansion. Notice the change of sign occurring between $n = 7$ and 8 for $t^* \to 0$. (b) Nondimensionalized time t^* below which eigenfunction expansions of $\mathcal{E}(t^*)$ truncated at $n = 50$ and $n = 100$ becomes negative, evaluated using 64 and 128 digit precision Results obtained with given digit precision depend only on n and G, regardless of v_t. (c) First 30 eigenfunctions of $\mathcal{E}(t^*)$ (the individual series terms in eq. 2.74) for $G = 0.0075$ and $v_t = 0$, and two selected values of t^*. Notice the quasi-logarithmic scale used to represent alternating terms spanning 16 orders of magnitude. (d) Numerical evaluation of $\mathcal{E}(t^*)$ as sum of the eigenfunction shown in (c) obtained in *Mathematica* using 16-digit precision (dashed line) and 32-digit precision (solid line). Notice the sharp truncation of 16-digit results at $t^* \approx 0.9$.

$$\left\langle t_e \right\rangle = \frac{L}{v_b - v_t} \lim_{\mathcal{E}\to 0} e^{-1/2G} \sum_{k=1}^{\infty} \frac{sin\lambda_k}{\gamma_k \lambda k} \frac{4G + (1 + 4G^2\lambda_k^2)\mathcal{E}}{1 + 4G^2\lambda_k^2} e^{-(1/4G + G\lambda_k^2)\mathcal{E}} \tag{2.81}$$

for $v_t > v_b$ (with $i\lambda_1$ instead of $i\lambda_1$ if the first eigenvalue is imaginary), and

$$\left\langle t_e \right\rangle = \frac{L}{v_b} \lim_{\mathcal{E}\to 0} \sum_{k=1}^{\infty} \frac{sin\lambda_k}{\gamma_k \lambda k} \frac{1 + G\lambda_k^2\mathcal{E}}{G\lambda_k^2} e^{-G\lambda_k^2\mathcal{E}} \tag{2.82}$$

for $v_t = v_b$. In absence of grain size segregation ($v_t = 0$), the expected escape time of tracer particles coincides with the transit time L/v_b through the mixed layer resulting from the burial

velocity. Grain size segregation increases the escape time of large particles, reflecting their lessened burial velocity. Accordingly, $\langle t_e \rangle$ is a monotonic function of v_t, which increases at a double exponential rate once v_t exceeds a certain threshold determined by G_0 (Fig. 2.14). In case of dominant advection ($G_0 \ll 1$), the increase of $\langle t_e \rangle$ is particularly rapid once v_t exceeds v_b, because the net upward velocity is hardly overcome by diffusion.

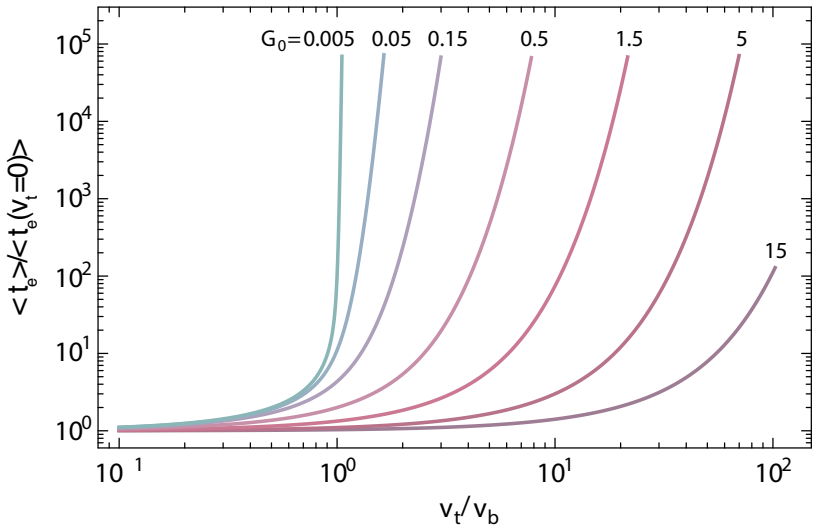

Figure 2.14: Expected escape time $\langle t_e \rangle$ of a tracer particle with segregation velocity v_t, normalized by the $v_t = 0$ case, as a function of v_t/v_b, for selected values of the inverse Péclet number G_0. These values correspond to a mixed layer with thickness $L = 10$ cm, burial velocity $v_b = 2$ cm/kyr, and bulk diffusion coefficients $D_s = 0.1$, 1, 3, 10, 30, 100, and 300 cm^2/kyr, respectively. Notice the logarithmic scale on the vertical axis.

2.8.5.2 Impulsive tracer profiles in the historical layer

Consider a tracer with impulsive input $F_t = \Phi_t \delta(t)$ at $t = 0$, where Φ_t is the fluence of this event, expressed as total deposited amount (e.g. particle counts) per unit of area. In a sediment with constant porosity, the resulting volume concentration below a mixed layer with thickness L at any time $t > 0$ is given by

$$C(z,t) = \frac{\Phi_t}{v_b} E\left(t - \frac{z-L}{v_b}\right) \tag{2.83}$$

where E is the probability density function of the escape time of tracer particles with given size from the mixed layer, and $(z-L)/v_b$ the additional time required for a sediment particle to be buried from just below the mixed layer to $z > L$. The negative sign of z in eq. (2.83) means that the long tail of E is directed upwards: tracer particles that required more time to escape the mixed layer entered the historical layer at a later time and are buried less deep.

Using the nondimensionalized results of Section 2.8.5.1, eq. (2.83) becomes

$$C(z,t) = \frac{\Phi_t}{v_b \tau} \mathcal{E}\Big(\frac{v_b t - z + L}{v_b \tau}\Big), \tag{2.84}$$

where $\mathcal{E}(t^*)$ is the probability density function of the nondimensionalised escape time t^*, given by eq. (2.74-2.76), and $\tau = dt/dt^*$ a time constant defined by the variable transformation $t \to t^*$, that is:

$$\tau = \begin{cases} L v_b^{-1}, & v_t = v_b \\ L|v_b - v_t|^{-1}, & else \end{cases} \tag{2.85}$$

One can easily verify that the integration of C over z yields Φ_t, as expected from tracer conservation. In experimental works, the tracer amount is more conveniently normalised by dry sediment mass, obtaining the mass concentration $C_m = C/\varphi_s \varrho_s$, where φ_s is the fraction of total volume occupied by solids, and ϱ_s the density of sediment particles.

Compaction of the historical layers alters the age model and thus the tracer concentration profiles. In this case, profiles can be expressed by eq. (2.84) after replacing the burial time $(z - L)/v_b$ with the corresponding expression $t_b(z)$ derived from the age model in eq. (2.24):

$$C(z,t) = \frac{\Phi_t}{\tau} \frac{dt_b}{dz} \mathcal{E}\Big(\frac{t - t_b(z)}{\tau}\Big) \tag{2.86}$$

The factor dt_b/dz in eq. (2.86) originates from the variable substitution $z \to t_b(z)$ and accounts for the volume concentration increase produced by compaction. Using the definition of t_b in eq. (2.24):

$$\frac{dt_b}{dz} = \frac{d}{dz} \int_L^z \frac{du}{v_b(u)} = \frac{1}{v_b(z)}, \tag{2.87}$$

where $v_b(z)$ coincides with the sedimentation rate derived from the age model. At depths largely exceeding the thickness of the mixed layer, v_b does not change significantly over the depth range covered by the deposition event and can be considered as a constant. Using the Taylor expansion $t_b(z) = t_b(z_0) + (z - z_0)/v_b$ of the age model relative to a reference depth z_0 related to the deposition event, eq. (2.86) becomes

$$C(z,t) = \frac{\Phi_t}{v_b(z_0)\tau} \mathcal{E}\Big(\frac{v_b(z_0)t - z}{v_b(z_0)\tau} - \frac{v_b(z_0)t_b(z_0) - z_0}{v_b(z_0)\tau}\Big) \tag{2.88}$$

with $\tau = L/\eta v_b(L)$ and $\eta = 1$ for $v_t = v_b$ or $\eta = |1 - v_t/v_b|$ for $v_t \neq v_b$. Mass conservation

imposes $v_b(L)/v_b(z_0) = \varphi_s(z_0)/\varphi_s(L) = \phi$, so that

$$C(z,t) = \Phi_t \frac{\eta\phi}{L} \mathcal{E}\Big(\frac{\eta\phi}{L}(v_b t - z + z_0 - v_b t_b)\Big) \tag{2.89}$$

where $\phi = \varphi_s(z_0)/\varphi_s(L) \geq 1$ is the compaction ratio. The mass concentration is finally given by

$$C_m(z,t) = \frac{\Phi_t}{\varphi_s \varrho_s} \frac{\eta\phi}{L} \mathcal{E}\Big(\frac{\eta\phi}{L}(v_b t - z + z_0 - v_b t_b)\Big) \tag{2.90}$$

Size segregation effects can be quantified by evaluating the difference $\langle \Delta z \rangle$ between the expected depths of the tracer concentration profile and the corresponding concentration profile of a tracer with same size as the sediment particles. In this case,

$$\langle \Delta z \rangle = \frac{L}{\eta\phi} \mathcal{E}\Big[\langle t^* \rangle - 1\Big] \tag{2.91}$$

where $\langle t^* \rangle$ is the expected unitless escape time given by eq. (2.80-2.82) (Fig. 2.14). Increasing segregation effects move the concentration profiles upwards and makes them broader, similarly to what occurs in the time domain (Fig. 2.12). This effect grows rapidly when v_t increases beyond v_b, leading to a homogeneous spread of large tracer particles over the whole sedimentary column.

2.8.6 Steady-state solutions

Steady-state solutions of the diffusion advection equation for a homogeneous mixed layer are obtained by solving eq. (2.41-2.43) for a constant flux F_t of tracer particles. In this case, C does not depend on time, and the nondimensionalised diffusion-advection equation becomes

$$G\frac{\partial^2 C}{\partial x^2} \mp \frac{\partial C}{\partial x} = 0 \tag{2.92}$$

with boundary conditions

$$\begin{aligned} \pm C - G\frac{\partial C}{\partial x} &= \frac{F_t}{|v_b - v_t|}, \quad x = 0 \\ wC + G\frac{\partial C}{\partial x} &= 0, \quad x = 1 \end{aligned} \tag{2.93}$$

The general solution of eq. (2.92) is

$$C = C_0 + A\Big[cosh(x/G) \pm sinh(x/G)\Big] \tag{2.94}$$

with the boundary conditions yielding

$$\begin{aligned} C_0 &= \pm\frac{I_t}{|v_b - v_t|} \\ A &= -\frac{I_t}{|v_b - v_t|}\frac{v_t}{v_b}\frac{1}{sinh(1/G) \pm cosh(1/G)} \end{aligned} \tag{2.95}$$

The corresponding tracer concentrations at the sediment-water interface and at the bottom of the mixed layer

$$\begin{aligned} C(0) &= \frac{\pm F_t}{|v_b - v_t|}\left[1 - \frac{v_t}{v_b}\frac{1}{cosh(1/G) \pm sinh(1/G)}\right] \\ C(1) &= \frac{F_t}{v_b} \end{aligned} \tag{2.96}$$

define the concentration ratio

$$R_t = \frac{C(0)}{C(1)} = \frac{1}{1 - v_t/v_b}\left[1 - \frac{v_t}{v_b}\frac{1}{cosh(1/G) \pm sinh(1/G)}\right] \tag{2.97}$$

which is a measure for the concentration gradient generated by grain size segregation. This gradient is fully contained within the mixed layer, since tracer concentrations do not change below the mixed layer. The case $v_t = v_b$ is singular and must be treated differently. Defining $G = D/Lv_b$, as for the impulse response, we obtain

$$R_t = 1 + \frac{1}{G} \tag{2.98}$$

The concentration gradient increases rapidly with increasing segregation, similarly to the escape time (Fig. 2.15). This can be qualitatively explained by mass conservation: in the stationary case, the tracer flux is constant and equal at all depths, so that the lower sinking rate of large tracer particles inside the mixed layer must be compensated by a steeper concentration gradient. This leads to the selective accumulation of larger particles near the sediment-water interface. A notable example of this phenomenon is the accumulation of ferromanganese nodules on the ocean floor, with a steep concentration gradient in the top ∼40 cm of the sedimentary column (*Finney et al., 1984*).

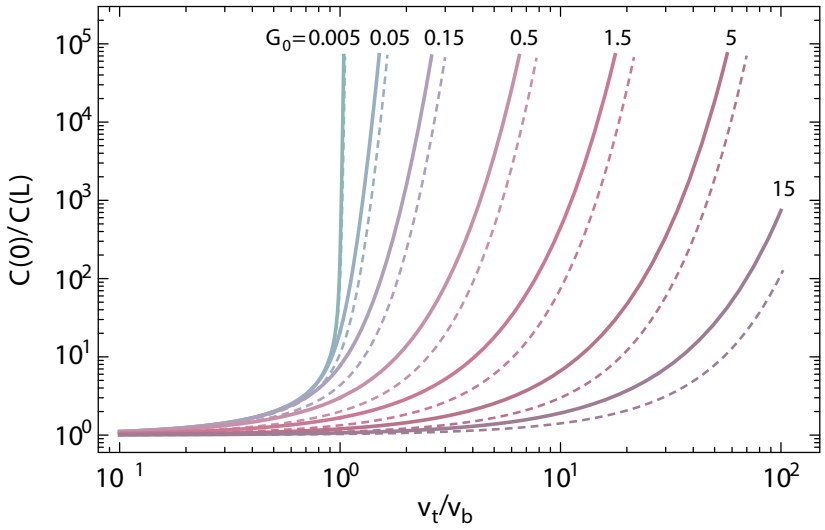

Figure 2.15: Ratio between the tracer concentration at the sediment-water interface and at the bottom of the mixed layer, as a function of v_t/v_b, for selected values of the inverse Péclet number G_0 (solid lines). The normalised escape time expectation of Fig. 2.14 is shown for comparison (dashed lines). The values of G_0 correspond to a mixed layer with thickness $L = 10$ cm, burial velocity v_b = 2 cm/kyr, and bulk diffusion coefficients D_s = 0.1, 1, 3, 10, 30, 100, and 300 cm^2/kyr, respectively. Notice the logarithmic scale on the vertical axis.

2.8.7 Size segregation and age models

Consider tracer particles whose age coincides with that of deposition, up to a constant offset. In the case of an impulsive deposition event, particles with identical age will be spread over a range of depths upon burial, due to the statistical nature of the time required to escape the mixed layer. Using eq. (2.89), the probability of finding a particle of deposition age T at a depth $z \geq L$ is proportional to

$$C(z,T) = \Phi_t(T)\frac{\eta\phi}{L}\mathcal{E}\left(\frac{\eta\phi}{L}v_b(T - t_b(z))\right) \tag{2.99}$$

Because the fluence $\Phi_t(T)$ is a measure for the total amount of particles with age T, the probability density function for the age of particles fount at depth z, due to a time-varying deposition flux $I_t(T)$ is given by

$$f(T|z) = \frac{\Phi_t(T)\mathcal{E}\left(\frac{\eta\phi}{L}v_b(T - t_b(z))\right)}{\int_0^\infty \Phi_t(T)\mathcal{E}\left(\frac{\eta\phi}{L}v_b(T - t_b(z))\right)dT} \tag{2.100}$$

In case of a constant deposition flux, Φ_t is independent of time, and eq. (2.100) becomes

$$f(T|z) = \frac{\eta\phi}{L} v_b \mathcal{E}\left(\frac{\eta\phi}{L} v_b (T - t_b(z))\right) \tag{2.101}$$

The age expectation $\langle T \rangle$ is obtained by setting the argument of $\mathcal{E}$ in eq. (2.101) equals to the expectation $\langle t^* \rangle$ of $\mathcal{E}$, whence

$$\langle T \rangle = t_b(z) + \frac{L}{\eta\phi v_b} \langle t^* \rangle, \tag{2.102}$$

with $\langle t^* \rangle$ being a function of tracer particle size (Fig. 2.14). Tracer particles whose size does not exceed the segregation threshold behave like the bulk sediment, which means that $v_t = 0$, $\eta = 1$, and $\langle t^* \rangle = 1$. In this case, eq. (2.102) coincides with the age model prediction $\langle T \rangle = t_b(z) + L/\phi v_b$. Above the critical size threshold

$$\frac{s}{s_0} = \psi_c + \frac{v_b}{D_s \beta_0} \tag{2.103}$$

for which $v_t \approx v_b$, $\langle t^* \rangle$ increases very rapidly, leading to the occurrence of particles that are much older than the typical sediment age. The size threshold is inversely related to $D_s\beta_0/v_b$ and is tendentially lower in cores with small sedimentation rates and strong bioturbation.

The relation between age offset, particle size, and sedimentation rate is clearly demonstrated by the difference between foraminifera and bulk sediment radiocarbon ages in two cores with similar water depths and different sedimentation rates (*Thomson et al, 1995; Brown et al., 2001*). In this example, the age offset of >150 µm foraminiferal calcite with respect to the bulk carbonate amounts to ∼1.2 kyr in the slowly accumulating site ($v_b \approx 3$ cm/kyr) and 0.7 kyr in the faster accumulating site ($v_b \approx 5.9$ cm/kyr).

2.9 Fitting tektite profiles

2.9.1 Fitting function

Consider a sedimentary column with a homogenous surface mixed layer of thickness L and age model given by

$$t_s(z) = \frac{L}{t_b(L)} + \int_L^z \frac{du}{v_b(u)} \tag{2.104}$$

where t_s is the mean time required by a sediment particle to reach the depth z, and v_b the depth-dependent burial velocity, with $v_b = v_b(L)$ for $z \leq L$. Tektite profiles produced by an

impulsive event with fluence Φ_t and age T are modelled using the mass concentration

$$C_m(z,T) = \frac{\Phi_t}{\varphi_s \varrho_s} \frac{\eta\phi}{L} \mathcal{E}\left(\frac{\eta\phi}{L} v_b(z_0)(T - t_b(z)) + \frac{\eta\phi}{L}(z_0 - z) + \eta \right) \tag{2.105}$$

obtained from the solution of the diffusion-advection equation inside the mixed layer (see Section 2.8.5). In this equation, ϱ_s is the density of sediment particles, φ_s the volume fraction of solids, z_0 a reference depth within the range of tektite occurrence, $\phi = \varphi_s(z_0)/\varphi_s(L)$ the compaction ratio, and $\mathcal{E}$ the probability density function of the non-dimensionalised escape time from the mixed layer. For tracer particles with diffusion coefficient D and segregation velocity v_t, the relation between the escape time t_e and its non-dimensionalised form is given by $t_e^* = \eta v_b t_e / L$ with $\eta = 1$ for $v_t = v_b$ and $\eta = |1 - v_t/v_b|$ for $v_t \neq v_b$. The probability density function $\mathcal{E}$ depends on η and the inverse Péclet number $G = D/L\eta v_b$ and is given by eq. (2.67-2.69). If z_0 is identified with the maximum depth of the tektite layer, $T = t_s(z_0)$ by definition of age model, and eq. (2.98) becomes

$$C_m(z,z_0) = \frac{\Phi_t}{\varphi_s \varrho_s} \frac{\eta\phi}{L} \mathcal{E}\left(\frac{\eta\phi}{L}(z_0 - z); G, \eta \right) \tag{2.106}$$

(e.g. Fig 2.16 below).

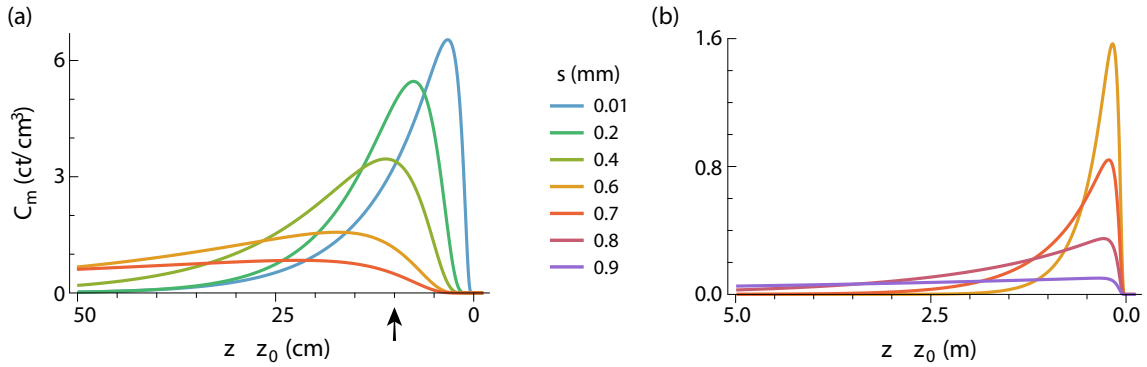

Figure 2.16: Simulated tracer profiles generated by an impulsive input with the following parameters: ϱ_s = 2.3 g/cm^3, φ_s = 0.6, ϕ = 1, v_b = 3.8 cm/kyr, L = 10cm, D_s = 30 cm^2/kyr, s_0 = 10 µm, ψ_c = 3, q = 0.5, $\beta_0 = 0.2$ m^{-1}, Φ_t = 100 ct/cm^2, and selected tracer particle sizes s in mm. The corresponding segregation velocities range from v_t = 0 for $s \leq 0.03$ mm to v_t = 5.4 cm/kyr for s = 0.9 mm. (a) Tracer profiles within 50 cm from z_0: the event horizon, defined as the stratigraphic depth where the tracer would be found without bioturbation, is marked by an arrow. (b) Tracer profiles within 5 m from z_0: notice how tracer particles with $v_t \geq v_b$ are homogeneously spread in the sediment column

For tektites of the same size class, the concentration profile of eq. (2.106) is controlled by the four aggregated parameters: (1) $\Phi_t/\varphi_s\varrho_s$ for the profile amplitude, (2) $\eta\phi/L$ for the profile width, (3) $\eta\phi z_0/L$ for the profile offset, and (4) $G = D/L\eta v_b$ for the profile shape. This means that some individual parameters need to be fixed using plausible values or additional measurements. For instance, φ_s, ϱ_s, and ϕ are measurable physical properties of the sediment core, and v_b is fixed by the age model. This leaves the following free parameters (1) Φ_t for the profile amplitude, (2) L for the profile width, (3) z_0 for the profile offset, and (4) D for the profile shape, for optimisation. The last parameter, η, cannot be determined without additional constraints. Because η is a function of the segregation velocity, the required additional constraint is provided by the fit of concentration profiles corresponding to different size classes, including smaller sizes for which $v_t = 0$ and therefore $\eta = 1$, using suitable models for the grain size dependence of D, and v_t. A grain size class with size limits $[s_1, s_2]$ is then fitted by

$$C_m(z, z_0) = \frac{\Phi_t}{\varphi_s\varrho_s}\frac{\phi}{L}\int_{s_1}^{s_2} g_t(s)\eta\mathcal{E}\Big(\frac{\eta\phi}{L}(z_0 - z); G, \eta\Big)ds \tag{2.107}$$

where g_t(s) is the empirical tektite size distribution obtained for instance from total counts.

2.9.2 Poisson regression

The primary measured quantity in case of discrete tracer particles, such as tektites, is a particle count per unit of sediment mass. Model profiles must therefore be fitted using Poisson regression to correctly account for skewness of Poisson error distributions. For this purpose, consider a set of counts n_{kl} for tracers belonging to size intervals $\mathbf{s}_l = [s_l^{min}, s_l^{max}]$ obtained from samples with masses m_k taken at various depths. The empirical grain size distribution of the tracer is given by the total concentrations

$$S_l = \frac{\sum_k n_{kl}}{\sum_k m_{kl}} \tag{2.108}$$

in each grain size class l. This distribution is fitted using a model function $g_t(s)$ with unit integral, such that

$$S_l = S_0 \int_{\mathbf{s}_l} g_t(s)ds, \tag{2.109}$$

where S_0 is a normalization constant obtained from the fit, with no further use. The counts n_{kl} yields estimates $c_{kl} = n_{kl}/m_k$ of the l-th size class concentration at various depths in the sediment column. These estimates need to be compared with modelled concentration profiles given by $C_m(z_{kl}, \iota;)$ in eq.(2.100), where = (Φ_t,z_0,L,D_s,q,β_0) is the vector formed by the unknown parameters Φ_t (the total fluence), z_0 (the maximum occurrence depth), L (the

thickness of the surface mixed layer), D_s (the diffusion coefficient of sediment particles, q (the power exponent for the tracer diffusivity), and β_0 (the coupling constant between diffusivity and grain size segregation).

The maximum likelihood (ML) model is obtained by maximizing the probability of obtaining the measured counts n_{kl} as random realizations of Poisson processes with corresponding rates $\lambda_{kl} = m_k C_m(z_{kl},\ \iota;\ )$. These counts are then described by the Poisson distribution

$$\mathcal{P}(n,\lambda) = \frac{\lambda^n e^{-\lambda}}{n!} \tag{2.110}$$

The validity of this approach is limited only by the assumption that the bioturbation process is homogeneous at the sample scale, so that the randomness of the counts n_{kl} is entirely associated with the Poisson statistics. Maximization of the joint probability of all realizations n_{kl} is equivalent to the minimization of

$$-\sum_{k,l} ln\Big[\mathcal{P}(n_{kl},\lambda_{kl})\Big] = -\sum_{kl} n_{kl}\ ln\ \lambda_{kl} - \lambda_{kl} - ln\ n_{kl}!. \tag{2.111}$$

Since the last term in eq. (2.111) is independent of the model parameters, it is sufficient to minimize the negative log-likelihood

$$- \qquad = \sum_{k,l} m_k C_m(z_{kl},\ \iota;\ ) - n_{kl}\ ln\ m_k C_m(z_{kl},\ \iota;\ ) \tag{2.112}$$

with respect to the model parameters in . One problem with the use of eq. (2.112) is that non-numerical outputs are generated when C_m is exactly zero, that is, before the event onset. The inclusion of zero counts before the event onset, however, is essential for constraining the time range. Therefore, needs to be regularized by assigning a small, non-zero lower limit λ_0 for the Poisson rate, so that

$$- \qquad = \sum_{k,l} max\Big[\lambda_0, m_k C_m(z_{kl},\ \iota;\ )\Big] - n_{kl}\ ln\ max\Big[\lambda_0, m_k C_m(z_{kl},\ \iota;\ )\Big] \tag{2.113}$$

The minimum rate λ_0 can be interpreted as the probability of "spurious" counts, due for instance to misattribution, contamination, or other error sources.

2.9.3 Uncertainty estimates and statistical tests

The effects of counting uncertainties can be estimated with Monte Carlo simulations. For this purpose, actual counts are replaced by simulated ones, based on empirical probability distributions. For the derivation of such distributions, consider first the case of N realizations $\mathbf{n} = (n_1, n_2, ..., n_N)$ of a Poisson variate n with rate λ. The corresponding probability mass

function is

$$p(n|\lambda) = \mathcal{P}(n,\lambda) = \frac{\lambda^n e^{-\lambda}}{n!} \tag{2.114}$$

for any integer $n \geq 0$. In Bayesian theory, the unknown rate $\lambda > 0$ is itself a random variate for which a prior probability distribution $p_{prior}(\lambda)$ is assumed. This distribution might reflect some physical constraints, but it is mostly unknown. In this case, the most unassuming choice of p_{prior} is the limit case of a uniform distribution over $(0, \infty)$. The corresponding unnormalised posterior distribution

$$p_{post}(\lambda|\ \ ) \propto p(\ \ |\lambda) p_{prior}(\lambda) \propto \lambda^{n_1+n_2+\cdots} e^{-N\lambda} \tag{2.115}$$

of λ for a given **n** is proportional to the Gamma distribution

$$\Gamma(\lambda;\alpha;\beta) = \frac{\beta^\alpha}{\Gamma(\alpha)} \lambda^{\alpha-1} e^{-\beta x}, \tag{2.116}$$

with $\alpha = 1 + n_1 + n_2 + ... + n_N$, and $\beta = N$. This result can be generalized to the case where p_{prior} is a Gamma distribution with parameters (α_0, β_0). The corresponding posterior distribution is also a Gamma distribution, with parameters $\alpha' = \alpha_0 + \alpha$ and $\beta' = \beta_0 + \beta$. For this reason, the Gamma distribution is the conjugate prior of the Poisson distribution. The posterior parameters α' and β' become increasingly dominated by the data as the size of **n** increases. Monte Carlo simulations require the generation of simulated counts according to the so-called posterior predictive distribution

$$p_{pred}(n|\ \ ) = \int_0^\infty \mathcal{P}(n|\lambda) p_{post}(\lambda|\ \ ) d\lambda \tag{2.117}$$

Using the Gamma distribution as $p_{post}(\lambda)$, eq. (2.116) yields the negative binomial distribution

$$\mathcal{B}\_(n;\alpha',(\beta'+1)^{-1}) = \frac{\Gamma(n+\alpha')}{n!\Gamma(\alpha')} \left(\frac{\beta'}{\beta'+1}\right)^{\alpha'} \left(\frac{1}{\beta'+1}\right)^n \tag{2.118}$$

for all integers $n \geq 0$.

In the case of tracer profiles, there is one sample with count n_i for each depth and size class, whereby all counts are assumed to be independent from each other. Each count is the random realisation of a Poisson variate with rate λ_i. The posterior distribution of λ_i obtained from a uniform prior is a Gamma distribution with parameters $\alpha_i' = n_i$ and $\beta_i' = 1$. In the case of $n_i = 0$, the Gamma distribution is evaluated for the limit $\alpha_i' \to 0$. The corresponding posterior predictive distribution is thus $\mathcal{B}\_(n; n_i, 1/2)$. The limit case of this $\mathcal{B}\_$ for $n_i = 0$ is

unit probability for $n = 0$ and zero probability for $n > 0$. The simulated Monte Carlo values $\tilde{n}_i$ corresponding to n_i are therefore random variates generated by $\mathcal{B}\_(\tilde{n}_i; n_i, 1/2)$.

The significance of grain size effects predicted by the bioturbation model represents the hypothesis H_1 with free parameters $_1 = (\Phi_t, z_0, L, D_s, q, \beta_0)$ to be tested against the following null hypotheses H_0: (1) $H_{0,1}$— diffusion is grain size-dependent ($q > 0$), but size segregation does not occur ($\beta_0 = 0$), as in *Wheatcroft (1992)*, and (2) $H_{0,2}$— no grain size effects ($q = 0$, $\beta_0 = 0$). The goodness of H_1 with respect to H_0 is quantified by the likelihood ratio

$$\Lambda = \frac{(\ _0\ )}{(\ _1\ )} \tag{2.119}$$

where **c** = $(c_1, c_2, ...)$ is the vector of all concentrations $c_i = m_i n_i$ obtained from tracer counts n_i in samples with masses m_i, and $_0$ is the vector of free parameters in H_0. The smaller Λ, the higher is the probability that H_1 is a better model than H_0. Accordingly, the null hypothesis that the two models are equivalent descriptions of the data within the error range is rejected if Λ is small than a certain critical threshold. The Wilks theorem states that, as the sample size approaches infinity, the test statistics -2ln Λ will asymptotically approach a random variate with a chi-squared distribution χ^2_f with degrees of freedom f equal to the difference in the dimensionality of $_1$ and $_0$. The rejection limit of the test statistics at a confidence level p_0 is thus given by the solution of $F(x, f) = p_0$ with respect to x, where

$$F(x, f) = 1 - \frac{\Gamma(f/2, x/2)}{\Gamma(f/2)} \tag{2.120}$$

is the cumulative distribution of $\chi^2 f$, with Γ being the (incomplete) gamma function. The limit for rejecting the null hypothesis of no grain size segregation ($f = 1$) at a 95% level is 3.8415, while the limit for rejecting the null hypothesis of no grain size effects ($f = 2$) at a 95% level is 5.9915. The same limits at a 99% confidence level are 6.6349 and 9.2103, respectively.

2.10 Fit of microtektite counting in MD90-0961

As outlined in the previous section, tektite counts obey to a Poisson statistics. Few counts per samples are common at the typical concentrations encountered in sediments that are not very close to the impact event, and are associated with correspondingly large uncertainties. Such uncertainties do not enable to capture subtle but important details of the bioturbation mechanism, such as size-dependent diffusion, as seen with the example of *Ruddiman and Glover (1972)* and *Weatcroft and Jumars (1987)*. Therefore, a particular effort has been undertaken to obtain sufficient counting statistics for supporting the gran size effects predicted by the mixing model developed in this Chapter. Three counting campaigns have been conducted as described in the following.

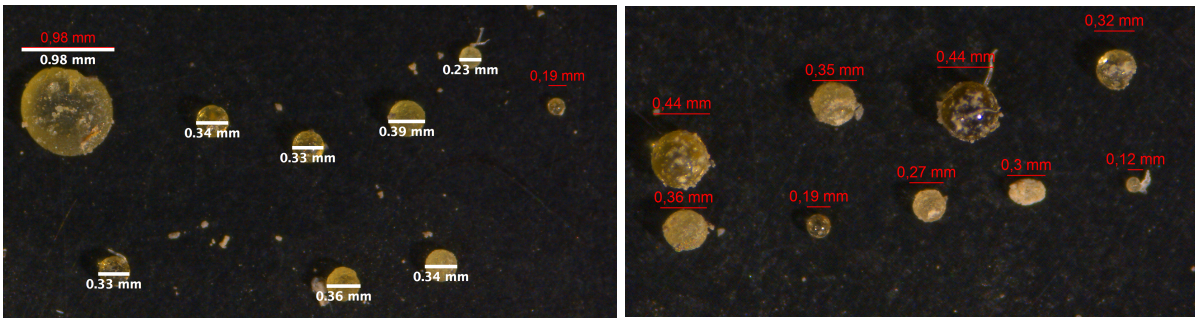

Figure 2.17: Photographs of identified microtektite particles in MD90-0961. Left panel - counted fragments at 3721 cm, right panel - at 3729 cm in core.

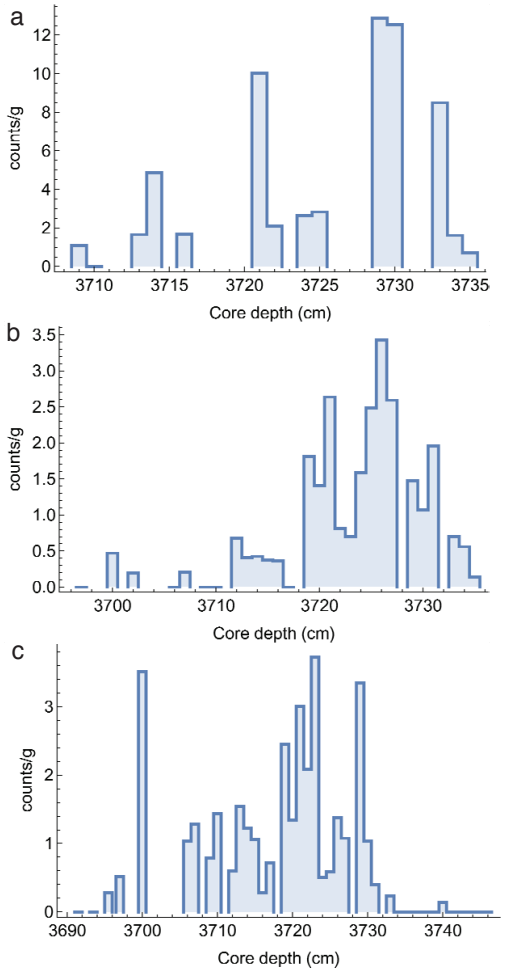

Figure 2.18: Microtektite counted fragments in core MD90-0961: a)Campaign-2014; b)Campaign-2019; c)Campaign-2020.

Prior to counting, about 3 g of dry sediments were sieved at 125 μm and consequently treated with hydrochloric acid to remove the carbonate content. At each sampled level, we counted the number of fragments and estimated their sizes, that vary from $\leq$0.1 mm to 0.98 mm (e.g. Fig.2.17). The results of total number of counts per level are plotted on the Fig. 2.18. Due to the different sampling depth and class sizes, microtektite counts obtained from three sampling sessions, have been grouped into the size classes for the samples sharing the same depth. Based on the distribution of particle sizes, we have defined three size classes : small ($\leq$ 0.2 mm), intermediate (0.2-0.45 mm), and large ($\geq$ 0.45 mm) (Fig.2.19). Please note that count numbers are normalised by the sediments mass used for the analysis.

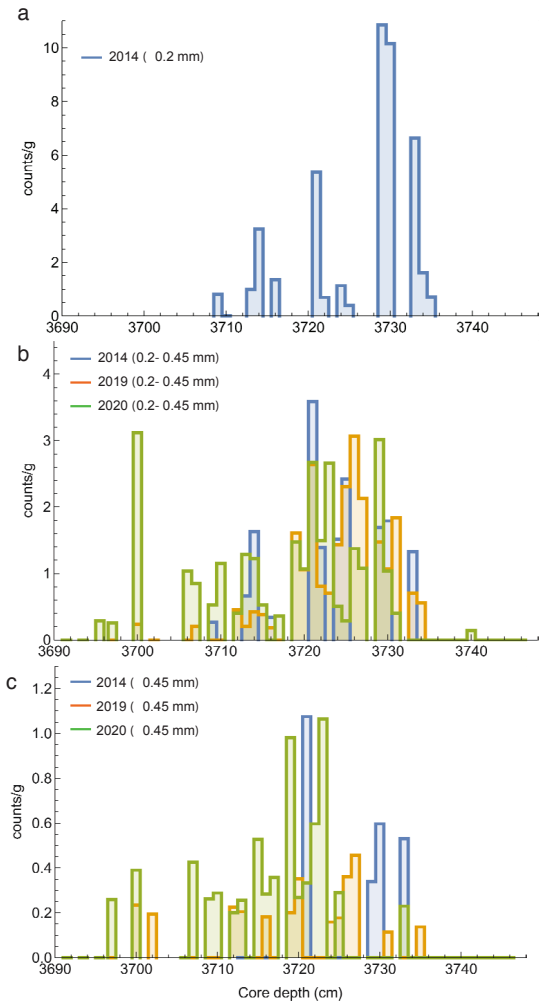

Figure 2.19: Profiles for redefined size classes: a) small fragments $\leq$ 0.2 mm; b)intermediate (0.2-0.45 mm); c)large ($\geq$ 0.45 mm)

Finally, fragments obtained from three counting were merged by summing all the fragments and diving by the total mass. The tektite concentrations obtained in this manner have been fitted with the theoretical profiles given by eq. (2.107) by maximizing the model likelihood associated with the Poisson statistics (Table 2.2, Fig. 2.20).

		***F* (tektites/g)**	**z_0 (cm)**	***L* (cm)**	***D* (cm^2/kyr)**	
0	0	289.5	3736.1	23.4	55.1	-590.2
0.466	0	278.1	3736.7	22.8	138.9	-595.4
0.252	0.00075	282.4	3736.5	19.2	55.69	-599.4

Table 2.2: Optimized parameters of Maximum Likelihood (ML) model, obtained by maximizing the probability of obtaining the measured counts n_{kl} as random realisations of Poisson processes.

The significance of this model ($\alpha \neq 0$ and $\beta \neq 0$) has been tested against the null hypothesis of no size segregation ($\alpha \neq 0$ and $\beta = 0$), and no selective diffusion ($\alpha = 0$ and $\beta = 0$). The corresponding log-likelihood values are –599.4, –595.4, and –590.2. The complete model passes the likelihood ratio test against both alternate models at a 95% confidence level, since the minimum log-likelihood difference required in this case is 3.84. This means that grain-size dependent diffusivity and size segregation are significant phenomena occurring in this sediment. The mean upward migration of the 0.05-0.2 mm, 0.2-0.45 mm and 0.45-0.9 mm tektite size fraction due to size segregation are 0.8, 3.4, and 10.9 cm respectively. If these size intervals are identified with those of foraminifera tests used for dating, the corresponding age offsets with respect to the bulk sediments would be 0.2, 0.9, and 2.9 kyr, respectively. This example demonstrates the importance of the size segregation effect for sediment dating with foraminifera.

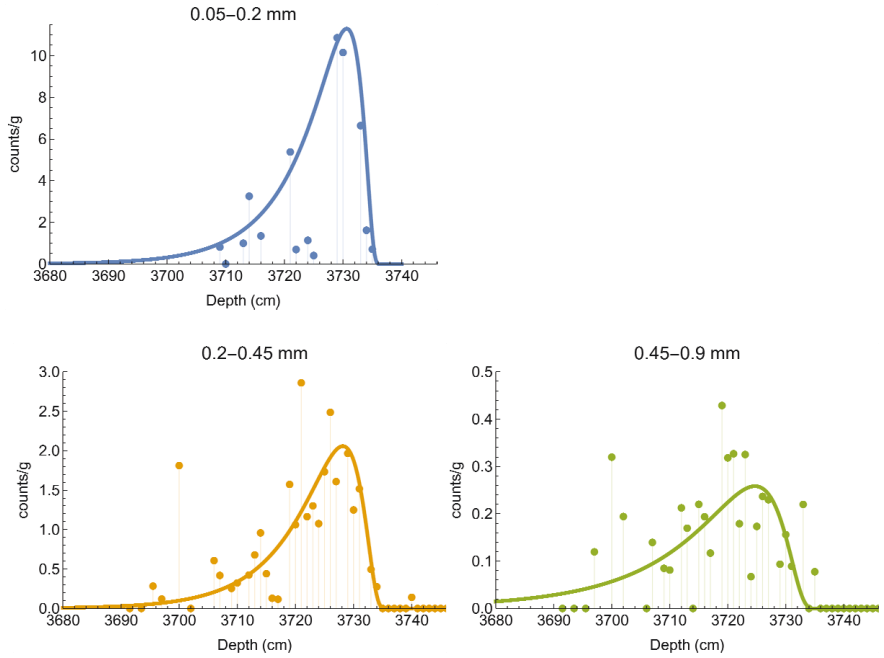

Figure 2.20: Fit of each defined size class with microtektite model

Chapter 3

Disentangling magnetic and environmental signatures of sedimentary $^{10}Be/^{9}Be$ records

Abstract

Reconstructions of the global production rate of the cosmogenic isotope ^{10}Be from sedimentary records of authigenic $^{10}Be/^{9}Be$ ratios have been successfully used to obtain independent estimates of geomagnetic dipole moment variations caused by field excursions or reversals. In this study, we assess the reliability of $^{10}Be/^{9}Be$ as a proxy for the cosmogenic ^{10}Be production rate by evaluating two potential biasing sources represented by sediment composition and climatic modulation. For this purpose, we compare five high-resolution $^{10}Be/^{9}Be$ records of the Matuyama-Brunhes (M-B) field reversal from sediment cores of the Indian, West Pacific, and North Atlantic oceans. Results do not support the existence of a direct proportionality between the $^{10}Be/^{9}Be$ ratio and the cosmogenic ^{10}Be production rate, as shown by the presence of large offsets and inconsistent variations during and outside the M-B reversal in the studied records. These variations do not appear to be related to an incomplete correction of variable sediment scavenging efficiencies by ^{9}Be normalization. Instead, major record differences can be explained by a common climatic modulation model, assuming a linear relation between $^{10}Be/^{9}Be$ and the global ^{10}Be production rate. The required site-specific additive and multiplicative coefficients are linear functions of a single global climate proxy, identified with the benthic δ^{18}O record. Additive coefficients are almost constant in time and can represent up to ~60% of the signal during periods of stable polarity. They originate from a small fraction of exchangeable Be entrained by pore water and expelled at the ocean floor. Multiplicative coefficients are also site-specific, with mean values representing the bulk scavenging efficiency of the site, and variations about this mean expressing a multiplicative modulation of the ^{10}Be production rate related to climatic changes. The amplitude of this modulation amounts to 10-15% of the maximum variations recorded during the M-B reversal and is sufficiently large

to mask minor dipole moment variations during stable polarity periods. The bulk scavenging efficiency can vary by up to ~60% and is controlled mainly by oceanic circulation. Reconstructions of the geomagnetic dipole intensity can benefit from the information about climatic modulation effects gained with our modeling approach, which enables us to evaluate the quality of $^{10}Be/^{9}Be$ records and select an optimal reference site. This site should be characterized by minimal Be-recycling contributions and minimal climatic modulation, as far as it can be determined from relative comparisons with other records. Such conditions are most likely encountered in open basins at sites (1) with <2.8 km water depth, (2) >200 km offshore, and (3) located underneath a large current system extending over regions with minimum terrigenous inputs. Scaling all records on the chosen reference enables to produce a $^{10}Be/^{9}Be$ record with reduced noise and short-term environmental effects that cannot be accounted by a global climate proxy.

3.1 Introduction

Geomagnetic field intensity reconstructions over the last million years rely mostly on relative paleointensity (RPI) records that have been gathered for the past 30 years, and on their calibration with absolute paleointensity data, for instance from volcanic records (Valet, 2003). Production rate of cosmogenic nuclides offers an alternative way of tracking the geomagnetic intensity through time (Elsasser et al., 1956). The cosmogenic nuclide Beryllium-10 (^{10}Be) forms mostly in the atmosphere by a spallation process involving collisions of high-energy cosmic particles with nitrogen and oxygen atoms (Lal and Peters, 1967; Beer et al., 2012). The production rate depends on variations of the incoming flux of primary galactic cosmic rays, which is modulated by the geomagnetic field strength and by solar activity (Kocharov et al., 1989; Beer et al., 2012; Lal and Peters, 1967; Blinov, 1988). During periods of low geomagnetic dipole strength and, therefore, lower cutoff-rigidity, the increased cosmic ray flux generates additional atomic collisions, increasing the cosmogenic nuclides production rate. The relationship between dipole strength and production rate is well constrained by cosmic ray trajectory calculations (Masarik and Beer, 1999, 2009; Poluianov et al., 2016). These calculations predict a ~2.2× enhancement of the global ^{10}Be production rate when the geomagnetic dipole moment decreases from its modern value (~$7.8 \times 10^{22} \mathrm{Am}^2$) to zero (Heikkila et al., 2009; Poluianov et al., 2016).

Cosmogenic ^{10}Be is readily removed from the atmosphere by aerosols (Heikkila et al., 2008a) and, for the most part, by wet precipitation (Arnold et al., 1956; Goel et al., 1956; Heikkilä and Smith, 2013). After reaching the Earth's surface, ^{10}Be is further transported on land and in the oceans, where it is scavenged by suspended matter and finally deposited in sediments (von Blackenburg and Bouchez 2014). Accordingly, the geomagnetic dipole moment can be reconstructed from properly normalized ^{10}Be records using the inverse geomagnetic modulation function obtained from production models (e.g. Raisbeck et al., 1985; Frank et

al., 1997). A major advantage of this technique is that ^{10}Be records are much less sensitive to local field anomalies than paleomagnetic reconstructions of the virtual axial dipole moment (VADM), owing to the global atmospheric redistribution of cosmogenic ^{10}Be (Heikkilä and Smith, 2013). On the other hand, the sedimentary ^{10}Be flux is strongly modulated by atmospheric scavenging patterns, by the transport paths on land and in the oceans, and by the sediment scavenging efficiency (Measures and Edmond, 1983; von Blanckenburg et al., 2012).

Scavenging of dissolved Be by suspended particles proceeds through incorporation in a continuously growing authigenic rim (Wittmann et al., 2017). The scavenging efficiency depends on particle size and composition (Mangini et al., 1984; Chase et al., 2002; Christl et al., 2003; Wittmann et al., 2012): opal and lithogenic phases are important beryllium scavengers contrary to $CaCO_3$ (Chase et al., 2002). The effect of scavenging efficiency variations can be eliminated by normalizing ^{10}Be with the stable ^{9}Be isotope that is released by weathering rocks (Measures and Edmond, 1983; von Blanckenburg et al., 2012), which is uptaken by the same particles (Sharma et al., 1987). The isotopic ratio ^{10}Be/^{9}Be obtained from the measurement of reactive ^{9}Be selectively extracted from the authigenic rim is therefore identical to that of the dissolved isotopes (Southon et al., 1987; Bourlès et al., 1989a; Anderson et al., 1990; Ku et al., 1990; McHargue and Damon, 1991; Simon et al., 2016b). Even so, the ^{10}Be/^{9}Be ratio is not a globally homogeneous proxy of cosmogenic ^{10}Be production, due to the different distribution of ^{10}Be and ^{9}Be sources, which make the two isotopes undergo different transport paths (von Blanckenburg et al., 2012). These paths are responsible for systematic differences between the oceans (Bourlès et al., 1989a; Ku et al., 1990; Blanckenburg and Bouchez, 2014; Simon et al., 2018b) As long as the beryllium redistribution patterns are constant over time, ^{10}Be/^{9}Be records remain proportional to the global cosmogenic production rate and can be used for magnetic moment reconstructions after proper site-specific normalization (e.g. Simon et al., 2016). Climatic variations might change the beryllium redistribution patterns, introducing an unwanted environmental modulation, which, contrary to geographic differences, has never been properly quantified.

The most direct evidence for the field recording capability of sedimentary ^{10}Be/^{9}Be records is the existence of a large peak during the last geomagnetic reversal (Matuyama-Brunhes, shortly M-B) in marine sediments and loess deposits (Raisbeck et al., 1985; Carcaillet et al., 2004; Suganuma et al., 2010; Ménabréaz et al., 2014; Valet et al., 2014; Zhou et al., 2014; Simon et al., 2016a, 2018a) as well as in the EPICA Dome C polar ice core (Raisbeck et al., 2007). Here, we compare sedimentary ^{10}Be/^{9}Be records of the M-B reversal from the North Atlantic, Indian and Pacific oceans, showing that a site-specific normalization, on which current dipole moment reconstructions are based, is not sufficient for estimating the global ^{10}Be production rate required by dipole moment reconstructions. We modelled pairwise differences between ^{10}Be/^{9}Be records using site-specific, time-dependent modulations of the global production rate from two processes: scavenging of non-synchronous ^{10}Be sources, mainly from diagenetic release at the ocean floor, and the accumulation of freshly produced

^{10}Be along the path of surface oceanic currents. The modulation functions are proportional to a single global climatic proxy, identified with the oxygen isotope ratio. It is, therefore, possible to remove global climatic components from individual records and stack the corrected isotopic ratios onto a suitably chosen reference record. While only relative differences caused by global climatic changes can be removed with this procedure, it is still possible to minimize the residual signal contamination. The gained information can be used to obtain optimised reconstructions of the geomagnetic dipole, as shown in a following article.

3.2 Environmental setting and lithology

Detailed beryllium measurements were conducted on 5 piston cores from the Indian, western equatorial Pacific and North Atlantic Oceans (Fig.3.1) (Horng et al., 2002; Valet et al., 2014, 2016; Simon et al., 2018 a, b). Cores MD90-0949 (2° 06.90' N; 76° 06.50' E) and MD90-0961 (5° 03.71' N; 73° 52.57' E) were collected during the SEYMAMA research cruise of the R/V Marion Dufresne in 1990. The 28-meter long core MD90-0949 is dominated by green to grey calcareous nannofossil ooze with coccoliths and foraminifera while the non-carbonate fraction mostly consists of terrigenous clays and, to a lesser extent, biogenic silica (Bassinot, 1993). Core MD90-0961 is 45-meter long and composed of calcareous nanofossil ooze with abundant foraminifera (Valet et al., 2014). It was retrieved on the eastern margin of the Chagos-Maldive-Laccadive Ridge, which stretches nearly 3000 km (Backman et al., 1988) along the 73° meridian.

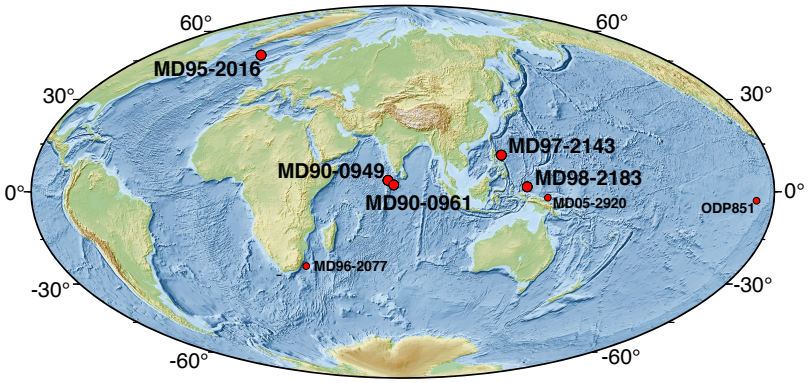

Figure 3.1: Bathymetric map showing the location of investigated cores.

Core MD98-2183 (2° 00.82' N; 135° 01.26' E) was sampled by the R/V Marion-Dufresne in the West Caroline basin of the Western Pacific Ocean during the IMAGES IV cruise and consists of hemipelagic clay with calcareous and siliceous microfossils (Yamazaki and Oda, 2004). The basin is mainly influenced by nutrient supply from coastal regions in the Philippine and Indonesian Islands while the lithogenic matter is dominated by clay minerals (Kawahata et

al., 1998). The site is located on the path of the Equatorial counter current (surface/intermediate layer), which includes the west-east return current (Tchernia 1980), the Atlantic Intermediate waters and the Upper Circumpolar Deep Water. The deep-water circulation is dominated by the Lower Circumpolar Water that partially proceeds along the southern boundary of the east Caroline Basin, flowing northward in the western East Caroline Basin (Kawabe et al., 2010). Core MD97-2143 was taken from the Benham Rise in the West Philippine Sea (15° 52.26' N; 124° 38.96' E) during the IMAGES III-IPHIS-Leg II Cruise. The site is characterized by the absence of significant bottom currents. The Benham Rise is 230 km away from Luzon Island, which has a narrow continental coast (Yu et al., 2016). The late Quaternary sediments are mainly composed of calcareous nannofossil ooze with foraminifera and volcanic debris (Wei and Lee, 1998). Terrigenous detrital material is virtually absent and minor amounts of pelagic clay confirm that that the Benham Rise has been shielded from supply of terrigenous Luzon Island and other continental landmass detritus. Yu et al. (2016) carried out a clay mineralogy analysis of sediment from the closeby core MD06-3050 (15° 57.09' N, 124° 46.77' E) and concluded that the detrital material mainly originated from Luzon volcanic rocks and eolian dust from Asian deserts.

Finally, core MD95-2016 consists of a mixture of silt clay and nano-ooze. It was taken during the IMAGES I leg IV campaign in the North Atlantic Ocean (57° 42.46' N; 29° 25.44' W) approximately 800 km away from the coast on the crest of the Reykjanes Ridge located on the pathway of the Iceland-Scotland Overflow water (Zou et al., 2017) which plays an important role for sediment composition and redistribution (Gehrke et al., 1996). At high northern latitudes, terrigenous input dominated during glacial periods in the northeast Atlantic Ocean. Turbidity currents, bottom currents, wind, and ice are potential transporters of terrigenous detritus from the continents (Ruddiman and McIntyre, 1976).

Additional beryllium measurements from three cores were included in this study for comparison purposes. MD96-2077 (33° 17' S; 31° 25' E) was retrieved from 3781 m depth at the Natal Valley in the subtropical Indian Ocean during the MD105 (Images II) campaign. The sediments consist of nanno and nannofossil oozes with periodically occurring gray to brownish layers of mud and clay intraclasts, frequently bioturbated. Site ODP 851 (2° 46'N; 110° 34' W) is located near the northern extent of the westward-flowing South Equatorial Current (SEC) and near the southern limit of the seasonal migration of the boundary between the North Equatorial Countercurrent (NECC). The sedimentary sequence can be described as a single lithologic unit composed of a mixture of foraminifer nannofossil and diatom nannofossil oozes (Mayer, Pisias, Janecek et al., 1992). Environmental setting and sediment description of core MD05-2920 (2° 51' S; 144° 32' E) are detailedly presented in Ménabréaz et al. (2012).

3.3 Methods and measurements

3.3.1 Beryllium isotope measurements

Samples of ~1 g dry sediment were processed for Be isotope analyses following the chemical procedure described in Simon et al. (2016b). The leaching technique of Bourlès et al. (1989) allows extracting both isotopes in the phase that corresponds to the equilibrated authigenic fraction of soluble ^{10}Be and ^{9}Be. Because both isotopes have identical chemical properties, ^{10}Be/^{9}Be obtained by this technique is supposedly insensitive to downcore lithological changes (Henken-Meillies et al., 1990, Simon et al., 2016b). The natural authigenic ^{9}Be concentration was measured using a graphite-furnace atomic absorption spectrophotometer (AAS) with double-beam correction. The ^{10}Be concentration was measured after chemical preparation at the French accelerator mass spectrometer (AMS) national facility ASTER (CEREGE). Concentration values were corrected for radioactive decay using the ^{10}Be half-life of 1.387±0.012 Myr (Chmeleff et al., 2010; Korschinek et al., 2010).

3.3.2 Oxygen isotopes and age model

Age-depth correlations for the five cores were established using high-resolution stable oxygen isotopic records from benthic and planktonic foraminifer species. Depending on the amount of available foraminifers, analyses were performed on a VG-Optima or an Elementar Isoprime dual-inlet mass spectrometer. All results are expressed as δ^{18}O vs V-PDB (in). The external analytical reproducibility is ± 0.05‰ (1σ) and was determined from replicate measurements of a laboratory carbonate standard. Astronomical age models for cores MD90-0949/961, MD95-2016 and MD98-2183 were derived by tuning the benthic δ^{18}O records of *Cibicides wuellestorfi* to the LR04 stack (Lisiecki and Raymo, 2005) using a two-steps approach (Simon et al., 2018b; Valet et al., 2019). First, uncalibrated depth-age models were constructed by assigning a common depth to all records after correlating the individual δ^{18}O records. The composite record of the sister cores MD90-0961/963 with the largest depositional rates and highest oxygen isotope resolution was then chosen as internal reference (Bassinot et al., 1994; Valet et al., 2014). At the beginning of termination IX (transition from the Marine Isotopic Stage 20 (MIS20) to MIS19), identification of the Australasian microtektite event (e.g. Valet et al., 2016) provided an additional, independent tie-point for the two Indian Ocean cores. After correlating all individual δ^{18}O profiles to the MD90-0961/0963 reference record, the age model was developed by tuning the benthic δ^{18}O record from MD90-0961/0963 depth scale to the LR04 stack. This strategy allowed us to represent all records on a common time scale using coherent stratigraphic approach. Age model for MD97-2143 was obtained after correlating ^{10}Be/^{9}Be records with that of core MD90-0961. The ages were assigned by the same procedure as described above. The deposition rates derived from the age model of each

core are summarised in Table 1. They are comprised between 1.2 cm/kyr (core MD97-2143) and 3.8 cm/kyr (core MD90-0961).

3.3.3 Calcium carbonate measurements

Calcium carbonate ($CaCO_3$) measurements were performed on samples taken at 4 cm intervals in cores MD90-0949, MD90-0961, MD95-2016, MD97-2143 and MD98-2183. Total carbonate content (in weight $\%$) was determined from the pressure of CO_2 released through the reaction of 1 mg of dry grounded sediment with hydrochloric acid. $CaCO_3$ contents range from a few percents to more than 75$\%$ with small fluctuations in each core (Table 3.1). For comparison reasons, we added data from core MD05-2920 (western equatorial Pacific Ocean, 2.51°S, 144.32°E) (Tachikawa et al., 2011), ODP site 851D (eastern equatorial Pacific) (Mayer et al., 1992), and MD96-2077 (subtropical Indian Ocean, 33.17°S, 31.25°E) (Bard and Rickaby, 2009), which are plotted in Fig. 3.5.

3.4 Sedimentary $^{10}Be/^{9}Be$ records of the M-B reversal

The underlying assumption of present ^{10}Be-based geomagnetic dipole moment reconstructions is that $^{10}Be/^{9}Be$ is directly proportional to the global ^{10}Be production rate, due to the dominant dipolar control and fast mixing atmospheric processes. In this case, a site-specific, time-independent proportionality constant for each record can be empirically derived from the comparison of measured $^{10}Be/^{9}Be$ values with the ^{10}Be production rate predicted for a given time with known VADM, or with a long-term average. In this scenario, records of the same geomagnetic event, here the M-B reversal, should be proportional to each other. This is not the case, however, as seen from the maximum relative $^{10}Be/^{9}Be$ increase during the M-B transition with respect to background levels before and after this event (Fig. 3.2a), which ranges from ~150% for MD90-0949 to ~220% for MD90-0961. On the other hand, all records share very similar features during the M-B reversal (e.g. the main bell-shaped peak at ~774 kyr and a shoulder at ~790 kyr), and, for certain core subsets, also outside the reversal interval (e.g. at ~730 kyr). These similarities suggest a common primary modulation of the ^{10}Be input. Differences between cores cannot be attributed to ^{9}Be normalization artifacts (Fig. 3.2b), nor do they correlate with oxygen isotope records (Fig. 3.2c). These observatious apparently support the conclusion that climatic contaminations are effectively removed (Bourlès et al., 1989a; Leduc et al., 2006; Valet et al., 2014). In the following, we describe a method for quantifying the different $^{10}Be/^{9}Be$ responses observed during the M-B reversal, and discuss possible relations with core location and sediment properties.

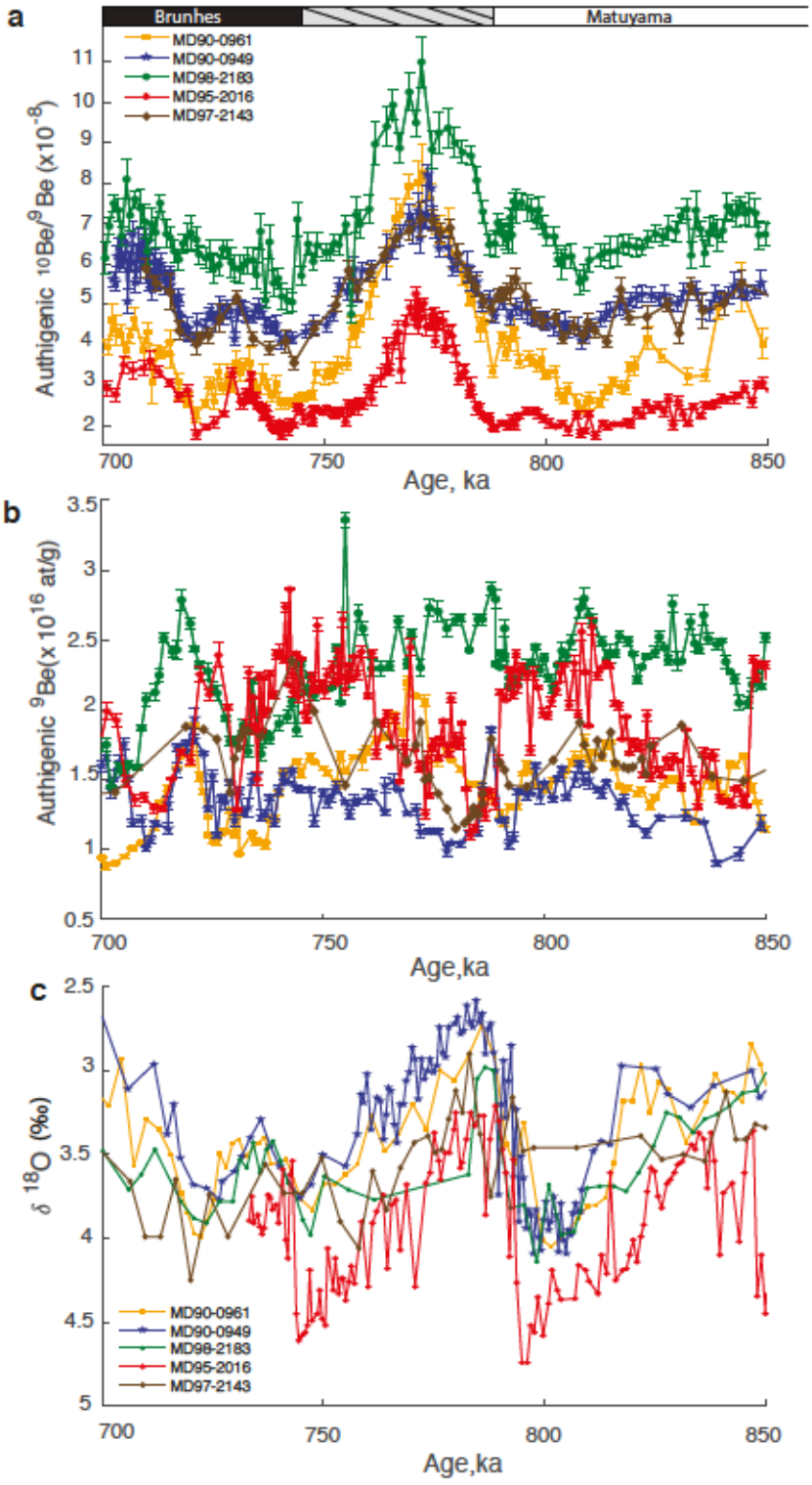

Figure 3.2: **(a)** $^{10}Be/^{9}Be$ records tuned to match the age model of MD90-0961. **(b)** Same as (a) for ^{9}Be concentrations. **(c)** $\delta^{18}O$ records from planktonic foraminifera for the same cores in (a.

3.4.1 Scaling of $^{10}Be/^{9}Be$ records

Obtaining a proper quantification of the $^{10}Be/^{9}Be$ increase during the M-B reversal is not a trivial task, since maximum values are affected by short-term variations (particularly in MD98-2183) damped by site-specific, bioturbation-induced sediment mixing (Anderson, 2001; Christl, 2007). These problems are effectively overcome by considering the integral of the $^{10}Be/^{9}Be$ excess during the M-B reversal. Because $^{10}Be/^{9}Be$ is a lithology-insensitive proxy of ^{10}Be concentration, it can be understood as a fluence, that is, the integral of sedimentary ^{10}Be flux over time, where (flux) = (volume concentration)×(deposition rate). Mass conservation makes fluences insensitive to bioturbation-related smoothing effects, while random variations are largely suppressed by the integral. However, the definition of a proper baseline is required, since fluences are defined for events producing a finite input over a finite amount of time. Defining such baseline represents a major difficulty, because of relatively strong and sometimes uncorrelated $^{10}Be/^{9}Be$ variations with typical ~20 kyr duration, and different long-term quasi-linear trends, especially before the transition (Fig. 3.2a), as shown in Supplementary Figure 3.12.

Quantitative comparisons require therefore a common baseline definition. This definition relies on matching all records over the two time intervals immediately preceding (808-853 kyr) and following (707-743 kyr) the M-B reversal, after applying a proper linear scaling to each of them. Rescaled $^{10}Be/^{9}Be$ records are defined by

$$R'_i = (R_i - a'_i)/b'_i, \tag{3.1}$$

where R'_i is the rescaled version of R_i for core i (see Table 3.2 for the core indices), with coefficients a'_i and b'_i that minimize the residual squared differences between R'_i and a reference record, chosen to be MD90-0961 due to its highest deposition rate and, therefore, temporal resolution. The use of additive coefficients a'_i violates the assumption that the isotopic ratio is proportional to the global ^{10}Be production rate; however, these coefficients are necessary to eliminate the large offsets seen in Fig. 3.2a. An overall good agreement is obtained for all R'_i (Fig. 3.3a), which now share the same long- and short-term trends outside the M-B reversal. A partial exception is represented by core MD95-2016 outside the 735-845 kyr interval. The average of all rescaled profiles in Fig. 3.3a defines a common baseline R'_{bk}, which can be subtracted to obtain the net $^{10}Be/^{9}Be$ increase during the M-B reversal. Different net increases are obtained for the five cores during the M-B reversal (Fig. 3.3b), which means that the rescaling coefficients obtained with eq. (3.1) are not valid for the whole record duration. This is the first hint that points to different mechanisms, controlling smaller variations during stable polarity intervals on the one hand, and major $^{10}Be/^{9}Be$ increase during a geomagnetic event on the other. As it will be discussed in Section 3.5, these mechanisms are associated with a climatic and a geomagnetic modulation of the ^{10}Be flux.

A second linear transformation is applied to the net rescaled enhancements $R'_i - R'_{\rm bk}$, this time using $a''_i = 0$, since the baseline has been already subtracted, to collapse them onto the chosen reference. The final result is a set of normalized curves $\Delta R''_i$ (Fig. 3.3c), which are supposedly proportional to the ^{10}Be flux increase during the M-B reversal. Small residual differences are nearly random and limited to short time intervals, mostly <10 kyr. They are effectively removed by building an average $\Delta R''$ of all $\Delta R''_i$, except MD95-2016, which has a much larger noise level. The lack of systematic differences between individual $\Delta R''_i$ reconstructions means that smoothing effects are likely absent, down to the ~10 kyr duration of the precursor event at 795 kyr.

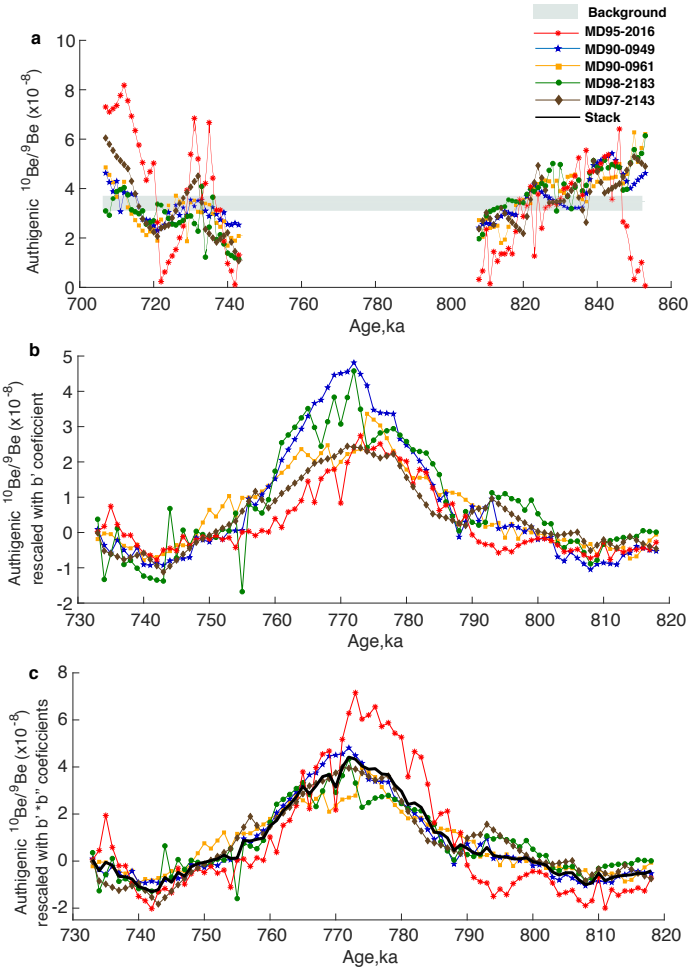

Figure 3.3: **(a)** Linearly scaled ^{10}Be/^{9}Be records adjusted to match of core MD90-0961 outside the M-B interval. The thick gray line represents the mean offset of all records, except MD95-2016. **(b)** Same as (a) for the M-B interval, after removing the mean offset. **(c)** Stack obtained from (b) after a second rescaling step used to remove the residual differences with respect to core MD90-0961. The thick black line is the average of all rescaled records, except MD95-2016.

Robust quantification of the unnormalized total ^{10}Be/^{9}Be excesses caused by the M-B re-

versal is finally obtained by integrating $b_i' b_i'' \Delta R''(t)$, with b_i' and b_i'' being the scaling coefficients of the first and second scaling transformation, respectively. The integrated ^{10}Be/^{9}Be excess $\Delta R_{\rm tot}$ obtained in this manner varies significantly among cores (Fig. 3.4a), with the smallest and the largest values for MD95-2016 and MD98-2183, respectively. Moreover, $\Delta R_{\rm tot}$ correlates significantly with the water depth of the corresponding sites (except MD90-0961 for reasons explained later), but not with other parameters, such as sedimentation rate and calcium carbonate content. A similar correlation, with the same exception of core MD90-0961, is also found for the additive coefficients a_i' used to rescale the baselines outside the M-B transition (Fig. 3.4c). In both cases, a linear extrapolation of the observed trend leads to the unlikely conclusion that ^{10}Be/^{9}Be variations during and outside the M-B reversal drop to zero at water depths comprised between ~1.1 and 1.7 km. The multiplicative coefficients b_i', on the other hand, display a much weaker correlation with water depth (Fig. 3.4d), probably because of the limited amplitude and the mixed nature of ^{10}Be/^{9}Be variations (i.e. short- and long-term) occurring outside the M-B transition interval. The linear relation between baseline and total ^{10}Be/^{9}Be excess on the one hand, and water depth on the other is difficult to reconcile with modern dissolved ^{10}Be/^{9}Be profiles in the oceans (Kusakabe et al., 1990), which do not show a systematic increase below 1-2 km depth.

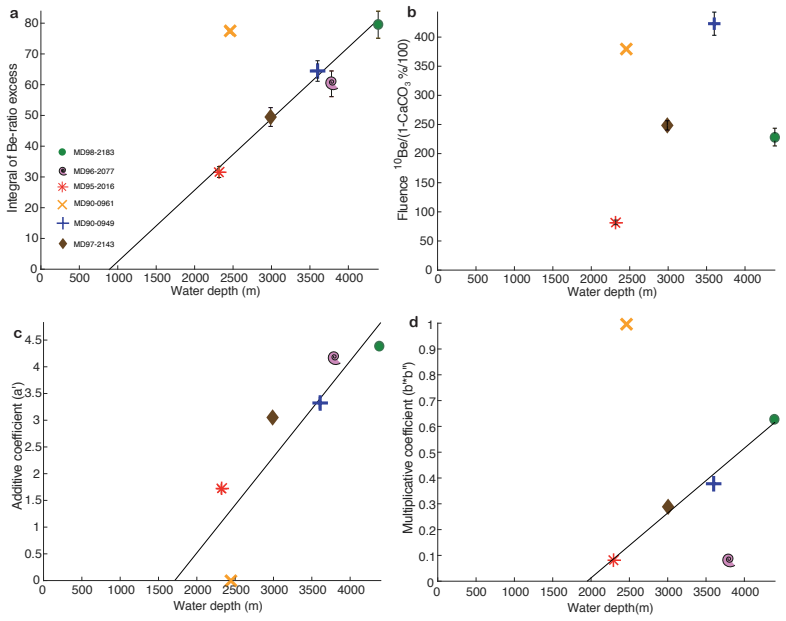

Figure 3.4: **(a)** Integral of ^{10}Be/^{9}Be excess vs. water depth. In addition to five discussed so far ^{10}Be/^{9}Be profiles, we include estimates for MD96-2077 from subtropical Indian Ocean in this study. **(b)** Same as (a) with the calcium carbonate-corrected ^{10}Be fluence. **(c-d)** Additive and multiplicative scaling coefficients used to create the ^{10}Be/^{9}Be stack of Fig. 3.3, vs. water depth.

In summary, this preliminary analysis suggests that there are three distinct processes

controlling the isotopic ratio: (1) the geomagnetic modulation, which dominates during the M-B reversal and is responsible for the observed peak at ~774 kyr, (2) a different modulation, which is probably a mixture of geomagnetic and environmental effects, which controls small variations during periods of stable polarity, and (3) a site-specific, constant ^{10}Be flux providing a different baseline to each record. Before proceeding with the quantification of these processes, we need to exclude the presence of significant residual effects due to lithologically-controlled changes of the sediment scavenging efficiency.

3.4.2 Investigating the calcium carbonate impact on beryllium scavenging

A possible source of globally-inconsistent ^{10}Be/^{9}Be records is the incomplete or incorrect compensation for sediment-specific scavenging efficiencies. Strong positive correlations exist between beryllium concentration on the one hand, and fine aluminosilicate particles and opal on the other, due to the high Be affinity linked to silicates with large specific surface area (Yuan-Hui Li, 1982, Balistrieri and Murray, 1984; Chase et al., 2002; Belmaker et al., 2014; Simon et al., 2016b). In contrast, increased carbonate fractions lower the bulk scavenging efficiency, as demonstrated by the negative correlation existing between authigenic beryllium concentration and $CaCO_3$ (Southon et al., 1987; Henken-Meillies et al., 1990; Chase et al., 2002). As both isotopes are affected in the same manner, the ratio should not be affected. On the other hand, large carbonate contents might affect the leaching procedure used for beryllium measurements, for instance by limiting the amount of authigenic isotopes that can be extracted to the outmost layers of authigenic rims with a radial ^{10}Be/^{9}Be gradient.

Given the important role played by the comparison of sites particularities in our interpretation of sedimentary ^{10}Be/^{9}Be records, it is important to exclude artefacts arising from large differences in calcium carbonate content among the five cores. For this purpose, we compare ^{9}Be-normalized records with a simple scavenging efficiency correction based on $CaCO_3$ concentration. Assuming a scavenging efficiency of zero for sediments composed solely of $CaCO_3$ fraction, and identical efficiencies for the other minerals, a carbonate-free ^{10}Be record is obtained by normalising the ^{10}Be concentration with $1 - [CaCO_3]$, where $[CaCO_3]$ is the mass-normalized carbonate fraction. The integrated ^{10}Be excess obtained with this type of correction does no longer correlate with water depth (Fig. 3.4b). The lack of systematic differences between the two normalizers indicates that $CaCO_3$-related artefacts are either absent, or not proportional to the carbonate content. In the former case, the disagreement between the two normalizers is explainable by the different scavenging efficiencies of the other minerals. For the latter case, we checked the relation between carbonate content and the concentration of both beryllium isotopes, using the measurements of individual specimens, as well as site means (Fig. 3.5). The expected proportionality between authigenic ^{9}Be concentrations and $CaCO_3$ holds within cores, provided that carbonate contents are sufficiently variable (e.g. MD95-2016

and MD90-0961 in Fig. 3.5a), and between the sites (Fig. 3.5b), with a residual scatter due to site-specific differences of the mean ^{9}Be content. Such differences are also responsible for the apparent discontinuity of single specimen measurements at ~50% $CaCO_3$ (Fig. 3.5a), as seen from the disappearance of any overall correlation between ^{10}Be/^{9}Be and the carbonate content (Fig. 3.5c). The residual correlation within core MD98-2183 can be explained by a significant $CaCO_3$ dissolution episode during the M-B reversal.

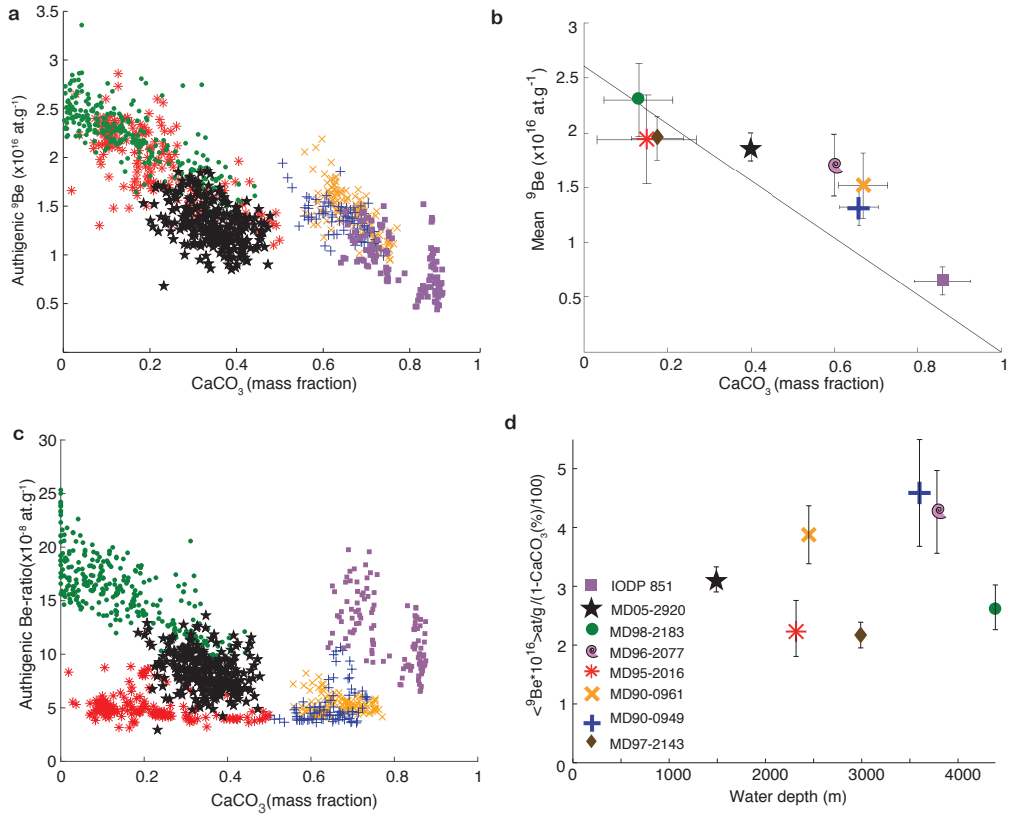

Figure 3.5: Be scavenging by non-carbonatic particles. **(a)** ^{9}Be vs. calcium carbonate content for individual specimens of 6 cores covering different time intervals. **(b)** Same as (a) for site means. Error bars correspond to standard deviations. **(c)** ^{10}Be normalized by authigenic ^{9}Be vs. calcium carbonate content for the same specimens as in (a). **(d)** Same as (c) for site means. In the current study, only the variations of ^{9}Be from core ODP851 are presented for comparison with calcium - carbonate content. The ^{10}Be/^{9}Be record from ODP 851 will be presented and discussed elsewhere.

We therefore, conclude that the observed differences between ^{9}Be-normalized and carbonate-free ^{10}Be concentrations are caused by the scavenging efficiency of other (non-carbonate) minerals. The combined effect of scavenging efficiency and site-specific ^{9}Be concentrations does not show any systematic relation with water depth (Fig. 3.5d). The fact that only ^{10}Be/^{9}Be depend on water depth, and that this dependence is not replicable with the carbonate-free ^{10}Be

content, can only be explained by true depth dependence of dissolved ^{10}Be in the water column.

3.5 The environmental modulation of $^{10}Be/^{9}Be$ records

As seen in the section 3.4, there are strong evidences for a joint geomagnetic and environmental modulation of $^{10}Be/^{9}Be$ records across the M-B reversal. In the following, we analyse possible environmental modulation mechanisms and develop an empirical model that explains inter-core differences by a combination of climatic effects and recycled ^{10}Be inputs from sources that are not synchronised with the global atmospheric ^{10}Be production rate.

3.5.1 Theory

Particles suspended in ocean water containing dissolved beryllium grow an authigenic rim in which the Be concentration C_{r} is related to the dissolved concentration C_{d} by $K = C_{\mathrm{r}}/C_{\mathrm{d}}$, where K is the intrinsic solid-liquid partition coefficient of beryllium. The practically used bulk partition coefficient (Chase et al., 2002; Wittmann et al., 2017) differs from the intrinsic coefficient by the use of bulk solid concentrations, instead of rim concentrations, which makes it sensitive to grain sizes. The authigenic rim grows continuously, acquiring the isotopic composition of dissolved Be in water (Wittmann et al., 2017). In the following, it is assumed that the rim thickness increases at a rate λ while particles are in suspension. The bulk beryllium mass concentration accumulated on suspended matter of type i when reaching the ocean floor is thus given by

$$C_i = \rho_i \sigma_i \int_0^{T_i} \lambda_i K_i C_{\mathrm{d}} \mathrm{d}t, \tag{3.2}$$

where T_i is the residence time of particles in water, K_i the intrinsic partition coefficient of this phase, λ_i the accretion rate of the authigenic rim (thickness per unit of time), σ_i the specific surface (area per unit of mass) of sinking particles of type i, and ρ_i their density. Each component contributes to the bulk sedimentary concentration C in proportion to its mass fraction q, so that

$$C = \sum_i q_i \rho_i \sigma_i \int_0^{T_i} \lambda_i K_i C_{\mathrm{d}} \mathrm{d}t. \tag{3.3}$$

Suspended matter can be divided into two pools: a pool of fine particles with negligible sinking velocity, which are carried by oceanic currents, and a pool of fewer, much larger, rapidly sinking particle aggregates (flocs), which are the effective scavenging carriers (McCave, 1975; Bacon et al. 1985). The same particle might be exchanged several times between a freely suspended, non-sinking state and a rapidly sinking aggregate, which yields a mean

effective sinking velocity of 0.3-1 km/yr (Bacon et al. 1985), >3 orders of magnitude less than the typical velocity of oceanic currents. Therefore, Be scavenging is controlled mainly by lateral transport, which means that the arguments of the integral in eq. (3.3) must be evaluated along the paths $\Gamma(t, \boldsymbol{x}_0, T)$ of suspended particles from their starting points $\boldsymbol{x}_0$ at the ocean surface (in case of directly deposited dust) or along a coast (in case of continental provenance) to the sediment core location. Because several starting points are connected to the same endpoint, eq. (3.3) is integrated over all paths ending at the core location, obtaining

$$C = \sum_i \rho_i \sigma_i \int_{\Omega_i} p_i(\boldsymbol{x}_0) \mathrm{d}\boldsymbol{x}_0 \int_0^{T_i} \lambda_i K_i C_\mathrm{d}(\Gamma_i(t, \boldsymbol{x}_0, T)) \mathrm{d}t, \tag{3.4}$$

with $p_i(\boldsymbol{x}x_0)$ being the probability of Γ_i, and Ω_i the "catchment" area of the core location for sediment particles of type i. The set of p_i values corresponding to all combinations of start and endpoints defines the so-called surface-bottom transportation matrix (Nooteboom et al., 2019). The surface-ocean area Ω_i connected to the bottom is largest along large current systems, such as the western boundary currents (e.g. the Gulf Stream), because strong currents are often accompanied by eddies, which promote mixing. According to this model, sedimentary Be concentrations are affected by three main factors: (1) the uptake efficiency, expressed by σ_i, λ_i, K_i, (2) the dissolved Be concentration C_d along the settling paths Γ_i, and (3) the settling times T_i. The associated scavenging flux, which is obtained by multiplying C with the vertical flux of suspended matter, removes dissolved Be from the water column. This effect is more pronounced at places with large sedimentary fluxes, for instance near the coasts, where it is known as boundary scavenging (Bacon, 1988; Anderson et al., 1990, 1994).

The isotopic ratio

$$R = \frac{1}{C^9} \sum_i \rho_i \sigma_i \int_{\Omega_i} p_i(\boldsymbol{x}_0) \mathrm{d}\boldsymbol{x}_0 \int_0^{T_i} \lambda_i K_i C_\mathrm{d}^9(\Gamma_i) R_\mathrm{d}(\Gamma_i) \mathrm{d}t \tag{3.5}$$

obtained from eq. (3.4) is formally equivalent to a weighted average of the ratio R_d of dissolved isotopes along Γ_i, with weights given by the concentration C_d^9 of dissolved ^{9}Be. All factors affecting Be concentrations will also affect isotopic ratios; however, some effects are greatly reduced. For instance, R is insensitive to changes that occur homogeneously over the area covered by significant probability values of the surface-bottom transport matrix, because both isotopes are affected in the same manner. This is the zero-order assumption underlying present Be-based reconstructions of major geomagnetic events. Time-dependent environmental effects on R always require inhomogeneous changes of dissolved isotope ratios (horizontally, vertically, or both), or changes of the surface-bottom transportation matrix in areas with inhomogeneous isotope ratios, or both.

The geomagnetic modulation of R depends only on R_d, with a maximum delay controlled by the ^{10}Be residence time in the water. Residence times are comprised between ~100 years

at margins sites and ~3000 years at red-clay sites in the deep Central Pacific (Anderson et al., 1990). Sites with largest residence times might therefore produce significantly smoothed records of short geomagnetic events, such as excursion (Christl, 2007). The 200-700 year deep water residence times at the five sites investigated in this study (von Banckenburg et al., 1996) are small compared to the duration of the M-B reversal, so that significant smoothing effects, if any, are caused only by bioturbation.

We now need to link R_{d} with the ^{10}Be production rate. Assuming rapid and complete mixing of authigenic Be, von Blanckenburg and Bouchez (2014) obtained the following expression for the dissolved $^{10}\mathrm{Be}/^{9}\mathrm{Be}$ ratio from the oceanic mass balance:

$$R_{\mathrm{d}} = \frac{(A_{\mathrm{oc}}/A_{\mathrm{riv}})F^{10}_{\mathrm{oc}} + \phi_{\mathrm{del}}F^{10}_{\mathrm{riv}}}{\phi_{\mathrm{del}}D_{\mathrm{riv}}[^{9}\mathrm{Be}]_{\mathrm{parent}}(f^{9}_{\mathrm{reac}} + f^{9}_{\mathrm{diss}})} \tag{3.6}$$

where A_{oc} and A_{riv} are the total areas of the oceans and river whatersheads, respectively, F^{10}_{oc} and F^{10}_{riv} are the atmospheric ^{10}Be fluxes to the oceans and the river watersheds, respectively, ϕ_{del} <1 is the efficiency of overall riverine Be delivery, D_{riv} is the average denudation rate in the basins drained by rivers, $^{9}\mathrm{Be}_{\mathrm{parent}}$ is the mean ^{9}Be concentration of parent rocks delivering eroded material to the river, and f^{9}_{reac}+ f^{9}_{diss} the fraction of ^{9}Be released during weathering from the parent rock, either in reactive phases or dissolved. The main point to retain from this equation is that R_{d} is proportional to the atmospheric ^{10}Be fluxes F^{10}_{oc} and F^{10}_{riv}, which are in turn proportional to global cosmogenic production rate P, given the very short atmospheric residence time. Upon writing $F^{10}_{\mathrm{oc}} = \phi_{\mathrm{oc}}P$ and $F^{10}_{\mathrm{riv}} = \phi_{\mathrm{riv}}P$, where ϕ_{oc} and ϕ_{riv} are the efficiencies of atmospheric ^{10}Be scavenging to the oceans and to the river basins, respectively, eq. (3.6) becomes

$$R_{\mathrm{d}} = \frac{(A_{\mathrm{oc}}/A_{\mathrm{riv}})\phi_{\mathrm{oc}} + \phi_{\mathrm{del}}\phi_{\mathrm{riv}}}{\phi_{\mathrm{del}}D_{\mathrm{riv}}[^{9}\mathrm{Be}]_{\mathrm{parent}}(f^{9}_{\mathrm{reac}} + f^{9}_{\mathrm{diss}})}P. \tag{3.7}$$

The form of eq. (3.7) makes clear that the environmental modulation of R_{d} is purely multiplicative.

In the more realistic case of incomplete mixing, expressions similar to eq. (3.7) might be applied to smaller pools, or to poorly mixing water masses (e.g. deep waters), with boundary conditions given by the exchange rates of dissolved Be between all pools. The direct proportionality relation between R_{d} and P is thereby maintained, as long as the Be residence times of all pools remain small compared to the timescale of geomagnetic variations. A similar conclusion can be drawn for the link between R and R_{d} (eq. 3.5). With these assumptions in place, combination of eq. (3.5) and (3.7) yields a result of the type $R = \beta_{\mathrm{d}}\beta_{\mathrm{s}}P$, where β_{d} and β_{s} are site- and time-dependent factors expressing the environmental modulation of R_{d} (eq. 3.7) and of the scavenging flux (eq. 3.5). This result supports current geomagnetic dipole reconstruction techniques based on the normalisation of R with a calibration constant

R_0, which is chosen by matching R/R_0 with the global ^{10}Be production rate expected at a reference time with known VADM (e.g. Simon et al., 2016a, 2018a,b). However, as discussed in Section 3.4, we observed differences between ^{10}Be/^{9}Be records of the M-B reversal that can only be explained by the existence of a nearly constant, site-specific offset, which can be as large as the geomagnetic modulation caused by the reversal itself. This offset does not prevent the stratigraphic identification of the ^{10}Be increase associated with major geomagnetic events, but questions the accuracy of inter-core calibrations.

Constant ^{10}Be/^{9}Be offsets over the ~160 kyr time span of our records of the M-B reversal require a Be remobilisation mechanism that spans a considerable period of time. For instance, boundary scavenging of ^{10}Be-rich ice masses in the Baffin Bay provides enough additional inputs of previously accumulated ^{10}Be to obscure the paleomagnetic signal (Simon et al., 2016). A different source must be envisaged for open basins, for instance sedimentary Be release to the ocean floor (Measures et al., 1996; Wittmann et al. 2017), once-deposited sediment redistribution by bottom currents (Frank et al., 1995), or particle remineralisation (Frank, 2002). Because ^{10}Be is released by these sources once produced in the atmosphere, it can be considered as a recycled component of the total flux. A rigorous treatment of ^{10}Be recycling requires a modification of eq. (3.6) that includes additional Be fluxes $F^{10}_{\rm rc}$ and $F^{9}_{\rm rc}$ in the numerator and denominator, respectively, which are not synchronized with the cosmogenic production rate and the terrigenous flux, respectively. In this case, eq. (3.7) is replaced by

$$R_{\rm d} = \frac{F^{9}_{\rm rc}}{F^{9}_{\rm tot}} R_{\rm rc} + \left[1 - \frac{F^{9}_{\rm rc}}{F^{9}_{\rm tot}}\right] \beta_{\rm d}\beta_{\rm s} P, \tag{3.8}$$

where $F^{9}_{\rm tot}$ is the total ^{9}Be flux that includes recycled sources, and $R_{\rm rc}$ is the isotopic ratio of these sources. The first term on the right-hand side of eq. (3.8) introduces an offset that is modulated by the time dependence of $F^{9}_{\rm rc}$ (i. e. the rate at which recycled Be is introduced in the water), and of $R_{\rm rc}$. A constant offset requires a time-independent scavenging mechanism of recycled Be from sources with a sufficiently large residence time. In this case, offset subtraction restitutes ^{10}Be/^{9}Be values with unaffected multiplicative modulation of the production rate. This is not true for time-varying offsets, which introduce an additional multiplicative modulation through the $1 - F^{9}_{\rm rc}/F^{9}_{\rm tot}$ term in eq. (3.8).

In summary, ^{10}Be/^{9}Be records are independently controlled by five main variables: (1) the cosmogenic ^{10}Be production rate, which depends on the geomagnetic dipole moment, (2) the distribution of surficial Be sources (atmospheric scavenging, dust fluxes, riverine inputs, melting ice masses), (3) the release of recycled Be at the ocean floor, (4) the oceanic circulation (advective transport, mixing), and (5) sedimentary fluxes, which controls the scavenging flux. Variables 2-4 affect $\beta_{\rm d}$, while $\beta_{\rm s}$ is controlled by variable 5. The complex interplay between these variables is controlled mainly by the distance from the coast and by large current systems across ocean basins, as shown for the South Atlantic case (Measures et al., 1996).

3.5.2 Reconstructions of the environmental modulation

Additive and multiplicative environmental effects of individual ^{10}Be/^{9}Be records cannot be reconstructed without an independent estimate of the cosmogenic ^{10}Be flux. Here we propose a possible strategy to overcome this limit by disentangling geomagnetic and environmental contributions to several records of the same event, i.e. the M-B reversal. Following the preliminary profile processing discussed in Section 3.4, we consider pairs of records R_i and R_j at sites i and j, respectively, and model the differences introduced by environmental effects using a linear transformation to rescale R_j so that

$$R_i(t) = A_{ij} + B_{ij}R_j(t), \tag{3.9}$$

where A_{ij} and B_{ij} are site-specific functions representing the additive and multiplicative environmental modulation of site j relative to site i. Solution of eq. (3.9) with respect to R_j yields

$$R_j(t) = A_{ij} + B_{ij}R_i(t) = \frac{R_i(t) - A_{ij}}{B_{ij}}, \tag{3.10}$$

so that the reciprocal relations $A_{ji}(t) = -A_{ij}/B_{ij}$ and $B_{ji}(t) = B_{ij}^{-1}$ hold between the coefficients. Environmental changes make these coefficients depend on time. In case of global climatic responses, A_{ij} and B_{ij} can be assumed to be functions of a common global climate proxy $S(t - t_0)$, such as δ^{18}O , where t_0 is a time lag accounting for a possible delayed response of the beryllium signal modulation with respect to S, or vice versa, due to distinct phase lags (e.g. Tuenter et al., 2005) of specific processes controlling A, B, and S, respectively. The dependency of A_{ij},B_{ij} on S must be small, for beryllium records to be a useful proxy of cosmogenic production. Therefore, the first two terms of the Taylor series of $A_{ij}(S)$ and $B_{ij}(S)$ should adequately represent the global environment modulation. In this case we can write

$$\begin{aligned} A_{ij}(t) &= a_{ij}^0 + a_{ij}^1 S(t - t_{ij}^a) + \varepsilon_{ij}^a(t) \\ B_{ij}(t) &= b_{ij}^0 + b_{ij}^1 S(t - t_{ij}^b) + \varepsilon_{ij}^b(t) \end{aligned} \tag{3.11}$$

where a_{ij}^l , b_{ij}^l are the first two Taylor coefficients of $A_{ij}(S)$ and $B_{ij}(S)$, respectively, t_{ij}^a and t_{ij}^b are the time lags of additive and multiplicative modulations, and ε_{ij}^a, ε_{ij}^b are additional functions representing environmental effects that do not correlate with $S(t)$, which can be effectively treated as a noise source. The amplitude of temporal variations caused by the time dependence of A_{ij} and B_{ij} should be small compared to the geomagnetic response ΔR under consideration, in our case the M-B transition. This condition is fulfilled if

$$a_{ij}^1 \Delta S + \Delta\varepsilon_{ij}^a + (b_{ij}^1 \Delta S + \Delta\varepsilon_{ij}^b)\hat{R}_j \ll \Delta R_i, \tag{3.12}$$

where Δ indicates the maximum variation of S, R or ε, and $\hat{R}$ is the maximum value of $R(t)$ during the period under consideration.

Solutions for the coefficients a_{ij}^{l} and b_{ij}^{l} for a given set of records can be found by minimizing the sum

$$\sum_{k,j\neq i} [a_{ij}^{0} + a_{ij}^{1} S(t_k - t_{ij}^{a}) + (b_{ij}^{0} + b_{ij}^{1} S(t_k - t_{ij}^{b})) R_j(t_k) - R_i(t_k)]^2 \tag{3.13}$$

of squared differences between measured values of R and values reconstructed using eq. (3.9) and (3.11), respectively, with constraints given by the reciprocity relations for $j > i$. The necessary condition for obtaining meaningful solutions is the negligibility of ε_{ij}^{a} and ε_{ij}^{b}, which means that environmental effects not accountable by $S(t)$ must be small, or cover a frequency range that does not overlap with S or the geomagnetic modulation.

The scaling coefficients in eq. (3.11) are linear with respect to the coefficients a_{ij} and b_{ij}, but not with respect to the time lags t_{ij}^{a} and t_{ij}^{b}, due to the quasi-periodic character of the climatic proxy S. Therefore, distinct solutions might be obtained from different initial choices of t_{ij}^{a} and t_{ij}^{b}. In the following model implementation, the global climatic signal is identified with the mean δ^{18}O record of the Indian Ocean cores MD90-0949 and MD90-0961 (Fig. 3.6), which matches the classic glacial-interglacial sawtooth pattern of benthic δ^{18}O stacks (Lisiecki and Raymo, 2005). Our choice of a single climatic proxy might not be flexible enough to account for selective responses to individual forcing parameters, such as that of the thermohaline circulation to the obliquity band (Brickman et al., 1999; Antico et al., 2010). In this case, residual relative differences between records might direct the choice of more suited proxies of S.

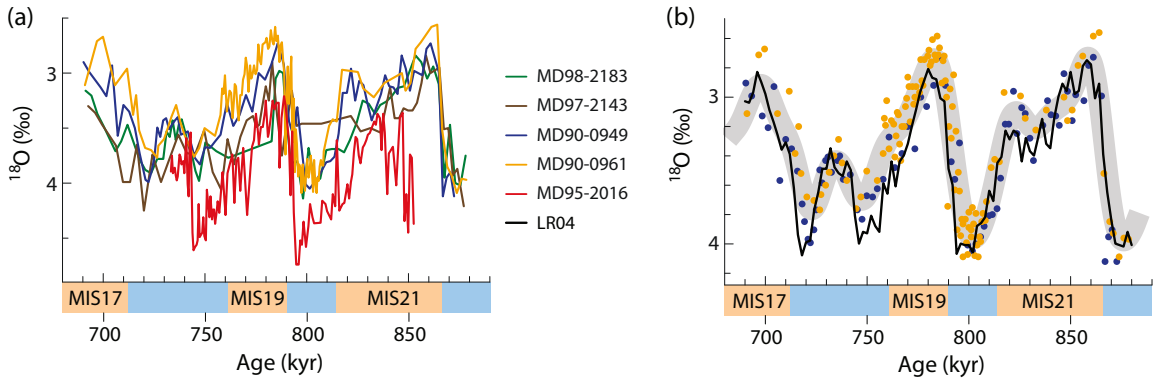

Figure 3.6: **(a)** Measured benthic δ^{18}O records over a time interval that includes the MB reversal. **(b)** Least-squares collocation fit (thick gray line) of the benthic δ^{18}O records of MD90-0949 (blue dots) and MD90-0961 (yellow dots). The benthic δ^{18}O stack LR04 (Lisiecki and Raymo, 2005) is shown for comparison (black line) after subtracting a constant offset of 0.75.

A least-squares collocation algorithm (Moritz, 1978) is used to produce a smoothed interpolation of the original δ^{18}O record, which is identified with the climatic function $S(t)$ (Fig. 3.6b). Least-squares collocation is particularly suited for the interpolation of irregularly sampled, noisy signals, and it is used here also to obtain slightly smoothed versions of the ^{10}Be/^{9}Be records of all cores between 715 and 830 kyr. This interval includes the whole period of enhanced ^{10}Be production associated with the field reversal, and some ~30 kyr of stable polarity before and after. The use of smoothed records facilitates the solution convergence by removing shallow local minima of eq. (3.13) caused by noise. Initial parameters are chosen to reproduce the case of no climatic modulation, that is $a^1_{ij} = a^2_{ij} = 0$ (no additive effects), $b^1_{ij} = 1$ (same responses at all sites), and $b^2_{ij} = 0$ (no multiplicative effects). Initial t^a_{ij} and t^b_{ij} values were comprised between $\pm$20 kyr, which is about $1/4$ of the main period of $S(t)$. Larger lags, if required by the minimization algorithm, are produced automatically by sign changes of a^2_{ij} and b^2_{ij}. A systematic variation of the initial values of t^a_{ij} and t^b_{ij} in 5 kyr steps yields 81 different combinations of initial values and 14 distinct solutions. These solutions correspond to 14 different ways to rescale four of the five Be records of Fig. 3.2 onto the fifth one.

As seen in Fig. 3.7, rescaled records are almost identical over the chosen 715-830 kyr interval. Few residual differences can be seen for the North Atlantic core MD95-2016 in some solutions, but the overall agreement is generally better than the random scatter of individual records. This means that a single climatic function is sufficient to explain all significant differences between the records. Solution multiplicity is due to the limited redundancy of eq. (3.9-3.11): the most evident common features of the five records can be represented with 11 points (arrows in Fig. 3.7a), yielding a total of 110 independent ^{10}Be/^{9}Be differences between

profiles, which need to be fitted using 60 model parameters. The goodness of each solution can be evaluated by comparing the original records with reconstructions obtained from stacks of rescaled records. For this purpose, a reference core is chosen (e.g. MD95-2016 as in Fig. 3.8), and the other records are rescaled to match this reference using the coefficients of a given solution (e.g. solution 14 in Fig. 3.8b), obtaining five rescaled records in accordance with the model assumptions. The selection of a reference core is arbitrary, since every solution contains the coefficients required to transform any record into any other record. Our choice of MD95-2016 ($i = 5$, Table 3.2) for displaying the model results is based essentially on the fact that it is the record with the smallest constant offset, so that $a_{5j} \leq 0$ for all j. Furthermore, MD95-2016 is characterized by an average increase of R during the M-B reversal.

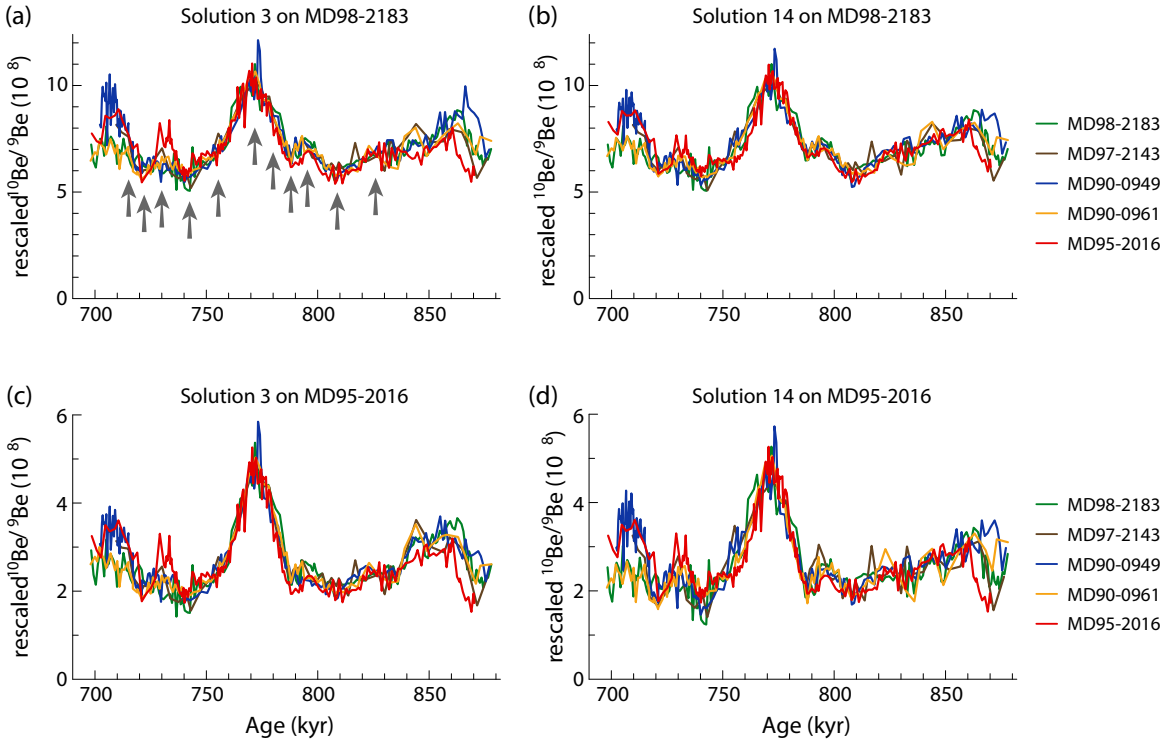

Figure 3.7: $^{10}Be/^{9}Be$ profiles rescaled according to eq. (3.11-3.12) and the climatic function of Fig. 3.6b to match the records of MD98-2183 **(a-b)** and MD95-2016 **(c-d)** for two of the 14 solutions that minimize the mean squared differences between rescaled profiles.

A stack for the given reference core is then constructed by averaging the rescaled records. This operation reduces the random scatter produced by noise and local environmental effects unaccountable by the common climate signal S, as seen by the relative smoothness of the stacks in Fig. 3.8. Finally, the stack obtained for the given reference core is rescaled to match each of the other four cores, producing a set of reconstructed records whose differences are entirely explainable by the climatic modulation model described above. Any systematic residual between measured and reconstructed records represents an environmental modulation of the

cosmogenic ^{10}Be production rate that does not correlate with the chosen proxy of the global climate signal. The residuals generated by all solutions are smaller, on average, than noise contributions in individual records, meaning that these solutions provide a mathematically adequate representation of environmental modulation differences between the five records. This result validates the initial assumption that environmentally-driven differences between records can be almost entirely explained by global climatic variations recorded by benthic δ^{18}O.

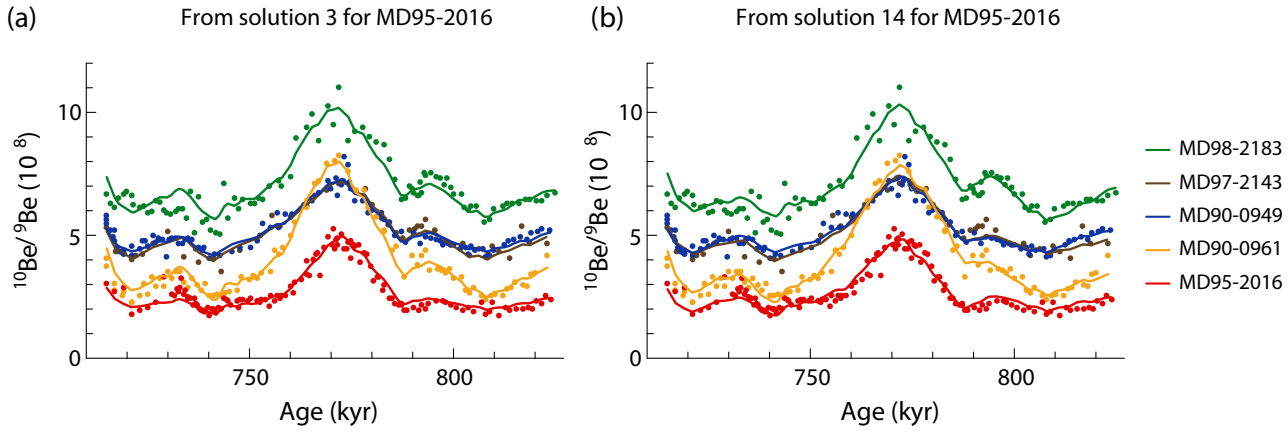

Figure 3.8: ^{10}Be/^{9}Be measurements (dots), and profiles reconstructed from solution 3 **(a)** and 14 **(b)**. The reconstruction involves two steps: first, all profiles are rescaled with eq. (3.11) to match MD95-2016 and a stack is created (continuous lines). This stack is then rescaled to match each of the five records, using the inverse transformation given by eq. (3.12). All differences between reconstructed records are entirely controlled by the climatic signal $S(t)$ and the model parameters.

The obtained solutions can be divided into three main groups with distinct time dependencies of A_{ij} and B_{ij}. The first group (Fig. 3.9a) is characterised by unrealistically large, strongly anti-correlated time variations of A_{ij} and B_{ij}. An implausibly fine-tuned cancellation of the opposite trends produced by the additive and multiplicative coefficients yields an environmental modulation that is very dissimilar to $S(t)$. A strong correlation between A_{ij} and B_{ij} is not expected, because of the different physical origin of additive and multiplicative environmental effects. This group of solutions is therefore discarded. Additive and multiplicative coefficients of the second solution group display much smaller temporal variations, with all A_{ij} being in-phase with S, and all B_{ij} being lagged by 25-30 kyr (Fig. 3.9b). The combined effect of additive and multiplicative coefficients result in an oscillatory modulation of all records relative to the North Atlantic core MD95-2016, whose ~40 kyr main period does not reflect glacial-interglacial cycles. Finally, the third solution group is characterised by nearly constant additive coefficients (with the moderate exception of core MD90-0961),

while the multiplicative coefficients generate small temporal variations that are in-phase with respect to S (Fig. 3.9c). The second and third solution groups predict environmental effects of similar amplitudes but different dependencies on glacial-interglacial cycles. Both groups indicate that the environmental modulation of the Atlantic core MD95-2016 is systematically different from that of the other cores, because of the similar time dependences of all B_{ij} with respect to MD95-2016.

The large temporal offset of the multiplicative coefficients of the second solution group with respect to δ^{18}O implies a ~28 kyr-delayed response to the MIS 20 glaciation, which is difficult to explain. For instance, numerical oceanic circulation models predict a maximum lag of ~10 kyr for the Atlantic Ocean thermohaline circulation with respect to precession and obliquity bands (Tuenter et al., 2005). Furthermore, the relatively large temporal modulation of the additive coefficients implies that recycled ^{10}Be inputs at the MD95-2016 site increased during the MIS 20 glacial, relative to the other cores. There are two likely sources of recycled ^{10}Be in the North Atlantic: (1) meltwater impulses from large ice-sheets (e.g. Simon et al., 2016) and (2) the Antarctic Bottom Water (AABW), which might have been enriched with diagenetic ^{10}Be releases from the seafloor. In the first case, Be recycling is expected to occur after termination 19. In the second case, the northern AABW limit is expected to expand during glacial times (Ferrari et al., 2014), but not as far as to reach the MD95-2016 site if the last glacial maximum (LGM) is used as a MIS 20 analogue (Seidov et al., 1996; Paul and Schäfer-Neth, 2003). Therefore, the environmental modulation predicted by the second solution group is also implausible, leaving the third group as the only candidate with a physical meaning.

3.5.3 Solution evaluation

Plausible solutions of our model (Fig. 3.9c) yield multiplicative environmental modulations that depend on glacial-interglacial cycles, with all cores showing very similar temporal changes relative to the North Atlantic site MD95-2016. These changes can be explained by a ^{10}Be concentration increase or a diagenetic ^{9}Be concentration decrease in MD95-2016, relative to all other cores, during the MIS 20 glaciation. Global oceanic circulation models (Seidov et al., 1996; Paul and Schäfer-Neth, 2003) indicate that MD95-2016 is located close to northern limit an anticlockwise gyre fed by the North Atlantic Drift (NAD). A sediment particle sinking at the MD95-2016 site would first cross this gyre and then its return path feeding the North Atlantic deep water (NADW). The isotopic ratio of this conveyor belt current system is dominated by the uptake of ^{10}Be-rich precipitations at mid-latitudes, along the western North Atlantic path of the Gulf stream (Heikkilä and Smith, 2013; Cao et al., 2019). Little or no currents are predicted at this site below ~2 km depth, so that the NAD can be regarded as the main source of non-recycled ^{10}Be.

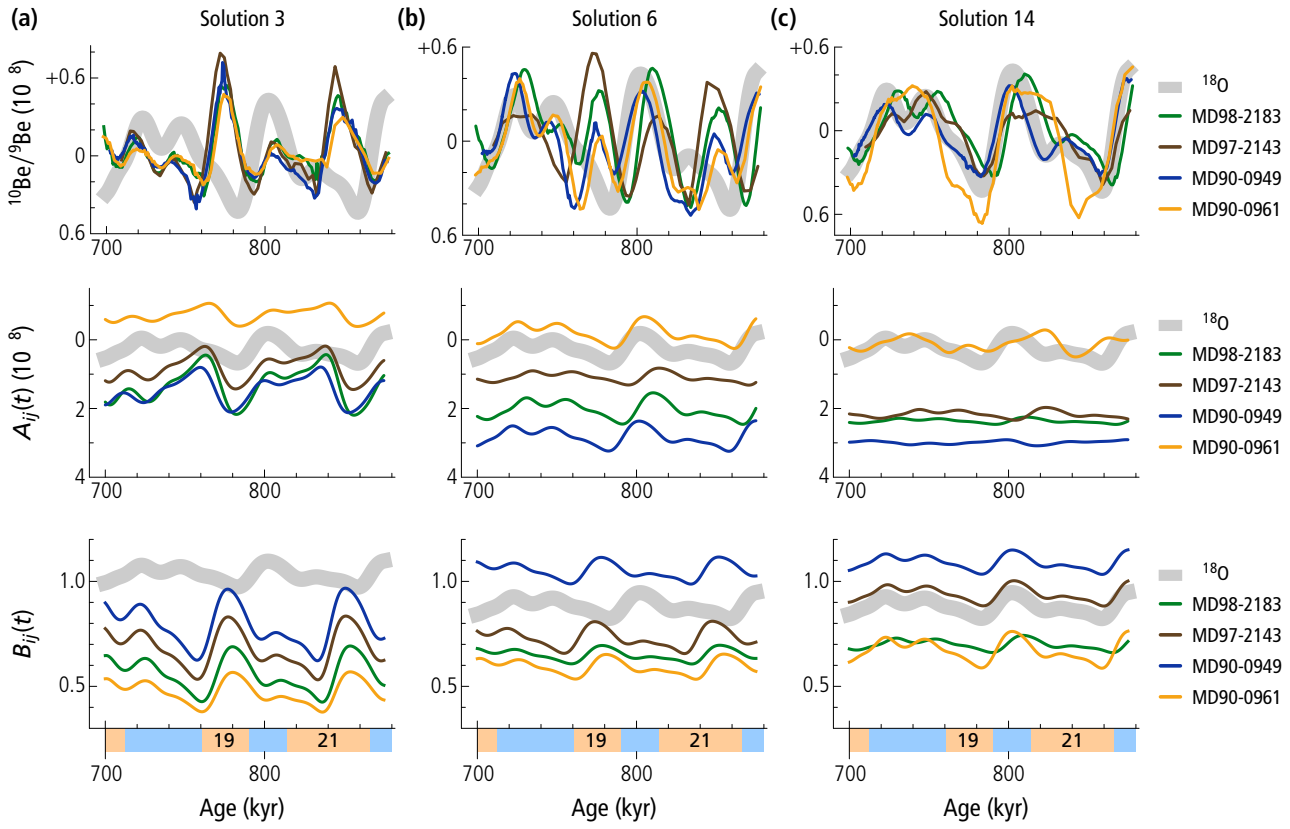

Figure 3.9: Total (first row), additive (second row) and multiplicative (third row) environmental modulation of $^{10}Be/^{9}Be$ relative to MD95-2016, predicted by representative examples **(a-c)** of three different groups of almost identical solutions obtained from different initial values. Additive and multiplicative modulations are defined by the coefficients A_{ij} and B_{ij}, with i corresponding to MD95-2016. The total modulation is defined as the difference between rescaled profiles obtained with original and time-averaged coefficients, respectively. A rescaled version of the climatic modulation function ($\delta^{18}O$) is shown with thick gray lines for comparison.

Following the scavenging model discussed in Section 3.5.1, we assume that the multiplicative environmental modulation of MD95-2016 is composed of an oceanic term is mainly controlled by the efficiency with which the NAD transports ^{10}Be from mid latitudes, and an atmospheric term mainly controlled by mid-latitude atmospheric precipitations over the Western Atlantic. Global oceanic circulation models suggest a slight decrease of superficial currents during the last glacial maximum (LGM) (Seidov et al., 1996; Paul and Schäfer-Neth, 2003). Moreover, mid-latitude precipitations over the NW Atlantic are also predicted to decrease during glacials (Cao et al., 2019), so that a decrease of dissolved ^{10}Be concentration is expected during the MIS 20 glaciation at the MD95-2016 site. This contradicts the trend suggested by the B_{ij} coefficients, unless it is assumed that a similar, but stronger modulation occurs in the other cores. On the other hand, less chemical weathering, and therefore less diagenetic ^{9}Be

production is expected during glacial times at high latitudes. Caution should be used with the identification of sedimentary ^{9}Be concentrations (Fig. 3.2b) with dissolved values, because of possible variations caused by changes of the scavenging efficiency or by the change of ^{9}Be source delivery. Nevertheless, MD95-2016 is affected by the largest ^{9}Be variations, with a marked drop at ~780 ka, just before the MIS 20 termination. It is, therefore, possible that the distinct climatic modulation of ^{10}Be/^{9}Be at MD95-2016 is due to relatively large ^{9}Be input variations that are negatively correlated with benthic δ^{18}O (Fig. 3.2).

As far as the additive coefficients are concerned, the third solution group (Fig. 3.9c) predicts large, almost constant differences between cores, which can be effectively regarded as fixed, site-specific offsets. All coefficients are negative with respect to MD95-2016, which means that MD95-2016 has the smallest absolute offset. This offset is in fact negligible, because the maximum ^{10}Be/^{9}Be increase of MD95-2016 during the M-B reversal is only slightly smaller than the ~2.2× maximum increase predicted by cosmogenic production models for the disappearance of the dipole field (Heikkilä et al., 2009; Poulianov et al., 2016; Simon et al., 2018b). Accordingly, the coefficients $-A_{5,j}$ (Table 3.2) can be identified with the absolute offset of each site. The most affected core is MD90-0949 with an offset of ~3×10^{-8}, corresponding to ~60% of the average ^{10}Be/^{9}Be level outside the M-B reversal. A similar offset is obtained for MD97-2143, while MD90-0961 has only a small offset, which, however, is less constant in time. Overall, 40-60% of the isotopic ratio of three cores from the Pacific and the Indian Ocean is controlled by a constant ^{10}Be input unrelated to the cosmogenic production rate. As discussed in Section 3.5.1, constant offsets can be subtracted without altering the production rate-dependent component of ^{10}Be/^{9}Be records. Beryllium release at the ocean floor is the only plausible source of the observed offsets, because the release rate is not expected to depend on climate variations, and the depth interval affected by diagenesis is probably large enough to mix Be isotopes with very different ages.

The above discussion shows the complexity of the environmental modulation of beryllium records. Site-specific differences are controlled by additive and multiplicative processes. The additive component is relatively constant in time, so that the environmental modulation of ^{10}Be/^{9}Be records depends ultimately on the product of atmospheric and oceanic scavenging efficiencies, with the latter being controlled by sedimentary fluxes and oceanic circulation patterns. Accordingly, atmospheric and oceanic responses to solar forcing are combined in a multiplicative manner. Oceanic convection is most sensitive to obliquity (~40 kyr cycles) and rectified precessional forcing (~20 kyr cycles), while the atmosphere is controlled by the net radiation, with the most power in the obliquity and eccentricity bands (~100 and ~400 kyr cycles) (Brickman et al., 1999; Antico et al., 2010; Schmittner and Clement, 2002). Contributions from the ~20 kyr band could be responsible for the residual discrepancies between rescaled ^{10}Be/^{9}Be records at 700-740 kyr and 860-880 kyr (Fig. 3.7). We limit the remaining discussion of model results to site-specific effects, which are summarized by the time averages of A_{ij} and B_{ij} coefficients. The time-averaged coefficients of the second

and third solution group are very similar, so that conclusions are not affected by solution multiplicity.

3.6 Discussion

The environmental modulation model of section 3.5 provides unique information about the main factors affecting the ratio of authigenic Be isotopes in sedimentary records. We begin with a comparison of mean $^{10}Be/^{9}Be$ values during periods of normal dipole strength before and after the M-B reversal on the one hand, and $^{10}Be/^{9}Be$ values calculated from a model of the modern atmospheric flux (Heikkilä and Smith, 2013) on the other (Fig. 3.10a). For this purpose, the atmospheric ^{10}Be flux at each core site has been normalized by the sedimentary ^{9}Be flux calculated from measured concentrations. Global mass balance models for the ratio R_{d} of dissolved isotopes (eq. 3.6) predict no relation with the atmosphere, since the atmospheric input gets completely mixed in the oceans. A 1:1 relation with atmospheric fluxes would be expected for a still water column with no lateral mixing and no riverine inputs. This relation holds well for the Atlantic and Indian Ocean cores; however, it disappears when $^{10}Be/^{9}Be$ values are corrected for recycled contributions using the additive coefficients of the climatic modulation model of Section 3.5.2 (Fig. 3.10b). This is expected, given the important role played by lateral transport of beryllium (Chase et al., 2002). On the other hand, a well-defined proportionality relation exists between sedimentary $^{10}Be/^{9}Be$ and isotopic ratios at the surface of ferromanganese crusts closest to the core sites (Fig. 3.10c), which are representative for the long-term average composition of deep waters (von Blanckenburg et al., 1996). Our sedimentary ratios are smaller than those of ferromanganese crusts by a factor of ~2, in contrast with the good agreement between crusts and surface sediments from the same sites (Bourlès et al., 1989a). We tentatively explain this discrepancy by the fact that most authigenic Be from the sites where ferromanganese crusts were collected was scavenged at the ocean bottom by the long exposure of Fe and Mn minerals to bottom waters with elevated isotopic ratios (Bourlès et al., 1989a). The more rapid sediment burial at sites with normal sedimentation rates, on the other hand, ensures that Be scavenging is more evenly distributed throughout the water column.

A significant part of the isotopic ratio is controlled by recycled Be sources during periods of normal dipole strength, as demonstrated by the additive component of the environmental modulation of each core relative to MD95-2016. This component correlates positively with ferromanganese $^{10}Be/^{9}Be$ values (Fig. 3.10e) and negatively with the sedimentary ^{9}Be flux (Fig. 3.10f), albeit only at a 85% confidence level. Furthermore, a step-like increase occurs at water depths comprised between 2.5 and 3 km (Fig. 3.10d), where ocean water reaches its maximum age (Koeve et al., 2015).

These trends point to a deep source of recycled Be, which accumulates in old waters, which explains the positive correlation with ferromanganese crusts and water depth. Recycled

Be is diluted by the incoming fluxes of freshly scavenged isotopes, which explains the negative correlation with the sedimentary ^{9}Be flux. The lack of recycled ^{10}Be inputs from ice-sheet melting in the North Atlantic site MD95-2016, contrary to the case of more closed basins such as Baffin Bay (Simon et al., 2016), restricts possible open basin recycling sources to compaction-driven pore water expulsion at the ocean bottom. In analogy with the laboratory protocols used for the extraction of exchangeable Be, the conterflux of porewaters with elevated salinity (e. g. Scholz et al., 2013) can remove small quantities of the exchangeable phase without significant alteration of the bulk sedimentary ^{10}Be/^{9}Be ratio. Biogenic silica dissolution is another possible source of porewater Be (Willey, 1978; Dixit et al., 2001), what is suggested by the strong correlation between Be and Si values in the pore-water (Bourlès et al., 1989ab). The rate of silica dissolution in sediment is highly variable and depends on the degree of the undersaturation of pore waters, differences in specific surface area and soluble aluminium concentration (Dixit et al., 2001). The incorporation of Al(III) in silica lattice was shown to have a significant impact on dissolution/re-precipitation rate of biogenic silica, emphasising that depositional fluxes of detrital material within the sediment is the main environmental factor controlling the Si dissolution in all types of sediments (Van Cappellen, P. and Qiu, L.,1997; Van Cappellen et al., 2002; Khali et al.,2007). If the Be release in the porewater is indeed closely linked to the Si dissolution process, smaller relative contribution of recycled Be that is observed at the shallower sites could be explained in terms of higher sedimentary fluxes, providing greater detrital input. The partial removal of exchangeable Be from the whole sedimentary column generates a recycled Be flux that is controlled only by the compaction rate and by the average isotopic ratio of compacting sediment with a wide range of ages.

Multiplicative environmental effects are expressed by the inverse rescaling coefficients $1/B_{ij}$ required to create a common stack of M-B records that coincides with the chosen reference (Table 3.2; Fig. 3.10g-i). For instance, $1/B_{5,1} = 1.43$ means that ^{10}Be/^{9}Be variations measured at site 1 (MD98-2183), for instance during the M-B reversal, are 1.43 times larger than those measured at site 5 (MD95-2016). These coefficients form two homogeneous groups of mean values: the first group includes MD97-2143, MD90-0949, and MD95-2016, and the second group with ~45% higher values is composed by MD98-2183 and MD90-0961 (Fig. 3.10g). Relative variations of the multiplicative coefficients over time are limited to 10-13% in all cores, except for MD90-0961, where these variations reach 26%.

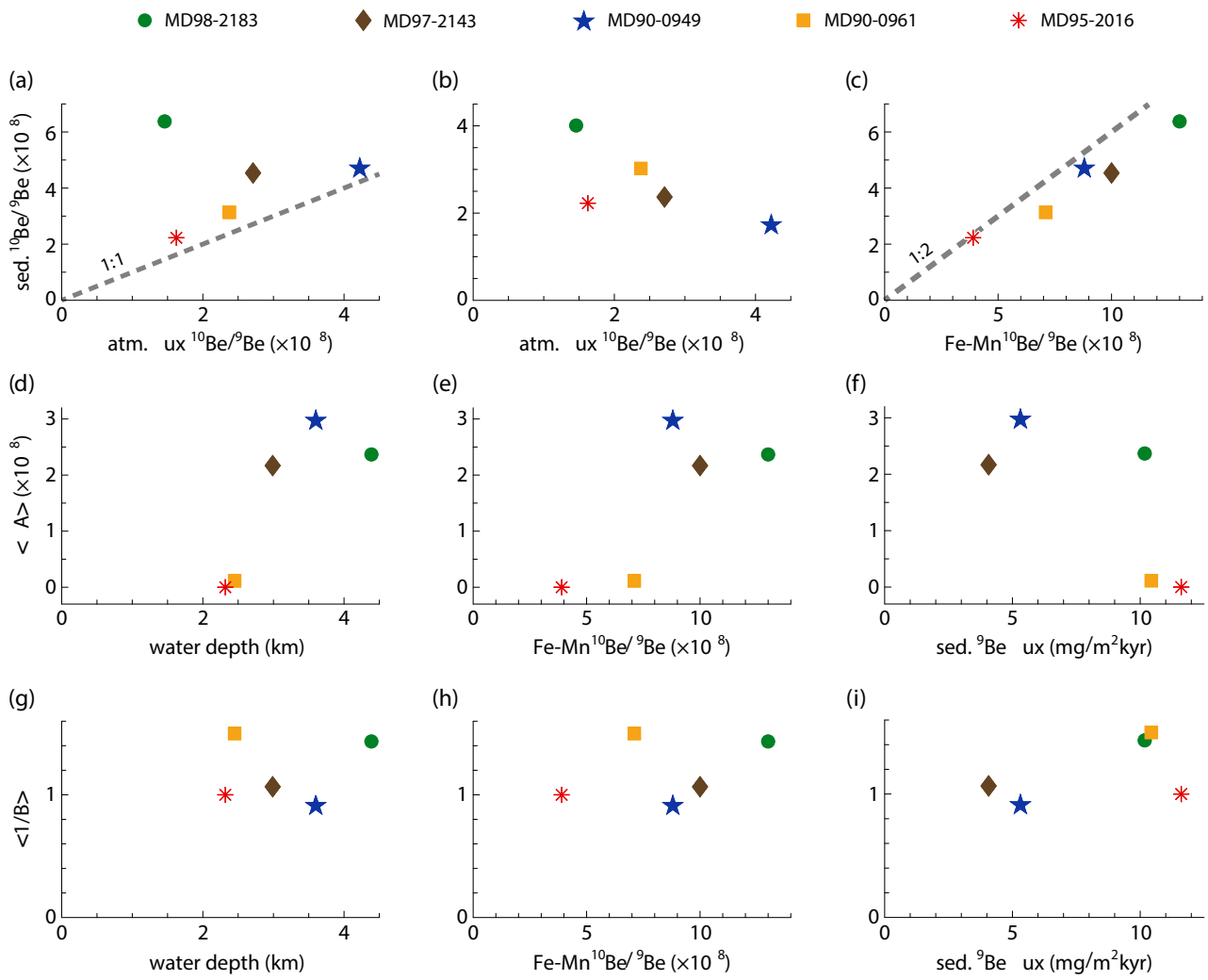

Figure 3.10: **(a)** Mean sedimentary $^{10}Be/^{9}Be$ before and after the M-B reversal (715-741 and 809-825 kyr) vs. values expected without oceanic circulation from present-day atmospheric ^{10}Be fluxes at the core sites (from Heikkilä and Smith, 2013), normalized by the sedimentary ^{9}Be flux. The dashed line is the 1:1 relation expected for a water column with no lateral mixing. **(b)** Same as (a), after subtracting the recycled Be contribution. **(c)** Mean sedimentary $^{10}Be/^{9}Be$ as in (a) vs. $^{10}Be/^{9}Be$ at the surface of ferromanganese crusts collected at the nearest sites (from von Blanckenburg et al., 1996). The dashed line indicates a 2:1 proportionality relation between ferromanganese crusts and sediment. **(d-f)** Mean additive climatic modulation coefficients relative to MD95-2016 (Table 3.2), vs. water depth, ferromanganese $^{10}Be/^{9}Be$ as in (b), and sedimentary ^{9}Be flux (as ^{9}Be concentration, multiplied by burial rate and sediment density, assuming 2.3 g/cm^{3} for solids and a volume fraction of 0.6). **(g-i)** Mean of inverse multiplicative climatic modulation coefficients with respect to MD95-2016 (Table 3.2) vs. the same parameters as in (d-f).

This means that the multiplicative modulation of $^{10}Be/^{9}Be$ is site-specific with limited, but non-negligible variations over time. It does not reflect geographic provenance (as seen by the difference between the two Indian Ocean cores), nor other site-specific characteristics such as water depth (Fig. 3.10g), the long-term average ratio of dissolved Be (Fig. 3.10h), or the ^{9}Be flux (Fig. 3.10i). Instead, it appears to be related to oceanic circulation, since the two sites with the largest multiplicative coefficients are located on the pathway of large conveyor belt circulation systems. Specifically, MD98-2183 is located underneath a turning point of the Minadao/New Guinea Coastal current, which is characterised by large vertically integrated fluxes of ~100 m^2/s and ~50 m^2/s above and below 300 m water depth, respectively (Wijeratne et al., 2018), while MD90-0961 is affected by the monsoon-driven East and West Indian Coastal Currents flowing between the Lakshadweep Islands and the Maldives archipelago (Schott et al., 2009; de Vos et al., 2014). Conveyor circulation systems intercept the incoming authigenic Be flux from large areas (Nooteboom et al., 2019), and continuing particle scavenging from surface waters and regeneration in deeper parts of the water column causes the concentrations of both Be isotopes to increase along the advective flow lines (Measures et al., 1996). The resulting increase in dissolved Be has been observed, for instance, along current paths running from the N Atlantic surface (30 ppb), to the deep N Atlantic (60 ppb), the deep S Atlantic (70 ppb), the circumpolar deep Pacific (90 ppb), and the surface Pacific (100-300 ppb) (Kusakabe et al., 1990; Ku et al., 1990). The preferential ^{10}Be enrichment can be explained by the surficial segments of these large current systems flowing at great distances from the coast, where terrestrial ^{9}Be inputs are minimal.

The temporal variability of environmental effects is inversely proportional to the distance from the coast (Fig. 3.11). Core MD90-0961, located only ~38 km offshore the closest island of the Maldives atoll, is the most affected. Two mechanisms can explain the effect of coast proximity on multiplicative climatic modulations: (1) boundary scavenging, which depends on sediment flux (Anderson, 1990), (2) atmospheric scavenging, which is controlled by rainfall, with glacial-interglacial differences showing prominent coastal effects (Cao et al., 2019), and (3) boundary effects on the surface-bottom transportation matrix representing the path of settling particles (Nooteboom et al., 2019). The relation between coast proximity and recycled Be fluxes is more difficult to explain. This relation depends essentially on a single large value corresponding to MD90-0961. Given the proximity of MD90-0961 to the Maldives and the capacity of corals to incorporate dissolved Be in their lattice structure (Lal et al., 2005), coral dissolution during sea level changes represents a possible source of episodic recycled Be inputs. The dissolution of coral carbonates is promoted by ocean acidification (Hoegh-Guldberg et al., 2007; Anderson et Gledhill, 2013; Cyronak et al., 2016), which is expected mostly during interglacials (Anderson and Archer, 2002). Indeed, the additive coefficient of MD90-0961 becomes more negative during the MIS 19 and 21 intergacials (Fig. 3.9c), pointing to higher recycled ^{10}Be fluxes.

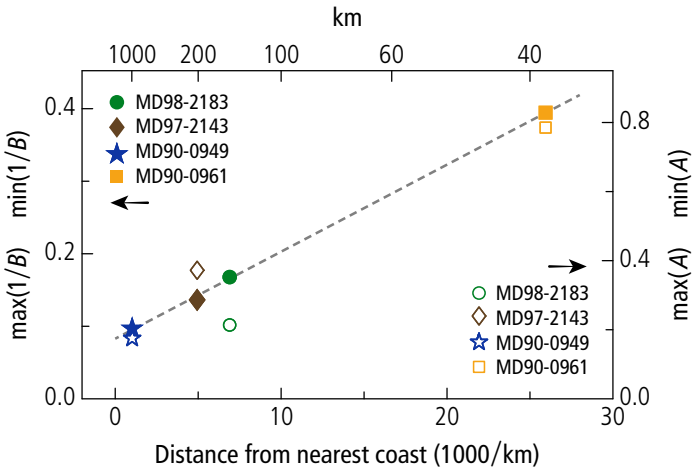

Figure 3.11: Maximum temporal changes of additive (A_{ij}) and multiplicative (B_{ij}) climatic modulation coefficients with respect to core MD95-2016 (Table 3.2), vs. inverse distance from the nearest coast. The dashed line is a linear fit for the multiplicative coefficients.

Be records of the M-B reversal obtained from continental shallow shelf/slope settings with very large sedimentation rates provide a useful term of comparison for the additive and multipicative environmental effects discussed above. For instance, the Montalbano Jonico marine succession from the semi-enclosed Mediterranean basin ($v_{\mathrm{sed}} \approx 80\ \mathrm{cm/ka}$) is characterized by much lower $^{10}Be/^{9}Be$ values (Simon et al., 2017), with a 754-766 kyr and 790-800 kyr mean of ~0.32×10^{-8} outside the transition, and a ~0.58×10^{-8} peak at 774 kyr during the transition. Both the average and the peak values are 7-8 times smaller than those of MD95-2016, which means that the two records are roughly proportional to each other, as expected in case of negligible offsets. The large proportionality factor can be explained by the combined effect of ~1.4 times larger and ~5 times smaller authigenic ^{9}Be and ^{10}Be concentrations, respectively. Another sequence with a similarly large sedimentation rate ($v_{\mathrm{sed}} \approx 50\ \mathrm{cm/ka}$) and shelf/slope setting (Chiba composite section, Simon et al., 2019) presents intermediate properties: average and peak $^{10}Be/^{9}Be$ values ~1.8-1.9 times smaller than MD95-2016. The proportionality factor results from ~1.2 and ~2.1 times smaller authigenic ^{9}Be and ^{10}Be concentrations, respectively. The different ^{10}Be concentrations and $^{10}Be/^{9}Be$ ratios of the Montalbano and Chiba sections can be explained by the latter being situated along the large Kuroshio current in the East China Sea, fed by the North Equatorial Current (Gallagher et al., 2015). Contrary to the case of the semi-enclosed Mediterranean basin, this large current system intercepts atmospheric ^{10}Be far from continental ^{9}Be sources. Foraminiferal proxies suggest an eastward deflection of the Kuroshio current during the last glacial maximum. A glacial current shift might explain the lower MIS20 $^{10}Be/^{9}Be$ values of the Chiba composite section with respect to a $^{10}Be/^{9}Be$ stack (Simon et al., 2019). Finally, the absence of significant offsets in the Montalbano and Chiba sections confirm the pelagic origin of recycled Be sources.

3.7 Conclusions

Detailed sedimentary records of authigenic ^{10}Be and ^{9}Be during the last geomagnetic reversal at five sites from the North Atlantic, Indian, and Pacific Oceans enabled us to test the consistency of the ^{10}Be/^{9}Be ratio as a proxy for the global ^{10}Be production rate. Relative differences between records can be explained by a linear relationship between global ^{10}Be production rate and authigenic ^{10}Be/^{9}Be, instead of the direct proportionality predicted by simple models of ^{10}Be transport and scavenging underlying current reconstructions of the geomagnetic dipole moment. The additive and multiplicative coefficients associated with this linear response are site-specific and time-dependent. A detailed investigation of the dependence of both isotope concentrations on the calcium carbonate content of sediment, which is one of the major factors affecting the scavenging efficiency, permits to exclude ^{10}Be/^{9}Be artefacts related to sediment composition.

A simple coupled model for ^{10}Be mass balance and scavenging has been used to confirm that the ^{10}Be/^{9}Be response can be represented by a linear function with climate-dependent additive and multiplicative terms. Non-zero additive terms reflect ^{10}Be inputs from sources with residence times significantly larger than the time period under consideration (Be-recycling). Multiplicative terms reflect the efficiency of atmospheric and oceanic Be scavenging, which are in turn controlled by precipitation, sediment fluxes, and oceanic circulation. While it is not possible to reconstruct these coefficients at each site without an independent knowledge of the global ^{10}Be production rate, it is possible to obtain solutions for relative record differences, provided that all records share a common period of time with large geomagnetic variations (in our case the M-B reversal), which is long enough to capture a full glacial-interglacial cycle. For this purpose, additive and multiplicative terms are assumed to be functions of a common global climatic signal, which we identified with the benthic δ^{18}O record of two cores. If environmental modulation effects are sufficiently small, the climatic dependence can be linearised, obtaining a solvable set of equations. The resulting solutions lead to the following conclusions:

1. Additive environmental effects are relatively large, accounting for up to ~60% of the average ^{10}Be/^{9}Be level outside the M-B reversal, with little variations over time, except for one site located near the Maldives. They thus represent a site-specific, constant offset that can be subtracted if the solution set includes at least one core that is negligibly affected. Corrected records are proportional to the global ^{10}Be production rate, as required by reconstructions of the geomagnetic dipole strength. Offsets are produced by the release of recycled beryllium at the ocean floor, through a constant flux of pore water carrying a small fraction of exchangeable Be removed from the sediment. The recycled Be flux is unaffected by climate, and the large range of involved sediment ages yields a homogeneous isotopic ratio, explaining the lack of time variations. We did not find evidences for post-glacial ice melting at the North Atlantic

site, but variable additive contributions have been detected at the Maldives site, presumably fed by coral reef dissolution.

2. Offsets display a step-like dependence on water depth, with a relatively sharp threshold of 2.8 km. This means that recycled Be inputs are confined to deep, old waters that are poorly mixed with overlying masses.

3. Multiplicative environmental effects are site-specific and reflect mainly glacial-interglacial cycles. The Indian and Pacific Ocean cores display a common modulation with respect to the North Atlantic: the difference between these two groups of records oscillates with a maximum amplitude of $\pm$10-15% relative to the maximum $^{10}Be/^{9}Be$ increase during the M-B reversal. This amplitude is sufficiently large to mask minor dipole moment variations during stable polarity periods. Because of the lack of an absolute reference for the ^{10}Be production rate, it is not possible to obtain absolute estimates of the multiplicative modulation at each site. Glacial-interglacial changes of atmospheric precipitation, sediment delivery, and oceanic scavenging efficiency are expected to occur in the North Atlantic and in the other basins, so that it is not possible to choose a reference record with minimal environmental effects. Time averages of the multiplicative coefficients represent the total site-specific ^{10}Be scavenging efficiency. Maximum differences between records amount to ~40%. These differences do not depend on water depth, sedimentation rate, or ^{9}Be fluxes. The main controlling factor appears to be the location along the path of large oceanic circulation systems, which selectively intercept the atmospheric ^{10}Be flux. Continuing particle scavenging from surface waters and regeneration in deeper parts of the water column causes the concentrations of both Be isotopes to increase along the advective flow lines. The preferential ^{10}Be enrichment comes from the surficial segments of these large current systems flowing at great distances from the coast, where terrestrial ^{9}Be inputs are minimal.

4. The environmental modulation amplitude is inversely related to the distance from the coast, with largest effects observed for a core located just ~38 km offshore the closest island of the Maldives atoll. Coastal amplification of climatic effects can be explained by boundary scavenging, and by the enhanced sensitivity of atmospheric scavenging and the surface-bottom transportation matrix on coastal proximity.

While the observed environmental contamination of $^{10}Be/^{9}Be$ records does not prevent stratigraphic recognition of large ^{10}Be increase episodes, geomagnetic dipole moment reconstructions can benefit in several ways from the climatic modulation information gained with our modelling approach. First, a sufficiently diverse set of core locations likely contains at least one $^{10}Be/^{9}Be$ record with optimal properties that can serve as a reference. These optimal properties are: (1) negligible Be-recycling contributions, which restores the required proportionality with the global atmospheric ^{10}Be production rate, and (2) minimum climatic modulation, as far as it can be determined from relative comparisons between records. Such conditions are most likely encountered in open basins at sites (1) with <2.8 km water depth, (2) >200 km offshore, and (3) located underneath a large current system extending over regions

with minimum terrigenous inputs. Scaling all records on the chosen reference enables us to produce a $^{10}Be/^{9}Be$ with reduced noise and artefact contributions. An example or artefacts isolated with our model is represented by incoherent short-term variations with typical periods of ~20 kyr, which are likely related to rectified precessional forcing of the oceanic circulation.

Acknowledgments This study was supported by the ERC advanced grant to JPV "GA 339899-EDIFICE" under the ERC's 7th Framework Program (FR7-IDEAS-ERC). The ASTER AMS facility is supported by INSU/CNRS.

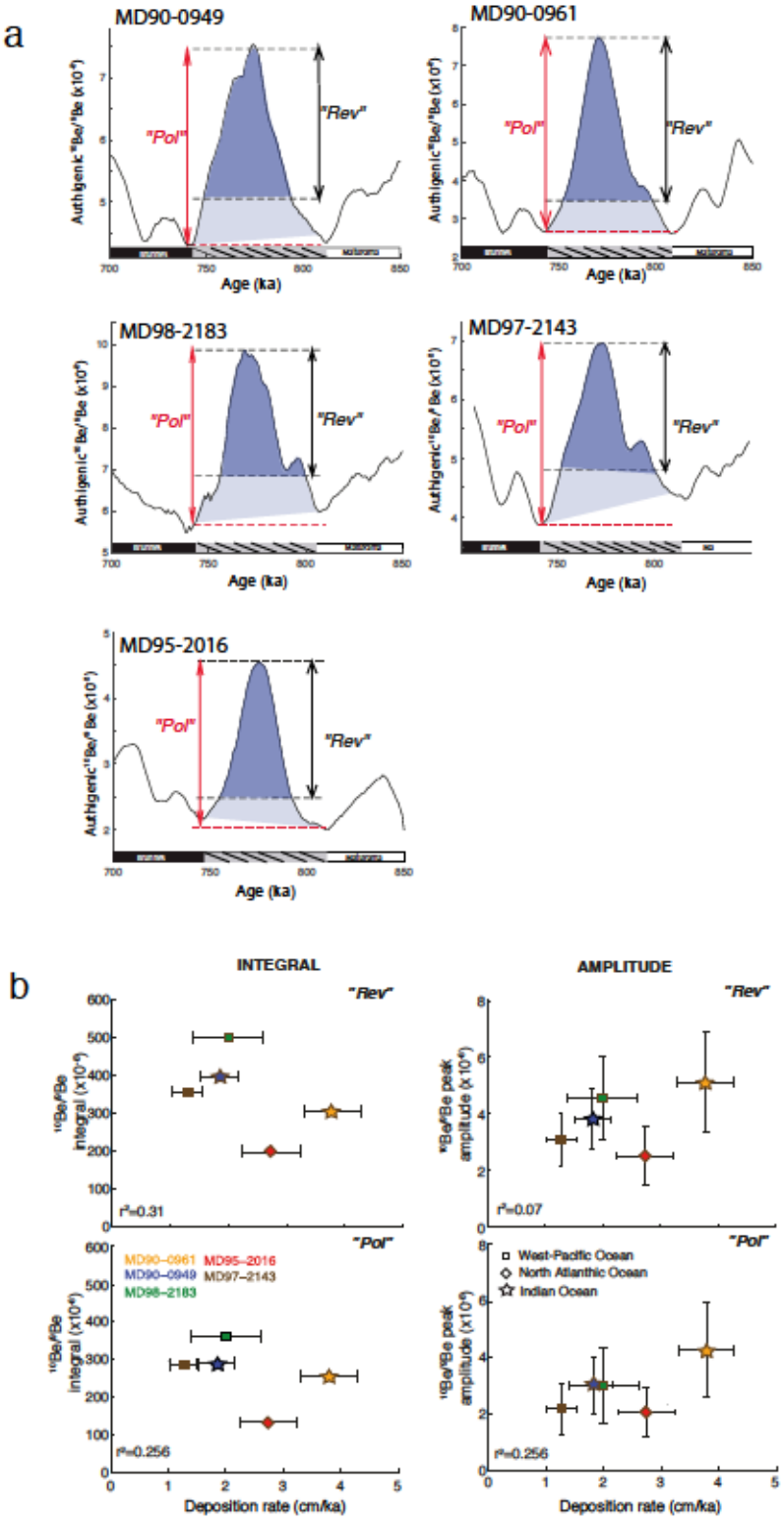

Figure 3.12: a) Be-ratio records spanning over the last geomagnetic reversal. The dashed lines indicate the 'Rev' and 'Pol' integration limits, that were used for Be-ratio integrals estimates over the M-B reversal. b) Comparison of cumulated Be-ratios and the amplitude of their enhancements estimated with "Pol" (lower right and left panels respectively), "Rev" baselines (upper right and left panels) with deposition rate.

core	$\mathbf{v_{sed}}$	$\mathbf{CaCO_3}$	**core depth**
	cm/ka	%	cm
MD98-2183	2±0.61	7.91±7.60	2980-3089
MD97-2143	1.2 ±0.26	18 ±6.39	1475 - 1634
MD90-0949	1.8±0.32	62.55±5.54	2022-2138
MD90-0961	3.8±0.49	63.93±2.68	3533-3800
MD95-2016	2.7±0.5	7.91±7.60	2997-3177

Table 3.1: Mean deposition rates (v_{sed}) deduced from the age model described in the section 3.2, mean $CaCO_3$ content, and variations measured within the indicated interval in the core.

index	**core**	$\langle -\boldsymbol{A} \rangle$	$\max(\delta \boldsymbol{A})$	$\langle 1/\boldsymbol{B} \rangle$	$\max(\delta(1/\boldsymbol{B}))$	$(^{10}\mathbf{Be}/^{9}\mathbf{Be})_{\mathrm{FeMn}}$	$(^{10}\mathbf{Be}/^{9}\mathbf{Be})_{\mathrm{at}}$
		10^{-8}	10^{-8}			10^{-8}	10^{-8}
1	MD98-2183	2.37	0.21	1.43	0.12	13.0	1.46
2	MD97-2143	2.17	0.37	1.07	0.13	10.0	2.71
3	MD90-0949	2.99	0.18	0.92	0.11	8.8	4.22
4	MD90-0961	0.11	0.79	1.50	0.26	7.1	2.38
5	MD95-2016	0.00	—	1.00	—	3.9	1.62

Table 3.2: Summary of model parameters corresponding to solution 14. A and B are the additive and multiplicative coefficients of eq. (3.11) with core MD95-2016 as a reference, and δA and δB the corresponding variations about the time averages $\langle A \rangle$ and $\langle B \rangle$, respectively. $^{10}Be/^{9}Be$ values at the surface of ferromanganese crusts collected at nearest sites (from Blackenburg et al., 1996) and $^{10}Be/^{9}Be$ values obtained by normalizing the modern atmospheric ^{10}Be flux at the core sites (from Heikkilä and Smith, 2013) with the sedimentary ^{9}Be flux for the same sites are listed for comparison.

Chapter 4

Comparison of relative paleointensity and cosmogenic beryllium records over the last 1100 ka

4.1 Introduction

Marine sedimentary sequences provide continuous records of paleomagnetic field variations through the analysis of the natural remanent magnetization acquired by magnetic minerals (e.g. relative paleointensity) and the concentration of cosmogenic isotopes, such as ^{10}Be, whose production by cosmic ray spallation is modulated by the intensity of the Earth's field. Sedimentary paleomagnetic records provide directional information about the local field at the site, as well as a measure of relative field intensity variations (relative paleointensity, RPI), which need to be calibrated with absolute field intensity records from rocks. Cosmogenic isotopes provide a global measure of the screening efficiency of the Earth's magnetic field against cosmic radiation, which depends essentially on the strength of the dipole component (see Chapter 1). Because of the dominance of the dipole component, the local RPI records and the "global" ^{10}Be record are expected to display similar variations in response to changes in the Earth's magnetic field, up to a field geometry factor related to Gauss coefficients of higher order (quadrupole, octupole, etc.). At the same time, both types of sedimentary records are affected by several additional processes ultimately related to the local and global environment: these include changes in sediment transport, lithology, mineralogy, and post-depositionary processes. Normalization of the natural remanent magnetization (NRM) with a properly chosen laboratory magnetization for RPI calculations, and normalization of ^{10}Be with the stable ^{9}Be isotope remove the effects of magnetic mineral concentration and Be scavenging efficiency variations. These corrections, however, do not remove RPI artifacts related to changes in the magnetic mineralogy and to changes in the oceanic circulation pattern. Finally, bioturbation additionally affects the efficiency of the magnetic recording process, and the depths at which

the RPI and the ^{10}Be signals becomes locked. The latter produces a systematic delay of the RPI signal, which is also controlled by the environment.

Systematic comparisons between ^{10}Be/^{9}Be and RPI records in marine sediments show similar trends, especially during events involving a significant field intensity decrease (*Knudsen et al., 2008; Valet et al., 2014; Simon et al., 2019*), as well as important differences (*Carcaillet et al., 2003; Suganuma et al., 2011; Simon et al., 2018*) attributable to unremoved climatic contaminations. In this Chapter, differences between cosmogenic and magnetic recording processes will be closely examined using the RPI and ^{10}Be records of two sedimentary cores over the last 1100 ka: core MD98-2183 from the Western Pacific, and core MD95-2016 from the North Atlantic Ocean. This time interval contains several geomagnetic events characterized by a strong decrease of the dipole field, including the Matuyama-Brunhes (MB) reversal. During these events, the amplitude of geomagnetic variations is maximized with respect to environmental signal contaminations, enabling a precise comparison of the physical principles underlying the two recording processes and their dependence on post-depositional processes.

4.2 Geographical and geological settings

Core MD98-2183 (2° 00.82' N; 135° 01.26' E) was sampled by the R/V Marion-Dufresne in the West Caroline basin of the Western Pacific Ocean during the IMAGES IV cruise and consists of hemipelagic clay with calcareous and siliceous microfossils (*Yamazaki and Oda, 2004*). The basin is mainly influenced by nutrient supply from coastal regions in the Philippine and Indonesian Islands, while lithogenic inputs are dominated by clay minerals (*Kawahata et al., 1998*). The site is located on the path of the Equatorial counter current (surface/intermediate layer), which includes the west-east return current (*Tchernia 1980*), the Atlantic Intermediate waters and the Upper Circumpolar Deep Water. The deep-water circulation is dominated by the Lower Circumpolar Water that partially proceeds along the southern boundary of the east Caroline Basin, flowing northward in the western East Caroline Basin (*Kawabe et al., 2010*).

The second core, MD95-2016 consists of a mixture of silt clay and nano-ooze. It was taken during the IMAGES I leg IV campaign in the North Atlantic Ocean (57° 42.46' N; 29° 25.44' W) ∼800 km away from the coast on the crest of the Reykjanes Ridge located on the pathway of the Iceland-Scotland Overflow water (*Zou et al., 2017*), which plays an important role for sediment composition and redistribution (*Gehrke et al., 1996*). At these relatively high northern latitudes, the terrigenous input dominates during glacial periods in the northeast Atlantic Ocean. Turbidity currents, bottom currents, wind, and ice are potential carriers of detrital material from the continents (*Ruddiman and McIntyre, 1976*).

4.3 Relative Paleointensity

Paleomagnetic measurements were carried out on discrete samples (∼8 cm2) collected with a relatively high resolution (1 sample each 4 cm). Discrete samples were used in order to avoid the smoothing effects of on U-channels measurements, due to the wide response curves of the long core SQUID magnetometer. Moreover, this approach enables performing magnetic, geochemical and isotope measurements on the same specimens, ensuring the best possible stratigraphic match between magnetic and geochemical parameters.

The natural remanent magnetisation (NRM) of discrete specimens was stepwise demagnetized by alternating fields (AF) up to 90 mT in 5 mT increments. The characteristic remanent magnetization was isolated between 20 and 50 mT. Rock magnetic parameters, such as the acquisition curves of isothermal (IRM) and anhysteretic remanent (ARM) magnetizations and the corresponding median fields, indicate that magnetite is the dominant magnetization carrier. In this study, NRM intensity was normalized by the ARM acquired in a 80 mT AF field with a 0.05 mT DC bias, subsequently demagnetized with the same AF peak fields as the NRM. This normalisation removes the effects of varying magnetic mineral concnetrations, as long as the magnetic mineralogy does not change significantly. Relative paleointensity was derived from the slope of NRM versus ARM plots at successive AF demagnetization steps.

4.4 Beryllium measurements

Beryllium measurements used to produce Be records of the geomagnetic field include the cosmogenic isotope ^{10}Be and the stable isotope ^{9}Be used as a normalizer to compensate for changes in the scavenging efficiency. Samples for ^{10}Be and ^{9}Be measurements were proceeded according to the protocol described by *Bourlès et al., (1989)* and updated by *Simon et al., (2016)* at the CEREGE National Cosmogenic Nuclides Laboratory (Aix-En-Province, France). The ^{9}Be measurements were made using a graphite-furnace atomic absorption spectrophotometer (AAS), while ^{10}Be concentration measurements were performed at the French AMS national facility.

4.5 Identification of major paleomagnetic events over the last 1100 ka

Magnetic excursions are empirically defined as deviations of the virtual geomagnetic pole (VGP) from the geographic pole in excess of 40-45° (*Merrill and McFadden, 1994*). Such deviations are generally accompanied by a large decrease of the dipole component, and thus of the total field intensity. Several such excursions have been identified in sedimentary records from both hemispheres during the Brunhes chron (*Champion et al., 1988; Worm, 1997; Lund et al., 2001*). Because of the signal smoothing caused by bioturbation, the temporal resolution of the recorded events ultimately depends on the sedimentation rate (*Bard, 1987; Anderson,*

2001). Records from the sites with moderate (>10cm/kyr) to high (>20 cm/kyr) sedimentation rates fairly reproduce local magnetic field changes, but still contain smoothing artefacts (*Lund et al., 2006*). Smoothing becomes important at lower sedimentation rates, to the point of completely obscure the shortest event.

Published compilations of geomagnetic events identified by RPI (*Laj and Channel, 2007; Roberts, 2008*) and ^{10}Be/^{9}Be (*Simon et al., 2016*) are used here as reference for the identification of corresponding events in cores MD98-2183 and MD95-2016, using age models obtained by matching the glacial-interglacial cycles recorded by benthic (MD98-2183) and planktonic (MD95-2016) foraminifera with the orbitally tuned benthic isotope stack LR04 (*Lisciecki and Raymo, 2005*).

Several known excursions, such as 'Iceland Basin', 'Big Lost', 'Delta', as well as the M-B reversal, are recorded by RPI and ^{10}Be/^{9}Be in a similar manner in West-Pacific core MD98-2183 (Fig. 4.1a). Other events are missed or recorded differently by the two methods: for instance 'Blake'($\sim$130ka, 1000 cm) and 'Calabrian Ridge 0'($\sim$256ka, 1685 cm) excursions are not recorded by ^{10}Be/^{9}Be. In other cases, the relative intensity decreases during the same excursion differ significantly, such as for 'Laschamp'and 'Jaramillo'. The relative lag of intensity minima is also highly variable, ranging from $\sim$0 ('Delta') to thousands of years (M-B). Overall, 17 geomagnetic events have been selected for further analysis. Much less agreement between RPI and ^{10}Be/^{9}Be records is found for MD95-2016 (Fig. 4.1b), where discrete time intervals appear to be affected by different offsets (e.g. 0-80 and 180-250 ka). As discussed later, this core is affected by stronger climatic contaminations, due to the high latitude of the site. Only 7 geomagnetic events have been selected in this core.

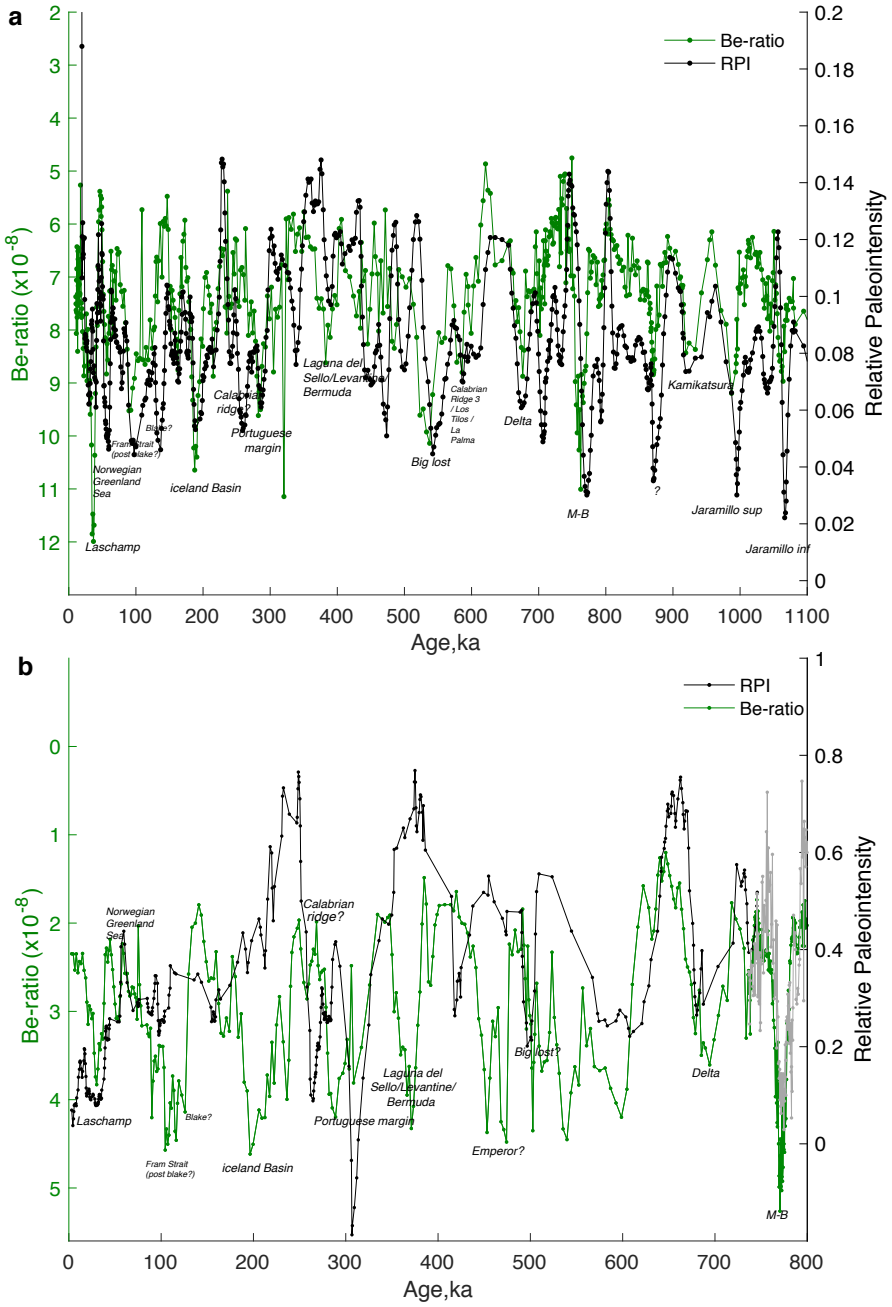

Figure 4.1: (a) RPI and ^{10}Be/^{9}Be records variations in a) West-Pacific core MD98-2183 over the last 1100 ka, and b) in North Atlantic core MD95-2016. The part of RPI curve highlighted by the gray colour corresponds to the Matuyama - Brunhes reversal period, that was sampled and measured with higher resolution rate, in comparison with the younger magnetic record (black curve). Noted geomagnetic events were identified from RPI and ^{10}Be/^{9}Be records based on *Laj and Channel, 2007; Roberts, 2008; Simon et al., 2016*.

4.6 Magnetic recording models in bioturbated sediment

As shown in Chapter 2, bioturbation, the physical reworking of sediment by benthic organisms, produces a significant redistribution of incoming matter, including cosmogenic isotopes and magnetic particles. Despite the common fate of ^{10}Be-carrying sediment particles and magnetic minerals, the effect of bioturbation on the corresponding field records is drastically different. In the case of cosmogenic isotopes, sediment mixing acts merely as a low-pass filter that attenuates rapid field variations, while the effect on magnetic particles is more profound, depending essentially on the final "freezing"of the particle's moment when entering the historical layer. The main outcome of this difference is that RPI records acquired in bioturbated sediment are systematically delayed with respect to the stratigraphic age, and thus also with respect to the ^{10}Be signal. Until present, the RPI recording process has been explained either by the alignment of magnetic particles or particle aggregates in the water column, in which case the magnetisation is instantaneously acquired during deposition, or by empirical models based on ad-hoc functions that describe the depth range where the orientation of magnetic minerals become locked (*Roberts et al., 2013*). Both acquisition models are completely disjoint from the bioturbation process, and for this reason they do not have predictive power.

A first step towards the explicit inclusion of bioturbation in RPI models has been recently made using a statistical description of particle orientation during diffusion in a surface mixed layer with generic properties (*Egli and Zhao, 2015*). Here, this model is extended to include more specific properties of bioturbation obtained from the tektite profile analysis performed in Chapter 2. This enables the construction of a model that explains the formation of ^{10}Be and RPI records in bioturbated sediment using a minimum set of assumptions. This model has predictive power and can be verified against actual records.

4.6.1 The effect of bioturbation on Be records

The physical reworking of sediment by benthic organisms is usually modelled by two types of sediment transport within the so-called surface mixed layer (SML): (1) advective transport, typically promoted by sediment feeders ingesting material at one depth and egesting it at a different depth (*Robbins, 1986*), and (2) diffusive transport associated with small-scale disturbances introduced by burrowing organisms (*Boudreau, 1986a*). Non-local (advective) transport models depend on poorly known, organism-specific parameters, such as burrowing depth, body size, and ingestion rates (*Shull, 2001; Meysman et al., 2003*), and are used only in forward models of bioturbation (*Boudreau et al., 2001*). In practice, most bioturbation models used to fit tracer concentrations assume a purely diffusive transport inside a homogenous SML of thickness L. *Goldberg and Koide (1962)* were the first to introduce the mixing model to explain the distribution of thorium and ionium isotopes in the pelagic sediments.

In the homogeneous diffusion model, the concentration C of a tracer (e.g. Beryllium) is governed by the diffusion equation

$$\frac{\partial C}{\partial t} = D\frac{\partial^2 C}{\partial z^2} - v_b\frac{\partial C}{\partial z}, \tag{4.1}$$

where $C(z,t)$ is the volumetric tracer concentration (cm^{-3}) depending on time t (kyr), and depth z (cm), D is the constant diffusion coefficient ($cm^2\ kyr^{-1}$) within the SML, and v_b the sedimentation rate ($cm\ kyr^{-1}$), with boundary condition

$$v_b C - D_t\frac{\partial C}{\partial z}\bigg|_{z=0} = \frac{1}{\phi_s \varrho_t}F_t(t) \tag{4.2}$$

at the sediment-water interface, where F is the tracer flux (e.g. the cosmogenic ^{10}Be input) (see Chapter 2 for a detailed treatment of the diffusion model and for the solution of eq. (4.1-2)). Long-term bioturbation effects converge to a diffusive model, except for systems heavily dominated by head-down feeders (*Boudreau and Imboden, 1987; Meysman et al., 2010; Reible and Mohanty, 2002*). Furthermore, the importance of nonlocal mixing decreases with increasing water depth (*Soetaert et al., 1996*), and increasing time integration (*Gerino et al., 1994; Aquino et al., 2017*). Diffusive models are based on fewer parameters that do not depend on the actual type of benthic fauna, and are therefore widely used to model radioactive (*Peng et al., 1979*) and stable (*Officer and Lynch, 1983*) tracer profiles.

From the point of view of individual tracer particles, bioturbation alters the deterministic age-depth relationship of undisturbed sediment (*Shull, 2009; Anderson, 2001*), with important consequences that are best understood by considering the two limit cases of an impulsive deposition event and stationary deposition. In case of an impulsive tracer input, individual particles will cross the SML at different times given by the first-passage of a biased random walk (*Wenocur,1987, Meysman et al., 2008*). The corresponding record that is formed in the historical layer, in form of a concentration profile, is spread over a range of depths, instead of a single depth represents the stratigraphic age of the event (*Guinasso and Schink, 1975*), and can be regarded as the impulse response of eq. (4.1-2). The lower limit of the concentration profile is associated with instantaneous delivery to the historical layer, while the mean depth

$$\langle z\rangle = \int_\infty^0 C(x,t)\mathrm{d}x \tag{4.3}$$

coincides with position predicted by the age-depth model in case of no bioturbation. The concentration profile thus evolves from a Dirac impulse if $D \to 0$ to an exponential function if $D \to \infty$, reflecting an increasing degree of smoothing introduced by diffusion. The length scale of profiles corresponding to the $D \to \infty$ limit is L, the thickness of the SML, with associated time constant L/v_b. Sediment mixing thus acts as a low-pass filter (*Schiffelbein,*

1984) by extending the input signal duration and reducing its amplitude, and by suppressing short-time variations (*Bard et al., 1987*).

In case of stationary deposition, a constant concentration profile is obtained, where the age of particles at any given depth is governed by a statistical distribution corresponding to the probability density function of the first-passage time across the SML, biased by the burial time between the bottom of the SML and the sediment horizon under consideration (*Lougheed et al., 2018*). The stationary case is highly relevant for sediment dating (see Chapter 2.8.7 for a discussion of the dating problem and age biases introduced by grain size segregation effects).

The above diffusive bioturbation model can be used to model the effect of bioturbation on sedimentary Be records of the Earth's magnetic field. In this case, ^{10}Be and ^{9}Be concentration profiles are given by the convolution

$$C_{\mathrm{Be}}(t) = \int_a^b I(t-\tau) F_{\mathrm{Be}}(\tau) d\tau \tag{4.4}$$

of the impulse response $I(t)$ obtained from the solution of eq. (4.1-2) with the incoming Be flux F_{Be} (see Chapter 2.8.5.2). In the ideal case of negligible environmental effects, F_{Be} is proportional to the geomagnetic response function $Q(M/M_0)$ of ^{10}Be production in the atmosphere, where $M = M(t)$ and $M_0 = M(t_0)$ are the dipole moments of the Earth magnetic field at time t and at a reference time for which the ^{10}Be production is modelled (usually modern times, *Masarik and Beer, 1999; Heikillä et al., 2013*). The geomagnetic response function might be conveniently approximated by

$$Q(x) = \left(\frac{\xi + 1}{\xi + x} \right)^q \tag{4.5}$$

with $x = M/M_0$, $M_0 \approx 7.8 \times 10^{22}$ Am^2, $\xi = 0.1774$, and $q = 0.529$.

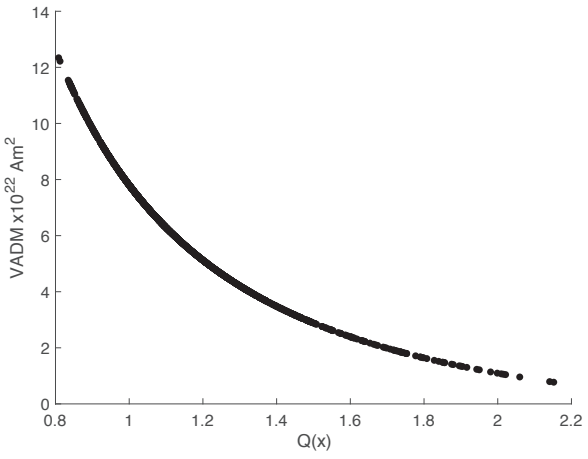

Figure 4.2: Virtual Axial Dipole Moment (VADM) corresponding to the ^{10}Be production rate Q, normalised by the modern production rate, as defined by eq. (4.5).

Bioturbation parameter estimates for sediment cores MD90-0961 and MD90-0949 have been obtained by fitting tektite profiles associated with the Australasian impact event at ≈ 788 ka (*Jourdan et al.,2019*). Such profiles correspond to a physical realisation of the impulse response function of bioturbated sediment, since the impact can be assumed produce a quasi-instantaneous delivery to the ocean floor, such that $F(t) = F_0\delta(t)$, where F_0 is the fluence, that is, the total amount of tektites deposited over time. Tektite counting profiles have been therefore fitted with the impulse response function obtained from the solution of eq. (4.1-2) (see chapter 2.9.1 and 2.10 for details). The resulting parameters (Table 4.1) have been used to simulate ^{10}Be records of geomagnetic events represented by a Gaussian drop of the dipole intensity over time intervals comprised between 743 kyr and 808 kyr (corresponding to the MB reversal). The impact of bioturbation on records the MB reversal is minimal (Fig. 2.7-8), owing to the relatively long duration of the field intensity minimum.

Core	L (cm)	D (cm^2/kyr)	F (tektites/g)	v_b (cm/kyr)
MD90-0961	14.7	55.7	282	3.8
MD90-0949	12.3	33.0	42.5	1.8

Table 4.1: Bioturbation parameters for a homogeneous SML obtained from fits of tektite profiles in cores MD90-0961 and MD90-0949 using eq. (4.1-2).

A major limitation of ^{10}Be records of short or weak geomagnetic events is represented by environmental modulations, which cannot be completely removed with ^{9}Be normalisation (see Chapter 3 and *Savranskaia et al., submitted*). In the case of M-B records, environmental effects account for 10-20 % of the full variation expected from the disappearance of the dipole moment, which means that environmental effects can be as large as the geomagnetic signal during minor geomagnetic events and during stable polarity intervals.

4.6.2 The effect of bioturbation on RPI records

Paleomagnetic records are based on the sediment magnetisation acquired through partial alignment of magnetic particles in the Earth's magnetic field. A straightforward representation of this mechanism exist for the so-called depositional remanent magnetisation (DRM), where the alignment of settling flocs containing magnetic particles occurs in the water column (*King, 1955; Nagata, 1961; Katari et al., 2000a; Katari and Bloxham, 2001; Carter-Stiglitz et al., 2006; Spassov and Valet, 2012*). In laboratory redeposition experiments, the high initial density of suspended sediment promotes the formation of a connected network of sediment particles during flocculation. The rigidity of this network increases until magnetic moments become blocked at a threshold concentration of $\sim$55% (*Valet et al., 2017*). The much lower concentration of suspended matter in typical oceanic settings leads to the formation of isolated flocs (*van Leussen, 1988*), which might possess a magnetic moment due to the inclusion of

magnetic particles. The magnetic torque exerted on the flocs by the Earth's magnetic field induces a progressive alignment of the magnetic moments against the viscous drag (*Yoshida and Katsura, 1985*), until the floc orientation becomes fixed upon hitting the sediment-water interface (*Jezek et al., 2012*). Owing to the partial alignment of the magnetic moments, a detrital remanent magnetization (DRM) is instantaneously acquired at the sediment-water interface (*Katari and Bloxham, 2001; Tauxe et al., 2006*). As noted by *Shcherbakov and Sycheva (2010)*, suspended flocs eventually become completely aligned with the Earth magnetic field at the infinite dilution limit, in which case the resulting DRM does no longer depend on the field intensity. Indeed, a progressive saturation of the DRM acquired in increasingly large fields has been observed in many redeposition experiments (e.g. *Katari and Bloxham, 2001*), violating the assumption of proportionality between field intensity and NRM required by RPI reconstructions.

The initially acquired DRM is progressively destroyed by the randomisation effects of bioturbation, if disturbances produces by benthic organisms last long enough to affect the entire sediment volume within the SML (*Verosub, 1977; Zhao et al., 2016*). Laboratory experiments are usually too short to capture a significant DRM decay (*Katari et al., 2000b*). DRM is also partially affected by compaction-induced changes in the sediment microstructure (*Irving and Major, 1964; Hamano, 1980; Otofuji and Sasajima, 1981; Anson and Kodama, 1987*). In the course of bioturbation- or compaction-induced plastic deformation of sediment, a certain fraction of magnetic particles might become free to rotate and align with the Earth magnetic field, acquiring what is termed a post-depositional detrital magnetisation (pDRM). The fraction of particles remobilized during compaction is small, as suggested by experiments where pDRM did not exceed $\sim$10% of the initial DRM (*Shcherbakov and Shcherbakova, 1987*), so that the contribution of compaction to pDRM acquisition is expected to be negligible.

The apparent age offset of paleomagnetic records is compatible with the existence of a fixed depth at which the sediment magnetization is apparently acquired (*DeMenocal et al., 1990; Glass et al., 1991*). Few available estimates of this so-called lock-in depth are comprised between $\sim$5 and $\sim$40 cm (*Glass et al., 1991; Lund and Keigwin, 1994; Meynadier and Valet, 1996; Channell and Guyodo, 2004; Sagnotti et al., 2005; Suganuma et al., 2010*). Lock-in depth estimates are very uncertain, as seen with two examples that are particularly relevant to this work, based on the comparison of paleomagnetic data with tektite profiles (*Glass et al., 1991*), and the cosmogenic ^{10}Be record of the MB reversal (*Suganuma et al., 2010*). In the first case, the stratigraphic depth of the tektite event has been determined by fitting tektite profiles with the impulse response of a homogeneous mixed layer as proposed by *Guinasso and Schink (1975)*. This correction is valid as long as tektites, which are significantly larger than sediment particles, are mixed in the same fashion the bulk sediment. However, as shown in Chapter 2, the mixing process appears to be strongly dependent on particle size, producing a vertical segregation that moves tektite profiles upwards with respect to coeval particles of the same size of sediment. This effect can add up to 5 cm to the $\sim$8 cm lock-in depth estimate of

Glass et al. (1991). The comparison of RPI and ^{10}Be records, on the other hand, is potentially biased by the superposition of environmental signals, which can move the apparent position of intensity minimima.

The similarity between mean lock-in depth estimates and the typical apparent thickness range of the SML (*Boudreau, 1994, 1998*) supports the hypothesis that the pDRM is acquired near the bottom of the bioturbated zone. *Bleil and Dobeneck (1999)* proposed a model that describes the delayed pDRM acquisition in terms of a so-called lock-in function

$$\Lambda(\zeta, d) = \lambda(\zeta/d) \tag{4.6}$$

defined as the cumulative probability that a magnetic particle becomes locked at a given depth ζ below the sediment-water interface. In this model, $\lambda(x)$ is a monotonic increasing function with $\lambda = 0$ for $x = 0$ (no acquisition at the sediment-water interface), and $\lambda = 1$ for $x \geq 1$, so that all particles are definitively blocked below the maximum lock-in depth d. *Bleil and Dobeneck (1999)* assumed d to be comprised between 15 and 35 cm for terrigenous and biogenic sediment end-members, respectively. *Roberts and Winklhofer (2004)* proposed a lock-in function with $\lambda = 0$ inside the SML (Fig. 4.3a), assuming that pDRM lock-in is produced by progressive sediment compaction and dewatering once significant bioturbation has ceased. While effectively explaining the delayed NRM acquisition, this model assumes that bioturbation and pDRM acquisition are mutually exclusive, as originally postulated by *Watkins (1968)*. In this case, pDRM must be acquired by the action of magnetic torques against interparticle forces in the consolidating sediment. Such forces, however, are too large for significant realignment to occur (*Shcherbakov and Shcherbakova, 1987*).

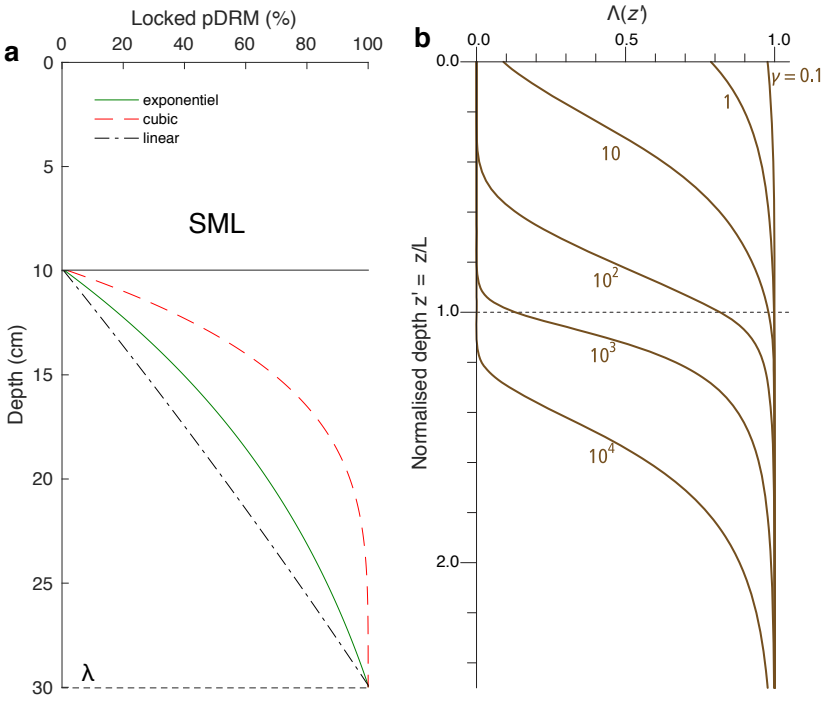

Figure 4.3: (a) Cumulative percentage of pDRM for exponential, linear, and cubic lock-in functions. The thickness of sedimentary mixed layer (SML) corresponds to the average estimate of bioturbation depth (*Boudreau,1998*). The pDRM acquisition is completed at a depth of 30 cm in all three examples. Redrawn from *Roberts and Winklhofer (2004)*. (b) Lock-in functions resulting from the rotational diffusion of magnetic moments in a bioturbated layer with an exponentially decaying diffusion coefficient $D = D_0 e^{-3z/L}$, for selected values of the rotational Péclet number γ. Notice the cases with $\Lambda(0) > 0$, which correspond to the partial preservation of the original DRM acquired at the sediment-water interface. Redrawn from *Egli et Zhao (2015)*.

Redeposition experiments with fresh sediment containing living microorganisms (*Zhao et al., 2016*) shed new light on the relation between pDRM and bioturbation, showing that pDRM is acquired through sediment mixing, and not despite it, as originally suggested by early sediment stirring experiments (*Kent, 1973*). In fact, the magnetisation of a rapidly mixed SML is the result of a dynamic equilibrium between the aligning torque of the magnetic field and the randomising torques associated with sediment reworking, very much like the magnetisation of a cooling rock above the blocking temperature of magnetic minerals (*Egli and Zhao, 2015*). Progressive burial brings magnetic particles further down in the SML, where bioturbation is less intense. Similarly to the case of a cooling rock, the equilibration time increases with decreasing perturbations, until the recorded directions become locked. In this model, particle orientation is described by a biased random walk with rate given by a rotational diffusion coefficient D_{r}.

Contrary to the case of bulk diffusion (Section 4.6.1), the depth dependence of D_{r} is important for determining the correct shape of the lock-in function. Consider for instance a homogeneous, strongly bioturbated SML with depth-independent D_{r}: in this case, magnetic particles are at equilibrium with the field, and thus unlocked, until they enter the historical layer. The resulting pDRM is acquired instantaneously at the bottom of the SML, yielding unrealistic magnetic records with a finite offset and no smoothing. General considerations about the consumption of organic matter in sediment (*Boudreau, 1998*), along with sparse empirical evidence (e.g. *Kadko and Heath, 1984; Powilleit et al., 1994; Swift et al., 1996; Michaud et al., 2003*), support the assumption that bioturbation intensity, and thus the associated bulk and rotational diffusion coefficients, decrease in an exponential fashion with depth. The resulting family of lock-in functions is governed by a single parameter, the so-called inverse rotational Péclet number (*Egli et Zhao, 2015*)

$$\gamma = \frac{2D_{\mathrm{r}}L_{\max}}{v_{\mathrm{b}}} \tag{4.7}$$

defined as the variance of the rotation angle accumulated over the time required by a particle to cross the SML, where $L_{\max}$ is the depth at which D_{r} has decreased to $\sim$3% of its maximum value at the sediment-water interface (Fig. 4.3b). For an exponential diffusivity profile $D_{\mathrm{r}} \propto e^{-z/L}$, $L_{\max} \approx 3L$. In the limit case of negligible bioturbation ($\gamma \leq 0.1$), the initial DRM is preserved. For $\gamma \geq 10$, DRM is completely replaced by a pDRM acquired at increasingly large depths. The lock-in depth range is fully comprised within $L_{\max}$ for $\gamma \leq 100$, while $\gamma \approx 1000$ yields a lock-in function similar to the model proposed by *Roberts and Winklhofer (2004)*.

From a formal mathematical perspective, the lock-in function Λ coincides with the integral of the pDRM impulse response, which is the magnetization profile resulting from a magnetic field impulse. The derivative of Λ is therefore the rotational equivalent of the impulse response of bulk diffusion discussed in Section 4.6.1. This analogy provides the mathematical framework to compare ^{10}Be and RPI records of the same geomagnetic event. For this purpose, it is necessary to link the rotational diffusion coefficient with bulk (translational) diffusion. In case of Brownian particles, this link is naturally provided by the Stokes-Einstein-Debye law

$$\frac{D_{\mathrm{r}}}{D} = \frac{\Gamma}{\Gamma_{\mathrm{r}}} \tag{4.8}$$

where Γ and Γ_{r} are the translational and rotational viscous drag coefficients, respectively, which depend on particle shape and size. For spherical particles of radius a

$$\frac{D_{\mathrm{r}}}{D} = \frac{3}{4a^2} \tag{4.9}$$

The relation between translational and rotational diffusion of dense particle aggregates, such

as sediments, is more complex and not well known. Significant deviations from the Stokes-Einstein-Debye relation have been reported for colloidal suspensions (*Koenderink et al., 2003*) and colloidal clay gels (*Jabbari-Farouji et al., 2012*). Of particular interest for sediments is the case of colloidal clay gels, where D_r/D is lowered by up to 2 orders of magnitudes with respect to equation 4.9 (*Kim et al., 2011*). In these examples, diffusion is driven by thermal agitation, as for Brownian particles, while sediment mixing is sustained by self-propelling organisms. Few terms of comparison exist in this case. While the diffusion of inert particles in a dense suspension of swimming bacteria remains Brownian, with bacterial cells acting as colliding molecules (*Peng et al., 2015*), significant departures from the Brownian regime are observed in case of shear-induced diffusion (*Leahy et al., 2013*). In this case, translational diffusion is strongly enhanced by flow gradients in what is known as Taylor dispersion, while only a limited enhancement of rotational diffusion is observed. As a result, D/D_r increases quadratically with the total plastic strain. The locomotion of benthic organisms produces a localized strain in the surrounding sediment, which is expected to lower the D_r/D ratio below the value expected from Brownian diffusion. Furthermore, clusters of tightly bounded sediment particles might behave as rigid units, in which case a coincides the cluster radius, rather than the size of individual particles. Finally, non-local particle transport by sediment feeders (*Shull, 2001; Shull and Yasuda, 2001*) and burrow infilling (*Tedesco and Aller, 1997*) increases the apparent bulk diffusion coefficient much more than rotational diffusion, since the displacement of single particles is limited only by the size of burrows, while the maximum rotation angle of a randomization event is limited to a full rotation.

With the above considerations in mind, the coupling between bioturbation effects on particle displacement and rotation near the bottom of the bioturbated layer is expected to depend on the plastic deformation caused by the locomotion of meio- and microbenthos, such as foraminifera (*Cullen, 1973; Severin et al., 1982; Gross, 2002*), and conveyor-belt feeders. The pDRM experiments of *Zhao et al. (2016)* are representative for the bioturbation effects of meio- and microbenthos, since the sediment was wet-sieved with a 63 μm mesh to remove larger organisms. The rotational diffusion coefficient obtained with fresh sediment was $D_\mathrm{r} \approx 0.1\mathrm{rad}^2/\mathrm{day}$. Unfortunately, a corresponding estimate of D is not available. Laboratory measurements of glass microspheres diffusion in Mediterranean Sea sediment subjected to a similar removal of macroscopic organisms yielded $D \approx 0.19\mathrm{cm}^2/\mathrm{day}$ (*Gross, 2002*). Assuming that the two studies are comparable, the minimum ratio $D_\mathrm{r}/D \approx 0.53\mathrm{cm}^2$ is obtained. This result is very uncertain, considering that the bulk diffusion coefficient might vary by $\approx$1 order of magnitude among sediments with similar settings (*Boudreau, 1994; Soetaert et al., 1996; Henderson et al., 1999; Lecroart et al., 2010*). Yet, it is the only result that can be used to link the effects of sediment mixing on ^{10}Be and RPI records.

4.6.3 Linking bioturbation and pDRM acquisition models

A well-defined relation between bioturbation models and pDRM lock-in depth is expected if the pDRM is acquired by magnetic particles during the last stages of sediment mixing, as postulated by *Egli and Zhao (2015)* and *Zhao et al. (2016)*, rather than below the mixed layer through the rotation of few unblocked particles, as suggested by earlier models. This relation is of theoretical and practical interest, since it links tracer transport, including Be isotopes, with magnetic records. In this case, the pDRM lock-in depth would be entirely controlled by sedimentary processes, rather than by the field intensity, as proposed for magnetic grain rotation in a resting sediment (*Lovlie, 1994*), where the magnetic torque produced by stronger fields would rotate particles in deeper, more compacted layers.

Modelling of bioturbation-induced pDRM requires to know how sediment mixing declines with increasing depth below the sediment-water interface. The widely used model of a homogeneous mixed layer, where mixing ceases abruptly at a certain depth, cannot be used, since it implies that pDRM is unrealistically acquired inside a narrow depth interval at the bottom of the mixed layer. This lack of graduality would produce delayed magnetic records with no smoothing, contradicting evidences from sediments with low accumulation rates (*Lund and Keigwin, 1994; Teanby and Gubbins, 2000; Roberts and Winklhofer, 2004; Valet et al., 2016*). On the other hand, the depth dependence of sediment mixing is very poorly resolved by radioactive tracer profiles (*Kadko and Heath, 1984; Kansanen and Seppälä, 1992; Swift et al., 1996*), and never by stable tracer profiles, such as tektites, as shown later in this section.

First-principle considerations about the consumption of organic matter by benthic organisms (*Boudreau, 1998*), the depth distribution of such organisms and their burrowing traces (*Shirayama, 1984; Snider et al., 1984; Mazik et al., 2008; Roche et al., 2016*) and tracer distribution observations (*Kadko and Heath, 1984; Kansanen and Seppälä, 1992; Swift et al., 1996; Fornes et al., 2001*), suggest that the long-term averaged sediment mixing rate is a monotonically decreasing function of depth. In simple terms, it can be assumed that the mixing rate, and thus the bulk diffusion coefficient D_{s} of diffusive models, is proportional to the total biomass, which is in turn proportional to the product of available organic matter and its consumption rate. *Boudreau (1998)* obtained a general expression for the depth dependence of D_{s} by assuming D_{s}= bC_{org} to be proportional to the concentration C_{org} of organic matter, whose consumption obeys a first-order kinetic reaction with rate k_{org}. The steady-state diffusion-advection equation for constant organic carbon input and negligible burial velocity is then given by

$$\frac{\partial}{\partial z}\left[bC_{\mathrm{org}}\frac{\partial C_{\mathrm{org}}}{\partial z}\right] - k_{\mathrm{org}}C_{\mathrm{org}} = 0 \tag{4.10}$$

with solution $C_{\mathrm{org}} \propto (1 - z/L)^2$ for $z \leq L$, where L is the depth at which organic matter is completely consumed. More realistic models must take the quality of organic matter into

consideration, with fresh organic material being consumed more readily than older matter (*Westrich and Berner, 1984; Middelburg, 1989; Boudreau and Ruddick, 1991*). In this case, eq. (4.10) is replaced by multi-pool model consisting of a set of equations of the same type, one for each pool of organic matter with specific consumption rate, which yields exponential-like profiles of total organic carbon (*Canfield, 1994; Rabouille et al., 1998; Arndt et al., 2013*). Fresher organic matter is more readily consumed and tend to be concentrated near the sediment-water interface, where it sustains a larger benthic organism community. Accordingly, the depth distribution of younger tracers, such as chlorophyll-a and short-lived radioactive isotopes, is explained by an equivalent homogeneous mixed layer with larger diffusivity and smaller thickness, compared to results obtained from older tracers (*Fornes et al., 2001; Lecroart et al., 2010*). This dependence of the apparent SML properties on tracer age emerges clearly from large collections of bioturbation data (Fig. 4.4). In principle, organic matter degradation continues to very large depths, due to the slow bacterial degradation of the refractory component (*Røy et al., 2012; Arndt et al., 2013; Stolpovsky et al., 2018*); however, the high energy requirements of locomotion limits the occurrence of motile organisms capable of sediment reworking to a surface layer with finite thickness $L_{\max}$ (*LaRowe and Amend, 2015*).

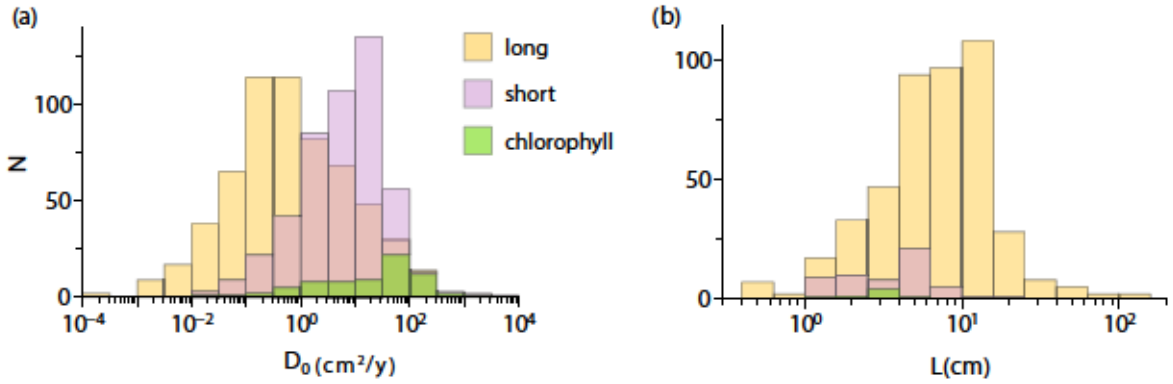

Figure 4.4: Apparent diffusivity (a) and thickness (b) of homogeneous surface mixed layers deduced from stable tracers or long-lived radioisotopes with half-lives >22 years (^{210}Pb, ^{137}Cs, ^{32}Si, ^{239}Pu/^{240}Pu, glass beads, tektites), short-lived radioisotopes (^{234}Th, ^{235}Th, ^{228}Th, ^{7}Be), and chlorophyll-a. Data from a worldwide compilation by *Solan et al. (2019)*.

The depth dependence of the diffusion coefficient is thus conveniently expressed by a pseudo-exponential function that becomes exactly zero below the maximum bioturbation depth L_{max}. In mathematical terms, the diffusivity of a tracer is given by $D_t(z) = D_0 y(z/L)$, where D_0 is the maximum diffusivity at the sediment-water interface, $L \leq L_{\max}$ the typical length scale of the mixed layer, and y a monotonic decreasing function with $y(0) = 1$ and $y(x) = 0$ for $x \geq x_0$ with $x_0 = L_{max}/L$. For instance, an exponential diffusivity profile is modelled by $y(x) = \tilde{\theta}(x/x_0)e^{-x}$, where $\tilde{\theta}$ is a function providing a smooth transition from 1 to 0 for

$x \leq x_0$. In case of negligible compaction inside the mixed layer, the diffusion-advection equation for the concentration C of tracer particles with diffusivity $D_\mathrm{t} = \alpha D_\mathrm{s}$ and segregation velocity $v_\mathrm{t} = \beta D_\mathrm{s}$ (see Section 2.8.4), where D_s is the bulk sediment diffusivity, is given by

$$\frac{\partial C}{\partial t} = \frac{\partial}{\partial z} D_\mathrm{t} \frac{\partial C}{\partial z} + (v_\mathrm{t} - v_\mathrm{b}) \frac{\partial C}{\partial z} \tag{4.11}$$

with a single boundary condition

$$\left[(v_\mathrm{b} - v_\mathrm{t}) C - D_\mathrm{t} \frac{\partial C}{\partial z} \right]_{z=0} = F_\mathrm{t}(t) \tag{4.12}$$

at the sediment-water interface, controlled by the incoming tracer flux F_t. Unlike the case of the homogeneous mixed layer discussed in Chapter 2.8.5, a second boundary condition is not needed, since $D_\mathrm{t} = v_\mathrm{t} = 0$ at $z = L_\mathrm{max}$, so that the tracer flux just above L_max is already equal to the flux $v_\mathrm{b} C$ to the historical layer.

General solutions of eq. (4.11-4.12) are not known, so that their use for modelling real concentration profiles is impracticable. However, a well-defined relationship exists between numerical solutions and the case of a homogeneous mixed layer, so that concentration profiles can be modelled using the solutions obtained in Chapter 2.8.5. As first step, the same variable substitutions $x = z/L$ and $t^* = v_\mathrm{b} t / L$ are used to convert eq. (4.11) into the scaled form

$$\frac{\partial C}{\partial t^*} = \frac{\partial}{\partial x} \left[\alpha G_0 y(x) \frac{\partial C}{\partial x} + (\beta L G_0 y(x) - 1) C \right] \tag{4.13}$$

with $G_0 = D_0 / L v_\mathrm{b}$ being the inverse Péclet number of regular sediment particles at the sediment-water interface. The corresponding boundary condition for calculating the impulse response is

$$\left[(1 - \beta L G_0) C - \alpha G_0 \frac{\partial C}{\partial x} \right]_{x=0} = \delta(t^*) \tag{4.14}$$

Eq. (4.12-4.13) depend on two parameters, αG_0 and $\beta L G_0$, which control the strength of scaled diffusion and size segregation, respectively. In case of tracer particles behaving like the bulk sediment ($\alpha = 1$ and $\beta = 1$) the resulting equations

$$\frac{\partial C}{\partial t^*} = \frac{\partial}{\partial x} \left[G_0 y(x) \frac{\partial C}{\partial x} - C \right] \tag{4.15}$$

and

$$\left[C - G_0 \frac{\partial C}{\partial x} \right]_{x=0} = \delta(t^*) \tag{4.16}$$

depend on a single parameter, G_0, and on the shape of y. Numerical solutions for a pseudo-exponential diffusivity profile $y(x) = \tilde{\theta}(x_0 - x)e^{-x}$ with $x_0 = 15$ and

$$\tilde{\theta}(x) = \frac{1}{2}\begin{cases} 0, & x < 0 \\ 1 - \cos(\pi x/2), & x < 2 \\ 2, & \text{else} \end{cases} \tag{4.17}$$

differ from those of a homogeneous mixed layer in their dependence on G_0 (Fig. 4.5).

The impulse response of a homogeneous mixed layer varies from a narrow, Gaussian-like peak around $\langle t^* \rangle$ for $G_0 \ll 1$ to a one-sided exponential for $G_0 \gg 1$, with a sharp left limit given by $\langle t^* \rangle - 1 = 0$. This limit corresponds to the instantaneous transport of tracer particles to the bottom of the mixed layer when diffusion is much stronger than advection. Exponential diffusivity profiles produce impulse responses with a qualitatively similar dependence on G_0; however, the impulse responses becomes increasingly wide without approaching a sharp left limit as with a homogenous mixing layer. This can be explained by the fact that the depth at which advection becomes dominant is always equal to L in the case of a homogeneous mixed layer, while it depends on G_0 in the case of an exponential diffusivity profile. Despite this important difference, the impulse response $\mathcal{E}(t^* - \langle t^* \rangle, G_0)$ of an exponential diffusivity profile with inverse Péclet number G_0 is almost perfectly matched by a rescaled version

$$\mathcal{E}'_{exp}(t^*) = \frac{1}{\omega}\mathcal{E}\left(\frac{t^* - \langle t^* \rangle}{\omega}, \chi G_0\right) \tag{4.18}$$

of the impulse response of a homogeneous mixed layer with a smaller inverse Péclet number χG_0 with $0 < \chi < 1$, where the dimensionless time axis is stretched by a factor ω (Fig. 4.5). The almost perfect match between the two mixed layer models means that impulsive tracer concentration profiles can be fitted equally well by both models.

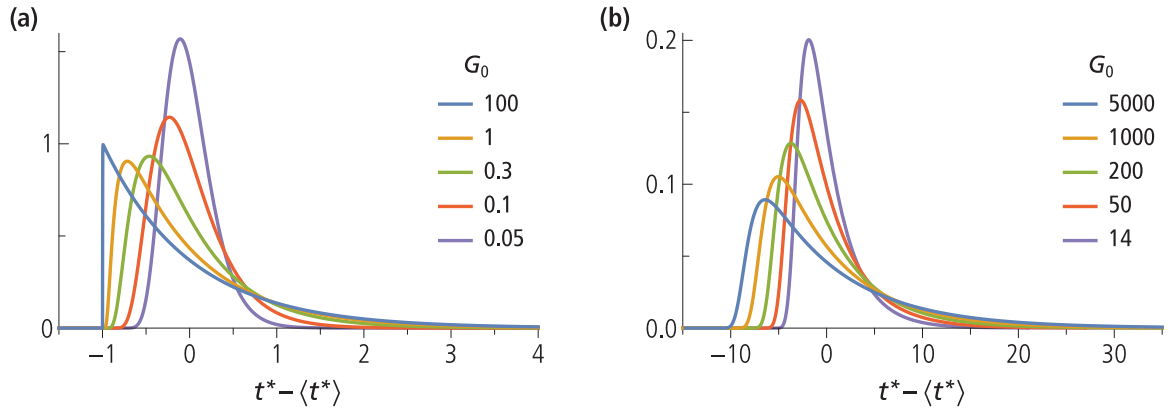

Figure 4.5: Nondimensionalized impulse responses for a homogeneous mixed layer (a) and a mixed layer with exponentially decaying diffusivity (b), for selected values of the inverse Péclet number G_0. In both panels, $t^* = v_\mathrm{b} t/L$ is the dimensionless time and $\langle t^* \rangle$ the corresponding expectation, with L being the thickness of the mixed layer in (a), and the depth at which the diffusivity has decreased to $1/e \approx 0.368$ of the value at the sediment-water interface in (b).

Since these two models represents the extremes of postulated profiles of diffusivity or other bioturbation rate measures (e.g. *Swift et al., 1996; Koretsky et al., 2002; Huang et al., 2007; Maire et al., 2008; Zhang and Wirtz, 2017*), it is intrinsically impossible to resolve the depth dependence of sediment mixing on the basis of stable tracer profiles. The relation between models based on constant and exponential diffusivity profiles can be understood by comparing the tracer concentration obtained from the corresponding impulse responses. It follows from eq. (2.99) that

$$C_\mathrm{exp}(z,T) = \Phi_t \frac{\phi}{L} \mathcal{E}_\mathrm{exp}\left(\frac{\phi}{L} v_\mathrm{b}(T - t_\mathrm{b}(z)), G_0\right) \tag{4.19}$$

is the concentration profile of tracer particles deposited at time T on a sediment with exponential diffusivity profile characterized by the inverse Péclet number G_0. The other parameters in eq. (4.19) are the tracer fluence Φ_t, the time t_b required for a particle to be buried from the maximum bioturbation depth L_max to the depth z, and the compaction ratio $\phi = \varphi_\mathrm{s}(z)/\varphi_\mathrm{s}(L_\mathrm{max})$. By virtue of eq. (4.18), a homogeneous mixed layer of thickness $L\omega$ and inverse Péclet number χG_0 produces the equivalent profile

$$C(z,T) \approx \Phi_t \frac{\phi}{L\omega} \mathcal{E}\left(\frac{\phi}{L\omega} v_b(T - t_b(z)), \chi G_0\right) \tag{4.20}$$

This means that an exponential diffusivity profile $D_\mathrm{s} = D_0 e^{-z/L}$ is equivalent to a homogeneous mixed layer with thickness $L\omega$ and diffusivity $\chi\omega D_0$, with ω and χ being functions of $G_0 = D_0/Lv_\mathrm{b}$. In the limit case of weak diffusion ($G_0 \to 0$), the equivalent homogeneous

mixed layer has a thickness $2L$ and a diffusion coefficient $D_0/2$ (Fig. 4.5b). As G_0 increases, the homogeneous layer becomes thicker and its diffusivity decreases. There is no limit to this trend, so that the tracer profiles produced by exponential diffusivity profiles with very large values of G_0 appear much thicker if modeled with a homogeneous SML.

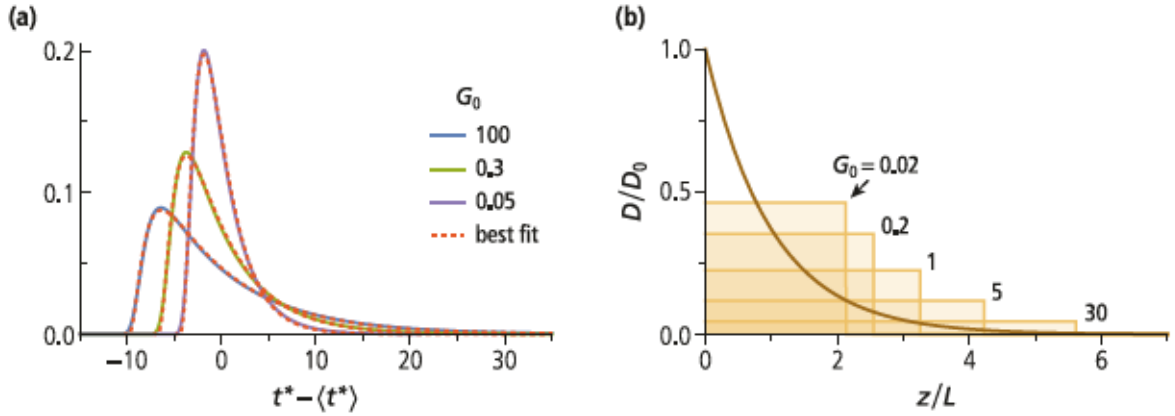

Figure 4.6: **(a)** Nondimensionalized impulse responses for a mixed layer with exponentially decaying diffusivity (solid lines) and corresponding least-squares fits with rescaled impulse responses for a homogeneous mixed layer, according to eq. (4.18) (dashed lines). The rescaling parameters are (χ, ω) = (0.322, 6.653) for $G_0 = 100$, (χ, ω) = (0.0360,2.687) for $G_0 = 0.3$ and (χ, ω) = (0.0986,2.214) for G_0 = 0.05. **(b)** Exponential diffusivity profile (brown line) and equivalent homogeneous mixed layers (shaded) for selected values of G_0. The thickness of the equivalent homogeneous mixed layer increases with increasing G_0.

The equivalency between the two models is expressed empirically by the diffusivity ratio

$$\frac{D^{\mathrm{hom}}}{D_0^{\mathrm{exp}}} = \frac{1}{2}\left[1 + 2.692 G_0^{0.7544} + 0.2722 G_0^{1.3723}\right]^{-0.5748} \tag{4.21}$$

and the ratio

$$\frac{L^{\mathrm{hom}}}{L^{\mathrm{exp}}} = 2 + 1.544 \ln\left[1 + 1.182 G_0^{0.611}\right] \tag{4.22}$$

between length scales, where "hom" and "exp" refer to the homogeneous mixing and the exponential diffusivity model, respectively (Fig. 4.7). These equations can be used to fit concentration profiles with the exponential diffusivity model in two steps: in the first step, a fit is obtained with the analytical solution corresponding to a homogeneous SML. The parameters of the equivalent exponential diffusivity model are then obtained by solving eq. (4.21-4.22) with respect to D^{exp} and L^{exp}, using $G_0 = D_0^{\mathrm{exp}}/(L^{\mathrm{exp}} v_{\mathrm{b}})$.

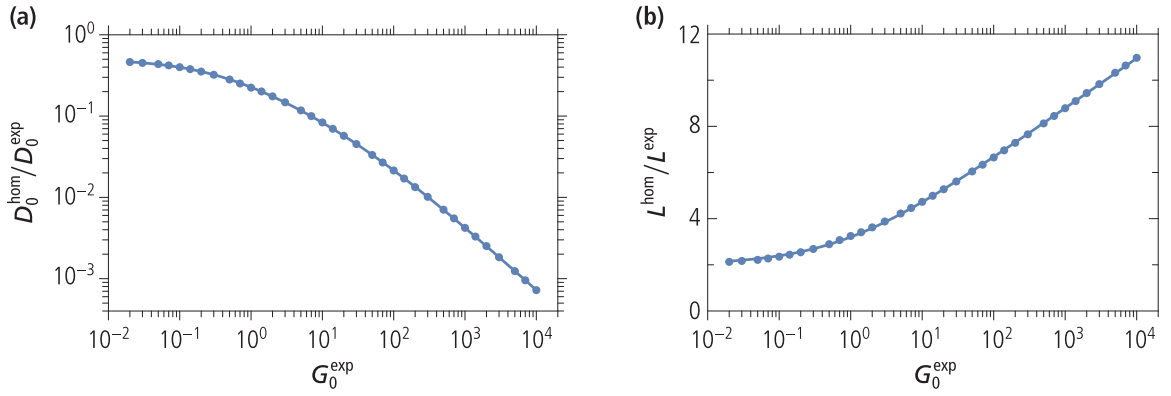

Figure 4.7: Diffusivity (**a**) and thickness (**b**) of a homogeneous mixed layer producing the same impulse response as a mixed layer with exponential diffusivity profile. Dots represent best-fit parameters obtained by fitting numerical solutions of eq. (4.13-14) with the impulse response of a homogeneous mixed layer. Lines are given by eq. (4.21-22).

Using the above equivalency between mixed layers with homogeneous and exponential diffusivity profiles, along with the tektite profile fits of Chapter 2, it is now possible to estimate the biouturbation parameters required to calculate the pDRM lock-in function of *Egli and Zhao (2015)* (Table 4.2).

Core	$\boldsymbol{D^{hom}}$ (cm^2/yr)	$\boldsymbol{L^{hom}}$ (cm)	$\boldsymbol{D_0^{exp}}$ (cm^2/yr)	$\boldsymbol{L^{exp}}$(cm)	$\boldsymbol{G_0}$	γ
MD90-0961	0.056	19	39	1.9	4.0×10^3	4.7×10^4
MD90-0949	0.033	16	200	1.3	6.9×10^4	3.6×10^5

Table 4.2: Diffusivity D^{hom} and thickness L^{hom} of the homogeneous SML used to fit the tektite profiles of cores MD90-0961 and MD90-0949 of the Indian Ocean (Chapter 2), and corresponding parameters D_0^{exp}, L^{exp} for the equivalent SML with exponential diffusivity profile obtained with eq. (4.20-4.21). These parameters define the inverse Péclet number $G_0 = D_0^{\mathrm{exp}}/Lv_{\mathrm{b}}$ and the inverse rotational Péclet number $\gamma = 2D_{\mathrm{r},0}L_{\mathrm{max}}/v_{\mathrm{b}}$, with $L_{\mathrm{max}} = 3L$ and assuming $D_{\mathrm{r}}/D = 0.53$.

Diffusivity and length scale estimates obtained by fitting the tektite profile of MD90-0961 with the exponential diffusivity model are ∼700 and ∼10 times larger than those obtained with a homogeneous SML. Even larger differences are obtained for MD90-0949. Interestingly, similar differences exist also between tektite and radioactive tracer estimates of D and L for several deep-sea sediments: for instance, *Matisoff (1982)* report $D \approx 0.005$ cm^2/yr and $L \approx 42$ cm from tektite profiles, and $D \approx 4.4$ cm^2/yr and $L \approx 4$ cm from ^{210}Pb data for Northern Equatorial Pacific sediment. A factor ≈100 difference is also observed between between long- and short-lived radioactive tracers (Fig. 4.4), and has been explained by the age dependency of

tracer mixing, which in turns implies faster mixing of fresh material near the sediment-water interface (*Lecroart et al., 2010*).

At this point it is possible to use the D_{r}/D estimate of the previous section to calculate the inverse rotational Péclet number $\gamma = 2D_{\mathrm{r},0}L_{\max}/v_{\mathrm{b}}$ for the sediment-water interface of cores MD90-0961 and MD90-0949, along with $L_{\max} = 3L$, the maximum depth of the bioturbation zone in the exponential diffusivity model used by *Egli and Zhao (2015)* to calculate the pDRM lock-in function (Table 4.1). The lock-in function is given by

$$\Lambda(x) = \exp\left[-\gamma \int_x^{\infty} e^{-u-\beta(u)}\mathrm{d}u\right] \tag{4.23}$$

with $x = z/L$, where β is the ratio between the minimum torque required to rotate a sediment particle against the bounding forces with its neighbours and the typical amplitude of perturbing torques produced by bioturbation. This ratio increases with depth as sediment gets compacted and is therefore proportional to a measure of sediment toughness, such as the shear strength or the tensile fracture toughness (*Egli and Zhao, 2015*). By analogy with the Arrhenius law, $e^{-\beta}$ is the probability that a sediment particle is reoriented by a bioturbation event. Mechanical properties of sediments in the uppermost tens of centimetres, which are relevant for the pDRM acquisition model, are rarely available, because of the special coring techniques required to avoid surficial sediment disturbances and the loose sediment consistence. *Egli and Zhao (2015)* identified β with the tensile fracture toughness of a thixotropic, clay-rich sediment, whose strength increases in time when at rest, creating a relatively sharp boundary at the bottom of the mixed layer. This boundary is not expected in carbonate-rich sediments; therefore, β is modelled with a $\tanh$ function (Fig. 4.8a) representing the typical monotonic increase of sediment strength with depth expected from standard consolidation models (e.g. *Berlamont et al., 1993; Radziejewska and Modlitba, 1999; Locat et al., 2002; Bartetzko and Kopf, 2007*). The choice of β is not particularly critical for the determination of the pDRM lock-in depth, as seen in the examples of Fig. 4.8b. Lock-in functions with $\gamma \quad 20$ begin with values > 0, which means that part of the final magnetization is acquired at the sediment-water interface in form of a DRM. For $\gamma \quad 100$, the initial DRM is completely replaced by a pDRM acquired at increasingly large depths.

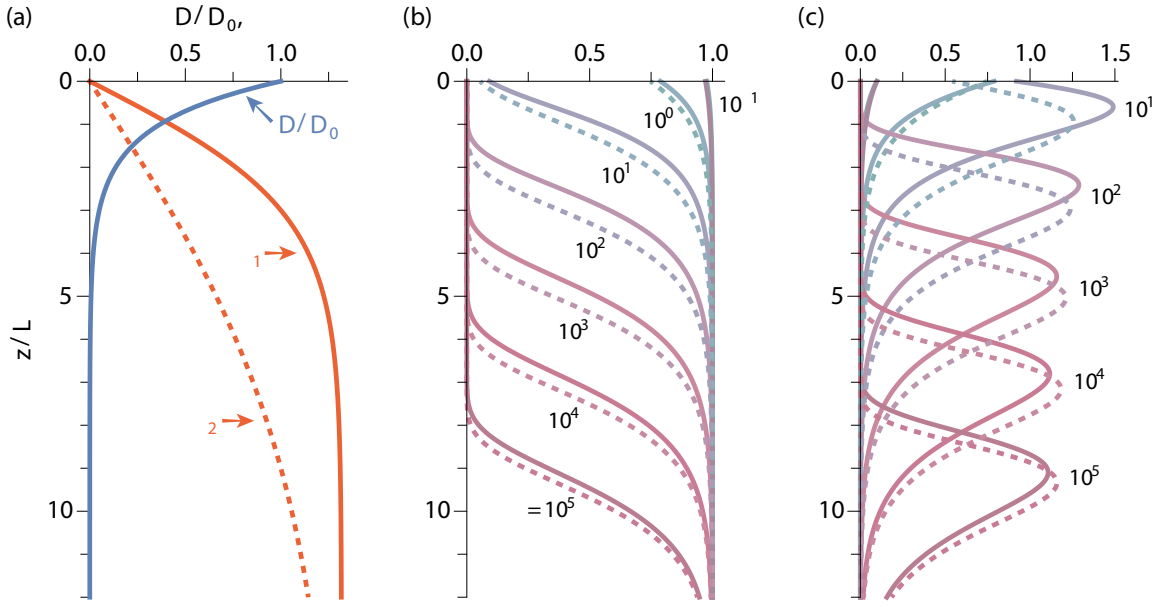

Figure 4.8: PDRM acquisition model, based on Egli and Zhao (2015). **(a)** Depth dependence of the bioturbation diffusivity, $D/D_0 = e^{(-z/L)}$, where L is the length scale of the SML, and of $\beta = b\tanh(z/z_\beta)$ with $b = 1.32$. Two examples are shown for $z_\beta = L$ (β_1, solid line) and $z_\beta = 3L$ (β_2, dashed line). The initial part of β_1 coincides with the example used by *Egli and Zhao (2015)*. **(b)** Lock-in functions $\Lambda(z/L)$ obtained from the parameters in (a) and selected values of the inverse rotational Péclet number γ. Solid and dashed lines correspond to β_1 and β_2, respectively. **(c)** Impulse responses $\lambda(z/L)$ of pDRM acquisition, defined as the first derivative of the lock-in functions shown in (b).

The pDRM impulse response, defined as the sediment magnetization produced by a field pulse, is given the first derivative

$$\lambda(x) = \Lambda(x)e^{-x-\beta(x)} \tag{4.24}$$

of the lock-in function (Fig. 4.8c). It can be regarded as the rotational, or magnetic, analogue of of the traditional impulse response of sediment mixing (Chapter 2). It is now possible to compare the translational and rotational response to an impulsive event of age T for a given bioturbation model. As discussed in section 4.6.1, the concentration profile corresponding to this event is

$$C(z,T) = \Phi_t \frac{\phi}{L\omega}\mathcal{E}\left(\frac{\phi v_\mathrm{b}}{L\omega}\left(T - t_\mathrm{b}\right), \chi G_0\right) \tag{4.25}$$

where Φ is the fluence (that is, the total deposited amount), ϕ the ratio between the sediment

volume fration at depth z and L, respectively, v_b the burial velocity at depth z, t_b the time required for burial from $z = L$ to z, and $\mathcal{E}$ the time-domain impulse response at the bottom of a homogeneous SML of thickness $L\omega$ and inverse Péclet number χG_0. The expected value of $C(z,T)$ coincides with the stratigraphic depth $\zeta(T)$, which satisfies the age model equation

$$T(\zeta) = \int_0^\zeta \frac{\mathrm{d}u}{v_\mathrm{b}(u)} \tag{4.26}$$

This means that tracer concentration records are smoothed by the width of the impulse response but not delayed. The magnetization profile produced by the same impulsive event of age T is obtained from the impulse response λ, shifted by the stratigraphic depth $\zeta(T)$, that is

$$M(z,t) \propto \frac{\phi}{L}\lambda\left(\phi\frac{z-\zeta(T)}{L}\right) \tag{4.27}$$

The offset Δz_M of M relative to a tracer concentration record is given by $L/\phi x_\lambda$, where x_λ is the expectation of the impulse response $\lambda(x)$ (Fig. 4.8c). An example for core MD90-0961 obtained with the bioturbation model derived from the tektite profiles analysed in Chapter 2 is shown in Fig. 4.9a. The pDRM lock-in range starts near the lower limit of the depth range occupied by a stable tracer responding to the same event, such as ^{10}Be. This result is apparently similar to what is predicted by standard lock-in models (*Roberts and Winkhofer, 2004*), except for the fact that pDRM lock-in is actually driven by residual mixing near the bottom of the SML, rather than compaction below the SML. This difference becomes more evident in case of less intense bioturbation or higher sedimentation rates leading to a smaller rotational Péclet number, as $\lambda(x)$ raises towards the sediment-water interface (Fig. 4.8c). Interestingly, *Channell and Guyodo (2004)* postulated a lock-in function with a similar sigmoidal shape as Λ in Fig. 4.8b with $\gamma \approx 30$. The mean lock-in depth in this particular example is ∼17 cm without compaction ($\phi = 1$) and $\sim$ 13 cm if the compaction of this core at the depth corresponding to the MB reversal is taken into account.

Another interesting feature of the pDRM acquisition model illustrated in Fig. 4.9a is that the magnetic record is predicted to be less smoothed than a tracer-based record, owing to the narrower shape of λ with respect of the tracer impulse response. This is a very important feature for the fidelity of paleomagnetic records, since smoothing effects are smaller than expected from the lock-in depth. In the example of Fig. 4.9a, the full width to half-maximum of the pDRM lock-in function is ∼4.5 cm, compared to the ∼17 cm mean lock-in depth. Similar small width-to-mean-depth ratios have been also used by *Channell and Guyodo (2004)* to model differences between paleomagnetic records of two cores with highly contrasting sedimentation rates. The symmetry of $\lambda(x)$ and the absence of one-sided heavy tails is another favourable property of the lock-in function, which excludes the possibility of an asymmetric pDRM response to abrupt intensity changes, as already postulated by *Meynadier and Valet (1996)*. This is a further

confirmation that the asymmetric reversal rates obtained from sedimentary records (*Valet et al., 2005*) reflect an intrinsic feature of the core dynamo, rather than a recording mechanism artefact (*Kok and Tauxe, 1996*).

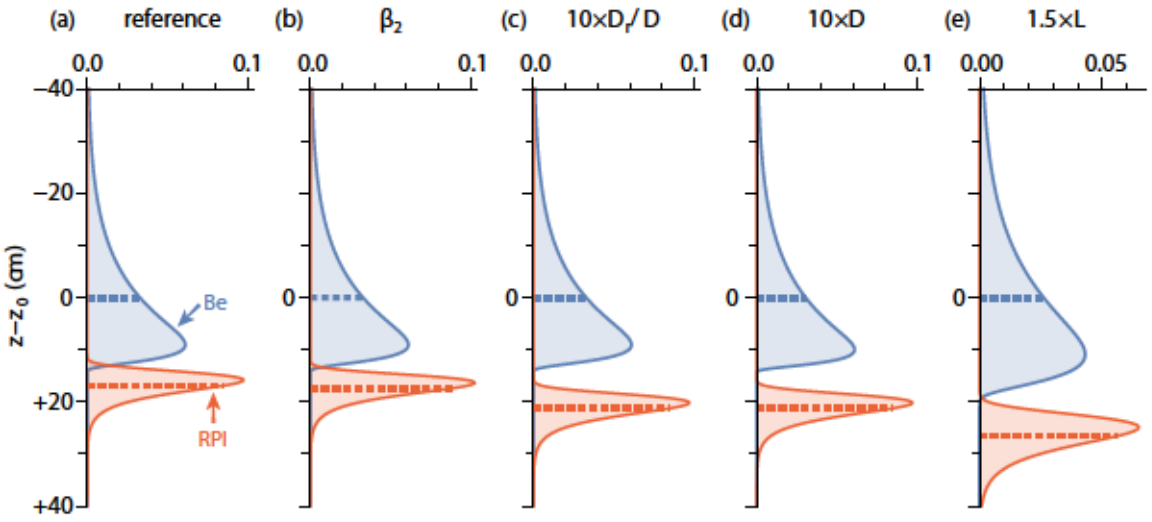

Figure 4.9: Predicted responses of core MD90-0961 to a field impulse by tracer concentration (e.g. ^{10}Be, blue curves), and by sediment magnetisation (red curves) for different scenarios. The dashed lines coincides with the offset of the magnetic record with respect to the tracer record. (**a**) Model obtained from the bioturbation parameters deduced from the tektite profile (Table 4.2), assuming $D_r/D = 0.53$ cm^2 and β_1 as in Fig. 4.8a. (**b**) Same as (a) for β_2 as in Fig. 4.8a. (**c**) Same as (a) for a 10 times larger D_r/D. (**d**) Same as (a) for a 10 times larger D. (**e**) Same as (a) for a 50% times larger L

A critical issue with the pDRM acquisition model proposed here is its dependence on very poorly known bioturbation parameters, in particular the ratio between rotational and bulk diffusivity, and the depth dependence of sediment strength. A sensitivity analysis, however, suggests that the pDRM lock-in depth depends only weakly on most parameters. For instance, the lock-in depth increases by a mere ∼3% if the sediment strength profile β_1 of Fig. 4.9a is replaced by β_2 (Fig. 4.9b), and by ∼26% if D_r/D or D is increased by a factor 10 (Fig. 4.9c,d). The only parameter that affects the pDRM lock-in depth in a proportional manner is the length scale L of the SML (Fig. 4.9e), for obvious reasons, since z/L is the argument of the impulse responses in eq. (4.27). Contrary to other bioturbation parameters, the thickness of the equivalent homogeneous SML used to model tracer profiles in very different sedimentary settings is relatively constant, with a global mean of ∼10 cm and most values comprised between 5 and 15 cm (Fig. 4.9) (*Boudreau, 1994, 1998*). Accordingly, the pDRM lock-in depth is expected to be relatively insensitive to the effects of environmental changes on

the SML thickness and on the mechanical properties of the SML. Adverse field recording artefacts due to rapid variations of the lock-in depth, such as repeated apparent reversals (*Bleil and Dobeneck, 1999; Spassov et al., 2003*), are therefore not expected during regular sedimentation intervals, when bioturbation is controlled by quasi-stationary conditions. On the other hand, sudden variations of the sedimentation rate, as with turbidites, can produce a complex chain of post-depositional processes, such as the sudden suppression of bioturbation, followed by re-colonization of the newly deposited sediment by burrowing animals (*Seike et al., 2011; deChanvalon et al., 2015*), which leads to a complex overlap of DRM and pDRM acquisition events with highly irregular timing.

Another condition for the applicability of (quasi-) stationary pDRM acquisition models such as in Fig. 4.9 is that the mixing process is insensitive to the type of magnetic minerals being involved, or that the magnetic mineralogy does not change in time, the latter being a condition required also for the NRM normalization used to generate RPI records (*Tauxe, 1993*). As far as the sensitivity of the mixing process on the type of minerals involved, a strong dependence on size *(Wheatcroft, 1992)*, and association with nutrients (*Fornes et al., 2001*) can be expected. As shown by *Fornes et al. (2001)*, tracer-dependent mixing is mainly caused by selective ingestion, so that the intrinsically diffusive component of bioturbation (e.g. by shear diffusion), which is the one that is relevant for pDRM acquisition, should not be affected. On the other hand, as discussed in Section 4.6.2, the relationship between bulk and rotational diffusion is affected by particle size, so that smaller minerals might be characterized by a larger rotational Péclet number γ. In summary, the apparent dependence of the bulk diffusivity on mineral size and composition might produce a compositional gradient in the SML, known as segregation, which has been documented in core MD90-0961 with tektites of different sizes (Chapter 2), and, as far as size is concerned, it might alter rotational diffusion. The consequences for pDRM acquisition are twofold. Firstly, a compositional gradient will not alter the lock-in function, which, however, needs to be convolved with the concentration profile. As a result, particles with reduced diffusion tend to remain on the surface of sediment and the corresponding lock-in depth is reduced, since a larger number of particles at the upper limit of the lock-in function will contribute to the pDRM. Secondly, the rotational diffusivity of larger particles is smaller, so that their lock-in function is characterized by a smaller γ. Both phenomena lead to smaller lock-in depth for larger particles and vice-versa. However, the grain size and compositional dependence of the pDRM lock-in depth is complicated by the fact that smaller magnetic remanence carriers are often attached to larger sediment particles (*Galindo-Gonzalez et al., 2009*), so that the magnetic grain size is not expected to be directly related to the effective size that matters for bioturbation. This issue is discussed in detail in Section 4.8.1.

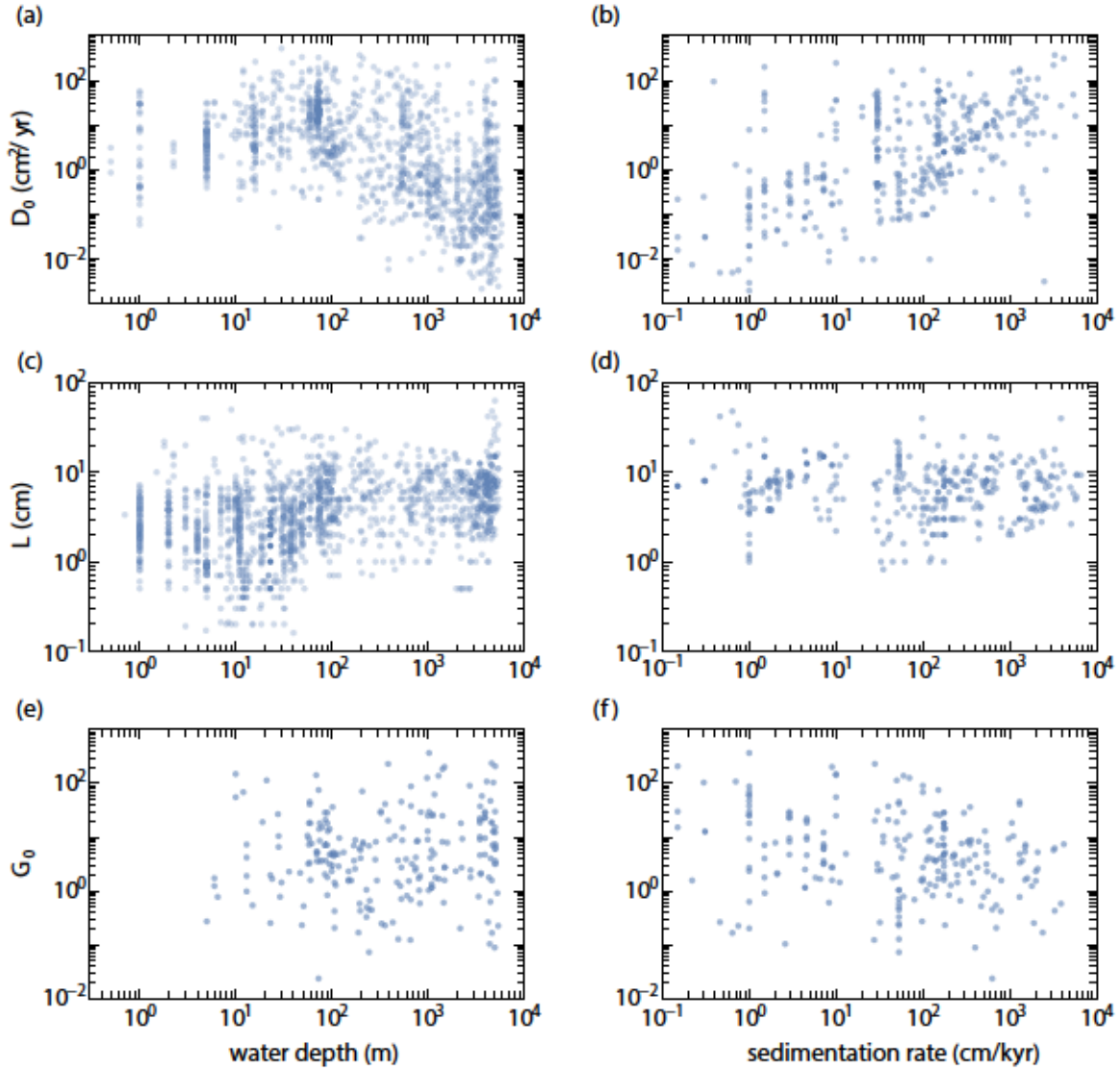

Figure 4.10: Diffusivity D_0 (**a-b**), thickness L (**c-d**), and inverse Péclet number G_0 (**e-f**), vs water depth (left) and sedimentation rate (right) for a global collection of over 2600 estimates of the SML properties of marine sediments collected by *Solan et al. (2019)*

While the environmental dependence of a bioturbation-induced pDRM is expected to be small, a certain degree of random variations over time is expected from the observed scatter of biouturbation parameters among sediments deposited under similar conditions (Fig. 4.10). Part of this scatter, especially at slow mixing regimes, is inherent to the stochastic nature of bioturbation and the involvement of benthic macrofauna, which produces a succession of discrete events, rather than continuous mixing. *Lecroart et al. (2010)* observed that the tracer-dependence of mixing in synthetic lattice-automation simulations of bioturbation (*Reed et al., 2006*) disappears when the total number of mixing events is larger than 20, which converts to a tracer-derived diffusivity >2 cm^2/yr. However, the tracer-dependent differences in D and L

shown in Fig. 4.4 persist even at larger diffusivities, especially in the case of L, suggesting that it is the natural consequence of a depth-dependent mixing intensity, rather than a statistical artefact. Furthermore, careful analysis of the tektite profiles of cores MD90-0961 and MD90-0949 (Chapter 2), shows significant localised deviation of tektite counts, on a cm length scale, imputable to sediment heterogeneity, despite diffusivity values >1 order of magnitude larger than the threshold indicated by *Lecroart (2010)*. This can, again, be explained by an exponential diffusivity profile, where only bioturbation events near the sediment-water interface are frequent enough to produce homogeneous mixing. As a sediment particle travels towards the bottom of the SML, bioturbation events become increasingly rare, until the discrete effects of individual events becomes permanently locked in the historical layer. Because pDRM lock-in occurs, by definition, in a slow mixing regime near the bottom of the SML, it is intrinsically more heterogeneous than bulk mixing. This can be easily seen with the bioturbation model of core MD90-0961 (Fig. 4.9a): here, the bulk diffusivity at the mean pDRM lock-in depth of $\sim$17 cm is only $\approx$0.005 cm^2/yr, well below the threshold indicated by *Lecroart (2010)* for homogeneous mixing, despite the much larger diffusivity of 39 cm^2/yr at the sediment-water interface.

Random variations of the lock-in depth can therefore be expected to occur over the typical timescale $\delta t = \delta l_\mathrm{b}/v_\mathrm{b}$ corresponding to the length scale l_b of discrete bioturbation events. The lower bound of l_b coincides with the minimum displacement required for plastic deformation, which, for muddy sediment, is of the order of 1-2 mm (*Dorgan et al., 2007*). This is also the smallest length scale resulting from lattice-automation simulations (*Reed et al., 2006*). The upper bound of l_b might be compared with the size of the strain field produced by the largest burrowing organisms reaching the bottom of the SML, which is of the order of $\sim$ 1 cm for a typical worm (*Dorgan et al., 2007*). The pDRM lock-in depth, and thus the time at which the Earth's field is recorded, is thus expected to change irregularly on a maximum length scale of the order of 1 cm, which is also the size of typical paleomagnetic specimens. This length scale corresponds to $\sim$0.3 kyr in core MD90-0961 and $\sim$0.6 kyr in core MD90-0949. The random nature of such lock-in depth variations is expected to add random noise to paleomagnetic records to an extent that is proportional to the rapidity of field variations. This noise-injection mechanism has important and not yet explored consequences for the evaluation of sedimentary paleomagnetic records (*Teanby and Gubbins, 2000; Tauxe and Kent, 2004*).

As shown above, the relative offset of RPI records with respect to cosmogenic ^{10}Be records provides a direct estimate of the pDRM lock-in depth (e.g. *Carcaillet et al., 2003; Knudsen et al., 2008; Suganuma et al., 2011; Valet et al.,2014; Simon et al., 2018, 2019*). Such estimates can be directly compared with lock-in models derived from bioturbation data (e.g. Fig. 4.9), providing, for the first time, a direct insight into the post-depositional processes affecting cosmogenic and magnetic records of Earth's field variations, as discussed in the next section.

4.7 Matching RPI and ^{10}Be/^{9}Be records

A systematic lag is observed between ^{10}Be/^{9}Be and RPI records of discrete geomagnetic events (excursions and reversals, fig 4.1), which can be explained by the pDRM acquisition model discussed in Sections 4.6.2-3. In the following, this lag is quantified systematically and its variations are related to possible environmental effects.

For this purpose, pairwise RPI and ^{10}Be/^{9}Be records of the same core are treated as discretely sampled time series represented by the vectors $R = (r_1, r_2, ..., r_n)$ and $B = (b_1, b_2, ..., b_m)$, respectively, of measurements performed on different specimens ($n \neq m$). Even in the ideal case where both signals depend only on the magnetic field, which is not the case due to environmental modulations (Chapter 3), the two time series are not directly comparable because (1) RPI is the response to the local field intensity while the production of cosmogenic ^{10}Be is mainly a function of the dipole strength, and (2) the ^{10}Be production rate is a nonlinear function of the dipole strength (*Masarik and Beer, 2009*). In most general terms, the dependence of the two time series on a common parameter describing the Earth's magnetic field intensity, assumed here to be the virtual axial dipole moment μ_{VADM}, is given by

$$B(t) = f_B(p)g(\mu_{\mathrm{VADM}}(t)) + a_B(p) \tag{4.28}$$

and

$$R(t) = f_R(p, s)h(r, t)\mu_{\mathrm{VADM}}(t - z_\lambda/v_{\mathrm{b}}) \tag{4.29}$$

where g is the geomagnetic modulation function, a_B and f_B represent additive and multiplicative environmental effects on the ^{10}Be/^{9}Be records (Chapter 3), which depend on a series of parameters p, and f_R is a RPI calibration factor given by the ratio between the acquisition efficiencies of the natural remanent magnetisation (NRM) and of a laboratory magnetisation used as a normaliser. The NRM acquisition efficiency might be affected by the same environmental parameters p as ^{10}Be/^{9}Be, and by additional parameters s related to the magnetic mineralogy, physical properties, and bioturbation intensity of sediment. The RPI lag associated with a pDRM is expressed by the mean lock-in depth z_λ discussed in Section 4.6.3, and the field geometry is accounted by the location- and time-dependent factor h.

In the following, the effects of a variable field geometry are assimilated with other environmental disturbances and ignored, since it is not possible to disentangle the two phenomena. Accordingly, RPI records can be assumed to be proportional to the virtual axial dipole moment (VADM) of the Earth's field. The nonlinearity of g is known through theoretical calculations (*Masarik and Beer, 2009*) and empirical calibration curves (e.g. *Simon et al., 2016*). However,

the uncertainty of such curves is large enough for a linear approximation of the form

$$B \approx a_B - b\mathrm{VADM} \tag{4.30}$$

to reproduce available data within the respective confidence intervals. Furthermore, a_B can be assumed to be constant in time for cores located far enough from coastal inputs (Chapter 3). These simplifications enable to formulate the simplest possible relationship between $B(t)$ and $R(t)$ as

$$B(t) \approx B_{\max} - b(t)R(t + z_\lambda(t)/v_\mathrm{b}(t)) \tag{4.31}$$

where $B_{\max}$ is the Be-ratio associated with the maximum ^{10}Be production when $\mu_{\mathrm{VADM}} = 0$, through a multiplicative coefficient b related to the response ratio between the two signals, and a lag z_λ/v_b due to the pDRM lock-in depth. Both coefficients depend on environmental and mineralogical parameters, and are therefore a function of time.

The linear relation between R and B in eq. (4.31) is essential for estimating the RPI lag. Two practical ways to obtain such estimates are illustrated in the following.

4.7.1 Dynamic Time Warping

Dynamic Time Warping (DTW) is an algorithm originally used to compare speech patterns in automatic speech recognition (*Sakoe and Chiba, 1978*). This technique allows to find the optimal correspondence between two time series that might have been recorded at different velocities. DTW has been successfully employed in several geophysical applications, including the comparison of RPI records (*Hagen et al., 2020*). By searching the best pairwise match between different records, the DTW algorithm can reduce stratigraphic biases caused by sediment disturbance, age model uncertainties, and variable pDRM lock-in depths.

The DTW algorithm assumes that the two signals being compared differ only by their timing. Therefore, signals with unequal amplitudes and offsets, such as R and B, needs to be pretreated by subtracting their long-term averages (offsets), and by normalising the offset-free results with their amplitude, which is typically identified with the standard deviation. In the specific case of R and B, the transformed signals are given by

$$R'(t) = \frac{R(t) - \langle R \rangle}{\mathrm{sd}(R)} \tag{4.32}$$

and

$$B'(t) = -\frac{B(t) - \langle B \rangle}{\mathrm{sd}(B)} \tag{4.33}$$

respectively.

The optimal alignement between two series is achieved by minimising the so-called cost function corresponding to a local distance measure. In a first step, the DTW requires the construction of matrix containing pairs of differences between the individual measurement of R and B, which is called distance or local cost matrix d. The Euclidean distance is typically used:

$$d(R_i, B_j) = \sqrt{(R_i - B_j)^2} = \|R_i - B_j\|\,, \tag{4.34}$$

where R_i and B_j are the i-th RPI and j-th Be records, respectively. Once the local cost matrix is built, the DTW algorithm searches for the best alignement path, defined as the sequence of (R_i, B_j) pairs that minimize the sum of the corresponding Euclidean distances. This is one of the many sequences obtained by mapping one time series onto the other with the warping function $W = (w_1, w_2, ..., w_k)$ defining the indices j of one time series pairwise associated with the indices i of the other series, which serves as reference. Not all minima of the sum of Euclidean distances makes sense, so that the following additional constraints are introduced:

1. Boundary conditions: the two signal share the same begin and ending point, which means that the optimal path W starts at the $(i = 1, j = 1)$ element of the cost matrix and ends at $(i = n, j = m)$.
2. Monotonicity: the time direction of the two signals cannot be inverted, which means that $i_{k-1} \leq i_k$ and $j_{k-1} \leq j_k$ for every element k of W.
3. Continuity: $i_k - i_{k-1} \leq 1$ and $j_k - j_{k-1} \leq 1$ restricts the optimal path W to single time steps of each series, so that no elements are discarded.
4. Sakoe-Chiba warping window: $|i_k - j_k| \leq r$, where $r > 0$ is the maximum offset allowed between the two time series at any point, so that W is restricted to a band along the diagonal of the cost matrix.
5. Slope constraint: $|j_s - j_k| / |i_s - i_k| \leq$ p for any pair of elements of W, so that one time series is not compressed or extended beyond a factor p with respect to the other.

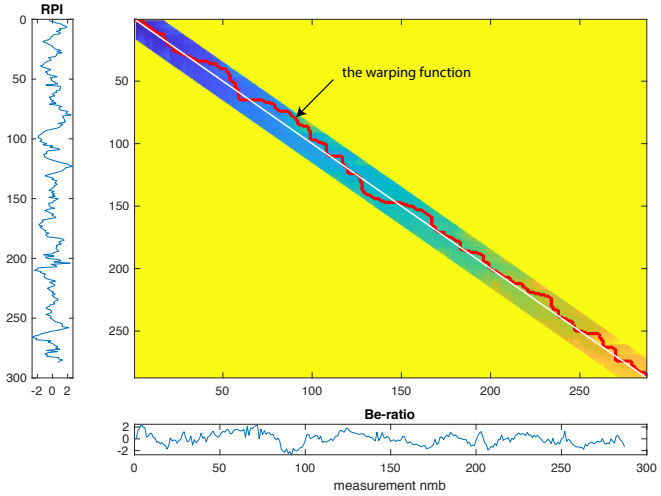

Figure 4.11: DTW mapping function for the standardized RPI and ^{10}Be/^{9}Be series in MD98-2183, constrained within a warping window of 30 points. The colour map within the warping window represents the Euclidean distance between the corresponding pair of data of the two time series, from blue (small) to red (large). Mapping function is plotted by using MATLAB.

In practice the warping path is constructed by calculating the accumulated, or global cost matrix $D(i,j)$ with

$$D(i,j) = d(i,j) + \min \begin{cases} D(i-1,j) \\ D(i,j-1) \\ D(i-1,j-1) \end{cases}, \tag{4.35}$$

Once the global matrix D is constructed, the warping path W can be found by backtracking from the end point of the matrix. A DTW mapping example for core MD98-2183 is shown in Fig. 4.11.

Results obtained by mapping RPI onto ^{10}Be/^{9}Be with DTW are shown for site MD98-2183 (Fig. 4.12) and MD95-2016 (Fig. 4.13). Although the coincidence between RPI and Be-records is greatly increased by DTW, some artefacts due to excessive contraction/stretching of the RPI signal are evident. If arising from the comparison of two different cores, such artefacts could reflect nonconformities, that is, periods of time with lacking sedimentation in one sequence or the other. In the case of two signals from the same core, such nonconformities could be associated with the recording process: for instance, a sudden increase of the pDRM lock-in depth can erase part of the previously recorded signal and even reverse the time-depth relationship. However, one must keep in mind that timing is not the only source of differences between the two signals: noise and other uncorrelated features can easily drive DTW into unrealistic or meaningless warping paths.

Nevertheless, DTW has been successfully employed for the preliminary identification of geomagnetic events subsequently analyzed with a more refined method illustrated in the next section.

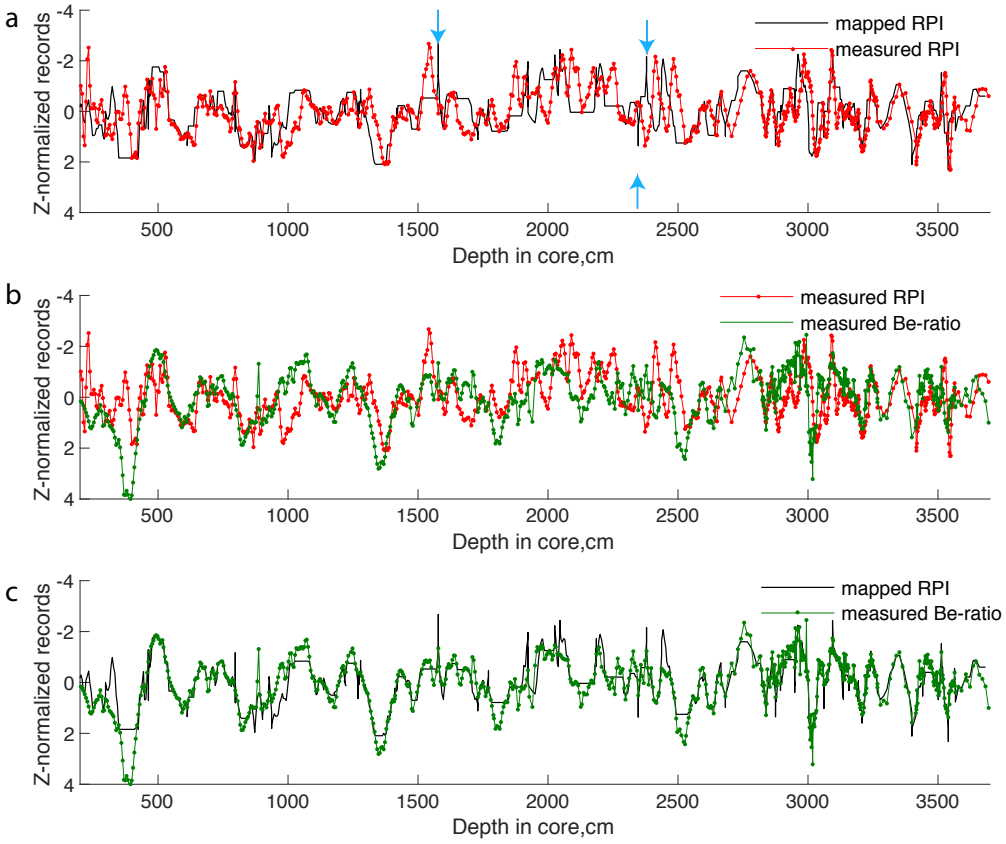

Figure 4.12: a) Comparison of measured and mapped RPI signal with Sakoe-Chiba band window in the core MD98-2183. Blue arrows indicate the artefacts produced by DTW algorithm. b)Original measurements of ^{10}Be/^{9}Be and RPI records. c) Original ^{10}Be/^{9}Be record and mapped RPI.

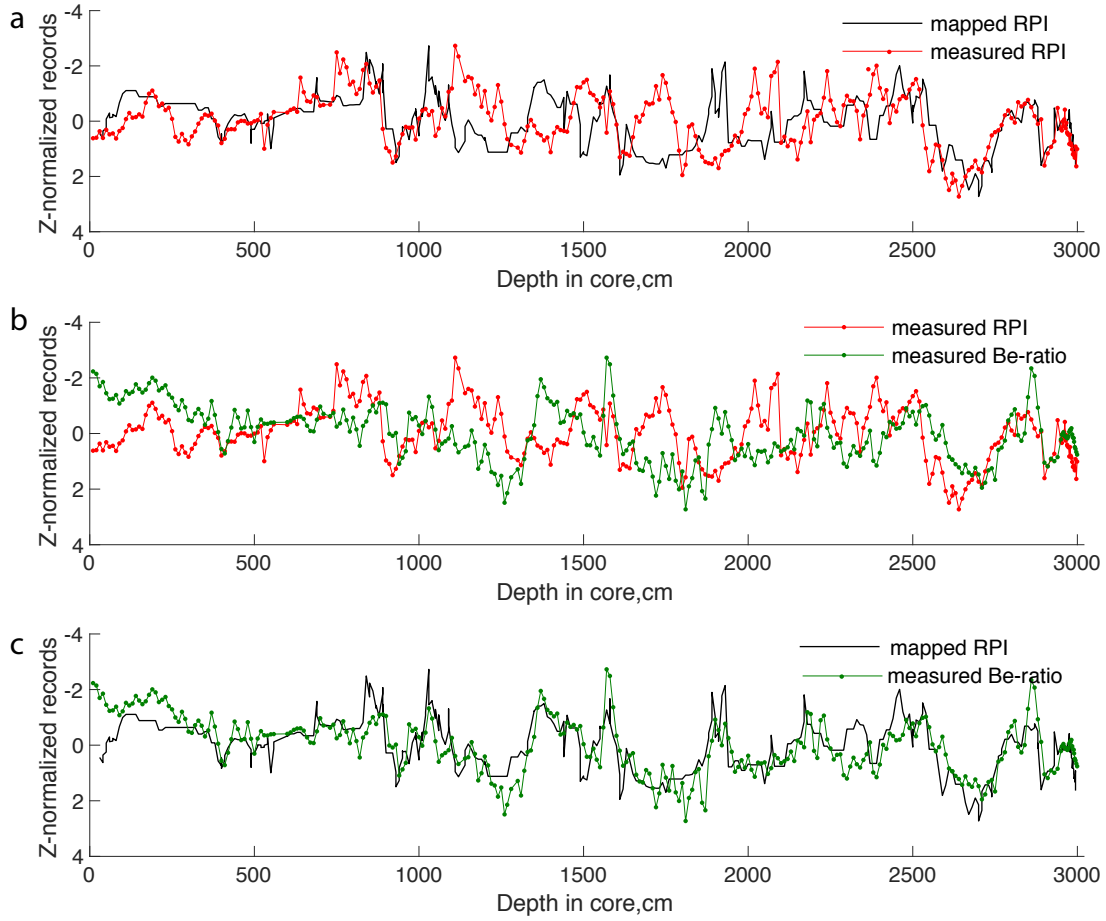

Figure 4.13: a) Comparison of measured and mapped RPI signal with Itakama band window in the core MD95-2016. Blue arrows indicate the artefacts produced by DTW algorithm. b)Original measurements of ^{10}Be/^{9}Be and RPI records. c) Original ^{10}Be/^{9}Be record and mapped RPI.

4.7.2 Cross-correlation

Another commonly used method for comparing two time series, in our case R and B, is based on the the so-called cross-correlation function

$$\rho_{R,B}(s) = \frac{\langle (R(t-s) - \mu_R)(B(t) - \mu_B) \rangle}{\sigma_R \sigma_B}, \tag{4.36}$$

where s is the so-called lag, $\mu_X = \langle X \rangle$ is the average of a signal X over time, and $\sigma_X = \langle (X - mu_X)^2 \rangle^{1/2}$ the standard deviation. In signal processing, the CC is also called the sliding dot product (*Usoro, 2015*). The autocorrelation function, AC, is a special case of CC with $R = B$. In this case, $\rho(s)$ is an even function with its maximum $\rho = 1$ at $s = 0$. Otherwise,

$\rho(s)$ is a generic function comprised between $+1$ (perfect correlation), and -1 (perfect anti-correlation). A very useful property of the CC function is the shift theorem, which states that, if one signal is a scaled copy of the other signal shifted by Δt, in our case $R(t) = a + bB(t - \Delta t)$, then the maximum amplitude $\rho_{R,B} = \mathrm{sign}(b)$ is obtained for $s = \Delta t$. This property enables to calculate the fixed time lag between to signals by searching for the maximum of the absolute value of the CC function. The solution is unique, as long as the linear relation between the two signals holds exactly.

In our case, both signals contain two components: the common response to magnetic field variations, and an additional, unwanted signal produced by environmental variations. As seen in Section 4.7.1, the two components of a Be-record are given by

$$B(t) = b(t)M_{\mathrm{VADM}}(t) + b_0(t), \tag{4.37}$$

where M_{VADM} is the virtual axial dipole moment, b a multiplicative coefficient affected by the environment (e.g. the efficiency of ^{10}Be transport, see Chapter 3), and b_0 an additive coefficient representing ^{10}Be inputs unrelated to the atmospheric production. The multiplicative coefficient $b(t) = b_1 + b_2(t)$ can be decomposed into a constant part b_1, which is the calibration coefficient enabling to convert VADM variations into ^{10}Be production changes, and an environmental modulation term b_2, so that

$$B(t) = b_1 M_{\mathrm{VADM}}(t) + \beta(t), \tag{4.38}$$

with $\beta(t) = b_2(t)M_{\mathrm{VADM}}(t) + b_0(t)$. If environmental effects are sufficiently small, $\langle b_1 \rangle = 0$ and β can be treated as a noise term. A similar reasoning holds for the RPI signal

$$R(t) = a_1 M_{\mathrm{VADM}}(t - \Delta z_{\mathrm{b}}/v_{\mathrm{b}}) + \alpha(t), \tag{4.39}$$

with $\alpha(t) = a_2(t)M_{\mathrm{VADM}}(t) + a_0(t)$, where $\Delta z_{\mathrm{b}}/v_{\mathrm{b}}$ is the time lag caused by the pDRM lock-in depth. In this case, a_1 is proportional to the ratio between the acquisition efficiencies of NRM and of the laboratory magnetisation used as a normaliser, respectively, a_2 contains the environmental modulations of these efficiencies, due to changes in magnetic mineralogy and other sedimentary properties, and a_0 is an additive term accounting for differences between the local field intensity and the dipolar field intensity associated with the VADM. It can be reasonably assumed that the noise terms α and β are uncorrelated to VADM variations, as long as a_2 and b_2 have zero expectation, which is true if the environmental modulation is small. In this case, the CC function of R and B is given by

$$\rho_{R,B}(s) \approx \left(\frac{\sigma_\beta^2}{b_1^2} + \frac{\sigma_\alpha^2}{a_1^2}\right)\rho_{M,M}(s - \Delta z_{\mathrm{b}}/v_{\mathrm{b}}) + \left(\frac{\sigma_\beta^2}{b_1^2} + \frac{\sigma_\alpha^2}{a_1^2}\right)\frac{\sigma_\alpha \sigma_\beta}{a_1 b_1 \sigma_M^2} \tag{4.40}$$

The first term on the right-hand side of eq. (4.40) is proportional to the autocorrelation function of M_{VADM}, shifted by the pDRM lag $\Delta z_{\mathrm{b}}/v_{\mathrm{b}}$, and the second term is proportional to the CC function of the environmental modulation terms α and β, respectively. The second term moves the amplitude maximum of $\rho_{R,B}$ away from the lag corresponding to the pDRM lock-in depth z_{b}, especially if α and β are correlated with each other. However, if the amplitude of the second term is small, the position of the amplitude maximum is mainly controlled by the geomagnetic signal components, yielding an approximated estimate of z_{b}.

A further complication arises from the fact that z_{b} might be directly affected by environmental factors, such as an increase of bioturbation intensity driven by higher primary production in the ocean. In this case, z_{b} is a function of time, which can be estimated only by calculating the CC function over shorter time intervals. This is achieved by defining the time average

$$\langle X \rangle = \int_{-\infty}^{+\infty} W_T(t) X(t) \mathrm{d}t \tag{4.41}$$

over a finite time interval T using a window function W_T of width T, such that the integral of W_T over time is equal to 1. Ideally, T should be as small as possible to maximize the temporal resolution of the reconstructed lock-in depth. On the other hand, however, the relative contribution of noisy terms increase with decreasing T, so that a compromise must be found between resolution and reliability. In principle, the $T \rightarrow 0$ limit of correlation analysis coincides with the warping path of DTW (Section 4.7.1). Vice-versa, correlation analysis is a time-averaged version of DTW that eliminates sudden time scale changes due to climatic signal contaminations.

As discussed in Chapter 3, environmental effects on individual Be-records of the MB reversal can be as large as 10-20% of the maximum ^{10}Be/^{9}Be increase produced by the disappearance of the dipole field. This means that the environmental contamination can be as large as the geomagnetic signal, or even larger, during stable polarity periods, violating the DTW and CC analysis requirements for reconstructing the RPI lag. Therefore, CC analysis has been restricted to a limited number of geomagnetic events characterised by a significant decrease of the dipole strength. A total of 17 and 7 geomagnetic events have been selected from the records of core MD98-2183 (Tables 4.3) and MD95-2016 (Tables 4.4), whereby most of them have been formally identified as geomagnetic excursions on the basis of RPI and ^{10}Be/^{9}Be records from other sites (*Lund et al., 2006; Simon et al.,2016*). The RPI lag for each selected event has been calculated upon minimising the CC function of the original ^{10}Be/^{9}Be and RPI data versus core depth (eq. 4.36) over the depth intervals shown in Fig. 4.13-4.14. The mean squared difference between the two records after shifting the RPI data upwards by the estimated lag is a measure of the mean variance σ_0^2 of the noise terms α and β, which

causes the uncertainty δz_{b} of the lag estimate. Accordingly, δz_{b} is calculated by shifting the RPI signal upwards or downwards until the CC function has increased by $\sigma_0^2/(\sigma_B\sigma_R)$.

RPI lag values for both cores are comprised between 0 and 30 cm, with means of 13.9 and 16.4 cm for MD98-2183 and MD95-2016, respectively. These values are in line with most estimates reported in the literature. Uncertainties are mostly comprised between 5 and 20 cm, and do not correlate with lag values or with the Pearson coefficient corresponding to the amplitude maximum of the CC function. The observed Pearson correlation coefficients can be explained by eq. (4.40) if $\sigma_\alpha\sigma_\beta/\sigma_M^2$ is comprised between 0.1 and 0.4, which means that the relative contribution of variable field geometry and climatic contaminations to a single record is of the order of the square root of this value, that is, 30-60%. If the ratio of $\sim$2 between the standard deviation and the maximum amplitude of the selected records (Fig. 4.14-15) is taken into account, these contributions amount to 15-30% of the maximum variation of the geomagnetic record associated with the disappearance of the dipole field. For comparison, the relative contribution of environmental contaminations to ^{10}Be/^{9}Be records of five marine sites during the M-B reversal, including MD98-2183 and MD95-2016, has been estimated to be comprised between 10 and 20% (Chapter 3, *Savranskaia et al., submitted*). Considering that unavoidable changes in field geometry contribute to the difference between ^{10}Be and RPI records of field excursions and reversals, we conclude that the amplitude of environmental contaminations in ^{10}Be/^{9}Be records is equivalent to a 10-20% change of the present-day dipole strength. The importance of these contaminations can be fully appreciated by considering that this analysis has been restricted to the most evident geomagnetic features of both cores.

4.8 The environmental modulation of sedimentary 10-Be and RPI records

Sedimentary records offer the unique advantage to trace continuous changes of the Earth's magnetic field, but, on the other hand, they are affected by three main problems: (1) lack of absolute calibration, which means that proper empirical normalizations are necessary to obtain absolute values of the field intensity, (2) the existence of post-depositionary processes leading to a significant smoothing or alteration of the original signal, and (3) environmental contaminations. Cosmogenic (^{10}Be) and RPI records are affected in very different manners by these problems. For instance, normalization by ^{9}Be effectively removes variations in ^{10}Be concentration produced by changes in the scavenging efficiency of sediment, so that post-depositionary processes are limited to a smoothing effect produced by bioturbation. Environmental contaminations of ^{10}Be/^{9}Be records originate entirely from differences in the oceanic transport path of both isotopes from their sources, and from the climatic sensitivity of ^{9}Be sources (see Chapter 3). On the other hand, RPI records are significantly affected by sediment properties, beginning with the magnetic mineralogy, which heavily affects NRM normalization and has therefore

№	Event	Core depth (cm)	Age (ka)	v_b (cm/ka)	z_b (cm)	δz_b (cm)	$CaCO_3$ (%)	$-r$
1	Lachamp	374-458	35-43	10.46	30	15	20	0.73
2	Norwegian Greenland Sea	527-701	49-66	10.18	5	20	13	0.82
3	Fram strait/Post Blake	797-862	84-101	3.67	5	16	11	0.78
4	?	1062- 1227	145-169	6.84	15	10	19	0.69
5	Iceland Basin	1313-1461	182-211	5.09	20	10	N/A	0.90
6	Pringle falls	1461-1541	211-229	4.38	22	13	N/A	0.71
7	Portuguese margin	1784-1878	279-302	3.94	16	8	N/A	0.82
8	?	1878-1907	302-311	3.31	10	4	N/A	0.37
9	Laguna del sello	2090-2175	370-398	3.02	4	4	N/A	0.83
10	Big lost	2483-2621	516-579	2.17	30	10	N/A	0.85
11	La palma	2621-2667	579-594	3.06	9	11	N/A	0.61
12	Delta	2778-2858	627-693	1.23	0	7.1	N/A	0.68
13	Matuyama-Brunhes	2984-3056	745-785	1.79	16.9	12.1	7	0.75
14	?	3194-3242	868-891	1.99	4.7	14.4	5.9	0.66
15	Kamikatsura	3242-3352	891-957	1.66	12	12	9.6	0.86
16	Jaramillo superior	3352-3472	957-1027	1.74	17.5	15	N/A	0.83
17	Jaramillo inferior	3528-3564	1058-1080	1.67	20	4.6	N/A	0.81

Table 4.3: Depth and age of selected geomagnetic events used for RPI and Be-ratio comparison in MD98-2183. z_b is the offset between the RPI minimum and $^{10}Be/^{9}Be$ maximum associated with each event, δz_b is the corresponding confidence interval, v_b is the sedimentation rate, and r is the Pearson coefficient corresponding to the amplitude maximum of the CC function.

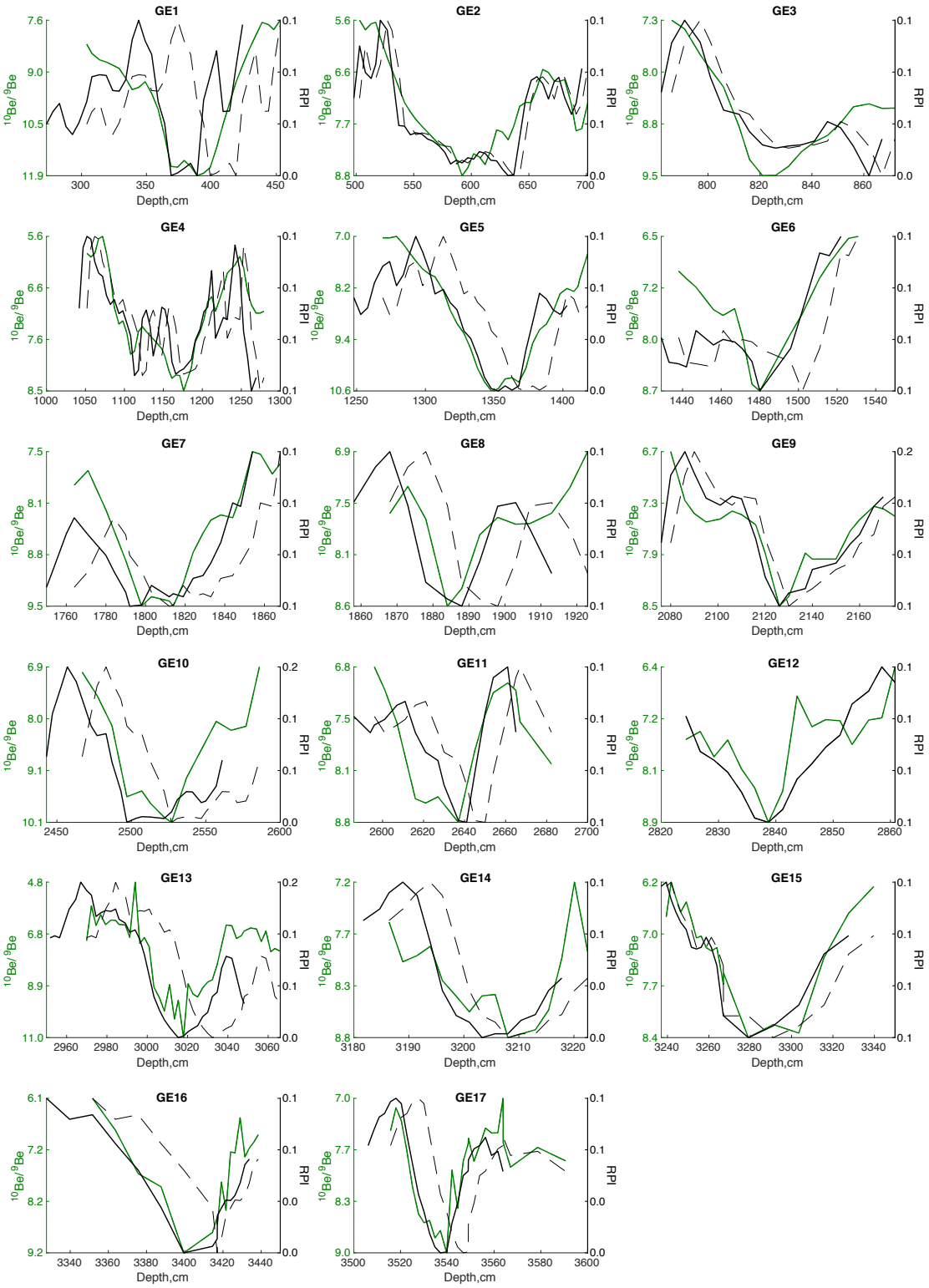

Figure 4.14: RPI and ^{10}Be/^{9}Be variations in MD98-2183 during intervals characterised by significant magnetic field intensity changes for the last 1100 ka (see Table 4.3 for age model). Dashed black lines corresponds to the measured RPI and solid black lines are the corresponding RPI records offset by the lag z_{b} determined with CC analysis.

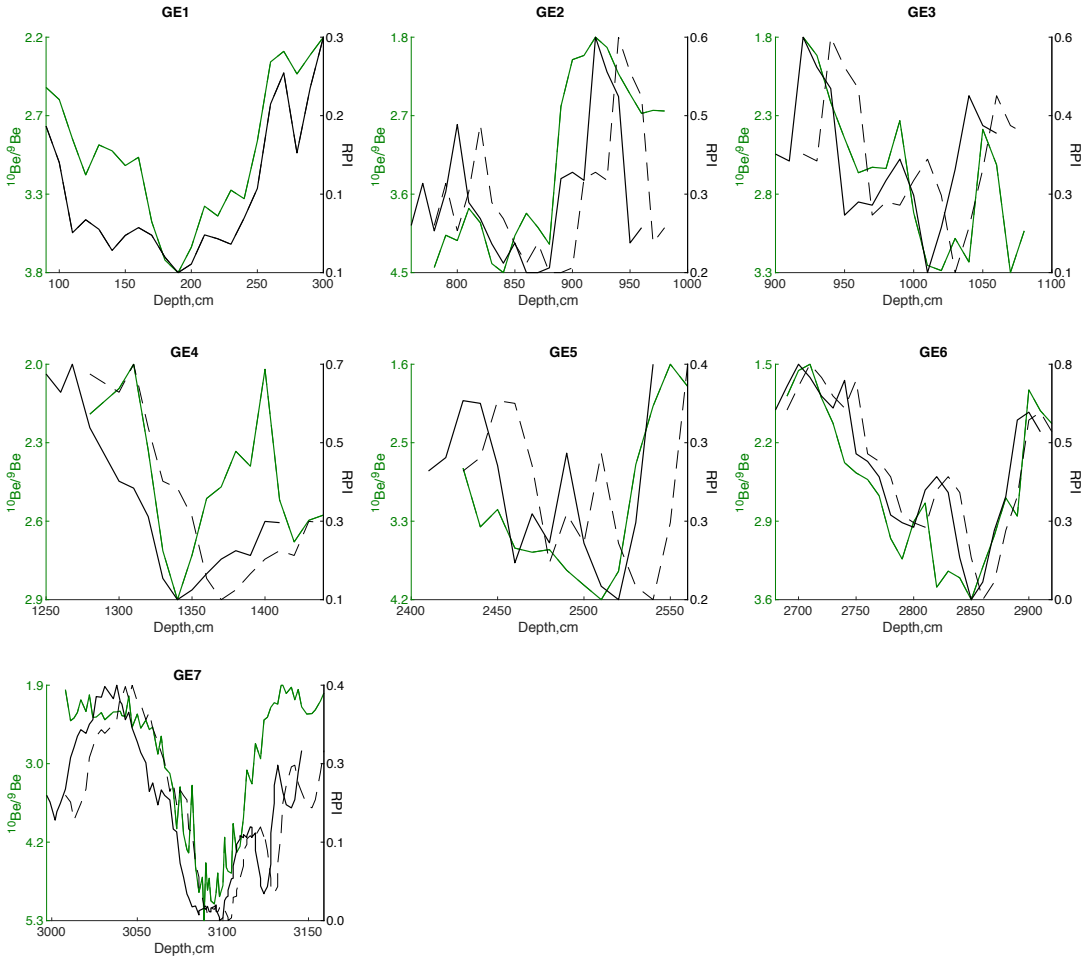

Figure 4.15: RPI and ^{10}Be/^{9}Be variations in MD95-2016 during intervals characterised by significant magnetic field intensity changes for the last 800 ka (see Table 4.4 for age model). Dashed black lines corresponds to the measured RPI and solid black lines are the corresponding RPI records offset by the lag z_{b} determined with CC analysis.

№	Event	Core depth (cm)	Age (ka)	v_b (cm/ka)	z_b (cm)	δz_b (cm)	$-r$
1	Laschamp	90-300	16-44.73	7.44	0	20	0.86
2	Blake	820-930	113-143	3.69	20	30	0.60
3	Iceland-Basin	920-1060	140-180	3.54	20	10	0.53
4	Calabrian Ridge 0 Fram Strait	1280-1420	243-271	5.01	30	20	0.66
5	Calabrian Ridge 2	1390-1650	539-648	2.38	30	10	0.86
6	Delta	2690-2890	657-713	3.58	10	30	0.85
7	Matuyama-Bunhes	3008-3175	740-803	2.7	5	11	0.81

Table 4.4: Depth and age of selected geomagnetic events used for RPI and Be-ratio comparison in MD95-2016. z_b is the offset between the RPI minimum and ^{10}Be/^{9}Be maximum associated with each event, δz_b is the corresponding confidence interval, v_b is the sedimentation rate, and r is the Pearson coefficient corresponding to the amplitude maximum of the CC function.

been the focus of extensive investigations (*Tauxe, 1993; Roberts et al., 2013*). However, the entire mechanism of NRM acquisition is potentially affected by the depositional and sedimentary environment. For instance, DRM acquisition is controlled by the flocculation process (*Lu et al., 1990; Katari and Tauxe, 2000; Valet et al., 2017; Shcherbakov and Sycheva, 2010*), which in turn depends on the hydrodynamic regime (*Griffiths et al., 1960; Tanty et al., 2016*) and the composition of suspended matter (*McCave, 1984; van Leussen, 1988*).

As shown in Section 4.7, DRM is completely replaced by a pDRM in bioturbated sediment. PDRM acquisition is controlled by the physical properties of the SML, by the bioturbation processes (*Zhao et al., 2016*), and, possibly, by sediment lithology. It is extremely difficult to discriminate between intrinsic variations of the pDRM acquisition efficiency, expressed by how well remanence carriers become aligned with the Earth's field, and normalization effects due to changes in magnetic mineralogy, which is also, in part, a function of sediment lithology. For instance, some of the weak correlations found between RPI and lithology (*Franke et al., 2004*), are equally well explainable by (1) a direct effect of clays on the sediment cohesiveness of the sediment matrix, (2) selective adhesion of ultra-fine magnetite particles and magnetosome chains on clay platelets (*Galindo-Gonzalez et al., 2009*), and (3) a correlation between lithology and magnetic mineralogy (*Ouyang et al., 2014; Chang et al., 2016*) affecting the laboratory magnetization used for normalization. A study of the orbital periods in RPI records North Atlantic (*Xuan and Channell, 2008*) concluded that the observed correlation between RPI and 41/100 kyr orbital cycles is introduced directly through magnetite grain size variations, driven for instance by bottom currents, rather than by the a climatic modulation of the NRM normalizers.

The first time availability of a complete model for the effects of bioturbation on Be-

and RPI-based records enable to test some of the above-mentioned contamination effects, as discussed in the following.

4.8.1 The delay of RPI records

As discussed in Section 4.7, a systematic lag is expected between tracer records of geomagnetic field variations, such as ^{10}Be/^{9}Be, and magnetic records, given by RPI. This lag is related to the lock-in depth z_{b} of pDRM acquisition. Estimates of z_{b} for selected geomagnetic events in cores MD98-2183 and MD95-2016 (Tables 4.3-4) enable to investigate possible environmental factors affecting RPI records. In the following, the discussion is focused on MD98-2183, for which more events are available. Results for MD95-2016 are qualitatively similar to those of MD98-2183 and are discussed at the end of this Chapter.

The RPI lag does not display any systematic dependence on the sedimentation rate (Fig. 4.16a) and on sediment physical properties for which continuous logs are available, such as wet bulk density and sediment lightness, which is widely used as a proxy of changes in carbonate or organic carbon content (*St-Onge et al., 2007*) (Fig. 4.16b,c). A slight positive correlation exists between the RPI lag and carbonate content for the few events where $CaCO_3$ concentration measurements are available (Table 4.3).

However, as it is shown by a significant negative correlation, the RPI lag is related to low-field magnetic susceptibility χ_{lf}, which is a measure for the total amount of magnetic minerals in the sediment (Fig. 4.16d), and to the anhysteretic remanent magnetization (ARM, Fig. 4.16e), which is a laboratory-imparted magnetization that is highly selective towards small magnetite particles, in particular single-domain ones (*Egli and Lowrie, 2002*), and magnetofossils (*Egli, 2004*). These particles are also stable carriers of the natural remanent magnetization (NRM) on which RPI estimate is based. For this reason, RPI is often calculated using the NRM/ARM ratio, with the assumption that this normalization eliminates the effect of concentration variations (e.g. *Tauxe, 1993*). In summary, ARM responds to a very restricted subset of magnetic minerals, which are also those responsible for the RPI signal, unlike less specific magnetic parameters such as χ_{lf}. The ARM/χ_{lf} ratio is a measure of the relative contribution of fine magnetic particles to the total magnetic mineral inventory, and has been widely used as a magnetic mineral size indicator for sedimentary materials (*King et al., 1982; Oldfield, 2007*). Noticeably, this ratio does not correlate with z_{b} in a similar manner as ARM or χ_{lf} (Fig. 4.16f).

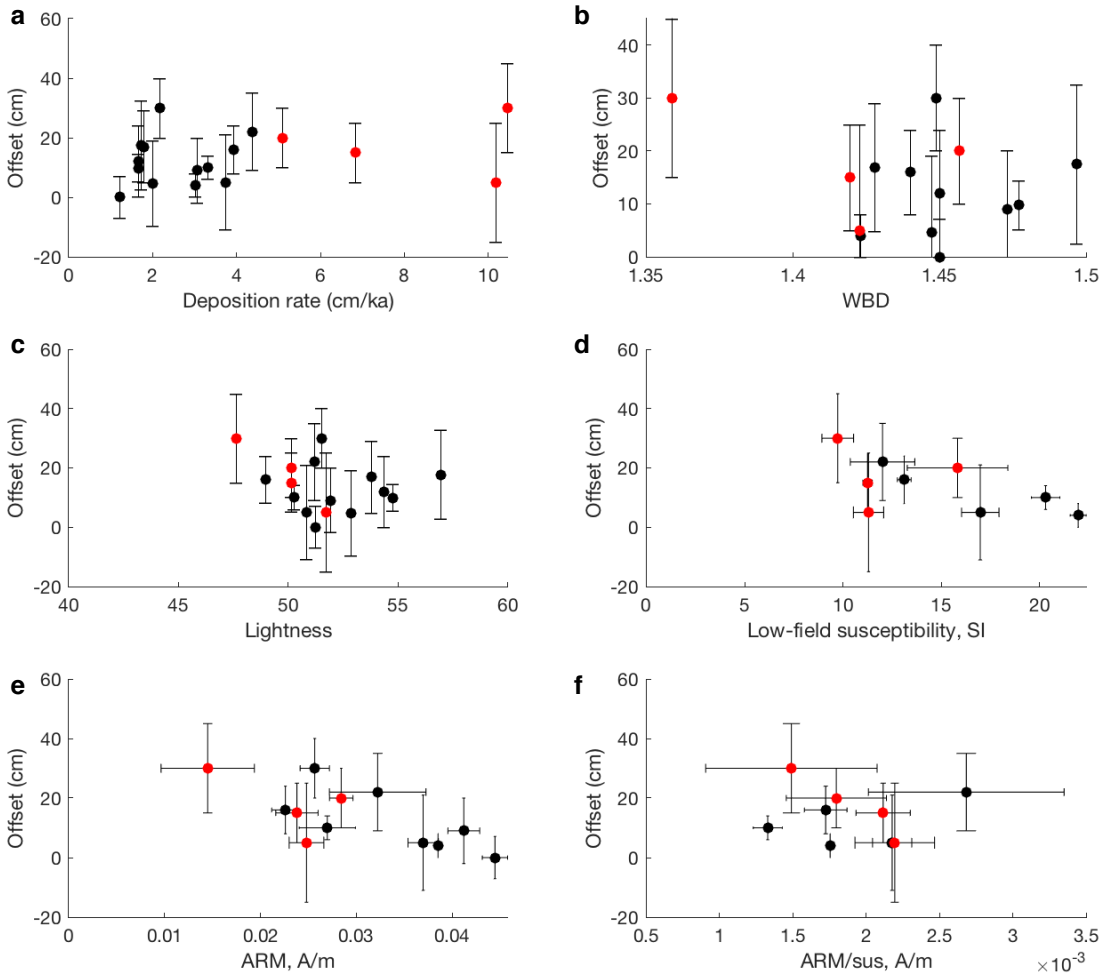

Figure 4.16: Comparison between estimated RPI offsets and selected sediment properties for 17 selected geomagnetic events at site MD98-2183 (Table 4.1). Error bars correspond to confidence intervals for the estimated RPI offsets and to the standard deviation over the corresponding sediment property, respectively, over the depth interval as indicated in table 4.3, used to calculate the RPI offset. Red dots correspond to geomagnetic events, characterised by sedimentation rates >5 cm/kyr. **a** Sedimentation rate, **b** wet bulk density, **c** lightness, **d** low-field magnetic susceptibility (χ_{lf}), **e** anhysteretic remanent magnetization (ARM), **f** ARM/χ_{lf}

The observed correlation between size of magnetic carriers and the pDRM lock-in depth might be explained by (1) a magnetic mineral selectivity of the pDRM acquisition mechanism, or (2) the concomitant variations of the lock-in depth and magnetic mineralogy in response to the the same environmental variations. As far as the magnetic mineral selectivity of the pDRM is concerned, previous works have reported an apparent dependence of NRM/ARM on the type of magnetic carriers, noticing a difference between detrital and biogenic magnetite contributions to the RPI signal (*Yamazaki et al., 2013; Ouyang et al., 2014; Chen et al., 2017*). This difference could be intrinsic to the pDRM acquisition mechanism, reflecting different alignment efficiencies of the two magnetic carrier categories, or it could be related

to the ARM normalizer selectivity towards magnetofossils. In the former case, the alignment efficiency could be related to the lock-in depth via the depth-dependent mechanical properties of sediment. Different lock-in depths for different magnetic minerals could in turn originate from (1) grain size segregation effects in the SML, as observed with the distribution of tektites (Chapter 2), or (2) production of magnetic minerals, in this case magnetosomes, within a certain depth range. *Ouyang et al. (2014)* concluded from the lack of a systematic lag between the detrital and magnetofossil contributions to the NRM that these two magnetic mineral categories share the same lock-in depth. On the other hand, *Valet et al. (2016)* reported coercivity-dependent directional changes during the M-B reversal at site MD98-2183, which might be explained by a lag between the lock-in depth of a low (0-20 mT) and higher (20-60 mT) coercivity components. The fixed end-member direction of low-coercivity component, however, is typical of a magnetic overprint.

As discussed in Chapter 2, grain size segregation can occur inside the SML, due to the selective ingestion of smaller particles by feeding organisms, and to the tendency of smaller particles to percolate through the sediment pores. As a result, larger particles inside the SML tend to posses a smaller sinking velocity and accumulate near the sediment-water interface, creating a grain size gradient. If such a size gradient involves magnetic carriers, either directly through the size of individual magnetic crystals or indirectly through adhesion to larger sediment particles, more particles of a certain size range will be available at the upper or the lower end of the pDRM lock-in range, shifting the mean lock-in depth. In order to assess the potential role of size segregation, one might consider the typical grain size range of sediment particles and magnetic minerals. The median grain size of site MD90-0949, where size segregation of tektites was detected, is 7 μm. Segregation of larger sediment particles begins above this size, affecting in particular biogenic carbonates. In this case, the segregation model of Chapter 2 with 100 μm for the maximum size of >90% of the biogenic carbonate particles, yields a maximum offset of <0.7 cm, which is much smaller than the observed lock-in depth range within individual cores.

The only other mechanism capable of producing a dependence of the pDRM lock-in depth on magnetic mineralogy is the post-depositional dissolution or precipitation of magnetic minerals (*Tarduno, 1995*). If diagenetic processes are excluded, the only source for a magnetic mineralogy gradient within or near the SML is given by magnetotactic bacteria, due to their preferential occurrence near the oxic-anoxic transition zone (*Blakemore, 1982; Faivre and Schüler, 2008*). In this case, the lock-in depth of a magnetofossil pDRM depends essentially on the fate of magnetotactic bacteria after their death. If the living range of these bacteria lies within the SML, their remains will undergo the same mixing process as the bulk sediment, acquiring a pDRM with the same lock-in range as other magnetic particles. If magnetotactic bacteria live below the SML, a pDRM is acquired in-situ during the process of cell dissolution, followed by adhesion of the "naked"magnetosome chains to other sediment particles. In this case, the lock-in function will coincide with the living range of magnetotactic bacteria, and

the associated pDRM is acquired below that of other magnetic particles, e.g. of detrital origin. There are strong arguments against this second hypothesis. First of all, magnetotactic bacteria spends a significant amount of time in the oxygenated zone of sediment, where bioturbation does occurs (*Mao et al., 2014*). For instance, the living range of magnetotactic bacteria in deep-sea sediment is confined within the uppermost $\sim$ 8 cm (*Petermann and Bleil, 1993*), which is well within the maximum depth of bioturbation. Second, the deepest lock-in depths in core MD98-2183 are associated with the smallest ARM values, which is the contrary of what can be expected if the magnetofossil pDRM contribution is acquired below that of other remanence carriers. Therefore, a dependency of the lock-in depth on magnetic mineralogy can only be expected for anoxic diagenetic contributions, such as greigite formation in sulfidic environments. A lock-in depth insensitivity to magnetic mineral changes does not preclude individual magnetic components from possessing distinct pDRM acquisition efficiencies, defined as the ratio between the natural and a laboratory-induced magnetisation acquired in the same field.

In order to explore the possibility of an environmentally-driven correlation between ARM and lock-in depth, additional comparisons have been performed with two climate proxies: δ^{18}O from benthic foraminifera in MD98-2183 (*Simon et al., 2018, Valet et al., 2019*), and reconstructed sea level fluctuations (*Spratt and Lisiecki,2016*) based on the seawater δ^{18}O record, dated fossil coral reef terraces (*Cutler et al., 2003*), insolation (*Moore et al., 2010*), and inverse ice volume model (*Bintanja et al., 2005*). The strong negative correlation between these two proxies (Fig. 4.17a), and the inverse relation with sedimentation rate (Fig. 4.17b) indicate a similar response to global climatic changes related to glacial-interglacial cycles, with colder periods characterised by larger δ^{18}O, lower sea level, and higher sediment fluxes caused by denudation (*Hay, 1988*) and increased aeolian transport (*Mahowald et al., 1999*). These climatic proxies correlate significantly with ARM in such a way that smaller ARM values are associated with colder climatic conditions (Fig. 4.17c-d). Interestingly, this correlation persists if ARM is replaced by χ_{lf} (Fig. 4.17e-f). At this stage, more detailed analysis of magnetic fabric is required to test whether the ARM and χ_{lf} variations are due to the principal contribution of magnetofossils to magnetic mineralogy.

The positive correlation between ARM and global temperature can be explained by the climatic control of primary productivity P: in the equatorial Pacific, P has been shown to increase by a factor ~ 2 during glacial-interglacial transitions (*Paytan et al., 1996*). A similar ARM increase can be assumed if ARM is entirely attributed to secondary magnetite particles, such as magnetofossils, produced by biologically-mediated iron diagenesis in sediment, and if magnetotactic bacterial abundance is limited by organic carbon flux (*Roberts et al., 2011*). Indeed, the same factor of ~ 2 defines full range of mean ARM values during the selected geomagnetic events. The positive relation between P and magnetofossil production is expected to occur whenever P is not limited by iron availability, which is another limiting factor for the occurrence of magnetotactic bacteria (*Roberts et al., 2011*). In this case, highly bioavailable

dust-borne iron acts as a fertiliser that increases P, and therefore magnetofossil production, during glacial periods (*Shoenfelt et al., 2018*). Iron limitation, however, is confined to the Southern Ocean and does not involve the sites analysed here.

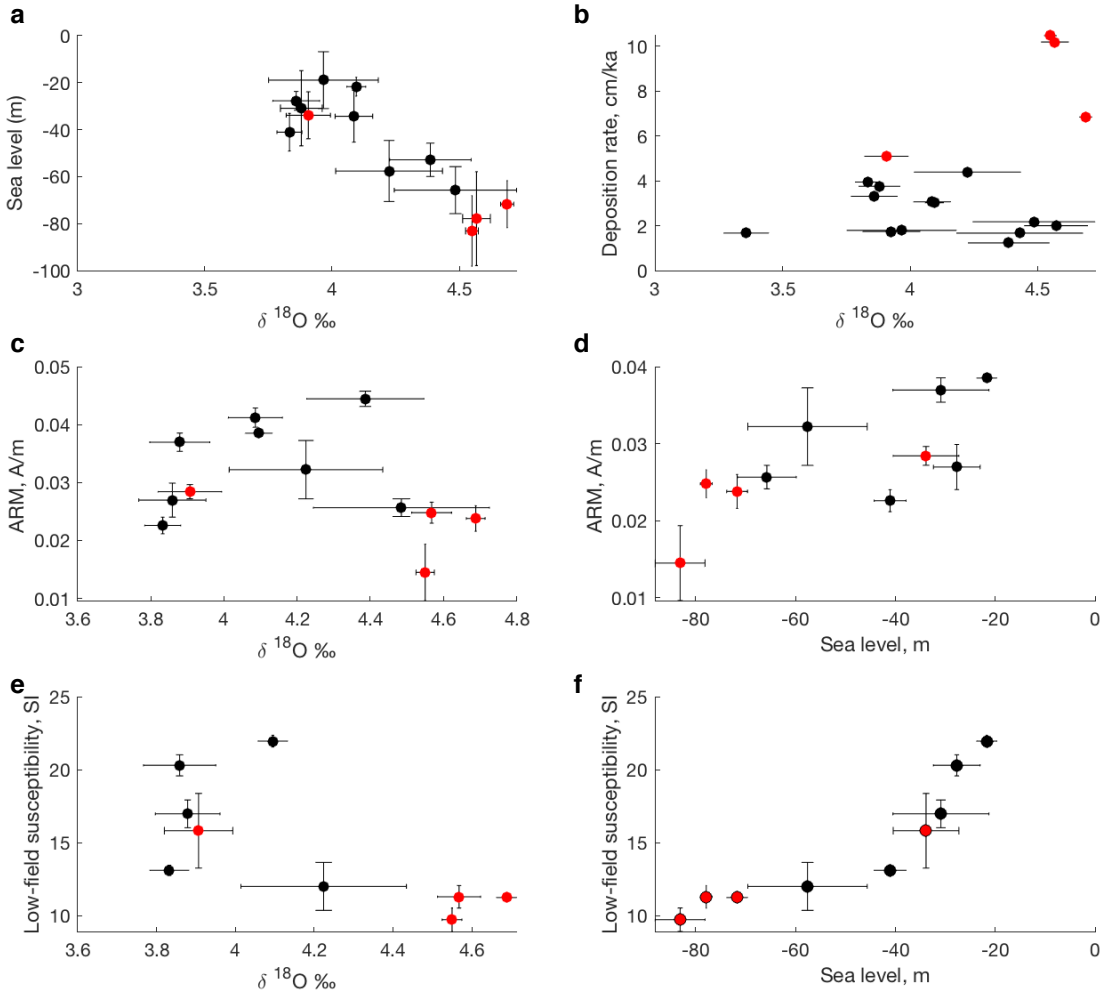

Figure 4.17: Comparison between the global climate proxies δ^{18}O (from benthic foraminifera, this study) and global sea level difference with respect to present (from *Spratt and Lisiecki,2016*), and various sediment properties for 17 selected geomagnetic events at site MD98-2183 (Table 4.3). Error bars correspond to standard deviations over the ∼300 cm depth interval used to calculate the RPI offset. Red dots correspond to geomagnetic events estimates, characterised by sedimentation rates >5 cm/kyr. **a** Correlation between the two climate proxies, and **b** with sedimentation rate, **c-d** anhysteretic remanent magnetization (ARM), **e-f** low-field magnetic susceptibility (χ_{lf}).

A negative correlation between ARM and lock-in depth via a climatically-driven mechanism (Fig. 4.16e) is less obvious. Bioturbation-driven pDRM is related to primary production via organic matter diagenesis, since bioturbation intensity, represented by the depth-dependent diffusivity $D(z)$, can be assumed to be proportional to the organic carbon oxidation rate. In

most early diagenetic models, D is either fully decoupled and treated as an independent model parameter (*Emerson et al., 1985; Rabouille et al., 1998*), or it is assumed to be proportional to the organic carbon concentration only (*Boudreau, 1998*). The bioturbation and oxygen penetration depths predicted by such models are both proportional to

$$L = \sqrt{\frac{K}{k}}, \tag{4.42}$$

where K is the maximum diffusivity at the sediment-water interface, or, alternatively, a proportionality factor coupling diffusivity and organic matter, and k is the oxidation rate (*Middelburg, 2019*). Unfortunately, fits of organic carbon profiles with curves resulting from diagenetic models allow to constrain L and K/k, but not K and k individually (*Soetaert et al., 1998*), so that it is not possible to use such model for predicting D and L changes as the primary productivity increases. The assumption of $D = KC$, where C is the organic carbon concentration, as in *Boudreau (1998)*, leads to the conclusion that L increases with increasing organic matter supply. This conclusion is apparently supported by the correlation found between organic carbon fluxes and L obtained from fits of radioactive tracer profiles with a homogeneous SML (*Trauth et al., 1997*). However, as discussed in Section 4.6, a similar increase of the apparent SML thickness is also obtained if tracer concentrations generated by an exponential diffusivity profile are fitted with the model curves obtained from a homogeneous SML. Opposite trends have been obtained with forward bioturbation models, which predict a decrease of the bioturbation depth, along with oxygen penetration, with increasing carbon fluxes (*Kanzaki et al., 2019*). Finally a model based on fixed exponential oganic carbon concentration profiles yields $L \propto F_{\mathrm{c}}^{-1}$, where F_{c} is the organic carbon flux (*Cai and Sayles, 1996*).

These contradictions are resolved by models featuring a complete coupling between organic carbon supply, oxygen concentration, and bioturbation, even if some arbitrary assumptions must be used to link $D(z)$ with the organic matter concentration. In this case, increasing organic carbon fluxes are associated with increasing values of D at the sediment-water interface, and decreasing bioturbation/oxygen penetration depths (*Dhakar and Burdige, 1996*). The increase of D and decrease of L produces opposite effects on the bioturbation-driven pDRM lock-in depth model of Section 4.16; however, the dependence on D is logarithmic and easily outcompeted by the linear dependence on L (Fig.4.9). For instance, two deep-sea sites (M and C) modeled by *Dhakar and Burdige (1996)* are characterized by organic carbon fluxes of 110 and 47 $\mathrm{mmol/m^2yr}$, respectively, differing by the same factor $\sim$2 that characterizes the hypothetical range of MD98-2183 fluxes deduced from ARM. The corresponding maximum bioturbation coefficients are 214 and 52 $\mathrm{cm^2/kyr}$, with oxygen and bioturbation depths of $\sim$4-5 and $\sim$8-10 cm respectively. The factor $\sim$2-4 increase in D corresponds to a maximum lock-in depth increase of $\sim$15-30%, while the factor $\sim$2-2.5 decrease in L would produce a

similar decrease in the lock-in depth. Doubling the organic carbon flux to deep-sea sediments will thus produce a net decrease of the lock-in depth by ∼40-50%. This decrement of the lock-in depth is compatible with the observed correlation between ARM and RPI offset (Fig. 4.16e), considering the large uncertainty that accompanies the offset estimate, and the fact that possible differences between organic matter degradation rates have not been considered.

RPI lags at site MD95-2016 are much more scattered, and fewer geomagnetic events are available for analysis (Fig. 4.18). In this case, the pDRM lag does not correlate significantly with any of the selected sediment property, including the magnetic mineralogy. The apparent lack of correlation between ARM and lock-in depth might be due to insufficient statistics, or to the fact that labile organic matter is completely consumed without a significant decrease in oxygen concentration. In this case, the maximum bioturbation depth would not depend on the organic carbon flux, giving no reason for a correlation between ARM and lock-in depth. This second explanation is indirectly corroborated by the overall smaller ARM and larger lock-in depths of MD95-2016, compared to MD98-2183, which is compatible with a sediment with a larger oxygen penetration depth, due to lower organic carbon fluxes.

Past organic carbon export to the sediment, which is the motor driving bioturbation, is difficult to reconstruct. Modern particulate organic carbon (POC) export fluxes from the euphotic zone are larger in the Equatorial Pacific than in the North Atlantic, with a factor ∼3 difference for the MD98-2183 and MD95-2016 sites (*Schlitzer, 2000; Buesseler et al., 2007*). This difference was expectedly even larger during the last glacial maximum (LGM) (*Palastanga et al., 2013*). LGM paleoproductivity in the North Atlantic was also lower (*Radi and de Vernal, 2008*), as also seen from microfossil fluxes and carbon accumulation rate in Labrador sea (*Stein and Stax, 1991; Hillaire-Marcel et al. 1994*). Low LGM productivity has been associated with permanent sea-ice cover (*Stein and Stax, 1991*), nutrient availability, and water column properties (*Radi and De Vernal, 2008*), including the general circulation pattern.

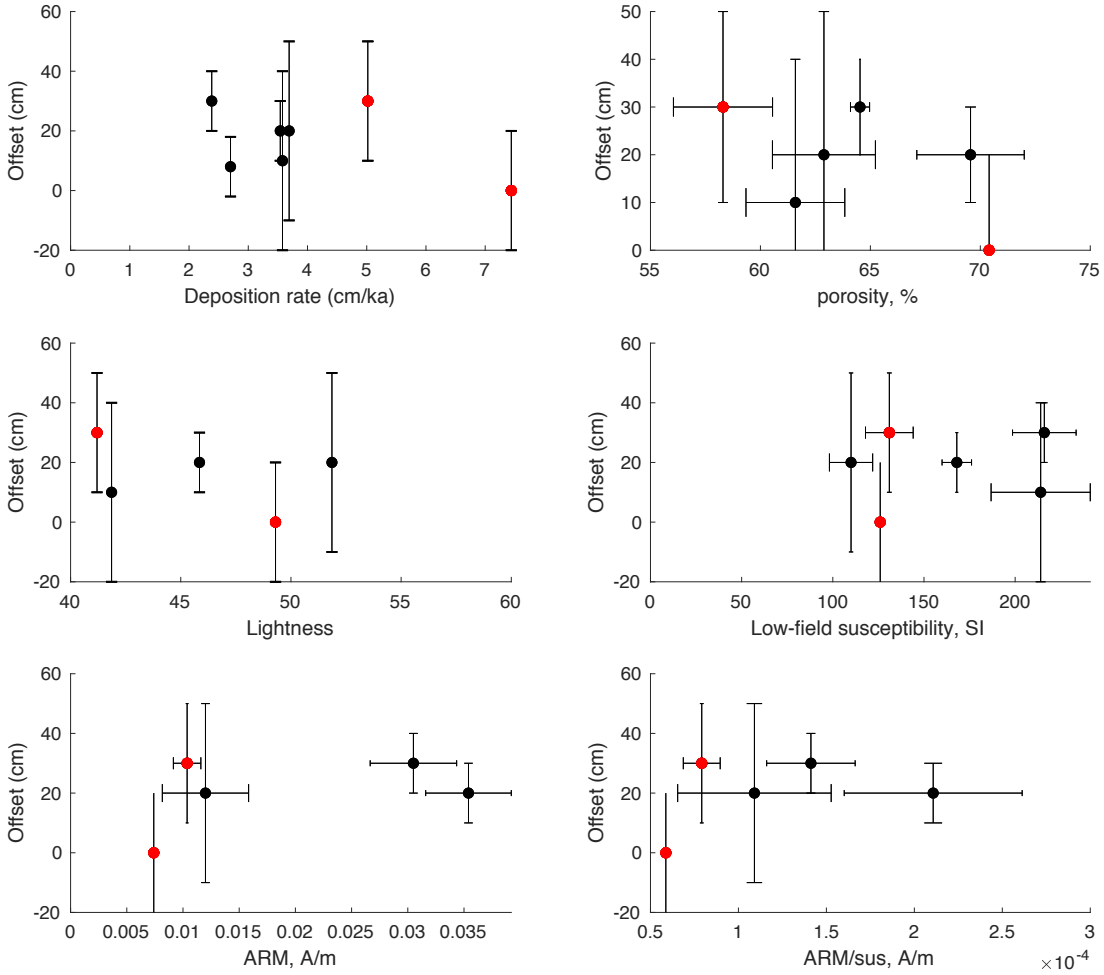

Figure 4.18: Comparison between estimated RPI offsets and selected sediment properties for 7 selected geomagnetic events at site MD95-2016 (Table 4.4). Error bars correspond to confidence intervals for the estimated RPI offsets and to the standard deviation over the corresponding sediment property, respectively, over the depth interval as indicated in table 4.4, used to calculate the RPI offset. Red dots correspond to geomagnetic events, characterised by sedimentation rates >5 cm/kyr. **a** Sedimentation rate, **b** wet bulk density, **c** lightness, **d** low-field magnetic susceptibility (χ_{lf}), **e** anhysteretic remanent magnetization (ARM), **f** ARM/χ_{lf}

4.8.2 Climatic modulation

Sedimentary records of the Earth's magnetic field contain unavoidable climatic contaminations, caused by the complex interplay between sediment lithology/mineralogy, the oceans, and the atmosphere, which is particularly evident at the level of glacial-interglacial climatic cycles (*Bramlette and Bradley, 1940*). In case of records based on cosmogenic isotopes, such as ^{10}Be and ^{10}Be/^{9}Be, these contaminations arise from the environmental modulation of the source distribution, transport, and sediment scavenging, as thoughtfully discussed in Chapter

3. In summary, ^{10}Be is produced in the higher atmosphere by cosmic ray spallation and transferred to the oceans, where it is removed (scavenged) by suspended matter, entering finally into the sedimentary record. The lithological dependence of the scavenging efficiency is removed by normalizing ^{10}Be with the terrestrial ^{9}Be. While effectively removing climatic contaminations caused by lithological variations of the sediment, ^{9}Be normalization introduces its own environmental effects, caused by changing sources (continental weathering), and transport paths. The environmental modulation of RPI records might arise directly from changes in the alignment efficiency of magnetic carriers (e.g. through sediment mechanical properties, in turn driven by lithology), or indirectly through the selective response of the laboratory magnetization used as a normalizer to compensate for concentration changes to changes in magnetic mineralogy. These climatic contaminations are responsible, together with changes in the field geometry, for the differences observed between ^{10}Be/^{9}Be and RPI records. A further complication comes from the proposed possibility that coupling effects between the Earth's magnetic field, the solar wind, and the higher atmosphere act as an additional climatic forcing parameter (e.g. *Wollin et al., 1971; Courtillot et al., 2007; Bard and Delaygue, 2008*).

In the following, the amplitude of climatic contaminations is investigated by comparing the ^{10}Be/^{9}Be and RPI records of the North Atlantic core MD95-2016 with benthic δ^{18}O and other environmental proxies obtained from elemental ratios measured in the same core. The elemental composition of sediments provide information about sources, transport, primary productivity, and atmospheric/oceanic circulation (*Calvert and Pedersen, 2007*). Elemental ratios have been obtained from high-resolution micro-core X-ray fluorescence (XRF) spectrometry using the XRF core scanner AVAATECH. Measurements were performed at EPOC laboratory in the Université de Bordeaux (UMR CNRS 5805). XRF spectra are obtained by measuring the fluorescence emitted by electrons excited by a primary X-ray source, in form of photon counts per photon energy interval (*Richter et al., 2006; Oyedotun, 2018*). Each element is characterized by a series of peaks, and the integrated intensity of these peaks is proportional to its concentration in sediment. Since the procedure for converting XRF outputs into absolute elemental concentrations requires non-trivial calibration procedures affected by large uncertainties (*Weltje and Tjallingii, 2008*), results are usually expressed as elemental ratios, that are widely used to track multiple provenance sources (*Richter et al.,2006*). Relevant elemental ratios and their interpretation in term of environmental proxies are listed in Table 4.5.

The cyclic variations of ^{9}Be, ^{10}Be/^{9}Be, and some environmental proxies (Fig. 4.20) are dominated by 80 ky periodicities associated with the orbital eccentricity (*Lobo and Ridente, 2013*), which are clearly visible in the corresponding spectrograms (Fig. 4.19). This periodicity is more subdued for ^{10}Be and RPI, as expected for signals depending mainly on the Earth's magnetic field, but not for ^{10}Be/^{9}Be. Climatic contaminations appear thus to be driven mainly by glacial-interglacial cycles, which are mostly affecting ^{10}Be/^{9}Be through ^{9}Be normalization.

Elemental ratio	**Interpretation**	**References**
Ca/Fe	Proxy for biogenic carbonate : detrital clay ratio. Ca and Fe reflect marine production and terrigenous input respectively. Ca/Fe might correlate strongly with sedimentary units and is a good proxy for sediment grading, reflecting heterogeneous sediment fabrics.	Rothwell et al., 2015
Si/Sr	Identifies layers rich in detrital silicates (e.g. quartz, feldspar) and poor in biogenic carbonate. Often used for the identification of ice-rafted debris. Si is an important terrigenous and productivity indicator.	Hodell et al., 2008; Rothwell et al., 2015
Sr/Rb	Proxy for the unweathered terrestrial fraction. Useful for discriminating between cold/dry and warm/wet climates. Rb is commonly associated with detrital clay, while Sr might indicate the presence of aragonite which requires a shallow water source.	Fedotov et al.,2012; Temmesfeld, 2014; Rothwell et al., 2015.
Ca/Sr	Discriminates between biogenic and detrital carbonates, with higher values associated with detrital carbonate. Used for ice-rafted debris identification (Heinrich Events).	Hodell et al., 2008
Sr/Ba	Commonly used to distinguish water masses with different salinities and paleo-depths. It is a good paleo-productivity indicator. Sr is fixed by calcifying organisms together with Ca, acting as a biogenic marker. Ba is commonly associated with biogenic aggregates, particularly with siliceous debris. Contrary to Sr, Ba is adsorbed on clay minerals.	Dehairs et al., 1980; Wei et al., 2019; Qi-Feng Xie et al., 2019
Ti/Fe	Used for sediment provenance identification, as a proxy for wind strength and hinterland aridity. Ti is a conservative element abundant in lithogenic sediment, and is not affected by diagenic processes as Fe. Ti is often used as a proxy of erosion and transport of silt and fine sand, increasing significantly during cold periods due to dust inputs. In contrast, Fe increases during the warm periods due to the enhanced run off. Elevated Ti/Fe ratios point to larger grain sizes.	Zarriess and Mackensen 2010.
Ti/Ca	Reflects variations in terrigenous sediment delivery and hinterland climate, correlating with textural changes, graded beds, and increased magnetic susceptibility. Higher values are characteristic of humid interglacial stages with increasing river-discharges.	Arz et al. (2001b, 2003); Litt et al., 2009; Temmesfeld, 2014

Table 4.5: Selected element ratios and their interpretation as environmental proxies.

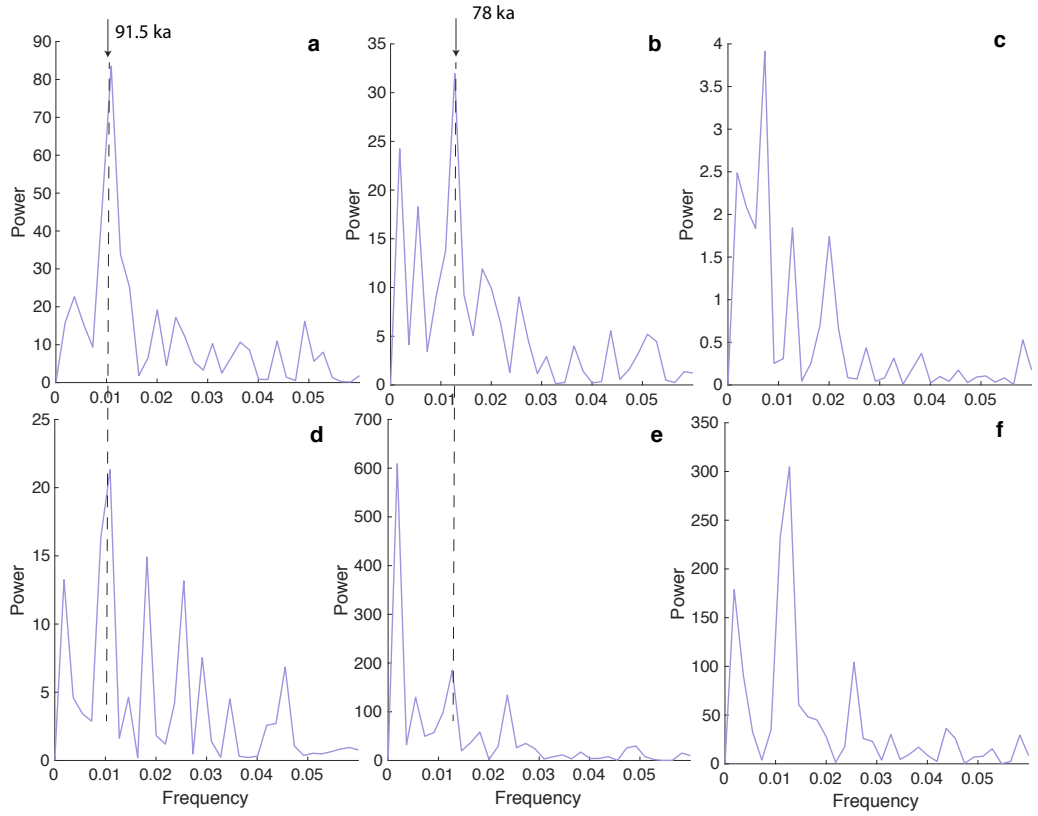

Figure 4.19: Spectrograms of Be-ratio (a), ^{9}Be (b), RPI (c), benthic δ^{18}O (d), ^{10}Be (e) and Si/Sr (f) records, obtained from the fast Fourier transform of the corresponding time series.

Climatic contaminations of the ^{10}Be/^{9}Be record through ^{9}Be normalization are also reflected by significant and opposed correlations existing between these records on the one hand, and benthic δ^{18}O, as well as all elemental ratios listed in Table 4.5 on the other hand. A group of positive correlations with ^{9}Be and negative correlations of similar amplitude with ^{10}Be/^{9}Be includes benthic δ^{18}O, Si/Sr, Fe/Ca, and Ti/Ca (Table 4.6, Fig. 4.20). The negative correlation between ^{9}Be and δ^{18}O implies that more terrestrial Be, released by rock weathering, is delivered to the North Atlantic during cold periods. This is confirmed by Si/Sr, which is a proxy for detrital silicates and ice-rafted debris. Additionally, higher ^{9}Be concentrations also results from lesser dilution by biogenic carbonates, as indicated by the larger Fe/Ca and Ti/Ca values. Finally, larger Ca/Sr values pointing at higher proportion of detrital carbonates, which is also typical of low productivity periods. Negative correlations between ^{9}Be and Sr/Ba, Sr/Rb confirm the same trend. A decrease of Sr/Rb is typically associated with an increase of the supply of detrital clays, and lower Sr/Ba values can be explained by the selective adsorption of Ba on clay minerals.

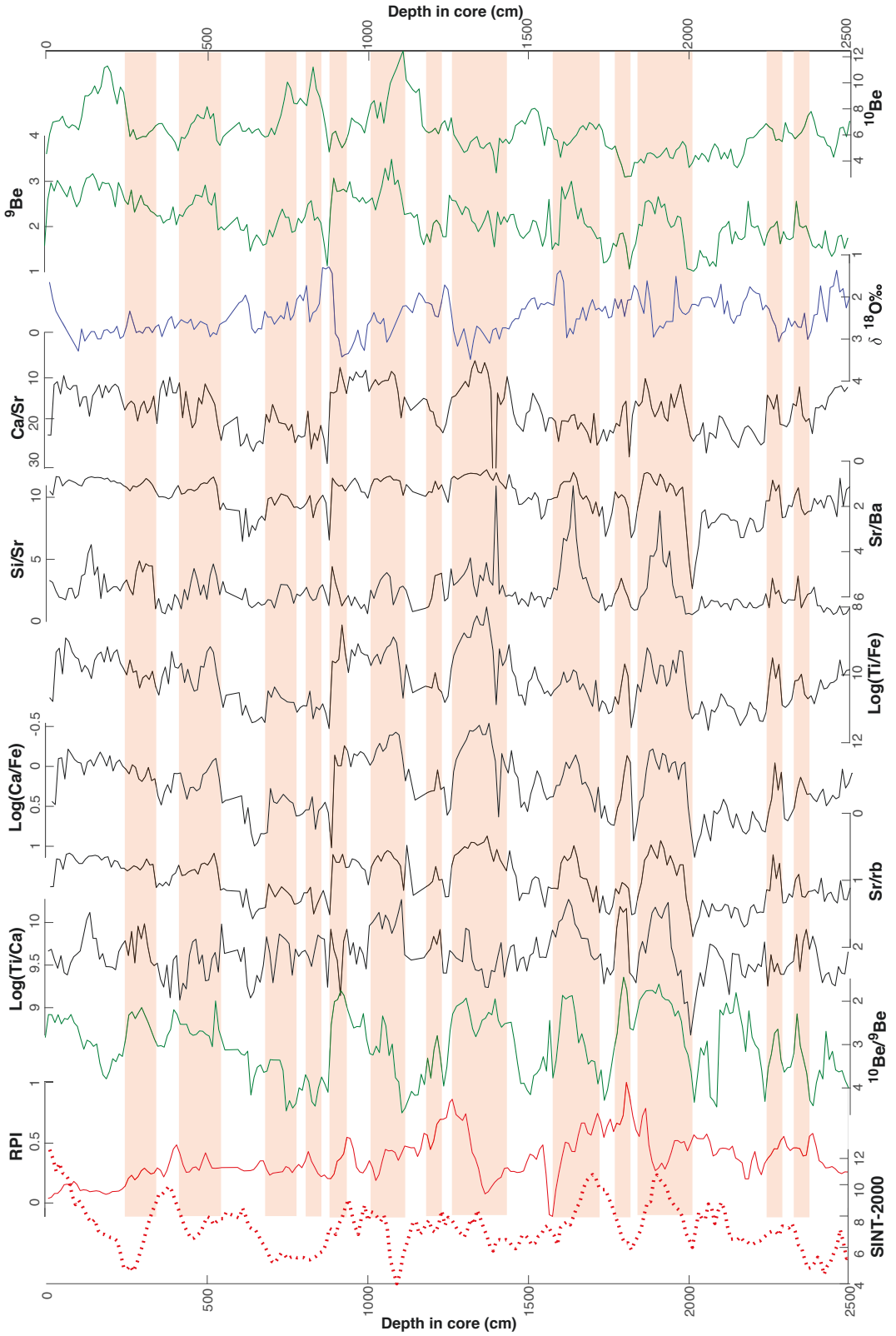

Figure 4.20: Downcore variations of geomagnetic records (^{10}Be, ^{10}Be/^{9}Be, RPI), benthic δ^{18}O, and elemental ratios in MD95-2016. The global RPI stack SINT-2000 (*Valet et al., 2005*) is shown for comparison. Shaded intervals highlight synchronous ^{9}Be and climatic proxy variations.

		NRM	**ARM**	**^{9}Be**	**^{10}Be**	**^{10}Be/^{9}Be**	**RPI**
^{18}O	r	-0.124	-0.19	**0.49**	0.14	**-0.32**	-0.17
	p	0.055	0.0026	2.6×10^{-16}	0.028	2.8×10^{-7}	0.007
Fe/Ca	r	0.0057	-0.124	**0.55**	0.12	**-0.43**	-0.086
	p	0.93	0.055	6.1×10^{-21}	0.07	4.8×10^{-12}	0.18
Ti/Ca	r	0.27	0.23	**0.38**	0.155	-0.22	0.034
	p	1.5×10^{-5}	4.0×10^{-4}	6.4×10^{-10}	0.016	7.4×10^{-5}	0.60
Sr/Ba	r	0.04	0.118	**-0.699**	-0.282	**0.403**	0.2139
	p	0.53	0.066	6.5×10^{-37}	9.0×10^{-6}	8.2×10^{-11}	8.0×10^{-4}
Si/Sr	r	-0.009	-0.051	**0.414**	-0.012	**-0.411**	-0.118
	p	0.88	0.43	2.16×10^{-11}	0.86	3.2×10^{-11}	0.068
Sr/Rb	r	0.089	0.177	**-0.697**	-0.165	**0.501**	0.210
	p	0.17	0.006	1.4×10^{-36}	0.01	1.9×10^{-17}	0.001
Ti/Fe	r	0.006	0.075	**-0.635**	-0.183	**0.438**	0.150
	p	0.93	0.25	1.1×10^{-28}	0.004	9.7×10^{-13}	0.02
^{10}Be	r	-0.025	0.0003	**0.539**	**1**	**0.53**	**-0.344**
	p	0.69	0.10	1.2×10^{-19}	0	5.5×10^{-19}	4.3×10^{-8}
^{10}Be/^{9}Be	r	0.043	0.179	**-0.346**	**0.531**	**1**	-0.033
	p	0.5	0.005	1.69×10^{-16}	5.5×10^{-19}	0	0.6
RPI	r	**0.509**	**0.407**	**-0.354**	**-0.344**	-0.033	**1**
	p	2.6×10^{-17}	5.0×10^{-11}	1.6×10^{-8}	4.3×10^{-8}	0.6	0

Table 4.6: Pearson correlation coefficients r and corresponding p-values p (the probability of $r = 0$), between parameters used for constructing geomagnetic records and environmental proxies in core MD95-2016. Bold values highlight significant correlations characterized by $p < 10^{-8}$.

Among all Be-related parameters, ^{10}Be is the only one that does not display any significant correlations with environmental proxies. This suggests that the correlations seen with ^{9}Be are dominated by the glacial-interglacial modulation of terrestrial Be fluxes, rather than the redistribution of Be inputs by oceanic circulation. Changes in the Be scavenging efficiency, which might be expected from lithological variations, must also play a minor role, since they do not appear in the ^{10}Be record. A similar conclusion about the dominant role of terrestrial Be sources in the North Atlantic was obtained from the comparison of MD95-2016 with Be records from the Indian and Pacific sites (Chapter 3, *Savranskaia et al., submitted)*.

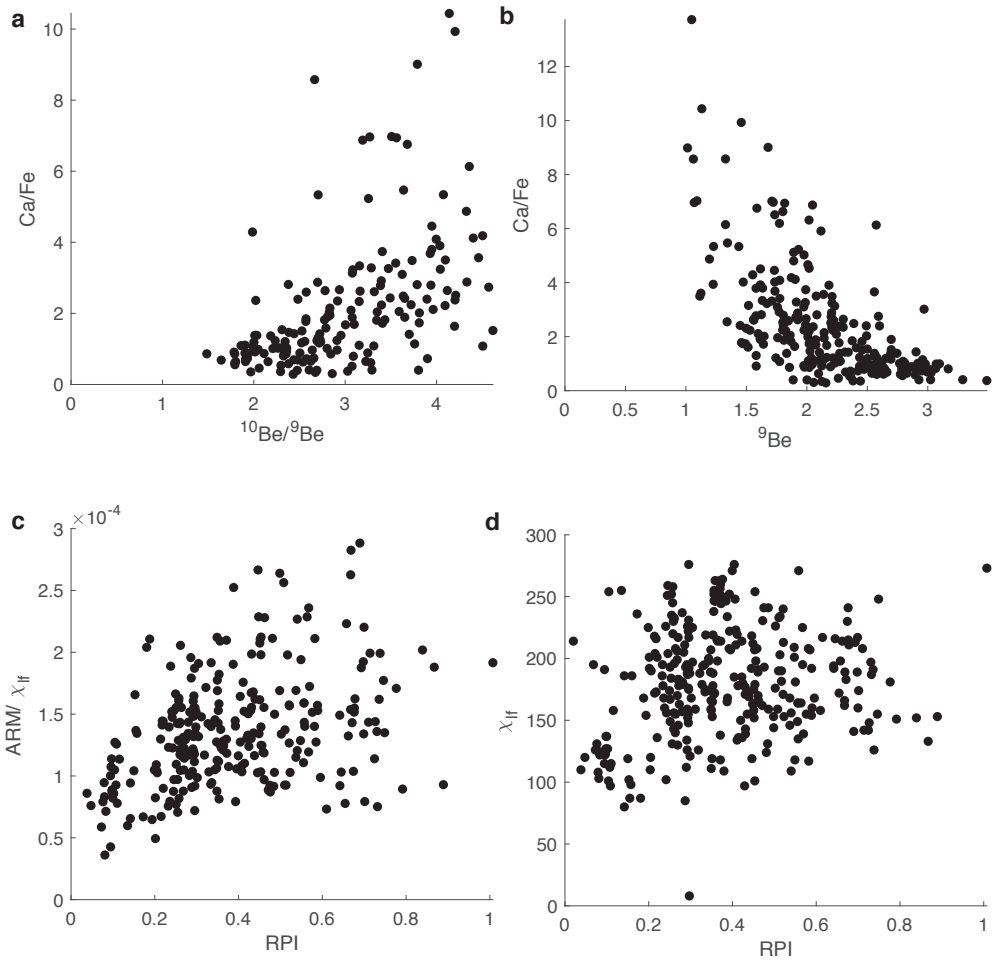

Figure 4.21: (a-b) Relation between Be records and Ca/Fe. (c-d) Relation between RPI and magnetic parameters.

RPI and related magnetic parameters do not show significant correlations with any of the environmental proxies listed in Table 4.6. This, however, does not imply that the RPI record is free of climatic contaminations, as seen by the existence of significant spectral power peaks with periods of ∼120, ∼80 and ∼50 kyr (Fig. 4.19c), close to the ideal ∼100 and 41 kyr orbital periods. The apparent lack of correlation with environmental proxies is therefore due either to its intermittent nature, or to variable phase relationships. The existence of residual contaminations in the RPI record is also suggested by significant positive correlations between RPI and its normaliser, ARM, as well as with the magnetic grain size indicator ARM/χ_{lf} (Fig. 4.21c). In case of fixed magnetic mineralogy and constant alignment efficiency of the remanence carriers, any NRM variation caused by changes in the concentration of remanence carriers (e.g. by dilution) is perfectly compensated by the ARM normalization. The efficient removal of concentration effects is proved by the lack of correlation between RPI and χ_{lf} (Fig. 4.21d). Contaminations of the RPI signal are thus caused by one of the following mechanism, or a combination of them: (1) an increase of the overall NRM acquisition efficiency during

climatic conditions favouring the supply of finer magnetic particles characterized by larger ARM/χ_{lf} values, or (2) an intrinsic dependence of NRM/ARM on magnetic grain size, with smaller magnetic particles being characterized by larger NRM/ARM values. In the first case, changes in NRM acquisition efficiency might be driven by lithology-related mechanical sediment properties, such as cohesiveness, or by changes in bioturbation intensity. The lack of a systematic relation between the pDRM lock-in depths reconstructed in Section 4.8.1 and ARM does not support evident changes of the bioturbation regime. A complex interplay between opposite climatic responses is produced if the relation between NRM and magnetic mineralogy is reversed for one of the two abovementioned mechanism. In this case, RPI might exhibit different dependencies to specific orbital periods, resulting in the intermittent or variable phase response to climatic changes reported by *Xuan and Channell (2008)*.

A direct comparison between RPI and ^{10}Be/^{9}Be shows a complete lack of correlation between the two records (Table 4.6); however, a significant correlation ($0.86 > -r > 0.53$) exists during major geomagnetic events (see Section 4.8). This result indicates that ^{10}Be/^{9}Be records during stable polarity periods are completely meaningless in this core. A slightly better agreement with RPI records ($-r = 0.354$) is obtained with unnormalised ^{10}Be measurements.

Chapter 5

Conclusions

Sediments represents one of the few sources of continuous records of Earth's magnetic field variations, providing fundamental data for understanding the geodynamo and for magnetostratigraphic applications. Sedimentary recording processes are complex and still poorly understood. The extraction of the geomagnetic signal is based on empirical normalization techniques for two types of recording mechanisms: the mechanical alignment of magnetic particles in the Earth's field, which yields so-called relative paleointensity (RPI) records of the local field amplitude, as well as the local field direction, and the accumulation of cosmogenic isotopes (specifically ^{10}Be) produced in the higher atmosphere by cosmic ray spallation at a rate that is modulated by the global strength of the Earth's field, mainly expressed by its dipole moment. Both processes are influenced by local and global environmental factors, leading to a climatic contamination of the geomagnetic records.

Sedimentary inputs of cosmogenic ^{10}Be depend mainly on oceanic transport patterns and on the scavenging efficiency of sediment. Variations of the scavenging efficiency are usually compensated by normalization of ^{10}Be records with authigenic ^{9}Be; however, sedimentary fluxes of terrestrial ^{9}Be are controlled by additional factors, including the distribution of terrestrial sources, the weathering rate, and different oceanic transport paths. The natural remanent magnetization (NRM) of sediment depends on the efficiency with which magnetic carriers becomes aligned with the Earth's magnetic field, which is in turn controlled by their magnetic moments and sizes, the concentration of such carriers, the tendency to form clusters with other sediment particles, the mechanical properties of sediment, and the bioturbation occurring in the surface mixed layer (SML). Variations of magnetic mineral concentrations are corrected by normalizing the NRM with a laboratory induced magnetization; however, the selectivity of this magnetization to certain types of magnetic carriers might introduce additional artifacts related to changes of the magnetic mineralogy.

A detailed comparative analysis of ^{10}Be and RPI records of sediment cores retrieved from the North Atlantic, the Equatorial Pacific, and the Indian Ocean, along with forward and inverse modeling of specific recording processes, has been used in this thesis to investigate the nature and extent of climatic contaminations and the dependence of the recording process on

specific environmental factors. These new insights gained with this work enable a process-based interpretation of differences between records and a more realistic confidence interval estimates of individual or grouped records, along with predictive modeling tools that can guide future laboratory experiments aimed at a better understanding of post-depositionary processes. Main results are summarized in the following.

5.1 The environmental modulation of ^{10}Be records

Because of the dominant role played by the dipolar component of the Earth's magnetic field in controlling cosmogenic ^{10}Be production, and because of the same scavenging efficiency of sediment towards both beryllium isotopes, differences between individual ^{10}Be/^{9}Be records can be expected to entirely reflect temporal changes in source distribution and transport patterns. For this purpose, five sedimentary ^{10}Be/^{9}Be records of the Matuyama-Brunhes (M-B) geomagnetic reversal from the North Atlantic, West Pacific, and Indian Oceans have been compared (Chapter 3). The time span of the MB reversal is sufficiently large for ^{10}Be/^{9}Be records to be practically unaffected by bioturbation-driven smoothing effects, which means that measured concentrations are directly proportional to the incoming Be fluxes.

The five records are characterized by different levels of ^{10}Be/^{9}Be enhancement during the MB reversal, ranging from $\sim$150% to $\sim$220%. The latter enhancement is very similar to the relative increase of the ^{10}Be production rate predicted by cosmic ray spallation models based on the complete disappearance of the modern value of the geomagnetic dipole moment. The wide range of enhancement values, however, points to a very heterogeneous distribution of cosmogenic ^{10}Be by oceanic currents. The main factor leading to higher enhancements appears to be water depth, owing to the increasing Be accumulation in deep water masses, followed by the site location along large conveyor-belt oceanic currents that collect atmospheric ^{10}Be along their surficial path. These factors introduce a multiplicative modulation of cosmogenic ^{10}Be productivity variations. Additive contributions unrelated to cosmogenic productivity exist as well, and are caused by the release of slowly accumulated, much older ^{10}Be (Be-recycling).

An inversion technique has been used to disentangle additive and multiplicative environmental effects. The additive and multiplicative effects are site-specific and time-dependent. A detailed investigation of the dependence of both isotope concentrations on the calcium carbonate content of sediment, which is one of the major factors affecting the scavenging efficiency, permits to exclude artefacts related to sediment composition. Additive environmental effects are relatively large, accounting for up to 60% of the average ^{10}Be/^{9}Be level outside the M-B reversal, with little variations over time, except for one site located near the Maldives. Additive contributions are produced by the release of recycled beryllium at the ocean floor, through a constant flux of pore water carrying a small fraction of exchangeable Be removed from the sediment. The recycled Be flux is unaffected by climate, and the large range of involved sediment ages yields a homogeneous isotopic ratio. Variable additive contributions at the Maldives site

are presumably fed by coral reef dissolution during periods of sea level changes. The additive component display a step-like dependence on water depth, with a relatively sharp threshold of 2.8 km. This means that recycled Be inputs are confined to deep, old waters that are poorly mixed with overlying masses.

Multiplicative environmental effects are site-specific and reflect mainly glacial-interglacial cycles. The Indian and Pacific Ocean cores display a common modulation with respect to the North Atlantic: the difference between these two groups of records oscillates with a maximum amplitude of $\pm$10-15% relative to the maximum ^{10}Be/^{9}Be increase during the M-B reversal. This amplitude is sufficiently large to mask minor dipole moment variations during stable polarity periods. Maximum differences between the enhancement at different sites amount to 40%. These differences do not depend on water depth, sedimentation rate, or ^{9}Be fluxes. The main controlling factor appears to be the location along the path of large oceanic circulation systems, which selectively intercept the atmospheric ^{10}Be flux. Continuing particle scavenging from surface waters and regeneration in deeper parts of the water column causes the concentrations of both Be isotopes to increase along the advective flow path. The preferential ^{10}Be enrichment comes from the surficial segments of these large current systems flowing at great distances from the coast, where terrestrial ^{9}Be inputs are minimal. The environmental modulation amplitude is inversely related to the distance from the coast. Coastal amplification of climatic effects can be explained by boundary scavenging, and by the enhanced sensitivity of atmospheric scavenging and the surface-bottom transportation matrix on coastal proximity.

Reconstructions of the geomagnetic dipole intensity can benefit in several ways from the climatic modulation information gained with our modelling approach. First, a sufficiently diverse set of core locations likely contains at least one ^{10}Be/^{9}Be record with optimal properties that can serve as a reference. These optimal properties are: (1) negligible Be-recycling contributions, which restores the required proportionality with the global ^{10}Be production rate, and (2) minimum climatic modulation, as far as it can be determined from relative comparisons between records. Such conditions are most likely encountered in open basins at sites (1) with <2.8 km water depth, (2) >200 km offshore, and (3) located underneath a large current system extending over regions with minimum terrigenous inputs. Scaling all records on the chosen reference enables us to produce a ^{10}Be/^{9}Be record with reduced noise and artefact contributions.

A systematic comparison of ^{10}Be, ^{9}Be, and ^{10}Be/^{9}Be records with environmental proxies, such as benthic δ^{18}O and elemental ratios (Chapter 4), led to the isolation of another source of climatic contaminations caused by the variability of terrestrial Be sources. This contamination is particularly strong in the North Atlantic, due to elevated continental discharges during glacial periods. In these cases, the unnormalized ^{10}Be record is a better field recorder than ^{10}Be/^{9}Be, as seen by the stronger correlation of ^{10}Be with RPI. Nonetheless, ^{9}Be is essential for identifying and removing the effects of sudden changes of the sedimentation regime. A mixed approach, were the adverse effects of glacial-interglacial cycles on ^{9}Be are selectively removed,

e.g. by band-pass filtering, might be used to overcome the disadvantages of unnormalized and normalized ^{10}Be records.

5.2 Forward and inverse modeling of sediment mixing

Sediment mixing produced by bioturbation is one of the main post-depositionary processes affecting sedimentary records. While the effect of sediment mixing on cosmogenic isotope records is limited to smoothing, being formally equivalent to a low-pass filter, the consequences of bioturbation on RPI records are by far more complex. In fact, contrary to what has been postulated until recently, the NRM of bioturbated sediment is acquired through sediment mixing, at the bottom of the so-called surface mixed layer (SML), rather than below this layer through consolidation. Therefore, RPI records are heavily dependent on post-depositionary processes, as far as the alignment process of magnetic minerals is concerned, in addition to the environmental modulation of the magnetic mineralogy.

Contrary to the transport of tracers across the SML, which is effectively modeled by a homogeneous SML with sharp boundaries, regardless of the real depth-dependence of mixing, the orientation of magnetic minerals depends heavily on details of the bioturbation process, in particular the depth dependence of the sediment reworking rate. Therefore, a new forward model for the translational and rotational components of particle motion in the SML has been constructed. The model links quantitatively the widely investigated tracer mixing, which includes the redistribution of Be-isotopes in sediment, with the acquisition of a post-depositionary detrital remanent magnetization (pDRM). For the first time, the existing lag between ^{10}Be and RPI records of the Earth's magnetic field has been explained by proposed model, that reproduces offsets dependence on several environmental factors.

In a first step, the new model has been used to model the depth distribution of microtektite fragments in the Indian Ocean, produced by the so-called Australasian impact event (Chapter 2). Downcore microtektite profiles represent a physical realization of the sediment response to an impulsive event (impulse response), which enables, through inverse modelling, to extract quantitative information about the mixing process. As postulated since early studies of tracer mixing, the apparent diffusion of sediment particles in the SML appears to depend on their size and association with nutrients, due to selective ingestion by feeding benthic organisms. This selectivity is also seen with larger tektite fragments, which appear to have diffused slightly less than smaller fragments. A definitive confirmation based on natural tracers, rather than short-time laboratory experiments has been obtained for the first time with this work. A detailed analysis of sorted tektite fragments enabled the discovery of an additional phenomenon, consisting in the selective, faster transit of smaller particles through the SML. This phenomenon is known in the context of powder mixing in food and pharmaceutical engineering as size segregation. It is easily visualized by shaking a pot containing nuts of different sizes and is therefore also known as the Brazil nut effect. This effect has been postulated to be responsible

for the long permanence of ferromanganese nodules on the surface of the ocean floor. Size segregation is responsible for the relative upward migration of coarser microtektites with respect to the finer fraction, resulting in a preferential spreading of larger particles above the stratigraphic position of the event. This phenomenon has important implications for sediment dating with benthic foraminifera, since large tests tend to occur above the bulk sediment of same age.

In a second step (Chapter 4), a simple model of organic matter diagenesis has been used to infer a reasonable depth dependence of mixing intensity within the SML. Forward solutions for the homogenoeus SML and depth-dependent mixing has been used to provide a formal proof of the equivalency on these models for describing tracer mixing, as well as obtaining an empirical relationship between the main parameters of the two models, which enables to link widespread sediment mixing information based on the homogeneous SML model with the depth-dependent model required to describe a bioturbation-induced pDRM acquisition.

Finally, a general model for pDRM acquisition has been developed on the basis of the rotational impulse response associated with a depth-dependent diffusion process (Chapter 4). The integral of this impulse response is equivalent to empirical lock-in functions that have been proposed in the past to explain the delay of RPI records. Contrary to empirical lock-in functions, which are based on ad-hoc assumptions about the progressive blocking of magnetic particles below a homogeneous SML, this model is directly rooted to the mechanical properties of sediment and to diffusive mixing in the SML, which is in turn linked to the consumption of organic matter by benthic organisms, and thus to organic matter fluxes. The primary advantage of this approach resides in its predictive power towards specific environmental influences on the RPI record.

5.3 The environmental modulation of RPI records

The newly developed model for sediment bioturbation and its consequences on translational and rotational particle diffusion in the SML enabled a first step towards a better understanding of post-depositionary processes affecting ^{10}Be and RPI records. The bioturbation model has been calibrated with the vertical distribution of Australasian tektites in the core from the Indian Ocean (Chapter 2). The rotational impulse response of sediment mixing has been obtained from the bioturbation model, and has been used to calculate the so-called lock-in depth at which the NRM is acquired. This lock-in depth coincides exactly with the lag of RPI relative to the ^{10}Be or ^{10}Be/^{9}Be record. The RPI lag obtained from this model, which is based exclusively on a physical description of the bioturbation process, has been finally compared with the lag obtained from the RPI and ^{10}Be/^{9}Be records of two sediment cores from the Equatorial Pacific and the North Atlantic. A good agreement exist between the RPI lag obtained from forward modelling and the observed values. The model is also capable of describing subtle, environmentally driven variations of the lock-in depth in one of the two

cores, as well as providing an explanation for the lack of variations in the other core (Chapter 4).

These results confirm previous findings that the original magnetization acquired during sediment deposition is progressively replaced by a pDRM resulting from the dynamic equilibrium between the aligning torque exerted by the Earth's magnetic field, and randomizing forces associated with the plastic deformation during the last stages of bioturbation, before burial in the historical layer. Bioturbation, and not compaction, is therefore the driving process of pDRM acquisition. This acquisition mechanism is applicable to a wide category of sediments characterized by continuous sedimentation, lack of lamination, and lack of early diagenesis processes involving the precipitation or dissolution of magnetic minerals below the surface mixed layer. The latter condition is also generally required for reliable RPI records. This bioturbation-induced NRM has several important characteristics considered necessary for good-quality RPI records: (1) the lock-in depth, and thus the temporal delay of the recording mechanism, depends only weakly on sediment mechanical properties, such as cohesiveness, and on the intensity of bioturbation, (2) the acquired magnetization is proportional to the intensity of the Earth's magnetic field, lacking the saturation effects observed in some redeposition experiments, and does not depend on the characteristics of the water column (e.g. bottom currents, flocculation of suspended matter), and (3) the lock-in range is 2-3 times smaller than the lock-in depth, which means that smoothing effects are not as large as the RPI lag might suggests, and (4) the lock-in function is relatively symmetric and does not possess heavy tails that could introduce temporal asymmetries in the recording process, such as saw-tooth patterns in response to geomangnetic excursions or reversals. Nevertheless, smoothing effects become increasingly important at sedimentation rates <10 cm/kyr. The most important factor controlling the RPI lag is probably given by the oxygen penetration depth, which also controls the maximum thickness of the bioturbation layer.

Magnetofossils, which are an important source of remanence carriers contributing to RPI records, are not expected to behave differently from other magnetic particles in bioturbated sediment, sharing with these particles the same lock-in depth. This confirms previous findings about the synchronous variations of NRM components associated with magnetofossils with those of other magnetic minerals (Ouyang et al., 2014). This finding is very important, since magnetofossils contribute significantly to the magnetic mineralogy of many sediment types.

Sudden variations of the sedimentation rate or sudden changes of the oxygen penetration depth are expected to produce profound alterations of the magnetic recording process. For instance, the rapid deposition of volcanic ash or a turbidite is expected to introduce a layer that instantly records the Earth's magnetic field. Later colonization by benthic organisms partially or completely erases the initial magnetization. If the deposited layer is sufficiently thick, this creates a front where the lock-in depth changes abruptly.

Unlike the lock-in depth, the efficiency with which remanence carriers align with the Earth's magnetic field in bioturbated sediment is expected to depend on specific parameters,

such as the mean magnetic moment, the effective size of magnetic crystals or aggregates of such crystals and sediment particles, and the mechanical strength of sediment at the lock-in depth. These parameters are presently unknown; however the predictive power of the abovementioned pDRM acquisition model provides very useful tools for designing dedicated experiments aiming at calibrating the NRM acquisition efficiency of different remanence carriers, as well as deducing such efficiencies from paleomagnetic records, e.g. by identification of specific coercivity components contributing to the NRM.

Overall, results from the Chapter 4 and from Chapter 3 suggest that RPI records are less affected by climatic contaminations than Be records, and that ^{9}Be normalization, while eliminating the adverse effects of a variable scavenging efficiency, might introduce its own artifacts, especially at sites where terrestrial Be inputs are heavily affected by the climatic modulation of terrestrial Be fluxes, as in the North Atlantic Ocean. While the climatic contamination of Be records appears to be mainly affected by glacial-interglacial cycles, climatic contaminations of RPI records are more subdued, but still not negligible. Such contamination can be divided into two main categories related to (1) changes in the mechanical properties of sediment, affecting the alignment efficiency of magnetic minerals, and (2) normalization errors, due to the selective response of laboratory magnetization to specific magnetic mineral categories. As far as (2) is concerned, unmixing techniques based on AF demagnetization of NRM can be used to isolate the contributions of individual magnetic components, which can then be normalized individually. Sediment mechanical properties are more difficult to reconstruct, require a whole new line of experimental investigations.

Overall, the pDRM acquisition model developed in Chapter 4 offers a whole new set of tools to improve our present knowledge about sedimentary records of the Earth magnetic fields, based on the analysis of RPI and cosmogenic isotope records, as well as dedicated laboratory or in-situ acquisition experiments. Comparison of climatic proxies such as sea level and $\delta^{18}O$ with magnetic mineralogy, expressed by the anhysteretic remanent magnetization (ARM), and pDRM lock-in depth, derived from the RPI lag with respect to Be records, suggests the following environmental modulation mechanism for RPI records acquired in bioturbated deep-sea sediments. Primary productivity and water depth determine the flux of organic matter to the sediment. This flux sustains benthic organisms responsible for organic matter oxidation and bioturbation, and drive the sedimentary iron cycle. Small organic carbon fluxes, e.g. during glacials, lead to the complete consumption of labile organic matter in an oxic environment. The large oxygen penetration depth promotes deeper, but less intense bioturbation. In this case, the pDRM lock-in depth is larger, and NRM is carried mainly by detrital minerals, given the reduced or absent contribution from magnetofossils produced by magnetotactic bacteria. As the organic matter supply increases during interglacials, oxygen is consumed at a higher rate and penetrates less deep in the sediment. Bioturbation is more intense, owing to the higher organic matter consumption rate, but limited in depth by oxygen availability. The

pDRM lock-in depth is smaller, and a larger proportion of biogenic magnetic particles, such as magnetofossils, contributes to the RPI.

As shown in Chapter 4, detrital and authigenic NRM contributions are acquired at the same depth near the lower end of the SML, confirming the previous findings of one study. However, the acquisition efficiencies of these two components, expressed by the NRM/ARM ratio, appear to be different, for reasons that are not yet clear. Possible explanations include different ratios between the magnetic moment and the size of magnetic particles or particle aggregates. The existence of magnetic component-specific ratios between NRM and a laboratory magnetization used as normalizer, means that there is not a single normalization capable of eliminating NRM variations due to magnetic mineralogy changes. Climatic contaminations are thus introduced by the environmental sensitivity of magnetic minerals. Another source of climatic contaminations is related to the dependence of the magnetic alignment efficiency on the mechanical properties of sediment, which are in turn influenced by lithological parameters.

The above model for the environmental dependence of RPI records applies to the specific conditions encountered in two cores from the Equatorial Pacific and the North Atlantic. Other mechanisms can be envisaged for different locations. For instance, primary productivity in the Southern Ocean, and thus also organic matter supply to the sediment, is limited by the supply of bioavailable iron, which is in turn strongly modulated by dust inputs. Finally, any magnetic product of the iron cycle below the SML, as well as diagenetic dissolution of remanence carriers, can overprint or completely erase the pDRM acquired at the bottom of the SML.

Chapter 6

Perspectives

This work revealed several details about the processes controlling sedimentary records of the Earth's magnetic field by ^{10}Be and by magnetic minerals (relative paleointensity, PRI), and their environmental modulation. The ultimate goal of future research in this field is to minimize or eliminate climatic contaminations of individual records.

As far as ^{10}Be or ^{10}Be/^{9}Be records are concerned, oceanic transport and the distribution of terrestrial Be sources appear to be the main factors that need to be taken into consideration for removing climatic effects. Besides the common dependence on oceanic circulation patterns of unnormalized ^{10}Be, the records are affected by variations of the scavenging efficiency of sediment, while ^{10}Be/^{9}Be records are contaminated by the variability of terrestrial Be sources affecting ^{9}Be supply. Empirical correlations with environmental proxies might be used to extract the common geomagnetic information from ^{10}Be and ^{10}Be/^{9}Be. Furthermore, the inclusion of ^{10}Be and ^{9}Be into global models of oceanic circulation might help in correcting the effects of changing circulation patterns. Finally, the Be scavenging efficiency of sediment seems to depend in a nonlinear manner on the carbonate content. A better definition of the efficiency of individual mineral components, e.g. by dedicated experiments, might support scavenging efficiency corrections that do no longer need ^{9}Be normalization, avoiding the effect of variable terrestrial source distributions.

The newly developed, bioturbation-based pDRM acquisition model can be used to design new laboratory experiments aimed at testing the influence of different parameters, such as mechanical and lithological sediment properties, magnetic mineralogy, and nutrient availability, on the efficiency and timing of the acquisition process. On the other hand, functional relationships between pDRM lock-in depth and environmental factors, such as those derived in Chapter 4, enable a better synchronization of RPI records, and possible partial correction of smoothing effects.

Bibliography

[1] HS Ahluwalia. "On galactic cosmic ray flux decrease near solar minima and IMF intensity". In: *Geophysical Research Letters* 27.11 (2000), pp. 1603–1606.

[2] Alison N Anderson, John W Crawford, and Alex B McBratney. "On diffusion in fractal soil structures". In: *Soil Science Society of America Journal* 64.1 (2000), pp. 19–24.

[3] David M Anderson. "Attenuation of millennial-scale events by bioturbation in marine sediments". In: *Paleoceanography* 16.4 (2001), pp. 352–357.

[4] David M Anderson and David Archer. "Glacial–interglacial stability of ocean pH inferred from foraminifer dissolution rates". In: *Nature* 416.6876 (2002), pp. 70–73.

[5] RF Anderson et al. "Anomalous boundary scavenging in the Middle Atlantic Bight: evidence from 230Th, 231Pa, 10Be and 210Pb". In: *Deep Sea Research Part II: Topical Studies in Oceanography* 41.2-3 (1994), pp. 537–561.

[6] RF Anderson et al. "Boundary scavenging in the Pacific Ocean: a comparison of10Be and231Pa". In: *Earth and Planetary Science Letters* 96.3-4 (1990), pp. 287–304.

[7] Andreas J Andersson and Dwight Gledhill. "Ocean acidification and coral reefs: effects on breakdown, dissolution, and net ecosystem calcification". In: *Annual review of marine science* 5 (2013), pp. 321–348.

[8] GL Anson and KP Kodama. "Compaction-induced inclination shallowing of the post-depositional remanent magnetization in a synthetic sediment". In: *Geophysical Journal International* 88.3 (1987), pp. 673–692.

[9] Andrés Antico, Olivier Marchal, and Lawrence A Mysak. "Time-dependent response of a zonally averaged ocean–atmosphere–sea ice model to Milankovitch forcing". In: *Climate dynamics* 34.6 (2010), pp. 763–779.

[10] Tomás Aquino et al. "A process-based model for bioturbation-induced mixing". In: *Scientific reports* 7.1 (2017), pp. 1–7.

[11] Sandra Arndt et al. "Quantifying the degradation of organic matter in marine sediments: a review and synthesis". In: *Earth-science reviews* 123 (2013), pp. 53–86.

[12] James R Arnold. "Beryllium-10 produced by cosmic rays". In: *Science* 124.3222 (1956), pp. 584–585.

[13] Helge W Arz et al. “Mediterranean moisture source for an early-Holocene humid period in the northern Red Sea”. In: *Science* 300.5616 (2003), pp. 118–121.

[14] Helge W Arz et al. “Millennial-scale changes of surface-and deep-water flow in the western tropical Atlantic linked to Northern Hemisphere high-latitude climate during the Holocene”. In: *Geology* 29.3 (2001), pp. 239–242.

[15] J Backman and RA Duncan. “Shipboard Scientific Party, 1988”. In: *Proc. ODP, Init. Repts. Ocean Drilling Program, College Station, TX* (), p. 115.

[16] Michael P Bacon and John N Rosholt. “Accumulation rates of Th-230, Pa-231, and some transition metals on the Bermuda Rise”. In: *Geochimica et Cosmochimica Acta* 46.4 (1982), pp. 651–666.

[17] Michael P Bacon et al. “Seasonality in the flux of natural radionuclides and plutonium in the deep Sargasso Sea”. In: *Deep Sea Research Part A. Oceanographic Research Papers* 32.3 (1985), pp. 273–286.

[18] MP Bacon. “Tracers of chemical scavenging in the ocean: boundary effects and large-scale chemical fractionation”. In: *Philosophical Transactions of the Royal Society of London. Series A, Mathematical and Physical Sciences* 325.1583 (1988), pp. 147–160.

[19] Laurie S Balistrieri and James W Murray. “Marine scavenging: trace metal adsorption by interfacial sediment from MANOP Site H”. In: *Geochimica et Cosmochimica Acta* 48.5 (1984), pp. 921–929.

[20] E Bard et al. “Bioturbation effects on abrupt climatic changes recorded in deep sea sediments. Correlation between δ 18 O profiles and accelerator 14 C dating”. In: *Abrupt Climatic Change*. Springer, 1987, pp. 263–278.

[21] Edouard Bard and Gilles Delaygue. “Comment on “Are there connections between the Earth’s magnetic field and climate?” by V. Courtillot, Y. Gallet, J.-L. Le Mouël, F. Fluteau, A. Genevey EPSL 253, 328, 2007”. In: *Earth and Planetary Science Letters* 265.1-2 (2008), pp. 302–307.

[22] Edouard Bard and Rosalind EM Rickaby. “Migration of the subtropical front as a modulator of glacial climate”. In: *Nature* 460.7253 (2009), pp. 380–383.

[23] Edouard Bard et al. “Solar modulation of cosmogenic nuclide production over the last millennium: comparison between 14C and 10Be records”. In: *Earth and Planetary Science Letters* 150.3-4 (1997), pp. 453–462.

[24] Anne Bartetzko and Achim J Kopf. “The relationship of undrained shear strength and porosity with depth in shallow (< 50 m) marine sediments”. In: *Sedimentary Geology* 196.1-4 (2007), pp. 235–249.

[25] Jonathan Barzilai and Jonathan M Borwein. “Two-point step size gradient methods”. In: *IMA journal of numerical analysis* 8.1 (1988), pp. 141–148.

[26] Franck C Bassinot. “Sonostratigraphy of tropical Indian Ocean giant piston cores: toward a rapid and high-resolution tool for tracking dissolution cycles in Pleistocene carbonate sediments”. In: *Earth and planetary science letters* 120.3-4 (1993), pp. 327–344.

[27] Frank C Bassinot et al. “The astronomical theory of climate and the age of the Brunhes-Matuyama magnetic reversal”. In: *Earth and Planetary Science Letters* 126.1-3 (1994), pp. 91–108.

[28] J Beer et al. “10 Be as an indicator of solar variability and climate”. In: *The solar engine and its influence on terrestrial atmosphere and climate*. Springer, 1994, pp. 221–233.

[29] Jürg Beer, Ken McCracken, and Rudolf Steiger. *Cosmogenic radionuclides: theory and applications in the terrestrial and space environments*. Springer Science & Business Media, 2012.

[30] Reuven Belmaker et al. “Beryllium isotopes as tracers of Lake Lisan (last Glacial Dead Sea) hydrology and the Laschamp geomagnetic excursion”. In: *Earth and Planetary Science Letters* 400 (2014), pp. 233–242.

[31] Jean Berlamont et al. “The characterisation of cohesive sediment properties”. In: *Coastal Engineering* 21.1 (1993), pp. 105–128.

[32] Robert A Berner. *Early diagenesis: a theoretical approach*. 1. Princeton University Press, 1980.

[33] Richard Bintanja, Roderik SW Van De Wal, and Johannes Oerlemans. “Modelled atmospheric temperatures and global sea levels over the past million years”. In: *Nature* 437.7055 (2005), pp. 125–128.

[34] Richard P Blakemore. “Magnetotactic bacteria”. In: *Annual Reviews in Microbiology* 36.1 (1982), pp. 217–238.

[35] Friedhelm von Blanckenburg, Julien Bouchez, and Hella Wittmann. “Earth surface erosion and weathering from the 10Be (meteoric)/9Be ratio”. In: *Earth and Planetary Science Letters* 351 (2012), pp. 295–305.

[36] Friedhelm von Blanckenburg and Heiner Igel. “Lateral mixing and advection of reactive isotope tracers in ocean basins: observations and mechanisms”. In: *Earth and planetary science letters* 169.1-2 (1999), pp. 113–128.

[37] U Bleil and T Von Dobeneck. “Geomagnetic events and relative paleointensity records—clues to high-resolution paleomagnetic chronostratigraphies of Late Quaternary marine sediments?” In: *Use of proxies in paleoceanography*. Springer, 1999, pp. 635–654.

[38] A Blinov. “The dependence of cosmogenic isotope production rate on solar activity and geomagnetic field variations”. In: *Secular Solar and Geomagnetic Variations in the Last 10,000 Years*. Springer, 1988, pp. 329–340.

[39] Bernard P Boudreau. “Is burial velocity a master parameter for bioturbation?” In: *Geochimica et Cosmochimica Acta* 58.4 (1994), pp. 1243–1249.

[40] Bernard P Boudreau. “Mathematics of tracer mixing in sediments: I. Spatially-dependent, diffusive mixing”. In: *Am. J. Sci* 286.3 (1986), pp. 161–198.

[41] Bernard P Boudreau. “Mathematics of tracer mixing in sediments; II, Nonlocal mixing and biological conveyor-belt phenomena”. In: *American Journal of Science* 286.3 (1986), pp. 199–238.

[42] Bernard P Boudreau. “Mean mixed depth of sediments: the wherefore and the why”. In: *Limnology and Oceanography* 43.3 (1998), pp. 524–526.

[43] Bernard P Boudreau and Dieter M Imboden. “Mathematics of tracer mixing in sediments; iii, the theory of nonlocal mixing within sediments”. In: *American Journal of Science* 287.7 (1987), pp. 693–719.

[44] Bernard P Boudreau and Barry R Ruddick. “On a reactive continuum representation of organic matter diagenesis”. In: *American Journal of Science* 291.5 (1991), pp. 507–538.

[45] D Bourles, GM Raisbeck, and F Yiou. “10Be and 9Be in marine sediments and their potential for dating”. In: *Geochimica et Cosmochimica Acta* 53.2 (1989), pp. 443–452.

[46] DL Bourles et al. “Beryllium in marine pore waters: geochemical and geochronological implications”. In: *Nature* 341.6244 (1989), pp. 731–733.

[47] MN Bramlette et al. “Geology and Biology of North Atlantic Deep-Sea Cores Between Newfoundland and Ireland: Part I: Lithologj’and Geologic Interpretations”. In: *US Geol. Survey Prof. Paper ig6-A* (1940).

[48] Andreas PJ Breu et al. “Reversing the Brazil-nut effect: competition between percolation and condensation”. In: *Physical review letters* 90.1 (2003), p. 014302.

[49] David Brickman, DG Wright, and William Hyde. “Filtering of Milankovitch cycles by the thermohaline circulation”. In: *Journal of climate* 12.6 (1999), pp. 1644–1658.

[50] J Bridgwater. “Mixing and segregation mechanisms in particle flow”. In: *Granular matter*. Springer, 1994, pp. 161–193.

[51] Erik Thorson Brown et al. “Continental inputs of beryllium to the oceans”. In: *Earth and planetary science letters* 114.1 (1992), pp. 101–111.

[52] Louise Brown et al. “Radiocarbon age profiles and size dependency of mixing in northeast Atlantic sediments”. In: *Radiocarbon* 43.2B (2001), pp. 929–937.

[53] Ken O Buesseler et al. “An assessment of the use of sediment traps for estimating upper ocean particle fluxes”. In: *Journal of Marine Research* 65.3 (2007), pp. 345–416.

[54] Armin Bunde and Shlomo Havlin. *Fractals and disordered systems*. Springer Science & Business Media, 2012.

[55] Oleg Burdakov, Yu-Hong Dai, and Na Huang. "Stabilized Barzilai-Borwein method". In: *arXiv preprint arXiv:1907.06409* (2019).

[56] Wei-Jun Cai and Frederick L Sayles. "Oxygen penetration depths and fluxes in marine sediments". In: *Marine Chemistry* 52.2 (1996), pp. 123–131.

[57] SE Calvert and TF Pedersen. "Chapter fourteen elemental proxies for palaeoclimatic and palaeoceanographic variability in marine sediments: interpretation and application". In: *Developments in Marine Geology* 1 (2007), pp. 567–644.

[58] Donald E Canfield. "Factors influencing organic carbon preservation in marine sediments". In: *Chemical geology* 114.3-4 (1994), pp. 315–329.

[59] Jian Cao, Bin Wang, and Jian Liu. "Attribution of the Last Glacial Maximum climate formation". In: *Climate Dynamics* 53.3-4 (2019), pp. 1661–1679.

[60] Julien T Carcaillet, Didier L Bourlès, and Nicolas Thouveny. "Geomagnetic dipole moment and 10Be production rate intercalibration from authigenic 10Be/9Be for the last 1.3 Ma". In: *Geochemistry, Geophysics, Geosystems* 5.5 (2004).

[61] Julien T Carcaillet, Nicolas Thouveny, and Didier L Bourles. "Geomagnetic moment instability between 0.6 and 1.3 Ma from cosmonuclide evidence". In: *Geophysical research letters* 30.15 (2003).

[62] Brian Carter-Stiglitz, Jean-Pierre Valet, and Maxime LeGoff. "Constraints on the acquisition of remanent magnetization in fine-grained sediments imposed by redeposition experiments". In: *Earth and Planetary Science Letters* 245.1-2 (2006), pp. 427–437.

[63] Duane E Champion, Marvin A Lanphere, and Mel A Kuntz. "Evidence for a new geomagnetic reversal from lava flows in Idaho: Discussion of short polarity reversals in the Brunhes and late Matuyama polarity chrons". In: *Journal of Geophysical Research: Solid Earth* 93.B10 (1988), pp. 11667–11680.

[64] Liao Chang et al. "Widespread occurrence of silicate-hosted magnetic mineral inclusions in marine sediments and their contribution to paleomagnetic recording". In: *Journal of Geophysical Research: Solid Earth* 121.12 (2016), pp. 8415–8431.

[65] JET Channell and Y Guyodo. "The Matuyama Chronozone at ODP Site 982 (Rockall Bank): evidence for decimeter-scale magnetization lock-in depths". In: *Timescales of the paleomagnetic field* 145.1 (2004), pp. 205–219.

[66] De Chanvalon et al. "Two-dimensional distribution of living benthic foraminifera in anoxic sediment layers of an estuarine mudflat (Loire estuary, France)". In: *Biogeosciences* 12.20 (2015), pp. 6219–6234.

[67] Zanna Chase et al. “The influence of particle composition and particle flux on scavenging of Th, Pa and Be in the ocean”. In: *Earth and Planetary Science Letters* 204.1-2 (2002), pp. 215–229.

[68] Liang Chen et al. “Remanence acquisition efficiency in biogenic and detrital magnetite and recording of geomagnetic paleointensity”. In: *Geochemistry, Geophysics, Geosystems* 18.4 (2017), pp. 1435–1450.

[69] Jérôme Chmeleff et al. “Determination of the 10Be half-life by multicollector ICP-MS and liquid scintillation counting”. In: *Nuclear Instruments and Methods in Physics Research Section B: Beam Interactions with Materials and Atoms* 268.2 (2010), pp. 192–199.

[70] Marcus Christl. “Sensitivity and response of beryllium-10 in marine sediments to rapid production changes (geomagnetic events): A box model study”. In: *Geochemistry, Geophysics, Geosystems* 8.9 (2007).

[71] Marcus Christl, Christopher Strobl, and Augusto Mangini. “Beryllium-10 in deep-sea sediments: a tracer for the Earth’s magnetic field intensity during the last 200,000 years”. In: *Quaternary Science Reviews* 22.5-7 (2003), pp. 725–739.

[72] Bradford M Clement. “Dependence of the duration of geomagnetic polarity reversals on site latitude”. In: *Nature* 428.6983 (2004), pp. 637–640.

[73] DJ Cooke et al. “On cosmic-ray cut-off terminology”. In: *Il Nuovo Cimento C* 14.3 (1991), pp. 213–234.

[74] Vincent Courtillot et al. “Are there connections between the Earth’s magnetic field and climate?” In: *Earth and Planetary Science Letters* 253.3-4 (2007), pp. 328–339.

[75] David J Cullen. “Bioturbation of superficial marine sediments by interstitial meiobenthos”. In: *Nature* 242.5396 (1973), pp. 323–324.

[76] KB Cutler et al. “Rapid sea-level fall and deep-ocean temperature change since the last interglacial period”. In: *Earth and Planetary Science Letters* 206.3-4 (2003), pp. 253–271.

[77] Tyler Cyronak and Bradley D Eyre. “The synergistic effects of ocean acidification and organic metabolism on calcium carbonate (CaCO3) dissolution in coral reef sediments”. In: *Marine Chemistry* 183 (2016), pp. 1–12.

[78] Frank Dehairs, Roger Chesselet, and Jacques Jedwab. “Discrete suspended particles of barite and the barium cycle in the open ocean”. In: *Earth and Planetary Science Letters* 49.2 (1980), pp. 528–550.

[79] Eric Deleersnijder, Jean-Marie Beckers, and Eric JM Delhez. “The residence time of settling particles in the surface mixed layer”. In: *Environmental Fluid Mechanics* 6.1 (2006), pp. 25–42.

[80] David J DeMaster and J Kirk Cochran. “Particle mixing rates in deep-sea sediments determined from excess 210Pb and 32Si profiles”. In: *Earth and Planetary Science Letters* 61.2 (1982), pp. 257–271.

[81] Peter B deMenocal, William F Ruddiman, and Dennis V Kent. “Depth of post-depositional remanence acquisition in deep-sea sediments: a case study of the Brunhes-Matuyama reversal and oxygen isotopic Stage 19.1”. In: (1990).

[82] Surya P Dhakar and David J Burdige. “A coupled, non-linear, steady state model for early diagenetic processes in pelagic sediments”. In: *American Journal of Science* 296.3 (1996).

[83] Jaume Dinarès-Turell et al. “Quaternary climatic control of biogenic magnetite production and eolian dust input in cores from the Mediterranean Sea”. In: *Palaeogeography, Palaeoclimatology, Palaeoecology* 190 (2003), pp. 195–209.

[84] Suvasis Dixit, Philippe Van Cappellen, and A Johan van Bennekom. “Processes controlling solubility of biogenic silica and pore water build-up of silicic acid in marine sediments”. In: *Marine Chemistry* 73.3-4 (2001), pp. 333–352.

[85] D.Lal and B.Peters. “Cosmic Ray Produced Radioactivity on the Earth”. In: *Encyclopedia of physics*. Ed. by S.FLUGGE. Vol. XLVI/2 Cosmic rays II. Springer-Verlag, 1967, pp. 551–612.

[86] Marco Dominé. “First passage time distribution of a Wiener process with drift concerning two elastic barriers”. In: *Journal of Applied Probability* 33.1 (1996), pp. 164–175.

[87] Kelly M Dorgan, Sanjay R Arwade, and Peter A Jumars. “Burrowing in marine muds by crack propagation: kinematics and forces”. In: *Journal of Experimental Biology* 210.23 (2007), pp. 4198–4212.

[88] J Duran et al. “Size segregation in a two-dimensional sandpile: Convection and arching effects”. In: *Physical Review E* 50.6 (1994), p. 5138.

[89] R Egli. “Characterization of individual rock magnetic components by analysis of remanence curves. 3. Bacterial magnetite and natural processes in lakes”. In: *Physics and Chemistry of the Earth, Parts A/B/C* 29.13-14 (2004), pp. 869–884.

[90] R Egli and W Lowrie. “Anhysteretic remanent magnetization of fine magnetic particles”. In: *Journal of Geophysical Research: Solid Earth* 107.B10 (2002), EPM–2.

[91] R Egli and X Zhao. “Natural remanent magnetization acquisition in bioturbated sediment: general theory and implications for relative paleointensity reconstructions”. In: *Geochemistry, Geophysics, Geosystems* 16.4 (2015), pp. 995–1016.

[92] Walter Elsasser, EP Ney, and JR Winckler. “Cosmic-ray intensity and geomagnetism”. In: *Nature* 178.4544 (1956), p. 1226.

[93] Steven Emerson et al. “Organic carbon dynamics and preservation in deep-sea sediments”. In: *Deep Sea Research Part A. Oceanographic Research Papers* 32.1 (1985), pp. 1–21.

[94] Damien Faivre and Dirk Schuler. “Magnetotactic bacteria and magnetosomes”. In: *Chemical Reviews* 108.11 (2008), pp. 4875–4898.

[95] Yi Fan et al. “Modelling size segregation of granular materials: the roles of segregation, advection and diffusion”. In: *Journal of fluid mechanics* 741 (2014), pp. 252–279.

[96] Nicolas Fatin-Rouge, Konstantin Starchev, and Jacques Buffle. “Size effects on diffusion processes within agarose gels”. In: *Biophysical journal* 86.5 (2004), pp. 2710–2719.

[97] AP Fedotov et al. “A reconstruction of the thawing of the permafrost during the last 170 years on the Taimyr Peninsula (East Siberia, Russia)”. In: *Global and Planetary change* 98 (2012), pp. 139–152.

[98] Raffaele Ferrari et al. “Antarctic sea ice control on ocean circulation in present and glacial climates”. In: *Proceedings of the National Academy of Sciences* 111.24 (2014), pp. 8753–8758.

[99] Bruce Finney, G Ross Heath, and Mitchell Lyle. “Growth rates of manganese-rich nodules at MANOP Site H (Eastern North Pacific)”. In: *Geochimica et Cosmochimica Acta* 48.5 (1984), pp. 911–919.

[100] J Leroy Folks and Raj S Chhikara. “The inverse Gaussian distribution and its statistical application—a review”. In: *Journal of the Royal Statistical Society: Series B (Methodological)* 40.3 (1978), pp. 263–275.

[101] William H Fonger. “Cosmic radiation intensity-time variations and their origin. II. Energy dependence of 27-day variations”. In: *Physical Review* 91.2 (1953), p. 351.

[102] William L Fornes, David J DeMaster, and Craig R Smith. “A particle introduction experiment in Santa Catalina Basin sediments: Testing the age-dependent mixing hypothesis”. In: *Journal of Marine Research* 59.1 (2001), pp. 97–112.

[103] Martin Frank. “Radiogenic isotopes: tracers of past ocean circulation and erosional input”. In: *Reviews of geophysics* 40.1 (2002), pp. 1–1.

[104] Martin Frank et al. “A 200 kyr record of cosmogenic radionuclide production rate and geomagnetic field intensity from 10Be in globally stacked deep-sea sediments1”. In: *Earth and Planetary Science Letters* 149.1 (1997), pp. 121–129. doi: `http://dx.doi.org/10.1016/S0012-821X(97)00070-8`.

[105] Martin Frank et al. “Sediment redistribution versus paleoproductivity change: Weddell Sea margin sediment stratigraphy and biogenic particle flux of the last 250,000 years deduced from 230Thex, 10Be and biogenic barium profiles”. In: *Earth and Planetary Science Letters* 136.3-4 (1995), pp. 559–573.

[106] Christine Franke, Daniela Hofmann, and Tilo von Dobeneck. “Does lithology influence relative paleointensity records? A statistical analysis on South Atlantic pelagic sediments”. In: *Physics of the Earth and Planetary Interiors* 147.2-3 (2004), pp. 285–296.

[107] Cecilia Galindo-Gonzalez et al. “Magnetic and microscopic characterization of magnetite nanoparticles adhered to clay surfaces”. In: *American Mineralogist* 94.8-9 (2009), pp. 1120–1129.

[108] Stephen J Gallagher et al. “The Pliocene to recent history of the Kuroshio and Tsushima Currents: a multi-proxy approach”. In: *Progress in Earth and Planetary Science* 2.1 (2015), p. 17.

[109] Yves Gallet, Vladimir Pavlov, and Igor Korovnikov. “Extreme geomagnetic reversal frequency during the Middle Cambrian as revealed by the magnetostratigraphy of the Khorbusuonka section (northeastern Siberia)”. In: *Earth and Planetary Science Letters* 528 (2019), p. 115823.

[110] B Gehrke, KS Lackschewitz, and H-J Wallrabe-Adams. “Late Quaternary sedimentation on the Mid-Atlantic Reykjanes Ridge: clay mineral assemblages and depositional environment”. In: *Geologische Rundschau* 85.3 (1996), pp. 525–535.

[111] Magali Gerino, Georges Stora, and JP Durbec. “Quantitative estimation of biodiffusive and bioadvective sediment mixing-in-situ experimental approach”. In: *Oceanologica Acta* 17.5 (1994), pp. 547–554.

[112] BP Glass, M_B Swincki, and PA Zwart. “Australasian, Ivory Coast and North American tektite strewnfields-Size, mass and correlation with geomagnetic reversals and other earth events”. In: *Lunar and Planetary Science Conference Proceedings*. Vol. 10. 1979, pp. 2535–2545.

[113] BP Glass et al. “Ivory Coast microtektite strewn field: Description and relation to the Jaramillo geomagnetic event”. In: *Earth and Planetary Science Letters* 107.1 (1991), pp. 182–196.

[114] LJ Gleeson and WI Axford. “Solar modulation of galactic cosmic rays”. In: *The Astrophysical Journal* 154 (1968), p. 1011.

[115] PS Goel et al. “Cosmic ray produced beryllium isotopes in rain water”. In: *Nuclear Physics* 1.3 (1956), pp. 196–201.

[116] Edward D Goldberg and Minoru Koide. “Geochronological studies of deep sea sediments by the ionium/thorium method”. In: *Geochimica et cosmochimica acta* 26.3 (1962), pp. 417–450.

[117] DH Griffiths et al. “The remanent magnetism of some recent varved sediments”. In: *Proceedings of the Royal Society of London. Series A. Mathematical and Physical Sciences* 256.1286 (1960), pp. 359–383.

[118] Onno Groß. “Sediment interactions of foraminifera: implications for food degradation and bioturbation processes”. In: *The Journal of Foraminiferal Research* 32.4 (2002), pp. 414–424.

[119] David Gubbins. “The distinction between geomagnetic excursions and reversals”. In: *Geophysical Journal International* 137.1 (1999), F1–F3.

[120] NL Guinasso Jr and DR Schink. “Quantitative estimates of biological mixing rates in abyssal sediments”. In: *Journal of Geophysical Research* 80.21 (1975), pp. 3032–3043.

[121] Yohan Guyodo and Jean-Pierre Valet. “Global changes in intensity of the Earth’s magnetic field during the past 800 kyr”. In: *Nature* 399.6733 (1999), pp. 249–252.

[122] Cedric J Hagen et al. “Dynamic Time Warping of Paleomagnetic Secular Variation Data”. In: *Geophysical Journal International* (2020).

[123] Yozo Hamano. “An experiment on the post-depositional remanent magnetization in artificial and natural sediments”. In: *Earth and Planetary Science Letters* 51.1 (1980), pp. 221–232.

[124] Bernward J Hay. “Sediment accumulation in the central western Black Sea over the past 5100 years”. In: *Paleoceanography* 3.4 (1988), pp. 491–508.

[125] G Ross Heath. “Burial rates, growth rates, and size distributions of deep-sea manganese nodules”. In: *Science* 205.4409 (1979), pp. 903–904.

[126] U Heikkilä, J Beer, and J Feichter. “Meridional transport and deposition of atmospheric 10 Be”. In: *Atmospheric Chemistry and Physics* 9.2 (2009), pp. 515–527.

[127] U Heikkilä, J Beer, and J Feichter. “Modeling cosmogenic radionuclides 10 Be and 7 Be during the Maunder Minimum using the ECHAM5-HAM general circulation model”. In: *Atmospheric Chemistry and Physics* 8.10 (2008), pp. 2797–2809.

[128] U Heikkilä and AM Smith. “Production rate and climate influences on the variability of 10Be deposition simulated by ECHAM5-HAM: Globally, in Greenland, and in Antarctica”. In: *Journal of Geophysical Research: Atmospheres* 118.6 (2013), pp. 2506–2520.

[129] U Heikkilä et al. “On the atmospheric transport and deposition of the cosmogenic radionuclides (10 Be): A review”. In: *Space Science Reviews* 176.1-4 (2013), pp. 321–332.

[130] James R Hein and Andrea Koschinsky. “Deep-ocean ferromanganese crusts and nodules”. In: (2014).

[131] Gideon M Henderson, Fara N Lindsay, and Niall C Slowey. “Variation in bioturbation with water depth on marine slopes: a study on the Little Bahamas Bank”. In: *Marine Geology* 160.1-2 (1999), pp. 105–118.

[132] WU Henken-Mellies et al. “10Be and9Be in South Atlantic DSDP Site 519: Relation to geomagnetic reversals and to sediment composition”. In: *Earth and Planetary Science Letters* 98.3-4 (1990), pp. 267–276.

[133] Dietrich Heye. “Growth conditions of manganese nodules Comparative studies of growth rate, magnetization, chemical composition and internal structure”. In: *Progress in Oceanography* 7.5-6 (1978), pp. 163–239.

[134] Claude Hillaire-Marcel et al. “Productivité et flux de carbone dans la mer du Labrador au cours des derniers 40 000 ans”. In: *Canadian Journal of Earth Sciences* 31.1 (1994), pp. 139–158.

[135] David A Hodell et al. “Onset of “Hudson Strait” Heinrich events in the eastern North Atlantic at the end of the middle Pleistocene transition (640 ka)?” In: *Paleoceanography* 23.4 (2008).

[136] Ove Hoegh-Guldberg et al. “Coral reefs under rapid climate change and ocean acidification”. In: *science* 318.5857 (2007), pp. 1737–1742.

[137] Chorng-Shern Horng, Andrew P Roberts, and Wen-Tzong Liang. “A 2.14-Myr astronomically tuned record of relative geomagnetic paleointensity from the western Philippine Sea”. In: *Journal of Geophysical Research: Solid Earth* 108.B1 (2003).

[138] Chorng-Shern Horng et al. “Astronomically calibrated ages for geomagnetic reversals within the Matuyama chron”. In: *Earth, planets and space* 54.6 (2002), pp. 679–690.

[139] Katherine Huang, Bernard P Boudreau, and Daniel C Reed. “Simulated fiddler-crab sediment mixing”. In: *Journal of Marine Research* 65.4 (2007), pp. 491–522.

[140] William H Hutson. “Bioturbation of deep-sea sediments: Oxygen isotopes and stratigraphic uncertainty”. In: *Geology* 8.3 (1980), pp. 127–130.

[141] E Irving and A Major. “Post-depositional detrital remanent magnetization in a synthetic sediment”. In: *Sedimentology* 3.2 (1964), pp. 135–143.

[142] Sara Jabbari-Farouji et al. “Dynamical heterogeneity in aging colloidal glasses of Laponite”. In: *Soft Matter* 8.20 (2012), pp. 5507–5512.

[143] J Jezek, S Gilder, and D Bilardello. “Numerical simulation of inclination shallowing by rolling and slipping of spherical particles”. In: *Computers & geosciences* 49 (2012), pp. 270–277.

[144] Pierre Josso et al. “Improving confidence in ferromanganese crust age models: A composite geochemical approach”. In: *Chemical Geology* 513 (2019), pp. 108–119.

[145] Fred Jourdan et al. “Ultraprecise age and formation temperature of the Australasian tektites constrained by 40Ar/39Ar analyses”. In: *Meteoritics & Planetary Science* 54.10 (2019), pp. 2573–2591.

[146] David Kadko and G Ross Heath. “Models of depth-dependent bioturbation at MANOP Site H in the eastern equatorial Pacific”. In: *Journal of Geophysical Research: Oceans* 89.C4 (1984), pp. 6567–6574.

[147] Pekka H Kansanen and Jyri Seppälä. “Interpretation of mixed sediment profiles by means of a sediment-mixing model and radioactive fallout”. In: *The Dynamics and Use of Lacustrine Ecosystems*. Springer, 1992, pp. 371–379.

[148] Yoshiki Kanzaki et al. “A lattice-automaton bioturbation simulator with coupled physics, chemistry, and biology in marine sediments (eLABS v0. 2)”. In: *Geoscientific Model Development* 12.10 (2019), pp. 4469–4496.

[149] K Katari, L Tauxe, and John King. “A reassessment of post-depositional remanent magnetism: preliminary experiments with natural sediments”. In: *Earth and Planetary Science Letters* 183.1-2 (2000), pp. 147–160.

[150] Kaushik Katari and Jeremy Bloxham. “Effects of sediment aggregate size on DRM intensity: a new theory”. In: *Earth and Planetary Science Letters* 186.1 (2001), pp. 113–122.

[151] Masaki Kawabe and Shinzou Fujio. “Pacific Ocean circulation based on observation”. In: *Journal of Oceanography* 66.3 (2010), pp. 389–403.

[152] Hodaka Kawahata, Masumi Yamamuro, and Hidekazu Ohta. “Seasonal and vertical variations of sinking particle fluxes in the West Caroline Basin”. In: *Oceanologica Acta* 21.4 (1998), pp. 521–532.

[153] Dennis V Kent. “Post-depositional remanent magnetisation in deep-sea sediment”. In: *Nature* 246.5427 (1973), pp. 32–34.

[154] K Khalil et al. “Constraining biogenic silica dissolution in marine sediments: a comparison between diagenetic models and experimental dissolution rates”. In: *Marine Chemistry* 106.1-2 (2007), pp. 223–238.

[155] N Khola and C Wassgren. “Correlations for shear-induced percolation segregation in granular shear flows”. In: *Powder Technology* 288 (2016), pp. 441–452.

[156] Minsu Kim et al. “Colloidal rotation near the colloidal glass transition”. In: *The Journal of chemical physics* 135.5 (2011), p. 054905.

[157] John King et al. “A comparison of different magnetic methods for determining the relative grain size of magnetite in natural materials: some results from lake sediments”. In: *Earth and Planetary Science Letters* 59.2 (1982), pp. 404–419.

[158] RF King. “The remanent magnetism of artificially deposited sediments”. In: *Geophysical Supplements to the Monthly Notices of the Royal Astronomical Society* 7.3 (1955), pp. 115–134.

[159] Mads Faurschou Knudsen et al. “In-phase anomalies in Beryllium-10 production and palaeomagnetic field behaviour during the Iceland Basin geomagnetic excursion”. In: *Earth and Planetary Science Letters* 265.3-4 (2008), pp. 588–599.

[160] GE Kocharov et al. “Temporal 10 Be and 14 C Variations: A Tool for Paleomagnetic Research”. In: *Radiocarbon* 31.2 (1989), pp. 163–168.

[161] Gijsberta H Koenderink et al. “On the validity of Stokes–Einstein–Debye relations for rotational diffusion in colloidal suspensions”. In: *Faraday discussions* 123 (2003), pp. 335–354.

[162] Wolfgang Koeve et al. “14C-age tracers in global ocean circulation models”. In: *Geoscientific Model Development* 8 (2015), pp. 2079–2094.

[163] Yvo S Kok and Lisa Tauxe. “Saw-toothed pattern of relative paleointensity records and cumulative viscous remanence”. In: *Earth and planetary science letters* 137.1-4 (1996), pp. 95–99.

[164] AN Konstantinov and GE Kocharov. “A 30,000-year record of the cosmic-ray intensity”. In: *Soviet Astronomy Letters* 10 (1984), p. 37.

[165] Carla M Koretsky, Christof Meile, and Philippe Van Cappellen. “Quantifying bioirrigation using ecological parameters: a stochastic approach”. In: *Geochemical Transactions* 3.3 (2002), pp. 17–30.

[166] Gunther Korschinek et al. “A new value for the half-life of 10Be by heavy-ion elastic recoil detection and liquid scintillation counting”. In: *Nuclear Instruments and Methods in Physics Research Section B: Beam Interactions with Materials and Atoms* 268.2 (2010), pp. 187–191.

[167] TL Ku et al. “Beryllium isotope distribution in the western North Atlantic: a comparison to the Pacific”. In: *Deep Sea Research Part A. Oceanographic Research Papers* 37.5 (1990), pp. 795–808.

[168] TL Ku et al. “The distribution of 10Be and 9Be in the South Atlantic”. In: *Deep Sea Research Part I: Oceanographic Research* 43 (1996), pp. 987–1009.

[169] Rep Kubo. “The fluctuation-dissipation theorem”. In: *Reports on progress in physics* 29.1 (1966), p. 255.

[170] Arshad Kudrolli. “Size separation in vibrated granular matter”. In: *Reports on progress in physics* 67.3 (2004), p. 209.

[171] Masashi Kusakabe, Teh-Lung Ku, John R Southon, et al. “Beryllium isotopes in the ocean”. In: *Geochemical Journal* 24.4 (1990), pp. 263–272.

[172] C Laj and JET Channel. *Geomagnetic excursions.—[in:] Treatise on Geophysics, Vol. 5*. 2007.

[173] J Lajoie. “1970: Flysch sedimentology in North America”. In: *Geol. Assoc. Can. Spec. Paper* 7 ().

[174] Devendra Lal et al. “Records of cosmogenic radionuclides 10Be, 26Al and 36Cl in corals: First studies on coral erosion rates and potential of dating very old corals”. In: *Geochimica et cosmochimica acta* 69.24 (2005), pp. 5717–5728.

[175] Douglas E LaRowe and Jan P Amend. “Power limits for microbial life”. In: *Frontiers in microbiology* 6 (2015), p. 718.

[176] Stefano Lazzari et al. “Fractal-like structures in colloid science”. In: *Advances in colloid and interface science* 235 (2016), pp. 1–13.

[177] Brian D Leahy et al. “Enhancing rotational diffusion using oscillatory shear”. In: *Physical review letters* 110.22 (2013), p. 228301.

[178] Pascal Lecroart et al. “Bioturbation, short-lived radioisotopes, and the tracer-dependence of biodiffusion coefficients”. In: *Geochimica et Cosmochimica Acta* 74.21 (2010), pp. 6049–6063.

[179] G Leduc et al. “Authigenic 10 Be/9 Be signature of the Laschamp excursion: A tool for global synchronisation of paleoclimatic archives”. In: *Earth and Planetary Science Letters* 245.1 (2006), pp. 19–28.

[180] Yuan-Hui Li. “Interelement relationship in abyssal Pacific ferromanganese nodules and associated pelagic sediments”. In: *Geochim. Cosmochim. Acta* 46.6 (1982), pp. 1053–1060.

[181] Kurt Liffman et al. “A segregation mechanism in a vertically shaken bed”. In: *Granular Matter* 3.4 (2001), pp. 205–214.

[182] Lorraine E Lisiecki and Maureen E Raymo. “A Pliocene-Pleistocene stack of 57 globally distributed benthic δ18O records”. In: *Paleoceanography* 20.1 (2005).

[183] Thomas Litt et al. “‘PALEOVAN’, International Continental Scientific Drilling Program (ICDP): site survey results and perspectives”. In: *Quaternary Science Reviews* 28.15-16 (2009), pp. 1555–1567.

[184] T.Janecek et al. L.Mayer L.Pisas. “Shipboard Scientific Party,1992.Site 851”. In: *Proc. ODP, Init. Repts.* 138 (1992), pp. 891–965.

[185] FJ Lobo and D Ridente. “Milankovitch cyclicity in modern continental margins: stratigraphic cycles in terrigenous shelf settings”. In: (2013).

[186] Jacques Locat et al. “Shear strength development with burial in Eel River margin slope sediments”. In: *Marine Georesources and Geotechnology* 20.2 (2002), pp. 111–135.

[187] Bryan C Lougheed et al. “Moving beyond the age-depth model paradigm in deep-sea palaeoclimate archives: dual radiocarbon and stable isotope analysis on single foraminifera”. In: *Climate of the Past* 14.4 (2018), pp. 515–526.

[188] Reidar Løvlie. “Field-dependent postdepositional grain realignment in the PDRM process: experimental evidence and implications”. In: *Physics of the earth and planetary interiors* 85.1-2 (1994), pp. 101–111.

[189] Ran Lu, Subir K Banerjee, and James Marvin. “Effects of clay mineralogy and the electrical conductivity of water on the acquisition of depositional remanent magnetization in sediments”. In: *Journal of Geophysical Research: Solid Earth* 95.B4 (1990), pp. 4531–4538.

[190] Steve Lund et al. “A summary of Brunhes paleomagnetic field variability recorded in Ocean Drilling Program cores”. In: *Physics of the Earth and Planetary Interiors* 156.3-4 (2006), pp. 194–204.

[191] Steve P Lund and Lloyd Keigwin. “Measurement of the degree of smoothing in sediment paleomagnetic secular variation records: an example from late Quaternary deep-sea sediments of the Bermuda Rise, western North Atlantic Ocean”. In: *Earth and Planetary Science Letters* 122.3-4 (1994), pp. 317–330.

[192] Steve P Lund et al. “10. Brunhes Chron Magnetic Field Excursions Recovered from Leg 172 Sediments”. In: (2001).

[193] Natalie Mahowald et al. “Dust sources and deposition during the last glacial maximum and current climate: A comparison of model results with paleodata from ice cores and marine sediments”. In: *Journal of Geophysical Research: Atmospheres* 104.D13 (1999), pp. 15895–15916.

[194] Olivier Maire et al. “Quantification of sediment reworking rates in bioturbation research: a review”. In: *Aquatic Biology* 2.3 (2008), pp. 219–238.

[195] A Mangini et al. “Mass-spectrometric 10Be dating of deep-sea sediments applying the Zürich tandem accelerator”. In: *Nuclear Instruments and Methods in Physics Research Section B: Beam Interactions with Materials and Atoms* 5.2 (1984), pp. 353–358.

[196] Xuegang Mao et al. “Magneto-chemotaxis in sediment: First insights”. In: *PLoS One* 9.7 (2014).

[197] J Masarik and J Beer. “An updated simulation of particle fluxes and cosmogenic nuclide production in the Earth’s atmosphere”. In: *Journal of Geophysical Research: Atmospheres* 114.D11 (2009).

[198] J Masarik and J Beer. “Simulation of particle fluxes and cosmogenic nuclide production in the Earth’s atmosphere”. In: *Journal of Geophysical Research: Atmospheres* 104.D10 (1999), pp. 12099–12111.

[199] Gerald Matisoff. “Mathematical models of bioturbation”. In: *Animal-sediment relations*. Springer, 1982, pp. 289–330.

[200] Michael Matuson. “SVD pseudoinverse deconvolution of two-dimensional arrays”. In: *The Journal of the Acoustical Society of America* 80.4 (1986), pp. 1264–1264.

[201] Krysia Mazik et al. “Accurate quantification of the influence of benthic macro-and meio-fauna on the geometric properties of estuarine muds by micro computer tomography”. In: *Journal of Experimental Marine Biology and Ecology* 354.2 (2008), pp. 192–201.

[202] IN McCave. “Biological pumping upwards of the coarse fraction of deep-sea sediments”. In: *Journal of Sedimentary Research* 58.1 (1988), pp. 148–158.

[203] IN McCave. “Size spectra and aggregation of suspended particles in the deep ocean”. In: *Deep Sea Research Part A. Oceanographic Research Papers* 31.4 (1984), pp. 329–352.

[204] IoN McCAVE. “Vertical flux of particles in the ocean”. In: *Deep Sea Research and Oceanographic Abstracts*. Vol. 22. 7. Elsevier. 1975, pp. 491–502.

[205] LR McHargue and PE Damon. “The global beryllium 10 cycle”. In: *Reviews of Geophysics* 29.2 (1991), pp. 141–158.

[206] CI Measures and JM Edmond. “The geochemical cycle of 9Be: A reconnaissance”. In: *Earth and Planetary Science Letters* 66 (1983), pp. 101–110.

[207] CI Measures et al. “The distribution of 10Be and 9Be in the South Atlantic”. In: *Deep Sea Research Part I: Oceanographic Research Papers* 43.7 (1996), pp. 987–1009.

[208] L Ménabréaz et al. “The Laschamp geomagnetic dipole low expressed as a cosmogenic 10Be atmospheric overproduction at˜ 41 ka”. In: *Earth and Planetary Science Letters* 312.3-4 (2011), pp. 305–317.

[209] Lucie Menabreaz, DL Bourlès, and Nicolas Thouveny. “Amplitude and timing of the Laschamp geomagnetic dipole low from the global atmospheric 10Be overproduction: Contribution of authigenic 10Be/9Be ratios in west equatorial Pacific sediments”. In: *Journal of Geophysical Research: Solid Earth* 117.B11 (2012).

[210] Lucie Ménabréaz et al. “The geomagnetic dipole moment variation between 250 and 800 ka BP reconstructed from the authigenic 10 Be/9 Be signature in West Equatorial Pacific sediments”. In: *Earth and Planetary Science Letters* 385 (2014), pp. 190–205.

[211] RT Merrill and PL McFadden. “Geomagnetic field stability: Reversal events and excursions”. In: *Earth and Planetary Science Letters* 121.1-2 (1994), pp. 57–69.

[212] Konstantin Mewes et al. “Impact of depositional and biogeochemical processes on small scale variations in nodule abundance in the Clarion-Clipperton Fracture Zone”. In: *Deep Sea Research Part I: Oceanographic Research Papers* 91 (2014), pp. 125–141.

[213] Laure Meynadier and Jean-Pierre Valet. “Post-depositional realignment of magnetic grains and asymmetrical saw-tooth patterns of magnetization intensity”. In: *Earth and planetary science letters* 140.1-4 (1996), pp. 123–132.

[214] Filip JR Meysman, Bernard P Boudreau, and Jack J Middelburg. “Modeling reactive transport in sediments subject to bioturbation and compaction”. In: *Geochimica et Cosmochimica Acta* 69.14 (2005), pp. 3601–3617.

[215] Filip JR Meysman, Bernard P Boudreau, and Jack J Middelburg. “Relations between local, nonlocal, discrete and continuous models of bioturbation”. In: *Journal of Marine Research* 61.3 (2003), pp. 391–410.

[216] Filip JR Meysman, Bernard P Boudreau, and Jack J Middelburg. “When and why does bioturbation lead to diffusive mixing?” In: *Journal of Marine Research* 68.6 (2010), pp. 881–920.

[217] Filip JR Meysman et al. “A generalized stochastic approach to particle dispersal in soils and sediments”. In: *Geochimica et Cosmochimica Acta* 72.14 (2008), pp. 3460–3478.

[218] Filip JR Meysman et al. “The influence of porosity gradients on mixing coefficients in sediments”. In: *Geochimica et cosmochimica acta* 71.4 (2007), pp. 961–973.

[219] Emma Michaud et al. “Use of axial tomography to follow temporal changes of benthic communities in an unstable sedimentary environment (Baie des Ha! Ha!, Saguenay Fjord)”. In: *Journal of Experimental Marine Biology and Ecology* 285 (2003), pp. 265–282.

[220] Jack J Middelburg. “A simple rate model for organic matter decomposition in marine sediments”. In: *Geochimica et Cosmochimica acta* 53.7 (1989), pp. 1577–1581.

[221] Jack J Middelburg. “Carbon Processing at the Seafloor”. In: *Marine Carbon Biogeochemistry*. Springer, 2019, pp. 57–75.

[222] John C Moore, Svetlana Jevrejeva, and Aslak Grinsted. “Efficacy of geoengineering to limit 21st century sea-level rise”. In: *Proceedings of the National Academy of Sciences* 107.36 (2010), pp. 15699–15703.

[223] Helmut Moritz. “Least-squares collocation”. In: *Reviews of geophysics* 16.3 (1978), pp. 421–430.

[224] Bruce M Moskowitz. “Anhysteretic Remanent Magnetization”. In: *Encyclopedia of Geomagnetism and Paleomagnetism*. Springer, 2007, pp. 572–580.

[225] Sandor Mulsow, Bernard P Boudreau, and John A Smith. “Bioturbation and porosity gradients”. In: *Limnology and Oceanography* 43.1 (1998), pp. 1–9.

[226] T NAGATA, Y SHIMIZU, and S UYEDA. “Detrital or Depositional Remanent Magnetization of Sedimentary Rocks”. In: *Rock Magnetism* (1961), p. 222.

[227] Peter D Nooteboom et al. “Transport bias by ocean currents in sedimentary microplankton assemblages: Implications for paleoceanographic reconstructions”. In: *Paleoceanography and Paleoclimatology* 34.7 (2019), pp. 1178–1194.

[228] Charles B Officer and Daniel R Lynch. “Determination of mixing parameters from tracer distributions in deep-sea sediment cores”. In: *Marine Geology* 52.1-2 (1983), pp. 59–74.

[229] Frank Oldfield. “Sources of fine-grained magnetic minerals in sediments: a problem revisited”. In: *The Holocene* 17.8 (2007), pp. 1265–1271.

[230] Yo-ichiro Otofuji and Sadao Sasajima. “A magnetization process of sediments: laboratory experiments on post-depositional remanent magnetization”. In: *Geophysical Journal International* 66.2 (1981), pp. 241–259.

[231] Tingping Ouyang et al. “Variable remanence acquisition efficiency in sediments containing biogenic and detrital magnetites: implications for relative paleointensity signal recording”. In: *Geochemistry, Geophysics, Geosystems* 15.7 (2014), pp. 2780–2796.

[232] Temitope D Timothy Oyedotun. “X-ray fluorescence (XRF) in the investigation of the composition of earth materials: a review and an overview”. In: *Geology, Ecology, and Landscapes* 2.2 (2018), pp. 148–154.

[233] V Palastanga, CP Slomp, and C Heinze. “Glacial-interglacial variability in ocean oxygen and phosphorus in a global biogeochemical model”. In: *Biogeosciences* 10.2 (2013), pp. 945–958.

[234] Vladimir V Palyulin et al. “First passage and first hitting times of Lévy flights and Lévy walks”. In: *New Journal of Physics* 21.10 (2019), p. 103028.

[235] ODP Leg 172 Scientific Party et al. “Geomagnetic field excursions occurred often during the last million years”. In: *Eos, Transactions American Geophysical Union* 79.14 (1998), pp. 178–179.

[236] Alison E Patteson et al. “Particle diffusion in active fluids is non-monotonic in size”. In: *Soft matter* 12.8 (2016), pp. 2365–2372.

[237] André Paul and Christian Schäfer-Neth. “Modeling the water masses of the Atlantic Ocean at the Last Glacial Maximum”. In: *Paleoceanography* 18.3 (2003).

[238] Adina Paytan, Miriam Kastner, and FP Chavez. “Glacial to interglacial fluctuations in productivity in the equatorial Pacific as indicated by marine barite”. In: *Science* 274.5291 (1996), pp. 1355–1357.

[239] T-H Peng, WS Broecker, and WH Berger. “Rates of benthic mixing in deep-sea sediment as determined by radioactive tracers”. In: *Quaternary Research* 11.1 (1979), pp. 141–149.

[240] Tsung-Hung Peng and Wallace S Broecker. “The impacts of bioturbation on the age difference between benthic and planktonic foraminifera in deep sea sediments”. In: *Nuclear Instruments and Methods in Physics Research Section B: Beam Interactions with Materials and Atoms* 5.2 (1984), pp. 346–352.

[241] Harald Petermann and Ulrich Bleil. “Detection of live magnetotactic bacteria in South Atlantic deep-sea sediments”. In: *Earth and Planetary Science Letters* 117.1-2 (1993), pp. 223–228.

[242] David Z Piper and Bradford Fowler. “New constraint on the maintenance of Mn nodules at the sediment surface”. In: *Nature* 286.5776 (1980), pp. 880–883.

[243] SV Poluianov et al. “Production of cosmogenic isotopes 7Be, 10Be, 14C, 22Na, and 36Cl in the atmosphere: Altitudinal profiles of yield functions”. In: *Journal of Geophysical Research: Atmospheres* 121.13 (2016), pp. 8125–8136.

[244] Martin Powilleit, Jarmila Kitlar, and Gerhard Graf. “Particle and fluid bioturbation caused by the priapulid worm Halicryptus spinulosus (v. Seibold)”. In: *Sarsia* 79.2 (1994), pp. 109–117.

[245] Christophe Rabouille et al. “Recycling of organic matter in Antarctic sediments: A transect through the polar front in the Southern Ocean (Indian Sector)”. In: *Limnology and Oceanography* 43.3 (1998), pp. 420–432.

[246] Taoufik Radi and Anne de Vernal. “Last glacial maximum (LGM) primary productivity in the northern North Atlantic Ocean”. In: *Canadian Journal of Earth Sciences* 45.11 (2008), pp. 1299–1316.

[247] Teresa Radziejewska, Igor Modlitba, et al. “Vertical distribution of meiobenthos in relation to geotechnical properties of deep-sea sediment in the IOM pioneer area (Clarion-Clipperton Fracture Zone, NE Pacific)”. In: *Third ISOPE Ocean Mining Symposium*. International Society of Offshore and Polar Engineers. 1999.

[248] G Raisbeck et al. “Direct north-south synchronization of abrupt climate change record in ice cores using Beryllium 10”. In: (2007).

[249] GM Raisbeck et al. “10Be concentration and residence time in the deep ocean”. In: *Earth and Planetary Science Letters* 51.2 (1980), pp. 275–278.

[250] GM Raisbeck et al. “Evidence for an increase in cosmogenic 10Be during a geomagnetic reversal”. In: *Nature* 315.6017 (1985), p. 315.

[251] Daniel C Reed et al. “Steady-state tracer dynamics in a lattice-automaton model of bioturbation”. In: *Geochimica et Cosmochimica Acta* 70.23 (2006), pp. 5855–5867.

[252] Danny Reible and Sanat Mohanty. “A levy flight—random walk model for bioturbation”. In: *Environmental Toxicology and Chemistry: An International Journal* 21.4 (2002), pp. 875–881.

[253] Thomas O Richter et al. “The Avaatech XRF Core Scanner: technical description and applications to NE Atlantic sediments”. In: *Geological Society, London, Special Publications* 267.1 (2006), pp. 39–50.

[254] Benham Rise and Western Philippine Sea. “Nannofossil Biochronology of Tephra Layers in Core MD972143”. In: ().

[255] John A Robbins. “A model for particle-selective transport of tracers in sediments with conveyor belt deposit feeders”. In: *Journal of Geophysical Research: Oceans* 91.C7 (1986), pp. 8542–8558.

[256] Andrew P Roberts. “Geomagnetic excursions: knowns and unknowns”. In: *Geophysical Research Letters* 35.17 (2008).

[257] Andrew P Roberts, Lisa Tauxe, and David Heslop. “Magnetic paleointensity stratigraphy and high-resolution Quaternary geochronology: successes and future challenges”. In: *Quaternary Science Reviews* 61 (2013), pp. 1–16.

[258] Andrew P Roberts and Michael Winklhofer. “Why are geomagnetic excursions not always recorded in sediments? Constraints from post-depositional remanent magnetization lock-in modelling”. In: *Earth and Planetary Science Letters* 227.3-4 (2004), pp. 345–359.

[259] Andrew P Roberts et al. “Magnetotactic bacterial abundance in pelagic marine environments is limited by organic carbon flux and availability of dissolved iron”. In: *Earth and Planetary Science Letters* 310.3-4 (2011), pp. 441–452.

[260] Kevin R Roche et al. “An integrated experimental and modeling approach to predict sediment mixing from benthic burrowing behavior”. In: *Environmental science & technology* 50.18 (2016), pp. 10047–10054.

[261] R Guy Rothwell et al. “Micro-XRF studies of sediment cores: a perspective on capability and application in the environmental sciences”. In: *Micro-XRF studies of sediment cores*. Springer, 2015, pp. 1–21.

[262] Hans Røy et al. “Aerobic microbial respiration in 86-million-year-old deep-sea red clay”. In: *Science* 336.6083 (2012), pp. 922–925.

[263] WF Ruddiman and LK Glover. “Vertical mixing of ice-rafted volcanic ash in North Atlantic sediments”. In: *Geological Society of America Bulletin* 83.9 (1972), pp. 2817–2836.

[264] WF Ruddiman and Andrew McIntyre. “Northeast Atlantic paleoclimatic changes over the past 600,000 years”. In: *Investigation of late Quaternary paleoceanography and paleoclimatology*. Vol. 145. Geol. Soc. of America Mem, 1976, pp. 111–146.

[265] Leonardo Sagnotti et al. “Evidence for a variable paleomagnetic lock-in depth in the Holocene sequence from the Salerno Gulf (Italy): Implications for “high-resolution” paleomagnetic dating”. In: *Geochemistry, Geophysics, Geosystems* 6.11 (2005).

[266] Hiroaki Sakoe and Seibi Chiba. “Dynamic programming algorithm optimization for spoken word recognition”. In: *IEEE transactions on acoustics, speech, and signal processing* 26.1 (1978), pp. 43–49.

[267] Brain Sanderson. “How bioturbation supports manganese nodules at the sediment-water interface”. In: *Deep Sea Research Part A. Oceanographic Research Papers* 32.10 (1985), pp. 1281–1285.

[268] Tatiana Savranskaia et al. “Disentangling magnetic and environmental signatures of sedimentary 10Be/9Be records”. In: *Quaternary Science Reviews* (Manuscript submitted for publication).

[269] Michael J Saxton. “Anomalous diffusion due to obstacles: a Monte Carlo study”. In: *Biophysical journal* 66.2 (1994), pp. 394–401.

[270] Paul Schiffelbein. “Effect of benthic mixing on the information content of deep-sea stratigraphical signals”. In: *Nature* 311.5987 (1984), pp. 651–653.

[271] Reiner Schlitzer. “Applying the adjoint method for biogeochemical modeling: export of particulate organic matter in the world ocean”. In: *GEOPHYSICAL MONOGRAPH-AMERICAN GEOPHYSICAL UNION* 114 (2000), pp. 107–124.

[272] Andreas Schmittner and Amy C Clement. “Sensitivity of the thermohaline circulation to tropical and high latitude freshwater forcing during the last glacial-interglacial cycle”. In: *Paleoceanography* 17.2 (2002), pp. 7–1.

[273] David A Schneider and Dennis V Kent. “Ivory Coast microtektites and geomagnetic reversals”. In: *Geophysical Research Letters* 17.2 (1990), pp. 163–166.

[274] Florian Scholz et al. “Submarine weathering of silicate minerals and the extent of pore water freshening at active continental margins”. In: *Geochimica et Cosmochimica Acta* 100 (2013), pp. 200–216.

[275] Friedrich A Schott, Shang-Ping Xie, and Julian P McCreary Jr. “Indian Ocean circulation and climate variability”. In: *Reviews of Geophysics* 47.1 (2009).

[276] Wolfgang Schwarz. “The Wiener process between a reflecting and an absorbing barrier”. In: *Journal of applied probability* 29.3 (1992), pp. 597–604.

[277] D Seidov et al. “North Atlantic ocean circulation during the last glacial maximum and subsequent meltwater event: a numerical model”. In: *Journal of Geophysical Research: Oceans* 101.C7 (1996), pp. 16305–16332.

[278] Koji Seike, Tomo Kitahashi, and Taisuke Noguchi. “Sedimentary features of Onagawa Bay, northeastern Japan after the 2011 off the Pacific coast of Tohoku Earthquake: sediment mixing by recolonized benthic animals decreases the preservation potential of tsunami deposits”. In: *Journal of oceanography* 72.1 (2016), pp. 141–149.

[279] Kenneth P Severin, Stephen J Culver, and Christian Blanpied. “Burrows and trails produced by Quinqueloculina impressa Reuss, a benthic foraminifer, in fine-grained sediment”. In: *Sedimentology* 29.6 (1982), pp. 897–901.

[280] P. Sharma et al. “Transport of10Be and9Be in the ocean”. In: *Earth and Planetary Science Letters* 86.1 (1987), pp. 69 –76. issn: 0012-821X. doi: `http://dx.doi.org/10.1016/0012-821X(87)90189-0`.

[281] Valeriy Shcherbakov and Natalia Sycheva. “On the mechanism of formation of depositional remanent magnetization”. In: *Geochemistry, Geophysics, Geosystems* 11.2 (2010).

[282] VP Shcherbakov and VV Shcherbakova. “On the physics of acquisition of post-depositional remanent magnetization”. In: *Physics of the earth and planetary interiors* 46.1-3 (1987), pp. 64–70.

[283] Y Shirayama. “Vertical-distribution of meiobenthos in the sediment profile in bathyal, abyssal and hadal deep-sea systems of the western pacific”. In: *Oceanologica Acta* 7.1 (1984), pp. 123–129.

[284] Elizabeth M Shoenfelt et al. “Highly bioavailable dust-borne iron delivered to the Southern Ocean during glacial periods”. In: *Proceedings of the National Academy of Sciences* 115.44 (2018), pp. 11180–11185.

[285] David H Shull. “Transition-matrix model of bioturbation and radionuclide diagenesis”. In: *Limnology and Oceanography* 46.4 (2001), pp. 905–916.

[286] David H Shull and Michie Yasuda. “Size-selective downward particle transport by cirratulid polychaetes”. In: *Journal of Marine Research* 59.3 (2001), pp. 453–473.

[287] Quentin Simon et al. “Authigenic 10 Be/9 Be ratios and 10 Be-fluxes (230 Th xs-normalized) in central Baffin Bay sediments during the last glacial cycle: Paleoenvironmental implications”. In: *Quaternary Science Reviews* 140 (2016b), pp. 142–162.

[288] Quentin Simon et al. “Authigenic 10Be/9Be ratio signature of the Matuyama–Brunhes boundary in the Montalbano Jonico marine succession”. In: *Earth and Planetary Science Letters* 460 (2017), pp. 255–267.

[289] Quentin Simon et al. “Authigenic 10Be/9Be ratio signatures of the cosmogenic nuclide production linked to geomagnetic dipole moment variation since the Brunhes/Matuyama boundary”. In: *Journal of Geophysical Research: Solid Earth* 121.11 (2016a), pp. 7716–7741.

[290] Quentin Simon et al. “Cosmogenic signature of geomagnetic reversals and excursions from the Réunion event to the Matuyama–Brunhes transition (0.7–2.14 Ma interval)”. In: *Earth and Planetary Science Letters* 482 (2018), pp. 510–524.

[291] Quentin Simon et al. “High-resolution 10Be and paleomagnetic recording of the last polarity reversal in the Chiba composite section: Age and dynamics of the Matuyama–Brunhes transition”. In: *Earth and Planetary Science Letters* 519 (2019), pp. 92–100.

[292] Quentin Simon et al. “Increased production of cosmogenic 10 Be recorded in oceanic sediment sequences: Information on the age, duration, and amplitude of the geomagnetic dipole moment minimum over the Matuyama–Brunhes transition”. In: *Earth and Planetary Science Letters* 489 (2018), pp. 191–202.

[293] LJ Snider, BR Burnett, and RR Hessler. “The composition and distribution of meiofauna and nanobiota in a central North Pacific deep-sea area”. In: *Deep Sea Research Part A. Oceanographic Research Papers* 31.10 (1984), pp. 1225–1249.

[294] Karline Soetaert et al. “Assessing organic matter mineralization, degradability and mixing rate in an ocean margin sediment (Northeast Atlantic) by diagenetic modeling”. In: *Journal of Marine Research* 56.2 (1998), pp. 519–534.

[295] Karline Soetaert et al. “Modeling 210Pb-derived mixing activity in ocean margin sediments: diffusive versus nonlocal mixing”. In: *Journal of Marine Research* 54.6 (1996), pp. 1207–1227.

[296] Martin Solan et al. “Worldwide measurements of bioturbation intensity, ventilation rate, and the mixing depth of marine sediments”. In: *Scientific data* 6.1 (2019), pp. 1–6.

[297] JR Southon et al. “10Be in a deep-sea core: implications regarding10Be production changes over the past 420 ka”. In: *Earth and planetary science letters* 85.4 (1987), pp. 356–364.

[298] S Spassov et al. “A lock-in model for the complex Matuyama-Brunhes boundary record of the loess/palaeosol sequence at Lingtai (Central Chinese Loess Plateau)”. In: *Geophysical Journal International* 155.2 (2003), pp. 350–366.

[299] Simo Spassov and Jean-Pierre Valet. “Detrital magnetizations from redeposition experiments of different natural sediments”. In: *Earth and Planetary Science Letters* 351 (2012), pp. 147–157.

[300] Rachel M Spratt and Lorraine E Lisiecki. “A Late Pleistocene sea level stack”. In: *Climate of the Past* 12.4 (2016), pp. 1079–1092.

[301] Guillaume St-Onge et al. “Chapter two continuous physical properties of cored marine sediments”. In: *Developments in marine geology* 1 (2007), pp. 63–98.

[302] Ruediger Stein and Rainer Stax. “Late Quaternary organic carbon cycles and paleoproductivity in the Labrador Sea”. In: *Geo-Marine Letters* 11.2 (1991), pp. 90–95.

[303] Zvi Steiner et al. “The effect of bioturbation in pelagic sediments: lessons from radioactive tracers and planktonic foraminifera in the Gulf of Aqaba, Red Sea”. In: *Geochimica et Cosmochimica Acta* 194 (2016), pp. 139–152.

[304] Konstantin Stolpovsky, Andrew W Dale, and Klaus Wallmann. “A new look at the multi-G model for organic carbon degradation in surface marine sediments for coupled benthic-pelagic simulations of the global ocean”. In: *Biogeosciences (BG)* 15 (2018), pp. 3391–3407.

[305] JS Stoner et al. “South Atlantic and North Atlantic geomagnetic paleointensity stacks (0–80 ka): implications for inter-hemispheric correlation”. In: *Quaternary Science Reviews* 21.10 (2002), pp. 1141–1151.

[306] Carl Störmer. *The polar aurora*. Clarendon Press, 1955.

[307] Yuri I Stozhkov, Peter E Pokrevsky, and Victor P Okhlopkov. “Long-term negative trend in cosmic ray flux”. In: *Journal of Geophysical Research: Space Physics* 105.A1 (2000), pp. 9–17.

[308] Yusuke Suganuma et al. “10 Be evidence for delayed acquisition of remanent magnetization in marine sediments: implication for a new age for the Matuyama–Brunhes boundary”. In: *Earth and Planetary Science Letters* 296.3 (2010), pp. 443–450.

[309] Yusuke Suganuma et al. “Post-depositional remanent magnetization lock-in for marine sediments deduced from 10Be and paleomagnetic records through the Matuyama–Brunhes boundary”. In: *Earth and Planetary Science Letters* 311.1-2 (2011), pp. 39–52.

[310] Donald JP Swift et al. “Contaminant dispersal on the Palos Verdes continental margin II. Estimates of the biodiffusion coefficient, DB, from composition of the benthic infaunal community”. In: *Science of the total environment* 179 (1996), pp. 91–107.

[311] Kazuyo Tachikawa et al. “The precession phase of hydrological variability in the Western Pacific Warm Pool during the past 400 ka”. In: *Quaternary Science Reviews* 30.25-26 (2011), pp. 3716–3727.

[312] Cyrielle Tanty et al. “Acquisition of detrital magnetization in four turbidites”. In: *Geochemistry, Geophysics, Geosystems* 17.8 (2016), pp. 3207–3223.

[313] John A Tarduno. “Superparamagnetism and reduction diagenesis in pelagic sediments: enhancement or depletion?” In: *Geophysical Research Letters* 22.11 (1995), pp. 1337–1340.

[314] L Tauxe and T Yamazaki. *Paleointensities. Geomagnetism, Treatise on Geophysics*. 2007.

[315] Lisa Tauxe. “Sedimentary records of relative paleointensity of the geomagnetic field: theory and practice”. In: *Reviews of geophysics* 31.3 (1993), pp. 319–354.

[316] Lisa Tauxe and Dennis V Kent. “A simplified statistical model for the geomagnetic field and the detection of shallow bias in paleomagnetic inclinations: was the ancient magnetic field dipolar?” In: (2004).

[317] Lisa Tauxe, Jason L Steindorf, and Andrew Harris. “Depositional remanent magnetization: Toward an improved theoretical and experimental foundation”. In: *Earth and Planetary Science Letters* 244.3-4 (2006), pp. 515–529.

[318] Paul Tchernia. “Descriptive regional oceanography”. In: (1980).

[319] Nicholas Teanby and David Gubbins. “The effects of aliasing and lock-in processes on palaeosecular variation records from sediments”. In: *Geophysical Journal International* 142.2 (2000), pp. 563–570.

[320] Lenore P Tedesco and Robert C Aller. “210 Pb chronology of sequences affected by burrow excavation and infilling; examples from shallow marine carbonate sediment sequences, Holocene South Florida and Caicos Platform, British West Indies”. In: *Journal of Sedimentary Research* 67.1 (1997), pp. 36–46.

[321] Felix Temmesfeld. “One million year multi-proxy record of environmental changes in NW Australia”. In: ().

[322] Emile Thellier. “Sur l’intensite du champ magnetique terrestre dans le passe historique et geologique.” In: *Ann. Geophys.* 15 (1959), pp. 285–376.

[323] John Thomson et al. “Radiocarbon age offsets in different-sized carbonate components of deep-sea sediments”. In: *Radiocarbon* 37.2 (1995), pp. 91–101.

[324] Anthony Thornton et al. “Modeling of particle size segregation: calibration using the discrete particle method”. In: *International journal of modern physics C* 23.08 (2012), p. 1240014.

[325] Martin H Trauth, Michael Sarnthein, and Maurice Arnold. “Bioturbational mixing depth and carbon flux at the seafloor”. In: *Paleoceanography* 12.3 (1997), pp. 517–526.

[326] P Tucker. “A grain mobility model of post-depositional realignment”. In: *Geophysical Journal International* 63.1 (1980), pp. 149–163.

[327] E Tuenter et al. “Simulation of climate phase lags in response to precession and obliquity forcing and the role of vegetation”. In: *Climate Dynamics* 24.2-3 (2005), pp. 279–295.

[328] Anthony E Usoro et al. “Some basic properties of cross-correlation functions of n-dimensional vector time series”. In: *Journal of Statistical and Econometric Methods* 4.1 (2015), pp. 63–71.

[329] Akira Usui and Tomoyuki Moritani. “Manganese nodule deposits in the Central Pacific Basin: Distribution, geochemistry, mineralogy, and genesis”. In: *Geology and Offshore Mineral Resources of the Central Pacific Basin*. Springer, 1992, pp. 205–223.

[330] Jean-Pierre Valet. “Time variations in geomagnetic intensity”. In: *Reviews of Geophysics* 41.1 (2003).

[331] Jean-Pierre Valet, Laure Meynadier, and Yohan Guyodo. “Geomagnetic dipole strength and reversal rate over the past two million years”. In: *Nature* 435.7043 (2005), pp. 802–805.

[332] Jean-Pierre Valet, Cyrielle Tanty, and Julie Carlut. “Detrital magnetization of laboratory-redeposited sediments”. In: *Geophysical Journal International* 210.1 (2017), pp. 34–41.

[333] Jean-Pierre Valet et al. “Constraining the age of the last geomagnetic reversal from geochemical and magnetic analyses of Atlantic, Indian, and Pacific Ocean sediments”. In: *Earth and Planetary Science Letters* 506 (2019), pp. 323–331.

[334] Jean-Pierre Valet et al. “Dynamical similarity of geomagnetic field reversals”. In: *Nature* 490.7418 (2012), pp. 89–93.

[335] Jean-Pierre Valet et al. “Geomagnetic, cosmogenic and climatic changes across the last geomagnetic reversal from Equatorial Indian Ocean sediments”. In: *Earth and Planetary Science Letters* 397 (2014), pp. 67–79.

[336] Jean-Pierre Valet et al. “When and why sediments fail to record the geomagnetic field during polarity reversals”. In: *Earth and Planetary Science Letters* 453 (2016), pp. 96–107.

[337] Philippe Van Cappellen, Suvasis Dixit, and Justus van Beusekom. “Biogenic silica dissolution in the oceans: Reconciling experimental and field-based dissolution rates”. In: *Global Biogeochemical Cycles* 16.4 (2002), pp. 23–1.

[338] Philippe Van Cappellen and Linqing Qiu. “Biogenic silica dissolution in sediments of the Southern Ocean. II. Kinetics”. In: *Deep Sea Research Part II: Topical Studies in Oceanography* 44.5 (1997), pp. 1129–1149.

[339] W Van Leussen. “Aggregation of particles, settling velocity of mud flocs a review”. In: *Physical processes in estuaries*. Springer, 1988, pp. 347–403.

[340] Loic Vanel, Anthony D Rosato, and Rajesh N Dave. “Rise-time regimes of a large sphere in vibrated bulk solids”. In: *Physical review letters* 78.7 (1997), p. 1255.

[341] Kenneth L Verosub. “Depositional and postdepositional processes in the magnetization of sediments”. In: *Reviews of Geophysics* 15.2 (1977), pp. 129–143.

[342] F Von Blanckenburg et al. “Global distribution of beryllium isotopes in deep ocean water as derived from Fe Mn crusts”. In: *Earth and Planetary Science Letters* 141.1-4 (1996), pp. 213–226.

[343] Friedhelm Von Blanckenburg and Julien Bouchez. “River fluxes to the sea from the oceans 10Be/9Be ratio”. In: *Earth and Planetary Science Letters* 387 (2014), pp. 34–43.

[344] U Von Stackelberg. “Growth history of manganese nodules and crusts of the Peru Basin”. In: *Geological Society, London, Special Publications* 119.1 (1997), pp. 153–176.

[345] A de Vos, CB Pattiaratchi, and EMS Wijeratne. “Surface circulation and upwelling patterns around Sri Lanka”. In: *Biogeosciences* 11.20 (2014), pp. 5909–5930.

[346] G Wagner et al. “Reconstruction of the geomagnetic field between 20 and 60 kyr BP from cosmogenic radionuclides in the GRIP ice core”. In: *Nuclear Instruments and Methods in Physics Research Section B: Beam Interactions with Materials and Atoms* 172.1-4 (2000), pp. 597–604.

[347] ND Watkins. “Short period geomagnetic polarity events in deep-sea sedimentary cores”. In: *Earth and Planetary Science Letters* 4.5 (1968), pp. 341–349.

[348] Kuo-Yen Wei, Teh-Quei Lee, et al. “Nannofossil biochronology of tephra layers in core MD972143, Benham Rise, western Philippine Sea”. In: *Terrestrial, Atmospheric and Oceanic Sciences* 9.1 (1998), pp. 153–163.

[349] Wei Wei and Thomas J Algeo. “Elemental proxies for paleosalinity analysis of ancient shales and mudrocks”. In: *Geochimica et Cosmochimica Acta* (2019).

[350] Gert Jan Weltje and Rik Tjallingii. “Calibration of XRF core scanners for quantitative geochemical logging of sediment cores: Theory and application”. In: *Earth and Planetary Science Letters* 274.3-4 (2008), pp. 423–438.

[351] Michael L Wenocur. “Diffusion first passage times: approximations and related differential equations”. In: *Stochastic processes and their applications* 27 (1987), pp. 159–177.

[352] Joseph T Westrich and Robert A Berner. “The role of sedimentary organic matter in bacterial sulfate reduction: The G model tested 1”. In: *Limnology and oceanography* 29.2 (1984), pp. 236–249.

[353] Robert A Wheatcroft. “Experimental tests for particle size-dependent bioturbation in the deep ocean”. In: *Limnology and Oceanography* 37.1 (1992), pp. 90–104.

[354] Robert A Wheatcroft. “Preservation potential of sedimentary event layers”. In: *Geology* 18.9 (1990), pp. 843–845.

[355] Robert A Wheatcroft and Peter A Jumars. “Statistical re-analysis for size dependency in deep-sea mixing”. In: *Mar. Geol* 77 (1987), pp. 157–163.

[356] Robert A Wheatcroft, Ilhan Olmez, and Francis X Pink. “Particle bioturbation in Massachusetts Bay: preliminary results using a new deliberate tracer technique”. In: *Journal of Marine Research* 52.6 (1994), pp. 1129–1150.

[357] Robert B Whitlatch. “On some mechanistic approaches to the study of deposit feeding in polychaetes”. In: *Ecology of marine deposit feeders*. Springer, 1989, pp. 291–308.

[358] Sarath Wijeratne, Charitha Pattiaratchi, and Roger Proctor. “Estimates of surface and subsurface boundary current transport around Australia”. In: *Journal of Geophysical Research: Oceans* 123.5 (2018), pp. 3444–3466.

[359] Joan D Willey. “Release and uptake of dissolved silica in seawater by marine sediments”. In: *Marine Chemistry* 7.1 (1978), pp. 53–65.

[360] H Wittmann et al. “The competition between coastal trace metal fluxes and oceanic mixing from the 10Be/9Be ratio: Implications for sedimentary records”. In: *Geophysical Research Letters* 44.16 (2017), pp. 8443–8452.

[361] H Wittmann et al. “The dependence of meteoric 10Be concentrations on particle size in Amazon River bed sediment and the extraction of reactive 10Be/9Be ratios”. In: *Chemical Geology* 318 (2012), pp. 126–138.

[362] Goesta Wollin et al. “Magnetism of the earth and climatic changes”. In: *Earth and Planetary Science Letters* 12.2 (1971), pp. 175–183.

[363] Horst-Ulrich Worm. “A link between geomagnetic reversals and events and glaciations”. In: *Earth and Planetary Science Letters* 147.1 (1997), pp. 55–68.

[364] Qi-Feng Xie et al. “Geochemical characteristics of the Permian marine mudstone and constraints on its provenance and paleoenvironment in the Fenghai area, Fujian Province, southeastern China”. In: *Petroleum Science* 16.3 (2019), pp. 527–540.

[365] Chuang Xuan and James ET Channell. “Origin of orbital periods in the sedimentary relative paleointensity records”. In: *Physics of the Earth and Planetary Interiors* 169.1-4 (2008), pp. 140–151.

[366] Toshitsugu Yamazaki and Hirokuni Oda. “Intensity-inclination correlation for long-term secular variation of the geomagnetic field and its relevance to persistent non-dipole components”. In: *Timescales of the Paleomagnetic Field* (2004), pp. 287–298.

[367] Toshitsugu Yamazaki et al. “Rock-magnetic artifacts on long-term relative paleointensity variations in sediments”. In: *Geochemistry, Geophysics, Geosystems* 14.1 (2013), pp. 29–43.

[368] Shoji Yoshida and Ikuo Katsura. “Characterization of fine magnetic grains in sediments by the suspension method”. In: *Geophysical Journal International* 82.2 (1985), pp. 301–317.

[369] Zhaojie Yu et al. “Co-evolution of monsoonal precipitation in East Asia and the tropical Pacific ENSO system since 2.36 Ma: New insights from high-resolution clay mineral records in the West Philippine Sea”. In: *Earth and Planetary Science Letters* 446 (2016), pp. 45–55.

[370] Michelle Zarriess and Andreas Mackensen. “The tropical rainbelt and productivity changes off northwest Africa: A 31,000-year high-resolution record”. In: *Marine Micropaleontology* 76.3-4 (2010), pp. 76–91.

[371] Wenyan Zhang and Kai Wirtz. “Mutual dependence between sedimentary organic carbon and infaunal macrobenthos resolved by mechanistic modeling”. In: *Journal of Geophysical Research: Biogeosciences* 122.10 (2017), pp. 2509–2526.

[372] La-La Zhao et al. “DEM study of size segregation of wet particles under vertical vibration”. In: *Advanced Powder Technology* 30.7 (2019), pp. 1386–1399.

[373] Xiangyu Zhao et al. “Microbially assisted recording of the Earth’s magnetic field in sediment”. In: *Nature communications* 7.1 (2016), pp. 1–7.

[374] Weijian Zhou et al. “Timing of the Brunhes-Matuyama magnetic polarity reversal in Chinese loess using 10Be”. In: *Geology* 42.6 (2014), pp. 467–470.

[375] Sijia Zou et al. “Observed and modeled pathways of the Iceland Scotland Overflow Water in the eastern North Atlantic”. In: *Progress in Oceanography* 159 (2017), pp. 211–222.